

Determination of Hydrogen Peroxide Concentration in Water-Hydrogen Peroxide Aerosols

Alexander James Porkovich

PhD Thesis

Faculty of Science, University of Technology, Sydney

Institute for Nanoscale Technology

2012

Certificate of Authorship

I certify that the work in this thesis has not previously been submitted for a degree, nor has it been submitted as part of requirements for a degree fully acknowledged within the text.

I certify that the thesis has been written by me. Any help that I have received in my research work and the preparation of the thesis itself has been acknowledged. I certify that all information sources and literature used are indicated in the thesis.

Signature: _____

Acknowledgements

I would first like to express my sincere gratitude to my principle supervisor Prof. Michael Cortie for the opportunity to work on this project and the guidance he provided through it. I would also like to extend my sincerest thanks to my co-supervisor Dr. Matthew Arnold for his guidance and input throughout, including his assistance with the matrix algebra developed for the optical absorption measurements.

Funding and generous material support of this project was provided by Nanosonics Limited, and I am grateful to them for this and for providing data on droplet sizes of hydrogen peroxide produced by their nebuliser. Two individuals at Nansonics Limited, Dr. Galina Kouzmina and Mr. Brian Hingley, were key to the successful implementation of this project and I wish to specifically thank them for their involvement and assistance. Mr Hingley's deep knowledge of practical electronics was a major factor in this project as was Dr Kouzmina's chemical engineering expertise.

Several people at the University of Technology Sydney helped me during the course of this project. I would like to thank Mr. Geoff McCredie and Dr. Angus Gentle for their invaluable assistance with the RTD coating, Mr. Mark Berkahn and Dr. Annette Dowd for their invaluable assistance in obtaining X-ray diffraction patterns of my samples, Dr. Ric Wuhrer for his assistance in obtaining scanning electron microscope images, Dr. Catherine Kealley for her insights on the prospect of a monochromatic refractometric sensor, and Dr. Andrew McDonagh for general ideas and discussion. My fellow PhD students, particularly Michael Coutts, Jonathan Mak, Jonathon Edgar, Pew Supitcha and Amir Moezzi, have been supportive too, providing both an exchange of ideas and encouragement.

Finally, I would like to thank the Australian Synchrotron for access to the Powder Diffraction beamline at the Australian Synchrotron, Victoria, Australia.

At a personal level, I also wish to take this opportunity to sincerely thank my family for the support, encouragement and guidance that they have provided both in life and through my studies. My sincerest thanks to my mother Marie Anne, my father Boris, my

step-mother Susan, my grandparents Helen and Peter and my auntie Sonja and uncle Joe for all your support, encouragement and guidance in reaching this point.

List of Publications Produced

A.J. Porkovich, M.D. Arnold, G. Kouzmina, B. Hingley, A.Dowd, M.B. Cortie, *Calorimetric sensor for use in hydrogen peroxide aqueous solutions*, *Sensors Letters*, **9** (2011) 695-697.

A.J. Porkovich, M.D. Arnold, G. Kouzmina, B. Hingley, M.B. Cortie, *Calorimetric Sensor for H₂O₂/H₂O Mist Streams*, *IEEE Sensors Journal*, **12** (2012) 2392-2398.

C.S. Kealley, M.D. Arnold, A. Porkovich, M.B. Cortie, *Sensors based on monochromatic interrogation of a localised surface plasmon resonance*, *Sensors and Actuators, B*, **148** (2010) 34-40.

Table of Contents

Certificate of Authorship.....	i
Acknowledgements	ii
List of Publications Produced	iv
List of Figures	viii
List of Tables.....	xxii
Abstract	xxiv
Chapter 1 Introduction	1
Chapter 2 Chemical Hydrogen Peroxide Sensors	6
2.1 Amperometric Sensors.....	6
2.2 Potentiometric Sensors.....	8
2.3 Optochemical Sensors.....	9
2.4 Calorimetric Sensors	11
2.5 Catalysts for the Decomposition of Hydrogen Peroxide.....	13
Chapter 3 Physical Chemical Sensors.....	17
3.1 Refractometric Sensors.....	17
3.1.1 Angular Refractometric Sensors	17
3.1.2 Waveguide Sensors.....	19
3.1.3 Standing Wave Resonators	30
3.2 Electroluminescence Sensors.....	38
3.3 Spectroscopic Sensors.....	38
Chapter 4 General Experimental.....	44
4.1 Data Analysis.....	44
4.1.1 Linear Regression	44
4.1.2 Non-Linear Regression	45
4.1.3 Multiple Linear Regression	45
4.1.4 Analysis of Variance	45
4.2 Determination of Concentration of Hydrogen Peroxide	46
4.3 Porous Platinum Films	47
4.3.1 Method of Deposition and Analysis.....	47

4.3.2 Results of Platinum Alloy and Porous Platinum Analysis.....	49
4.3.3 Summary of Porous Platinum Films	56
4.4 Construction of Calorimetric Sensors	57
4.4.1 Porous Pt-coated RTD Construction	57
4.4.2 MnO ₂ -coated RTD Construction.....	59
4.4.3 Uncoated RTD Construction.....	60
4.4.4 Summary of Sensor Construction	60
4.5 Measurement of Pt-coated, MnO ₂ -coated and uncoated RTD behaviour in air, liquid water and water mist.....	61
4.5.1 Heat Transfer in Air	62
4.5.2 Heat Transfer in Other Fluids.....	65
Chapter 5 Response of the Calorimetric Sensor in Bulk Liquids and Non-mist Droplets	69
5.1 Sensor Behaviour during Immersion in Aqueous Hydrogen Peroxide.....	69
5.1.1 Method	69
5.1.2 Results and Discussion	73
5.1.3 Concentration determination during the immersion period.....	78
5.1.4 Concentration determination during the post immersion period.....	80
5.1.5 Summary of immersion testing.....	87
5.2 Sensor Behaviour Due to Hydrogen Peroxide Droplets on the Sensor in the Test Rig.....	88
5.2.1 Method for Ambient Investigation	88
5.2.2 Results from Ambient Investigation	89
5.2.3 Ambient Droplet Investigation Summary	97
5.2.4 Method for Heated Investigation	98
5.2.5 Results from Heated Investigation.....	99
5.2.6 Heated RTD Investigation Summary	104
5.3 Summary of Immersion Experiments	105
Chapter 6 Testing of the Calorimetric Sensor in Mist	108
6.1 Characterisation of the Mist	110
6.1.1 Method for Determination of Mist Flux	111
6.1.2 Results for the Determination of Mist Flux.....	111
6.1.3 The Size of Mist Droplets	113
6.2 Detection of Hydrogen Peroxide Concentration in Mist Using Unheated RTDs.....	114

6.2.1 Method for Detection of Hydrogen Peroxide in Mist Using Unheated RTDs	114
6.2.2 Results for Detection of Hydrogen Peroxide in Mist Using Unheated RTDs for 2 Minute Mist Cycles.....	116
6.2.3 Determining a Signal from Data During the Mist Cycle ('On-Line')	120
6.2.4 Determining a Signal from Data During the Drying Cycle ('Off-Line').....	123
6.2.5 Results for Detection of Hydrogen Peroxide in Mist Using Unheated RTDs for 3 Minute Mist Cycles.....	126
6.2.6 Determining a Signal from Data During the Mist Cycle ('On-Line')	127
6.2.7 Determining a Signal from Data During the Drying Cycle ('Off-Line').....	129
6.2.8 Comparison of 2 and 3 Minute Cycles to Shorter and Longer Cycles	133
6.2.9 Summary of Experiments Using Unheated RTDs.....	134
6.3 Detection of Hydrogen Peroxide Concentration in Mist Using Heated RTDs.....	137
6.3.1 Method of Detection of Hydrogen Peroxide Concentration in Mist Using Heated RTDs	137
6.3.2 Results of Detection of Hydrogen Peroxide Concentration in Mist Using Heated RTDs	138
6.3.3 Summary of experiments using Heated RTDs.....	144
6.4 Overall Summary of Mist Sensor Experiment.....	146
Chapter 7 Physical Optical Sensor	150
7.1 Refractometric Sensor	150
7.1.1 Theoretical Refractometric Nanoparticle LSPR Response to Hydrogen Peroxide ...	150
7.1.2 Method of Investigation of Refractometric Nanoparticle Sensor	151
7.1.3 Results of Investigation of Refractometric Nanoparticle Sensor	152
7.1.4 Summary of Refractometric Hydrogen Peroxide Sensor	158
7.2 Hydrogen Peroxide Sensor Based on Absorption Spectroscopy	159
7.2.1 Method of Investigation of Hydrogen Peroxide Liquid Absorption.....	164
7.2.2 Results of Investigation of Hydrogen Peroxide Liquid Absorption	167
7.2.3 Investigation of spectroscopic specificity against other compounds	181
7.2.4 Absorption of Mist	185
7.2.5 Summary of Hydrogen Peroxide Absorption	192
7.3 Summary of Physical Optical Sensor Investigation.....	194
Chapter 8 Conclusions and Future Work.....	197
References	201
Appendix.....	A-1

List of Figures

Figure 2-1 Redrawn from <i>Study on a hydrogen peroxide biosensor based on horseradish peroxidase/GNPs-thionine/chitosan</i> [13]. Illustration of how the mediator is oxidised not the HRP.	7
Figure 3-1 Redrawn from <i>NIR spectroscopic application of a refractometric sensor</i> [92]. The schematic view of the U-bend waveguide sensor in measuring position, with an arbitrary ray trace.	20
Figure 3-2 Redrawn from <i>ARROW optical waveguides based sensors</i> [89]. The structure of an ARROW, n refers to refractive index and subscript to the n refers to the layer of the waveguide.....	21
Figure 3-3 Redrawn from <i>ARROW optical waveguides based sensors</i> [89]. Hollow core ARROW waveguide structure, n refers to refractive index.	22
Figure 3-4 Redrawn from <i>An intrinsic fibre optic chemical sensor based on light coupling phenomenon</i> [87]. The schematic diagram of hollow core waveguide.....	23
Figure 3-5 Redrawn from <i>An embedded optical nanowire loop resonator refractometric sensor</i> [75].The structure of an embedded optical nanowire loop resonator (ENLR) refractometric sensor.....	24
Figure 3-6 Redrawn from <i>Optical microfiber coil resonator refractometric sensor</i> [82]. The structure of the coated all-coupling nanowire microcoil resonator (CANMR).	25
Figure 3-7 Redrawn from <i>Interferometric biosensor based on planar optical waveguide sensor chips for label-free detection of surface bound bioreactions</i> [79]. The set-up of a Young interferometer refractive index sensor, and an example of the resultant interferogram.....	26
Figure 3-8 Redrawn from <i>Long-period grating Michelson refractometric sensor</i> [90]. The a) complete set-up of the sensor and b) the structure of the Michelson interferometer.....	27
Figure 3-9 Redrawn from <i>Label-free highly sensitive detection of (small) molecules by wavelength interrogation of integrated optical chips</i> [91]. The basic structure of the wavelength interrogated optical sensor (WIOS). The refractive index being measured is n_c	28
Figure 3-10 Redrawn from <i>Micro-fluidic analysis based on total internal light reflection</i> [83]. The schematic of a micro-fluidic analysis system based on total internal	

light reflection (TIR), with the following aspects highlighted 1-incident light beam, 2-TIR prism, 3-diffraction grating, 4-micro-fluidic channel, 5-inlet and outlet nozzles to the channel and 6-diffraction orders.	29
Figure 3-11 Redrawn from <i>Integrated photonic glucose biosensor using a vertically coupled microring resonator in polymers</i> [73]. A cross section of a schematic of a microring and bus in the pedestal type conformation.	31
Figure 3-12 Redrawn from <i>Refractometric sensors for Lab-on-a-Chip based on optical ring resonators</i> [81]. Schematic of liquid core optical ring resonator (LCORR) a) the set-up of capillaries and fibres and b) the inside of a capillary that has been functionalised for sensing biomolecules.....	32
Figure 3-13 Redrawn from <i>Refractometric sensors for Lab-on-a-Chip based on optical ring resonators</i> [81]. A schematic of a microsphere WGM resonator functionalised as a sensor for biomolecules.....	33
Figure 3-14 Redrawn from <i>Refractometric sensors for Lab-on-a-Chip based on optical ring resonators</i> [81]. The set-up of a sensor based on microsphere WGM resonators.	34
Figure 3-15 Redrawn from <i>Liquid-infiltrated photonic crystals-enhanced light-matter interactions for lab-on-a-chip applications</i> [69]. Schematic of the dielectric function variations in a photonic crystal. High refractive index material is labelled as ϵ_d (grey) and the liquid analyte is labelled as ϵ_l (blue).....	35
Figure 4-1 The X-ray diffraction patterns of alloyed samples with differing power applied to the aluminium target. Also shown are the known or calculated JC-PDF cards that appear to match up with some parts of the patterns. CuK α radiation was used for this data. Data obtained with assistance of Mr Mark Berkahn, UTS.	50
Figure 4-2 SEM micrographs of porous platinum samples. The left column is a view of the surface structure while the right hand column is a close-up on the pores of the sample.	52
Figure 4-3 Phase diagram of Pt-Al. Diagram is from Building a thermodynamic database for platinum-based superalloys: Part I, in <i>Platinum Metals Rev.</i> , by L.A. Cornish et. al.[165].....	53
Figure 4-4 The X-ray diffraction patterns taken by the synchrotron of porous Pt from alloy samples. Power applied to aluminium target during deposition is shown. Synchrotron radiation was used for this data. Data obtained with the assistance of the Dr Catherine Kealley and Dr Annette Dowd, UTS.....	54

Figure 4-5 The X-ray diffraction patterns taken by the synchrotron of alloy samples made at different substrate temperatures, which are shown with label. ALPT20, ALPT17 and the glass substrate are also shown together in a “zoomed” comparison in the figure on the right. Data obtained with the assistance of the Dr Catherine Kealley and Dr Annette Dowd, UTS.....55

Figure 4-6 The X-ray diffraction patterns taken by the synchrotron of porous Pt from alloy samples made at different substrate temperatures which are shown in the figure. Data obtained with the assistance of the Dr Catherine Kealley and Dr Annette Dowd, UTS.56

Figure 4-7 A picture of a) the rotor and the radiant heater and b) a close-up of the sample holder57

Figure 4-8 RTDs in metal housing.....58

Figure 4-9 SEM micrograph of the Coated RTD that covered in a) Al₂Pt and b) porous-Pt59

Figure 4-10 The XRD pattern of MnO₂ powder and the lines for the JC-PDF card 00-024-0735 β-MnO₂ (‘pyrolusite’). CuKα radiation was used. Data obtained with assistance of Mr Mark Berkahn, UTS.....60

Figure 4-11 An example of the calculation heat transfer coefficient, *h*, for RTDs A and B in still air. The dotted line represents the point at which the RTD temperature was stable and is the point that *h* is taken from. Each chart represents a different input power of a) 9 mW b) 75 mW c) 180 mW and d) 310 mW.62

Figure 4-12 The average heat transfer coefficient of RTD A (●) and RTD B (◆) for different temperatures of the RTD in air. Error bars represent 1 standard deviation.....63

Figure 4-13 The average heat transfer coefficient of RTD C (●) and RTD D (◆) for different temperatures of the RTD in a) still air and b) in flowing air. Error bars represent one standard deviation.64

Figure 4-14 The average heat transfer coefficient of RTD A (●) and RTD B (◆) for different temperatures of the RTD in water. Error bars represent 1 standard deviation. 65

Figure 4-15 The average heat transfer coefficient of RTD C (●) and RTD D (◆) for different temperatures of the RTD in 20% duty cycle water mist with an air flow of 7.5L/min. Error bars represent one standard deviation.66

Figure 4-16 Example of mist experiment at 82°C showing drop of *h* during period that is typically stable67

Figure 5-1 a) Picture of the sensor set-up showing the test tube rack holding the sensors in place; b) Picture showing the sensors in hydrogen peroxide. Bubbles are visible on the Pt coated RTD (top, circled), while there is no reaction on the uncoated (bottom).. 72

Figure 5-2 The mass of hydrogen peroxide loss due to decomposition using Pt-coated catalyst over time for 10% (×), 20% (▲) and 35% (●) hydrogen peroxide. 74

Figure 5-3 The power of hydrogen peroxide decomposition from a Pt coated RTD vs the concentration of hydrogen peroxide with regression line. Dotted lines are upper and lower limits of 2-sigma confidence interval. Note that the regression is constrained to pass through (0,0)..... 75

Figure 5-4 The calculated maximum change in temperature of the coated sensor based on the empirically calculated h for water and the calculated heat of decomposition of hydrogen peroxide assuming all heat generated in the boundary layer goes into the sensor. The dotted lines represent the calculation of temperature change using a sigma confidence interval for h 76

Figure 5-5 Recorded temperature of the coated (solid line) and uncoated (dotted line) RTDs plotted against time for, a) MilliQ water, b) 10% hydrogen peroxide, c) 25% hydrogen peroxide, d) 35% hydrogen peroxide, e) 42% hydrogen peroxide and f) 50% hydrogen peroxide..... 77

Figure 5-6 The difference in temperature between the Pt-coated and uncoated RTDs. The line represents the linear regression, while the dotted lines represent the upper and lower values of the 2-sigma confidence interval..... 78

Figure 5-7 The expected concentration from measured temperature difference in temperature between Pt-coated and uncoated RTDs during immersion vs the concentration of hydrogen peroxide (%(w/w)). The dotted lines indicated a 2-sigma confidence interval. 80

Figure 5-8 The heat energy of decomposition of hydrogen peroxide (solid black line) and vaporisation of water (dotted black line) and hydrogen peroxide (solid grey line) for each concentration of hydrogen peroxide from 0% to 50% (w/w). These values were determined from hydrogen peroxide’s molar heat of decomposition (shown in Equation 1-1) and the boiling point heat of vaporisation for hydrogen peroxide and water from Table 1-1. 81

Figure 5-9 Graphical representation of heat flows of catalyst surface and hydrogen peroxide droplets. This graph is not to any scale, just a qualitative representation of the

magnitude of heat flows during decomposition. The size of the arrow describes the magnitude of the heat flow.....	82
Figure 5-10 The difference between temperature of the Pt-coated RTD at its “peak” post-immersion and the Pt-coated sensor during immersion.	82
Figure 5-11 The time the taken for the reaction to reach a maximum temperature for each concentration of hydrogen peroxide (time started from 0).....	83
Figure 5-12 The regression line of the peak temperature vs the concentration of hydrogen peroxide, with 2-sigma confidence interval shown as the dotted line. Raw data points (•) are also shown.....	84
Figure 5-13 The regression line of the time to peak temperature vs the concentration of hydrogen peroxide, with 2-sigma confidence interval shown as a dotted line. Raw data points (•) are also shown.....	85
Figure 5-14 The calculated concentration from the regression vs the experimental concentration used, with raw data (•) shown.....	86
Figure 5-15 Picture of the mist test rig focused on the test chamber.....	89
Figure 5-16 The mass loss of hydrogen peroxide due to decomposition using MnO ₂ catalyst over time for 10% (×), 20% (▲) and 35% (●) hydrogen peroxide.	90
Figure 5-17 The power of hydrogen peroxide decomposition from a MnO ₂ coated RTD vs the concentration of hydrogen peroxide with regression line. Dotted lines are upper and lower limits of 2-sigma confidence interval.....	91
Figure 5-18 The change in temperature of the a) MnO ₂ coated RTD and the b) uncoated RTD in response to droplets of MilliQ water deposited on the RTDs in the presence of no airflow (dotted lines), 7.5 L/min airflow (solid black line) and 12.2 L/min airflow (solid grey line). Droplets were deposited every 100 seconds.....	92
Figure 5-19 Average final temperature of each water droplet run for coated (■) and uncoated (●). Error bars represent 1 standard deviation	93
Figure 5-20 The temperature difference between RTDs over time for each droplet of a) MilliQ water b) 10% hydrogen peroxide c) 22.5% hydrogen peroxide d) 35% hydrogen peroxide and e) 45% hydrogen peroxide. The different colours are different runs and all first runs have been omitted. All graphs are zeroed, however, there is a negative temperature spike when the droplet is added which overwhelms this.	94

Figure 5-21 The average temperature difference between the peak-initial temperature (temperature change) of the MnO₂-coated (●) and the uncoated (×) RTDs. Error bars represent 1 standard deviation..... 96

Figure 5-22 Concentration of hydrogen peroxide against the difference between peak temperature with linear regression line and 2-sigma confidence interval (dotted lines) 97

Figure 5-23 An example of the output data converted to watts from the LabVIEW program for the heated RTD experiment. Samples are a) water and b) 30% hydrogen peroxide, with RTDs heated to 105°C. The dotted lines represent the uncoated RTD, while the solid lines represent the coated RTD. The hydrogen peroxide pulses took longer to vaporise, therefore requiring longer runs and later pulses. The droplets were loaded onto each RTD by hand, and the delay between the pulses is the result of the time taken to load each one individually..... 99

Figure 5-24 The energy drawn over time of experiment when each RTD was set to 80°C. Graphs show a) water, b) 10% hydrogen peroxide, c) 20% hydrogen peroxide, d) 30% hydrogen peroxide, e) 35% hydrogen peroxide and f) 40% hydrogen peroxide. Solid lines are coated RTD, dotted lines are uncoated..... 101

Figure 5-25 The average energy drawn per droplet against concentration for sensors held at 80°C. Symbols represent coated RTD response (◇) and uncoated RTD response (◆)..... 102

Figure 5-26 The average energy drawn per droplet against concentration for a) 105°C and b) 130°C. Symbols represent coated RTD response (◇) and uncoated RTD response (◆)..... 103

Figure 6-1 Flow process diagram of calorimetric mist sensor test rig..... 109

Figure 6-2 Photo of the mist chamber during operation 110

Figure 6-3 The mist flux of water (●), 35% (■), 45% (○) and 50% (×) hydrogen peroxide determined as the slopes of each regression of mass lost from the bottle of hydrogen peroxide, and the quadratic regression calculated values of water (blue), 35%, (red), 45% (green) and 50% (black). The error bars represent the 2-sigma error of the mist flux. 111

Figure 6-4 The actual mist flux vs the calculated mist flux, with linear regression (solid line) and the 2-sigma confidence interval (dotted lines)..... 112

Figure 6-5 The size distribution of 35% hydrogen peroxide mist droplets produced using a voltage of 26V applied to the transducer. Study was commissioned by Nanosonics in collaboration with Sydney University..... 113

Figure 6-6 An example of the response of the bare (dotted line) and coated (solid line) RTD to hydrogen peroxide of concentrations a) 0%, b) 5% , c) 10%, d) 15%, e) 20%, f) 25%, g) 30% and h) 35%. Temperature measurements of the liquid in the cup (●) and air entering the fan (○) is also presented. Steps in the solid straight line at the bottom of each graph represents the period that the nebuliser was on for..... 117

Figure 6-7 A typical response of the coated (red line) and uncoated (blue line) RTDs to mist. The ambient temperature of the air entering the fan (■) and of the liquid in the cup (◆) are also shown connected with a dotted line (this was not measured but is included to show the overall trend of increasing and decreasing ambient temperatures). The solid steps indicate when the mist pulse was on. Specific times are marked on the graph where something important has occurred, t_1 is when the nebuliser is turned on and the mist pulse starts, t_2 is when the mist reaches the RTDs, t_3 is when the temperature of the RTDs reach the temperatures of the RTDs are the same, while t_4 is when the coated RTD begins to reach an thermal equilibrium with the mist, and t_5 is when the nebuliser is turned off and the mist pulse ended. At t_6 the coated RTD reaches a temperature minimum, at which point the energy of vaporisation is overcome by the decomposition of hydrogen peroxide and the temperature of the RTD begins to increase, as the RTD “dries”. At t_7 , the temperature of the uncoated RTD is also slightly increasing, however much slower than the coated as there is no decomposition to drive vaporisation, and at t_8 it can be seen that the coated RTD is almost back to the temperature it was before the mist cycle. Finally, at t_9 the next mist pulse starts, and the process repeats. The example given is from 15% hydrogen peroxide..... 118

Figure 6-8 The difference in temperature of the a) uncoated (○) and coated (●) RTDs from before the mist was turned on to after the mist was turned off and b) is only the hydrogen peroxide measurements on the coated RTD. 121

Figure 6-9 The concentration of hydrogen peroxide compared to the temperature response of the RTD. Line of linear regression predicts concentration from temperature response and dotted lines represent 2-sigma confidence interval. 122

Figure 6-10 The linear section of the concentration of hydrogen peroxide against the difference between uncoated and coated RTD response signal. Solid line represents the

linear regression of the data and the dotted lines represent a 2-sigma confidence interval. 122

Figure 6-11 a) The difference between the temperature of the coated RTD at the minimum temperature after the mist cycle and the temperature at the end of the mist cycle, b) the time that the coated RTD temperature is at a minimum after the mist cycle. Solid lines are 3rd order polynomial regressions and dotted lines are the 2-sigma confidence intervals. 123

Figure 6-12 Concentration of hydrogen peroxide as a function of temperature difference between the end of the mist cycle and minimum temperature reached after the mist. Solid line represents cubic regression and dotted lines represent 2-sigma confidence interval..... 124

Figure 6-13 Concentration of hydrogen peroxide as a function of the time the minimum temperature was reached. Solid line represents cubic regression and dotted lines represent 2-sigma confidence interval. 125

Figure 6-14 The actual concentration of hydrogen peroxide as a function of the average calculated hydrogen peroxide using the regressions for time to minimum temperature and difference between end of cycle temperature and minimum temperature. 125

Figure 6-15 The difference in temperature of the a) uncoated (○) and coated (●) RTDs from before the mist was turned on to after the mist was turned off and b) is only the hydrogen peroxide measurements on the coated RTD, for three-minute mist pulses. . 127

Figure 6-16 The concentration of hydrogen peroxide compared to the temperature response of the coated RTD exposed to three-minute mist pulses. Line of linear regression predicts concentration from temperature response and dotted lines represent 2-sigma confidence interval. 128

Figure 6-17 The difference between uncoated and coated RTD temperatures for different concentrations of hydrogen peroxide exposed to three minute mist pulses... 129

Figure 6-18 a) The difference between the temperature of the coated RTD at the minimum temperature after the mist cycle and the temperature at the end of the mist cycle, b) the time that the coated RTD temperature is at a minimum after a 3 minute mist cycle. Solid lines are 3rd order polynomial regressions and dotted lines are the 2-sigma confidence intervals..... 130

Figure 6-19 The mist flux of the hydrogen peroxide calculated from the calibration curve (○) and the corresponding calculated power predicted to be released due to

vaporisation of mist droplets (●). Decomposition of hydrogen peroxide is assumed to increase vaporisation of droplets.....	130
Figure 6-20 Concentration of hydrogen peroxide as a function of the time the minimum temperature was reached for 3 minute mist cycle. Solid line represents cubic regression and dotted lines represent 2-sigma confidence interval.	131
Figure 6-21 Concentration of hydrogen peroxide as a function of temperature difference between the end of the mist cycle and minimum temperature reached after 3 minute mist cycle. Solid line represents cubic regression and dotted lines represent 2-sigma confidence interval.	132
Figure 6-22 The actual concentration of hydrogen peroxide as a function of the average calculated hydrogen peroxide using the regressions for time to minimum temperature and difference between end of cycle temperature and minimum temperature for 3 minute mist cycles.....	133
Figure 6-23 The RTD response to 20% mist cycle for 35% hydrogen peroxide with mist cycle length lasting a) 30 seconds and b) 4 minutes. Solid lines denote coated RTD and dotted lines denote uncoated RTD.	133
Figure 6-24 The difference in response between uncoated and coated RTDs at the end of the mist cycle for 35% hydrogen peroxide for different mist cycle times.	134
Figure 6-25 The response of coated (blue line) and uncoated (red line) RTDs in a mist of a) water and b) 40% hydrogen peroxide. The black line shows the mist pulse (the step is when the mist is on). The mist duty cycle is set to 20%.	138
Figure 6-26 The average response of the uncoated (○) and coated (●) RTDs to different concentrations of hydrogen peroxide at duty cycles a) 7.5, b) 10%, c) 15%, d) 20%, e) 25% and f) 30%. Error bars represent 1 standard deviation.	139
Figure 6-27 The average energy drawn against the mist flux by the a) uncoated and b) coated RTDs at different concentrations of hydrogen peroxide. The error bars represent 1 standard deviation.	140
Figure 6-28 The actual mist flux from the calibration against the mist flux calculated from the regression of the energy drawn and hydrogen peroxide concentration for the a) uncoated and b) coated RTDs. Solid line represents the regression and the dotted lines represent a 2-sigma confidence interval.....	141
Figure 6-29 The average difference between energy drawn by the uncoated-coated RTDs for different concentrations of hydrogen peroxide for duty cycles of a) 7.5%, b)	

10%, c) 15%, d) 20%, e) 25% and f) 30%. The error bars represent 1 standard deviation. Solid lines are the polynomial regressions of the concentration of hydrogen peroxide and difference in energy drawn and the dotted lines represent the 2-sigma confidence interval of the regression. 142

Figure 6-30 The average drawn energy difference between uncoated and coated RTDs against the mist flux at different concentrations of hydrogen peroxide. The error bars represent 1 standard deviation. 143

Figure 7-1 The absorbance spectrum of the gold nanorods used. 153

Figure 7-2 The absorbance spectra of gold nanorods transverse peak (589) and surrounding area in different concentrations of a) sucrose and b) glycerol. 153

Figure 7-3 The relationship between the position of the gold nanorods' longitudinal peak and the concentration of a) sucrose and b) glycerol. Solid line denotes linear regression while 2-sigma confidence interval is described by the dotted lines. 154

Figure 7-4 The recorded peak shift for different refractive indices of both sucrose and glycerol. Solid line represents linear regression, while dotted lines represent 2-sigma confidence interval. 155

Figure 7-5 The absorbance measured at a wavelength of 621 nm for differing concentrations of a) sucrose and b) glycerol. 156

Figure 7-6 The recorded absorbance for different refractive indices of both sucrose and glycerol at a wavelength of 621 nm. Solid line represents linear regression, while dotted lines represent 2-sigma confidence interval. 156

Figure 7-7 The absorbance spectrum of gold nanorods and 35% hydrogen peroxide in 1:1 ratio. 157

Figure 7-8 The absorbance spectra of a) 35% hydrogen peroxide b) 35% hydrogen peroxide and CTAB in a ratio of 1:1. 158

Figure 7-9 The absorbance of gold seed solution. 158

Figure 7-10 The calculated transmission profile of water (dotted line), 10% hydrogen peroxide (solid line) and 20% hydrogen peroxide (grey line) for a thickness of a) 10 μm and b) 100 μm . Water data is calculated using Hale refractive index data while hydrogen peroxide mixtures are calculated from Voraberger data. 163

Figure 7-11 The experimental set-up of the IR spectrometer. 164

Figure 7-12 The calculated reflection from normal incidence from a) an air-fused silica interface and b) a water-fused silica interface using the Fresnel equations and the real refractive index data for water (Hale) and fused silica (Kitamura[172])..... 166

Figure 7-13 The estimated reflection term when a cuvette containing analyte is base-lined against an empty cuvette. 167

Figure 7-14 The transmission of the 10 micron cuvette (black line) and the 100 micron cuvette (grey line). These spectra are base-lined against air..... 168

Figure 7-15 Raw a) transmission and b) noise in transmission spectra from all runs of water(H₂O)-hydrogen(H₂O₂) peroxide in the 10 micron cuvette. Spectra run from water to 35% hydrogen peroxide. 168

Figure 7-16 Raw a) transmission and b) noise in transmission spectra from all runs of water(H₂O)-hydrogen(H₂O₂) peroxide mixtures in the 100 micron cuvette. Spectra run from water to 35% hydrogen peroxide..... 169

Figure 7-17 Absorbance (natural log) spectra of water-hydrogen peroxide mixtures for a thickness of a) 10 microns and b) 100 microns. Also shown is the noise in the absorbance signal for a thickness of c) 10 microns and d) 100 microns spectra run from 35% hydrogen peroxide to water. 169

Figure 7-18 The concentration of hydrogen peroxide in solution (v/v) against the optical absorbance of the solution for a) 10 μm thickness at a wavelength of 3520 nm and b) 100 μm thickness at a wavelength of 3860 nm. Solid lines are quadratic regression and dotted lines represent 2-sigma confidence interval..... 170

Figure 7-19 The transmission spectra of a) the 10 micron cuvette, b) a close up of 10 micron cuvette spectrum, c) the 100 micron cuvette spectrum and d) a close up of 100 micron cuvette spectrum. 172

Figure 7-20 The refractive index, κ , of hydrogen peroxide (black solid lines) and water (black dotted lines) calculated from K matrix for a thickness of a) 10 microns and b) 100 microns. Also shown are 20% hydrogen peroxide data (grey solid lines) and water (grey dotted lines) values of refractive index, κ , published in Voraberger and Hale papers respectively. 173

Figure 7-21 The effect of 0.08 micron broadening on the refractive index, κ , of water of thickness a) 10 micron and b) 100 micron The solid grey line represents the tabulated refractive index from Hale, the solid black line is the simulated refractive index with

broadening, and the black dotted line represents the calculated refractive index from our experimental water data. 174

Figure 7-22 The effect of 0.08 micron broadening on the refractive index, κ , of 20% hydrogen peroxide of thickness a) 10 micron and b) 100 micron. The solid grey line represents the tabulated 20% hydrogen peroxide refractive index from Vorabeger , the solid black line is the simulated refractive index with broadening and the black dotted line represents the measured refractive index from 20% hydrogen peroxide..... 175

Figure 7-23 The concentration of hydrogen peroxide and the average total cuvette thickness calculated (with error bars of one standard deviation) from the 10 thickness data using a) & c) the full wavelength range and b) & d) the 3.4-3.68 micron range. Dotted line represents a 1:1 linear line..... 177

Figure 7-24 The a) concentration of hydrogen peroxide and b) average total cuvette thickness calculated (with error bars of 1 standard deviation) using the data from 3.9-4.08 microns for the 10 thickness mixture. The concentration of hydrogen peroxide includes a linear regression (solid line) with a 2-sigma confidence interval (dotted lines)..... 178

Figure 7-25 The a) concentration of hydrogen peroxide and b) average total cuvette thickness calculated (with error bars of 1 standard deviation) using the data from 4-4.18 microns for the 100 thickness mixture..... 179

Figure 7-26 The refractive index, κ , of hydrogen peroxide (black solid lines) and water (black dotted lines) calculated from K matrix for both 10 and 100 micron data combined. Also shown are 20% hydrogen peroxide data (grey solid lines) and water (grey dotted lines) values of refractive index, κ , published in Voraberger and Hale papers respectively. 180

Figure 7-27 The a) concentration of hydrogen peroxide and b) average total cuvette thickness calculated (with error bars of 1 standard deviation) using the data from 3.74-3.92 microns for the combined 10 and 100 micron data set. Solid line represents linear regression, while dotted line represents 2-sigma confidence interval..... 181

Figure 7-28 The optical a) transmission, b) noise in transmission, c) absorbance (natural log) and d) noise in absorbance of 95% ethanol. The black line describes the 10 micron thickness and the grey line describes the 100 micron thickness. 182

Figure 7-29 The theoretical transmission of water at different effective path lengths. 186

Figure 7-30 The scattering (dotted line) and extinction coefficient (solid line) of different radius spheres of water.	187
Figure 7-31 The predicted extinction coefficient (solid black line), absorbance (grey line) and scattering (dotted black line) of mist droplets produced by the nebuliser.	188
Figure 7-32 The detector and source are held outside the mist chamber using retort stands.....	188
Figure 7-33 The transmission of spectra of water mist at different duty cycles, 5% (black solid lines), 7.5% (black dotted lines), 10% (grey solid lines) and 15% (grey dotted lines).....	189
Figure 7-34 The average attenuation of light of the mist (solid line) and the theoretical absorbance of water (dotted line) for a duty cycle of a) 5%, b) 7.5%, c) 10% and d) 15%.	190
Figure 7-35 The attenuation of light at a wavelength of 3 microns for a theoretical water path length (\diamond) and for the water mist (\blacksquare). Lines show linear regression of each data set.	190
Figure 7-36 The transmission of MilliQ water (dotted line) and the 35% hydrogen peroxide (solid line).	192
Figure A-1 An example of the calculation heat transfer coefficient, h , for RTDs A and B in still water. The dotted line represents the point at which the RTD temperature was stable and is the point that h is taken from. Each chart represents a different input power of a) 9 mW b) 75 mW c) 180 mW and d) 310 mW.	A-1
Figure A-2 An example of the calculation heat transfer coefficient, h , for RTDs C and D in still air. The dotted line represents the point at which the RTD temperature was stable and is the point that h is taken from. Each chart represents a different input power of a) 9 mW b) 75 mW c) 180 mW and d) 310 mW.....	A-2
Figure A-3 An example of the calculation heat transfer coefficient, h , for RTDs C and D in 7.5 L/min flowing air. The dotted line represents the point at which the RTD temperature was stable and is the point that h is taken from. Each chart represents a different input power of a) 9 mW b) 75 mW c) 180 mW and d) 310 mW.	A-3
Figure A-4 An example of the calculation heat transfer coefficient, h , for RTDs C and D in water mist with and airflow of 7.5 L/min. The dotted line represents the point at which the RTD temperature was stable and is the point that h is taken from. Each chart	

represents a different input power of a) 9 mW b) 75 mW c) 180 mW and d) 310 mW...
.....A-4

Figure A-5 The energy drawn over time of experiment when the each RTD was set to 105°C. Graphs show a) water, b) 10% hydrogen peroxide, c) 20% hydrogen peroxide, d) 30% hydrogen peroxide, e) 35% hydrogen peroxide and f) 40% hydrogen peroxide. Solid lines are coated RTD, dotted lines are uncoated.....A-12

Figure A-6 The energy drawn over time of experiment when the each RTD was set to 130°C. Graphs show a) water, b) 10% hydrogen peroxide, c) 20% hydrogen peroxide, d) 30% hydrogen peroxide, e) 35% hydrogen peroxide and f) 40% hydrogen peroxide. Solid lines are coated RTD, dotted lines are uncoated.....A-13

Figure A-7 The typical response of the coated (blue line) and uncoated RTDs (red line) in 3 minute mist streams of hydrogen peroxide with concentrations of a) water, b) 4.8%, c) 8.6%, d) 11%, e) 16%, f) 20%, g) 25%, h) 30%, i) 31.5%, j) 33%, k) 34%, l) 35%, m) 40%, n) 45% and o) 45.7% hydrogen peroxide.A-16

Figure A-8 The C_{cal}^{-1} for each concentration of hydrogen peroxide for thicknesses of a) 10 μm and b) 100 μm . The solid line represents the hydrogen peroxide values while the dotted line represents the water values.A-25

Figure A-9 The concentration of hydrogen peroxide and the total cuvette thickness calculated from the 100 thickness data using a) & c) the full range and b) & d) the 3.6-3.78 micron range. Dotted line represents a 1:1 linear line.A-26

Figure A-10 The C_{cal}^{-1} values using the combined 10 μm and 100 μm thickness data sets for different concentrations of hydrogen peroxide. Hydrogen peroxide data is represented by (\blacklozenge) and water data is represented by (\diamond).....A-26

Figure A-11 The concentration of hydrogen peroxide and total mixture thickness estimated using the combined data set using a) & b) the whole range, c) & d) 3.4-3.58 microns and e) & f) 3.6-3.78 microns.A-27

List of Tables

Table 1-1 Key physiochemical properties of water and hydrogen peroxide. The values come from <i>Applications of hydrogen peroxide and derivatives: Rsc clean technology monographs</i> [6].	1
Table 4-1 Power applied to Al target with substrate temperature fixed at 400°C.	48
Table 4-2 Al-Pt samples deposited with varying substrate temperature and power fixed at 27.5 W	49
Table 4-3 Summary of RTDs used for calorimetric sensors	60
Table 4-4 A summary of the heat transfer coefficients of RTDs A, B, C and D at a temperature of 29°C. The uncertainty given is one standard deviation.	68
Table 5-1 The regression statistics of the mass loss curves and the subsequently calculated mass loss rates	75
Table 5-2 Analysis of variance of concentration	86
Table 5-3 The regression statistics of the mass loss curves and the subsequently calculated mass loss rates	90
Table 5-4 Summary of calorimetric RTD performance as immersion and drop sensor	105
Table 6-1 Summary of calorimetric RTD performance as a mist sensor	146
Table 7-1 Terms and symbols describing variables related to absorption spectroscopy	160
Table 7-2 The calculated ethanol thickness and concentrations for 10 micron thickness of 95% ethanol/5% water (v/v) (three repeat measurements). The spurious H ₂ O ₂ signal calculated from these spectra using the calibration matrices is also shown.	183
Table 7-3 The calculated ethanol thickness and concentrations for 100 micron thickness of 95% ethanol/5% water (v/v) (three repeat measurements). The spurious H ₂ O ₂ signal calculated from these spectra using the calibration matrices is also shown.	183
Table 7-4 The calculated ethanol thickness and concentrations for the combined thickness data sets of 95% ethanol/5% water (v/v) (three repeat measurements). The spurious H ₂ O ₂ signal calculated from these spectra using the calibration matrices is also shown.	184
Table 7-5 The concentrations of hydrogen peroxide, water and ethanol calculated from the 10micron calibration matrix, using a sample containing 95% ethanol and 5% water.	185

Table 7-6 The concentrations of hydrogen peroxide, water and ethanol calculated from the 100micron calibration matrix, using a sample containing 95% ethanol and 5% water.	185
Table 7-7 The estimated effective path length of water for each duty cycle.	186
Table 7-8 Summary of Optical Sensor Performance	194
Table A-1 The h values for RTDs A and B in air at a stable value (approx. 400s) for each run at each heated power	A-5
Table A-2 The h values for RTDs A and B in water at a stable value (approx. 110s) for each run at each heated power	A-6
Table A-3 The h values for RTDs C and D in still air at a stable value (approx. 400s) for each run at each heated power	A-7
Table A-4 The h values for RTDs C and D in air flowing at 7.5L/min at a stable value (approx. 400s) for each run at each heated power	A-8
Table A-5 The h values for RTDs C and D in mist produced with 20% duty cycle at 7.5L/min at a stable value (approx. 140s) for each run at each heated power	A-9
Table A-6 The h values for RTDs C and D in mist produced with 20% duty cycle at 7.5L/min at a stable value (approx. 150s) for each run at each heated power	A-10
Table A-7 The h values for RTDs C and D in mist produced with 20% duty cycle at 7.5L/min at a stable value (approx. 175s) for each run at each heated power	A-11
Table A-8 Matrix K for 10 micron thickness shown with the wavelengths to which it corresponds	A-17
Table A-9 Matrix K for 100 micron thickness shown with the wavelengths to which it corresponds	A-20
Table A-10 Matrix K for both 10 micron and 100 micron thickness shown with the wavelengths to which it corresponds	A-23

Abstract

This project focuses on the development of methods for evaluating the concentration of hydrogen peroxide in the mist streams used in a new generation of sterilisation technologies. This application presents unique experimental difficulties in that a sensor must be able to measure the concentration of hydrogen peroxide in a mist of droplets, and be able to do so in the concentration range between 30% and 40% (by percentage weight). Three separate methods of analysis were investigated.

A calorimetric sensor was constructed using a resistance temperature detector (RTD), coated with a heterogeneous catalyst, to measure the heat released after hydrogen peroxide is decomposed. Various ways of implementing this scheme were investigated, including immersion into fluid, dipping followed by drying, and using a heated RTD. The sensor was capable of determining concentrations from 0% to 40% (w/w) in both liquid hydrogen peroxide and aerosol hydrogen peroxide mixtures, with at best 4% and 3% (w/w) precision respectively. Surprisingly, the unheated sensor responded to hydrogen peroxide in the mist by undergoing a *decrease* in temperature. The physical phenomena responsible for this were investigated and explained. The heated RTD worked well as a sensor for mist density, however it was unable to determine concentration.

Three kinds of optically-based sensor were explored. It was determined by simulation that localised surface plasmon resonance using gold nanorods was the best way of developing a sensor based on refractive index. However, in the proof-of-concept experiments the gold nanorods were oxidised by hydrogen peroxide, making this sensor scheme unsuitable for this project. Absorbance spectroscopy was more successful, and was performed on two different path lengths of liquid hydrogen peroxide, analysed with a Fabry-Perot mid-infrared spectrometer. The concentration of liquid hydrogen peroxide could be determined in the range 0% to 27% (volume percentage), with best precision of 1% (v/v). To deal with multiple thicknesses of path length, a numerical technique using a matrix was developed to simultaneously determine concentration and thickness. Finally, some preliminary absorbance measurements of water mist were performed, which showed that, while scattering was significant, there is still a possibility of using this technique in an aerosol, to determine some measure of density. However, this last idea was not explored further here due to lack of time.

Chapter 1 Introduction

Hydrogen peroxide is an important chemical used across a variety of industries, due to a wide range of uses including sterilization and disinfection[1, 2], rocket propellant[3], bleaching[4] and the production of epoxides and organic peroxides[5], with all these processes making use of the strong oxidation properties of H₂O₂. Concentration is an important aspect, with each industrial use requiring different concentrations of H₂O₂ to perform tasks. Unfortunately, H₂O₂ is a relatively unstable compound which decomposes to H₂O and O₂ over time, a process which can be exacerbated by high storage temperatures or chemical impurities. Therefore, concentration monitoring is important to ensure that H₂O₂ is of the correct concentration for use, both for quality assurance and the satisfaction of regulatory requirements. Table 1-1 describes some of the key physiochemical properties of hydrogen peroxide and how it compares to water.

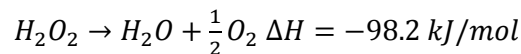
Table 1-1 Key physiochemical properties of water and hydrogen peroxide. The values come from *Applications of hydrogen peroxide and derivatives: Rsc clean technology monographs*[6].

Physiological Property	H ₂ O	H ₂ O ₂
Boiling Points (°C)	100	150.2
Vapour Pressure (25 °C) (kPa)	2.3	0.2
Viscosity (mPa.s) (20 °C)	1.002	1.249
Heat of Vaporisation (J.g ⁻¹ .K ⁻¹) (25 °C)	2443	1519
Heat of Vaporisation (J.g ⁻¹ .K ⁻¹) (boiling point)	2258	1387
Density (g/mL) (25°C)	0.9980	1.45
Refractive Index (<i>n_D</i> , 20°C)	1.3330	1.4084

Streams of gaseous H₂O₂ have been used to sterilize various products and medical equipment, typically in the concentration range of 5-10% (v/v). The sponsors of this project, Nanosonics, have developed a new generation of medical sterilization cabinets, in which a mist stream of H₂O₂ with a concentration of approximately 35%

(w/w) is used to sterilize medical equipment. The advantage of the technique is that it is a fast and effective way to sterilize equipment and produces no dangerous waste because the H₂O₂ ultimately decomposes to water and oxygen. The mist is produced using an ultrasonic transducer (a nebulizer) in a cup of liquid H₂O₂ to create a small fountain. By passing airflow through the fountain, droplets of H₂O₂ are captured and carried through a disinfection chamber. This environment presents a set of challenging requirements for a H₂O₂ sensor: it should work quickly and accurately in mist and be capable of detecting H₂O₂ in the concentration range between 30% and 40%. In addition, as the device is to be installed in a commercial product, the sensor should be cheap and simple in order to keep the decontamination unit economically viable.

There are some sensors for H₂O₂ concentration currently available, however, these sensors work in aqueous or gaseous environments exclusively, and none have a measurement range that Nanosonics are interested in. In general, the existing sensors use the decomposition of H₂O₂, seen in Equation 1-1, to monitor concentration.



Equation 1-1

This reaction can be monitored by various means, including the electrochemical potential of the redox reaction, an increase of heat energy due to the exothermic nature of the reaction or colorimetric evaluation. In addition there are some optical phenomena which may be developed into a sensor for H₂O₂ concentration. These are based mainly around refractometric and absorption properties. Water has a refractive index of 1.33, and pure hydrogen peroxide has a refractive index of 1.41 (at visible wavelengths of light), with aqueous solutions of hydrogen peroxide and water lying in between these values. As the concentration of hydrogen peroxide in the solution increases, it follows that the refractive index will increase, and by measuring the refractive index, it will be possible to determine a concentration of hydrogen peroxide.

Evanescent waves and localized surface plasmons have been used in refractive index sensitive sensors. This is based on the principle that the frequency of oscillation of an evanescent wave, or resonance of a surface plasmon, are due to the intrinsic properties of the sensor and the refractive index of the medium that the sensor is in.

Changes in concentration of the medium which result in changes to the refractive index of an analyte should be detectable using this method. One issue is that the sensor will not be chemically specific, as any other substances present will also alter the refractive index.

On the other hand, absorption spectroscopy is a well-known form of measurement for chemicals based on how well a chemical absorbs light at specific wavelengths. From this basis it follows that as a chemical becomes more concentrated, it absorbs more light proportionally. In addition, the wavelength at which this absorption occurs differs from one substance to another, which allows for possible identification of specific chemicals. This provides a way to determine hydrogen peroxide concentration specifically, overcoming the non-selectivity of refractometric sensors. It is well understood, however, that a mist stream will cause significant scattering. One challenge facing this project is whether an absorbance sensor can be made to work in a mist stream without becoming too expensive or complex.

This background is all further expanded upon in greater detail in Chapter 2 and Chapter 3.

Somewhat over half of this thesis is devoted to detection and quantification based on the calorimetric idea, Chapters 4 to 6. This sensor was based on two standard resistance temperature detectors (RTDs), one coated with a catalyst for H_2O_2 decomposition, and one uncoated. The principle is that the coated RTD registered an increase in heat, as a sample of hydrogen peroxide from the mist decomposed on it. Meanwhile, the uncoated RTD would act as a control measurement, and a signal could be determined by subtracting the control signal from the coated RTD signal. Chapter 4 describes the various methods of analysis used to determine whether there was a quantifiable relationship between the concentration of H_2O_2 and the signal derived from the RTD. This chapter also describes an investigation of a production method for heterogeneous platinum catalyst. A combination of physical vapour deposition and dealloying was used. The advantages of this would be the possibility of repeatable catalyst production, and using small quantities of catalyst to keep costs down.

After this, the construction of the sensor using either finely divided platinum films or MnO_2 powder is described. The different sensors and uncoated RTDs had their

thermal properties tested in a rig provided by Nanosonics which imitates the final product that the sensor would be installed in. The rig was used to generate different concentrations and flows of water/hydrogen peroxide mist in air, and the response of sensors in these different conditions was considered.

The catalysts themselves were also tested in liquid to determine how much decomposition they could create by determining how much oxygen mass was lost by decomposition. This is detailed in Chapter 5. This chapter also describes how the sensor functions when immersed in a liquid. In this case the sensor was dipped in different concentrations of H_2O_2 and the temperature was measured. This was done to confirm the theory of operation of the sensor, that as the concentration of H_2O_2 liquid increases, the temperature measured by the RTD increases in direct proportion. The response of the sensor when immersed in the analyte and then withdrawn was also examined.

Next, small droplets of H_2O_2 were tested on the sensor. This was achieved by reinstalling the sensor in the test rig and placing droplets of analyte on it with a pipette. In this case, the sensor was tested with an airflow moving past.

The aim of these tests was to ascertain the behaviour of the system when vaporization was also significant, since vaporization phenomena in the mist phase were found to be important too. Another possible measurement method was also tested during this time. While the RTDs used could function well as thermometers, they could also be fixed to a set point temperature well above room temperature by using the RTD as a heater (i.e. by passing a significant current). This configuration helps to clear prior deposits and has been proposed for faster tracking of changes in concentration. In this case, the voltage which powered the RTD was monitored. As heat is transported away from the sensor (due to vaporization), the sensor requires more voltage to maintain a constant temperature. In contrast, as the decomposition adds heat to the sensor, the higher the concentration of H_2O_2 , the smaller the voltage required.

A good understanding of the sensor's response to bulk and droplet H_2O_2 was essential to understanding the results of testing in a H_2O_2 mist. Having established this in Chapter 5, the investigation of the actual mist stream is covered in Chapter 6. In this case the sensor was tested in a mist using the RTD as a thermometer, and then later again using the RTD that was set to a fixed temperature. The purpose behind testing

using a thermometer was to gain an insight into how the H_2O_2 interacted with the catalyst and the surrounding mist medium itself. In addition, this was done to determine whether the H_2O_2 mist could be measured using the RTD as a thermometer. Once the RTD's response was determined, the fixed temperature mode of the RTD was investigated to determine whether it could act as a concentration sensor.

The investigation into detecting H_2O_2 concentration in a mist using optical sensors is covered in Chapter 7. The first part of this chapter is devoted to work on the refractometric sensor. This sensor was based on gold nanorods due to the size of the peak shift and the chemical inertness of gold. The nanorods were first tested in other liquids, sucrose and glycerol, to determine how well the rods worked as a sensor before being tested in liquid H_2O_2 solutions. The absorbance sensor is also described in Chapter 7. It was approached from two directions. As with the refractometric sensor, the absorbance sensor was first tested using liquid H_2O_2 , before an attempt was made to measure a mist. The sensor was made by using a standard transmission arrangement with the detector and the light source in a line with a cuvette holder in between. A cuvette was used to acquire the spectra of H_2O and various concentrations of H_2O_2 . Once these were determined, a calibration graph was made, from which the concentration of H_2O_2 could be determined. Due to variations in mist density, the effective path length of the liquid phase is variable, and ultimately this information is required to verify the amount of H_2O_2 delivered. Theory is presented that shows how to extract the path length from the absorbance data, however this process is complicated by limitations of the spectrometer and therefore it was necessary to verify this approach using cuvettes of different thicknesses. A matrix of absorbances of H_2O and various concentrations of H_2O_2 in two cuvettes of different thickness was collected. Using matrix division, the matrices could then be used to determine the absorbance coefficient of both H_2O and H_2O_2 , and these values could be used to determine the concentration and thickness of the liquid being measured. The effect of scattering was also assessed.

While each chapter summarises the work done and possible improvements, Chapter 8 summarises the final judgements made on each sensor's ability to function within the design envelope set by Nanosonics. There is also some discussion on other ways that the sensors can be used in the Nanosonics device. In addition, any future work needed to improve a sensor's function was discussed here.

Chapter 2 Chemical Hydrogen Peroxide Sensors

Here I review the previous use of hydrogen peroxide sensors of the ‘chemical’ type, which generally use the decomposition of hydrogen peroxide to detect hydrogen peroxide concentration. The extent or intensity of this reaction is transduced into an electrical or optical signal, based on the redox or calorimetric properties of the reaction. I will discuss amperometric and voltametric detection of the redox reactions, optical detection of chemical reactions, thermal detection and finally, suitable catalysts for the calorimetric reaction.

2.1 Amperometric Sensors

Amperometric sensors produce a current (proportional to concentration until the signal becomes saturated) due to a chemical redox reaction[7-11]. Most amperometric hydrogen peroxide concentration sensors are similar in design, consisting of a catalytic or catalyst coated anode, a cathode and an electrolyte. Hydrogen peroxide causes oxidation at the anode, producing a current related to the concentration of the hydrogen peroxide up until the signal is saturated. The most common way of making this measurement is using a platinum wire for an anode as the concentration can then be determined directly from the current[7-11].

Commonly, amperometric sensors for hydrogen peroxide are used in biological low range detection, generally 1 mmol.L^{-1} (for comparison, this is $3.4 \times 10^{-5}\%$ (w/w)), however there has been a range as high as 6.8 mmol.L^{-1} . This means that many sensors are based on enzymes such as peroxidase. The most commonly utilised peroxidase is Horse Radish Peroxidase (HRP), which is a catalyst for the reduction of hydrogen peroxide. Sensors are made by conjugating HRP to electrodes, which catalyse the reduction of hydrogen peroxide, producing a current which can be used to measure hydrogen peroxide concentration in a certain range[7-11]. While HRP is an effective catalyst, it has no direct electrochemistry itself[12]. To work selectively for hydrogen peroxide, it requires either an electron mediator[7, 8] or a bi-enzyme setup[9] with the effects of the hydrogen peroxide decomposition increasing the function of the second enzyme. This process is illustrated in Figure 2-1. This approach is advantageous over direct oxidation of the electrode, as it reduces the electrode potential required, which reduces any interference from other electroactive species which may be present[7-9].

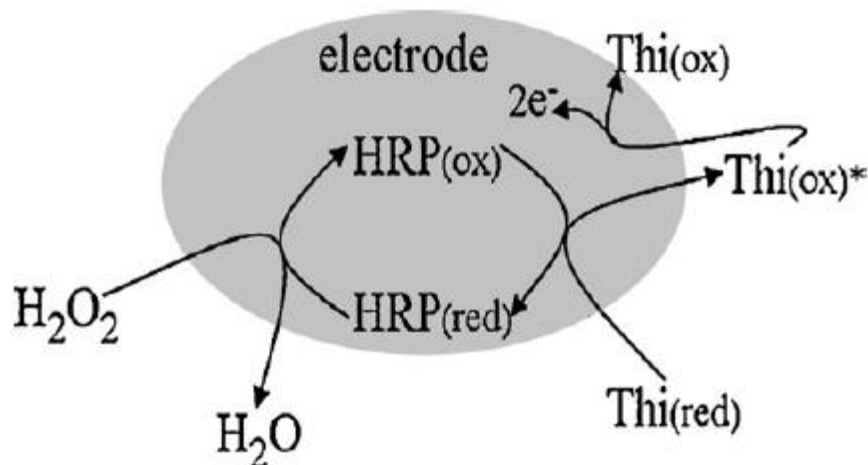


Figure 2-1 Redrawn from *Study on a hydrogen peroxide biosensor based on horseradish peroxidase/GNPs-thionine/chitosan*[13]. Illustration of how the mediator is oxidised not the HRP.

Alternative hydrogen peroxide sensors have been made using haemoglobin as the catalyst for hydrogen peroxide decomposition. Haemoglobin has been used as a catalyst[12, 14, 15] as it has acceptable catalytic activity and is commercially available and inexpensive, and has a well understood structure[12, 14, 15]. In addition, an unmediated haemoglobin-based hydrogen peroxide sensor has been developed[12]. This consists of a haemoglobin-sodium dodecyl sulfate film deposited on the electrode, which is able to catalyse the reduction of hydrogen peroxide and produce a current. This sensor is not as sensitive as a HRP-based sensor, but is cheap and simpler due to the lack of mediator[12].

Further improvements were made to this type of sensor by immobilising HRP on DNA films as a self-assembled monolayer (SAM) on functionalized (Cysteamine SAM) gold. This improved the coverage of HRP molecules over the surface of the electrode, which in turn improved the sensor signal[11]. This has also been done with non-enzymatic sensors such as the DNA-Cu²⁺ conjugate, which was electrodeposited onto a glassy carbon electrode. The DNA-Cu²⁺ was shown to be suitable to reduce hydrogen peroxide in a similar manner as HRP. This sensor has the advantage of good selectivity, stability and reproducibility[16].

One advantage of amperometric sensors is that as they are relatively simple, they can be mass produced through processes such as screen printing. Colloidal gold is incorporated into the carbon ink to form the electrode. HRP is then absorbed onto the surface of the electrode. The gold reduces the insulating effect of enzyme shell for

direct electron transfer, providing conducting tunnels for the electrode[10]. A similar sensor was developed which immobilised haemoglobin on the surface of SiO₂ nanoparticles. These are then dispersed within a carbon electrode, which is then immersed in hydroquinone to improve electron transfer in the electrode[15]. Other methods of screen printing electrodes include the electropolymerisation of pyrrole, which has had HRP entrapped in it[17].

While enzyme-based amperometric sensors are suitable for a biological context, higher concentration hydrogen peroxide creates an environment which denatures the enzyme rendering it useless. Many amperometric sensors intended for use in a chemical context are made using inorganic catalysts instead[18-28]. Multivalent metal oxide nanoparticles such as copper oxides[24], cerium oxide[18], manganese dioxide[19], perovskite-type oxide[20], copper hexacyanoferrates[25], cobalt hexacyanoferrates[27], Prussian Blue[25, 27] or iron oxide[23] are incorporated into the anode of an electrochemical cell. The mechanism is the same as the enzyme sensor: the hydrogen peroxide reduces or oxidises the metal oxide, depending on the characteristics of the oxide, before the metal oxide is then re-oxidised, or reduced, by the decomposition of hydrogen peroxide, and this is what produces the electric current. In addition some of these inorganics can be dispersed as nanoparticles on screen printed glassy carbon electrodes[19]. Other sensors just use metallic nanoparticles to modify electrodes such as silver nanoparticles which are dispersed in a PVA film on a platinum electrode or a sol-gel ceramic composite electrode[22, 26], palladium nanoparticles dispersed on a silicon electrode through galvanic displacement[21] or the electrochemically produced porous platinum electrodes[28].

2.2 Potentiometric Sensors

Sensors which determine concentration by measuring the potential difference between an “anode” and “cathode” are potentiometric sensors. The principles underpinning this type of sensor are similar to the amperometric sensors, in which the redox reaction is initiated on the anode, producing a flow of electrons. However, rather than measure the flow of electrons, the sensor measures the potential energy of the electrons that are migrating. The amperometric sensors above require a high overpotential (~0.6 V) for hydrogen peroxide oxidation, which is problematic for

selectivity. This can be dealt with by a redox mediator, generally hydroquinone, however, this problem can also be circumvented by using a potentiometric sensor.

The Electrolyte Metal Oxide Semiconductor Field Effect Transistor (^EMOSFET) has been used as a voltametric sensor for hydrogen peroxide concentration[29, 30]. The construction of the ^EMOSFET system is that a gate oxide is grown on a silicon substrate. A contact layer (e.g. platinum) is then deposited on top of the oxide, and then finally, a layer of electro-active gate material (iridium oxide, potassium ferric ferrocyanide etc.) is deposited over the contact. When a hydrogen peroxide solution contacts this sensor, it causes the gate material to reversibly oxidise (due to the platinum, and gate oxide contact). The redox ratio of the gate material is used to measure the contact potential of the gate material to the platinum, and from this the hydrogen peroxide concentration is calculated.

This system has been used for detecting hydrogen peroxide in vapour in breath. A cooling tube is used to condense the sample out of the vapour phase and direct it onto the ^EMOSFET sensor[29]. This is practical as a detection method for diseases related to lung function[29].

2.3 Optochemical Sensors

Optochemical sensors are sensors which rely on the optical detection of a chemical reaction, as distinct from physical optical sensors which rely on detection of a physical property of the analyte (i.e. refractive index). The chemical reaction will generally produce a colour change[31-34], while others rely on products of the chemical reaction obscuring an optical reading[35, 36].

Chromogenic sensors have been used in the determination and detection of hydrogen peroxide concentration. The main mechanism of the sensor is that the analyte causes a chemical reaction which causes a colour change. One such sensor was a self-assembled polymer containing Prussian Blue, an iron-cyanide complex which visibly changes colour when reduced[32]. Reduction was achieved by immersing the polymer in ascorbic acid, turning Prussian Blue to Prussian White. When hydrogen peroxide contacts the Prussian White impregnated polymer, it oxidises it causing the colour to change back to blue. The concentration can be determined through a spectroscopic system which is analysing light reflected from the sensor. The change from Prussian

White to Prussian Blue is observed through a change in reflected signal. The “slope of change” is used to determine the concentration of hydrogen peroxide.

Chemiluminescent sensors for hydrogen peroxide have been described using chemiluminescent esters cast in membranes. In this case the light was released by the esters and detected by a photo diode[32]. Chemiluminescence has also been used as the basis for hydrogen peroxide flow sensors. For example Li et. al. described a flow sensor in which haemoglobin was immobilised in a flow cell as the catalyst of decomposition[34]. Luminol was immobilised on an anion-exchange resin. As hydrogen peroxide flows through the cell, the resin is oxidised, releasing the luminol. Hydrogen peroxide is reduced by the haemoglobin which cause hydroxide salts to form. This causes the luminol to undergo a series of chemical reactions, resulting in a blue light. As with the previous sensors, it is not limited to haemoglobin as all it relies on is a catalyst for the reduction of hydrogen peroxide[34]. However, different catalysts may meet different needs especially sensitivity, response time and cost.

Fluorescence quenching has been used to determine hydrogen peroxide concentration. The main mechanism of this sensor technology is that a fluorescent dye is quenched by products of a reaction, in this case the decomposition of hydrogen peroxide to water and oxygen. It is the oxygen released by this reaction which causes the quenching of the fluorescent dye, and this in turn is monitored by a spectrofluorometer. Catalase and finely dispersed silver powder have both been proven to work as catalysts[35]. A similar hydrogen peroxide sensor has been constructed to detect hydrogen peroxide by luminescence quenching. An oxygen permeable membrane is covered in a layer of inorganic catalyst material (the best was reported as manganese dioxide, however, silver and platinum were also used), which decomposes the hydrogen peroxide to water and oxygen, the latter of which moves into the membrane which has been modified with a dye to produce the luminescence through excitation by an LED. As more oxygen enters the membrane, more luminescence is quenched, which is measured by a photodiode. This sensor has advantages over fluorescence sensor in that it has much less quenching due to hydrogen peroxide, it utilises more robust catalysts, and the colour of these catalyst being black reduces background stray light or ambient light caused by luminescence from the sample solution (this is called optical insulation)[36].

Recent developments show that colloidal silver nanoparticles can be used as a Localised Surface Plasmon Resonance (LSPR) sensor for hydrogen peroxide. The hydrogen peroxide is decomposed by the silver nanoparticles. This process causes the silver nanoparticles to become oxidised back to silver solution, which reduces the LSPR absorbance peak linearly with respect to concentration[31]. This sensor is not easily reusable as the particles are de-stabilised during use.

2.4 Calorimetric Sensors

Calorimetric sensors determine concentration based on the energy released by an analyte undergoing a physical or chemical reaction[37-41]. The most common mechanism of a calorimetric hydrogen peroxide sensor is to induce decomposition over a temperature measuring device[38]. This is usually done by coating the device in a catalyst[38]. Some different temperature measuring devices include thermocouples[37] and thermopiles[39, 40], thermistors[42], resistance temperature detectors[38] and optical detectors[41].

Thermocouples are based on the Seebeck effect, which is that a metal subject to a changing temperature will generate a voltage. This voltage is different for different metals[37]. Thermocouples measure temperature based on this voltage using two connected conductors which are different metals. One of these metals is a “hot” end of the thermocouple, which acts as the temperature sensor, and the other is a “cold” end, which connects the “hot” end to a voltmeter[37]. Both metals experience the changing temperature and generate different and opposing voltages. This difference is used to measure the temperature [37]. The voltage produced depends on the conductor, with different metals producing different effects. As the temperatures vary, this difference will vary, meaning that the temperature can be measured by the differences between the voltages[37]. Thermocouples can be connected in series to form thermopiles. All the “hot” junctions are exposed as the probe and all the “cold” junctions act as a reference. By connecting the thermocouples together, the voltages add to give a larger voltage and power, which produces a better signal[39, 40]. There is however, some question of the precision of thermocouples and thermopiles, and they are generally used across larger temperature ranges.

Early calorimetric biosensors were based on thermopile arrays in which the enzyme was immobilised above the active junctions of thermocouples. More recent developments have been in creating flow-through sensors[43]. An example of this was a microfluidic sensor which consisted of three microfluidic channels (two inlets and one outlet) as well as the microfluidic reaction chamber[43]. This chamber was attached to a substrate on top of a thermopile array. The peroxide was pushed through one inlet and the catalase was pushed through the other. These moved to the reaction chamber, where peroxide underwent decomposition and the heat of the reaction was deduced by the thermopile[43].

Thermistors are materials with resistances which vary rapidly and predictably with temperature[44]. There are two main groups of thermistors, the positive temperature coefficient thermistors (PTC) and negative temperature coefficient thermistors (NTC). PTCs resistance will increase as temperature increases, while NTCs resistance will increase as temperature decreases[44]. RTDs work on the same principle, however, RTDs are pure metals whereas thermistors are semi-conducting polymers or ceramics[44]. Platinum is most commonly used for RTDs due to its chemical inertness, and because there exists a well-defined linear relationship between the metal's resistance and temperature[44]. The thin film RTD consists of a film of platinum deposited in the shape of a wound wire on a ceramic substrate. This set-up can have stability problems due to different expansion rates between the platinum and the substrate. The other set-up is the wire-wound thermometer which consists of a platinum wire spiral being sealed in a ceramic tube. This set-up has a higher range, is more stable and generally has a higher accuracy. RTDs have a high accuracy across a high temperature range, however, RTDs are less sensitive to small temperature changes than thermistors.

This type of device has been used to detect hydrogen peroxide concentration of hydrogen peroxide vapour streams. The sensor determines concentration by the differential signal between two meander-shaped platinum resistance detectors. Both these detectors were passivated (made catalytically inert) by spin-coating perfluoralkoxy, before one was coated by a thin film of catalytically active material. The sensor's sensitivity is affected by the choice of catalyst, with thin film manganese

oxide particles having a higher temperature response than thin film palladium and platinum black[38].

While the above devices measure temperature through electrical properties, optical detectors can determine the heat of reaction through optical properties, specifically refractive index[45]. The refractive index of a medium is dependent on the medium itself, the concentration of that medium and temperature. By passing a beam of light through a constant medium, it will be possible to determine changes in temperature in the medium by measuring the refractive index, by way of measuring the beam deflection[45].

This has been utilised to determine hydrogen peroxide in liquid flow cells. The device consists of a reaction cell containing the catalase and sodium phosphate buffer solution, which was immersed in CCl_4 . The catalase enzymes were immobilised on the gold film at the base of the cell, and a probe beam was passed through the CCl_4 , beneath the cell. When hydrogen peroxide is pumped through the reaction chamber, its decomposition is catalysed by the catalase, and the ensuing temperature change causes a deflection in the beam, linear to the concentration of hydrogen peroxide over the range $0.025\text{-}0.05\text{ mol.L}^{-1}$ [45].

Optical detectors can also be used to determine the heat of reaction through interferometry[46]. Due to the different refractive indices, the interference patterns move out of phase as the temperature changes[46]. A hydrogen peroxide sensor was set up using an all fibre Mach-Zehnder interferometer. After the beam was split into a sensing beam and a reference beam, the sensing beam ran through a flow cell, while the reference beam ran through a separate chamber. When the beams exited, they were recombined, and this interference pattern is the signal. The flow cell was coated in catalase, and as hydrogen peroxide was added to the flow cell, it was observed that the phases of the interference patterns shifted linearly as concentration increased[46].

2.5 Catalysts for the Decomposition of Hydrogen Peroxide

There are many catalysts for the decomposition of hydrogen peroxide. These catalysts are important in chemical hydrogen peroxide sensors, as they facilitate the chemical reaction from which the sensor's signal is derived. Enzymes and other biological molecules, such as catalase, HRP and haemoglobin have the ability to

decompose hydrogen peroxide, and as explained above have been used predominantly in low concentration hydrogen peroxide sensors, such as biosensors. In addition, there are many metallic and metal oxide nanoparticles, which have been shown to catalyse hydrogen peroxide decomposition, which are not as limited by concentration or temperature as enzymatic catalysts. This section will focus on catalysts of hydrogen peroxide.

Many hydrogen peroxide sensors are enzyme-based as they can then be functionalised for biosensor use, such as detection of glucose and antigens[46, 47]. This is due to the fact that many enzymatic reactions produce hydrogen peroxide[9, 46, 47]. In this case, the initial reaction between glucose and glucose peroxidase or the antigen-anti-body releases hydrogen peroxide as a by-product. This by-product is then catalysed by the catalase or HRP, which produces heat or an electron transfer[46, 47].

Manganese dioxide is a multivalent oxide which catalytically decomposes hydrogen peroxide[19, 48]. It is believed that hydrogen peroxide decomposition is a multi step reaction featuring the oxidation and reduction of manganese. The proposed series of events is that hydrogen peroxide oxidises MnO_2 to form Mn^{2+} , oxygen and water. Mn^{2+} is then reduced by remaining hydrogen peroxide to form $\text{Mn}(\text{OH})_2$. Finally, the remaining hydrogen peroxide oxidises $\text{Mn}(\text{OH})_2$ back to MnO_2 and water. The reason for this belief is the observation that the reaction doesn't proceed forward until there is excess $\text{Mn}(\text{OH})_2$ [48]. This has proven to be a good catalyst in hydrogen peroxide calorimetric sensors[38].

In addition to the various multivalent oxides used to decompose hydrogen peroxide, there are also some metallic catalysts. Such metals include silver, nickel, copper and platinum group[49, 50] metals: all catalyse the destruction of hydrogen peroxide. Platinum in particular is an interesting catalyst. It is highly active, and is very resistant to oxidation[51].

Bulk platinum, like any bulk metal, is generally unsuitable for catalysis as there is little surface area[52, 53]. Effective heterogenous catalysis (where the catalyst and reactant are different phases, e.g. solid catalyst and liquid reactants) requires a large surface area of catalyst. The catalyst adsorbs the chemical reactants onto its surface[53]. It is here that the reaction occurs. Therefore, a larger surface area means a more

efficient catalyst. Since the late 1800s many types of high surface area platinum catalysts have been made. This started with colloidal platinum[54] and an unrefined platinum black, a porous material formed by oxidising chloroplatinate in the presence of formaldehyde. 'Platinum black' was difficult to use as the catalytic activity varied from batch to batch due to the fact that there were many ways to prepare this catalyst[55-57].

Adam's catalyst was developed as new way to produce 'platinum black'. The idea was to oxidise a chloroplatinate solution, producing platinum dioxide[55, 58]. This was then reduced using hydrogen [55, 58]. This platinum black compound was more uniformly catalytically active[59]. Recent developments have seen the deposition of platinum dioxide films through sputtering of platinum with oxygen and argon, before the films are reduced using hydrogen gas to produce porous platinum[60].

Also in the 1920's, Murray Raney developed a system of creating porous metals through alloying and de-alloying[61]. The process was shown to work with nickel, silver, gold, copper and platinum, which lead to the catalysts made from these elements by this process to be dubbed "Raney metals"[61]. The basic process is that the Raney catalyst metals are alloyed with aluminium and a very small percentage of silicon. Once this has occurred, the aluminium and silicon is de-alloyed from the alloy using an acid or base. This leaves behind a highly porous surface of Raney metal[61].

More recent developments have included platinum metal sponge[53, 62, 63]. This is formed in a similar manner to platinum black, however, ammonium chloroplatinate solution is heated until all that remains is a divided platinum metal sponge. The porosity of the platinum depends on temperature and concentration, and due to this, the sponges produce a variable catalytic activity[53, 63].

Platinum black has been used to manufacture electrodes through platinisation. This process involves a platinum surface submerged in chloroplatinic acid and lead nitrate. Platinum black is then formed on the cathode as chlorine evolves at the anode[53]. High stability and activity porous platinum electrodes have also been made by co-electrodeposited copper and platinum. The copper is then leached out of the electrode using electrochemical methods[64].

Recent developments have led to the creation of Raney metals catalysts using physical deposition systems. Platinum and aluminium are co-deposited on a heated

substrate for a period of time. This causes the two metals to alloy. Once this alloy is prepared, it is de-alloyed using sodium hydroxide which produces the highly porous Raney surface[65]. The size of pores can be affected by surface temperature and the power driving each of the targets[65]. This method is perfect for deposition of the alloy onto another substrate, such as a resistance temperature detector, for use as a calorimetric detector, and it is the method used in this thesis.

Chapter 3 Physical Chemical Sensors

Physical chemical sensors are capable of determining concentration of chemicals through the physical properties of those chemicals. Optical sensors are the most common type of physical sensor for aqueous, gaseous and mixed phase chemicals. Here I will discuss optical sensors that detect the concentration of a chemical by directly exploiting various physical constants, including refractive index, electroluminescence, and optical absorption.

3.1 Refractometric Sensors

The refractive index is a physical property of a transparent material which describes how fast light moves through it[66]. Refractive index can generally be described by Sellmeier equation for mixtures, and as such, refractometric sensors are able to determine the refractive index of a chemical in solution as an intermediary of the concentration of the solution[67-96], provided that the mixture is known.

There is a significant difference between the refractive index of water (1.333) and hydrogen peroxide solutions of 30-40% concentration (1.353-1.36)[97], with concentrations between these having related refractive indices between 1.333 and 1.36. Therefore, this appears to be a possible property to use to discriminate the concentration of hydrogen peroxide, since the sensor will only be needed to determine the concentration of a water-hydrogen peroxide mixture.

3.1.1 Angular Refractometric Sensors

The Abbe refractometer was the earliest such refractometer, resembling a microscope. The device consisted of two slightly separated prisms: an illuminating prism (of which the bottom liquid/prism interface is rough) and a polished refracting prism (which is required to have a larger refractive index than the analyte)[67]. The analyte fluid forms a thin film layer filling this gap[67]. Light from the illuminating prism passes through the sample and is refracted by the refracting prism at the critical angle[67]. Light then passes through a telescope, through which a light region and dark region can be observed. The point of the boundary between these is can be used to determine the critical angle of refraction, from which the refractive index of the analyte can be inferred[67].

There are a variety of later sensors which also use the deflection of a beam of light to determine the refractive index, and therefore concentration, of an analyte[93-96].

One such sensor was made using the displacement of a laser beam which passed through the analyte[96]. The analyte cell contained the analyte, an angled interface, a buffer solution and a position detector. The laser light moved through the cell and, depending on its difference in refractive index to the buffer and angled interface, deflected up or down. A linear relationship was shown to exist between change in concentration and the displacement of the beam. This meant that the higher the concentration, the higher the refractive index and the greater the displacement of the beam[96].

Other beam deflection sensors make use of waveguides. These sensors typically consist of a laser, a waveguide that the laser light couples to, and a photo detector on a turntable[93, 94]. As light moves through the waveguide, which is immersed in analyte, the refractive index of the external layer (analyte) affects the beam's propagation through the waveguide. This will be discussed in more depth in the section on waveguide sensors. The change in propagation of light affects the angle at which the light leaves the waveguide, which is detected by moving the photo detector around the turntable. The common effect is that a signal that is at a maximum at 0° and drops off as the detector moves to the left and right of the turntable, dropping to a zero signal just below 20° , forming a "peak". The effect of decreasing the refractive index (concentration) is to broaden this peak. When these are compared with theoretical values, the refractive index can be determined[93, 94].

In addition, a refractometric sensor based on displacement has also been demonstrated[95]. A waveguide takes light from a source, it travels into an analyte in a cell, is out-coupled from the guide, and reflects off of the base of the cell, coupling into another waveguide which connects to a photo detector. As the refractive index of the analyte in the cell changes, the angle that the light reflects at also changes. Adjusting the waveguide setup up and down allows the output power to be kept constant, and by recording the displacement, a relationship between refractive index and displacement

can be determined. This relationship is linear as displacement increases with refractive index[95].

Other possible ways to determine refractive index are based on evanescent wave transmission and LSPR. Sensors based on these phenomena function on similar basic principles. Evanescent waves are a consequence of light propagating through a waveguide (when the light interacts with the boundary of the waveguide, an evanescent wave is produced along the external surface of the waveguide), while LSPR is produced by photons of light interacting with electrons in metallic nanoparticles (In bulk metals, SPR is not limited to a particle and propagates along the surface in a similar fashion to evanescent waves). Both evanescent waves and LSPR are functions of, among other things, the refractive index of a surrounding medium. By keeping things constant (waveguide for evanescent sensors, material size and shape of nanoparticle for LSPR sensors), it is possible to determine a refractive index by immersing the waveguide or nanoparticles (for LSPR) in an analyte and measuring the beam of light which propagates through. The refractive index can be determined in evanescent waveguides, by how much light is lost through evanescent waves and the distance that the resonance peak of the LSPR has shifted for the nanoparticles[68-92].

I will now discuss various waveguide systems and standing wave resonators[68-96] and the Localised Surface Plasmon Resonance(LSPR)[98-137], all of which have been considered as the basis for a sensor.

3.1.2 Waveguide Sensors

Waveguides are structures, in this case fibre optic, which guide waves between points in a straight line[138]. Unlike in free space, in which a wave propagates outwards in all directions losing energy in proportion to distance travelled, a waveguide uses total internal reflection to move light in one dimension, with no power loss (in ideal circumstances)[138]. Waveguides have been used to determine refractive index using loss of light from a waveguide (evanescent coupling) or change in optical path length (interferometry). The light lost from the waveguide is based on whether a waveguide is single or multimode. If the waveguide has a single mode, light can be lost to the surroundings by evanescent waves. The amount of light lost is dependent on the refractive index of the medium surrounding the waveguide. This in turn changes the

distance that the light travels through the waveguide. The following sensors are examples on this phenomenon in some way.

Unclad optical fibres are sensitive to refractive index changes in the surrounding environment, and have shown promise as sensors for concentration change through refractive index measurements[92].

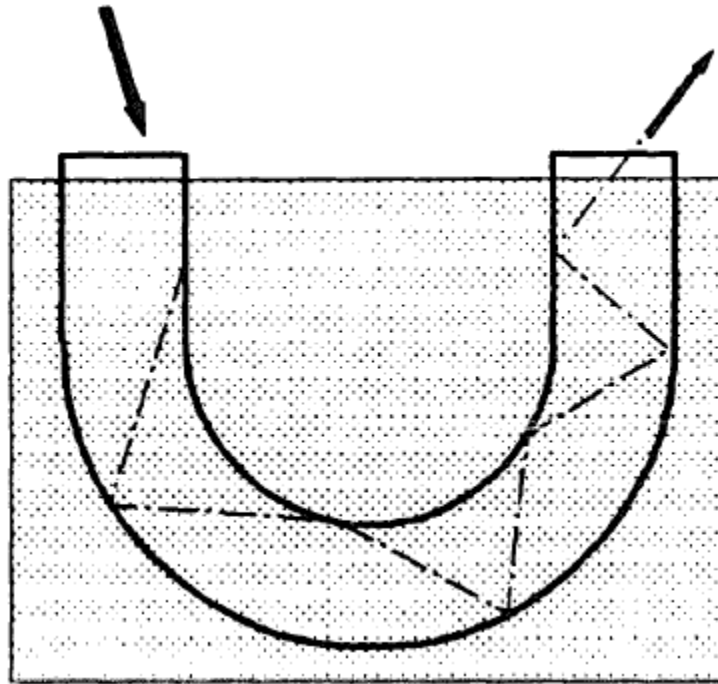


Figure 3-1 Redrawn from *NIR spectroscopic application of a refractometric sensor*[92]. The schematic view of the U-bend waveguide sensor in measuring position, with an arbitrary ray trace.

A wave that moves through an unclad waveguide is affected by the surrounding medium's refractive index, due to interaction with the evanescent waves that occur when the light interacts with the waveguide surface. This can be measured by the transmission of light through the waveguide, which varies linearly with respect to refractive index. By bending the waveguide in a "U"-conformation, as seen in Figure 3-1, a broader distribution of interaction angles of evanescent waves becomes possible which produces a smooth and spread transmitted intensity as a function of the refractive index[92]. One shortfall of this approach is that the sensor will not be able to record the spectra of materials. This is due to the fact that the larger interaction angles lead to a proportion of the light rays being lost, leading to a higher reduction in the cladding-influenced radiation (from the coupling fibres) as opposed to the total intensity, which produces a virtual amplification of the absorptive regions of the cladding[92]. It is

possible to make measurements by keeping coupling conditions constant and running a chemometric evaluation (extracting information from chemical systems by data-driven means). In this case the data can be used to model a chemical system to understand the underlying relationships and structure of the system or to predict new properties or behaviours of interest). In addition, it was shown that by coupling more high quality fibres together in a bundle, the influence of the cladding absorption due to attenuated total reflection (ATR) on the spectra is reduced[92].

Anti-resonant reflective optical waveguides (ARROWs) have also been used for as the basis of an evanescent field refractometric sensor.

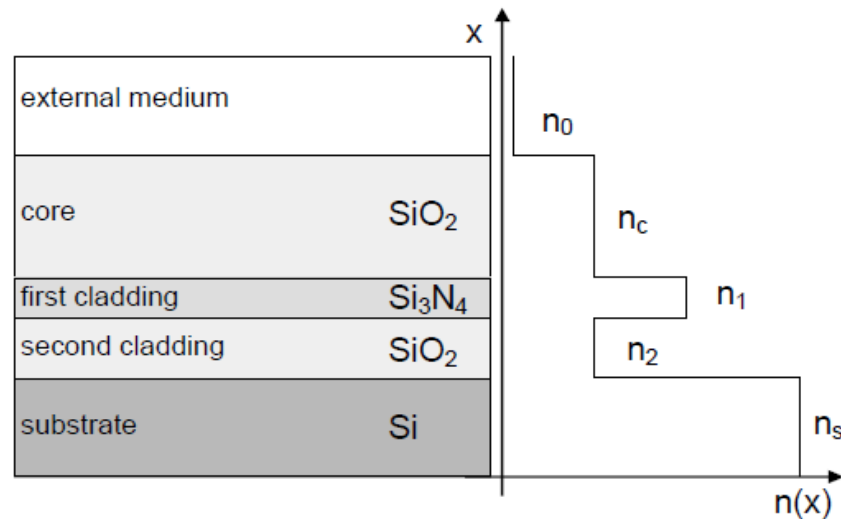


Figure 3-2 Redrawn from *ARROW optical waveguides based sensors*[89]. The structure of an ARROW, n refers to refractive index and subscript to the n refers to the layer of the waveguide.

The general make-up of an ARROW, shown in Figure 3-2, is multilayered: the top layer is an external medium with a varying refractive index to be measured (n_0), the next layer is the core (n_c), then the first cladding layer (n_1 which is much larger than n_c), followed by the second cladding layer (n_2 which has the same value as n_c), and finally this is on a substrate (n_s) with a very larger refractive index, e.g. silicon[89]. The only place the field is confined to the waveguide by total internal reflection is the upper interface when the anti-resonant condition is met. This is determined by the core, first and second cladding thicknesses, as an example, a core (d_c) with a thickness of 4 microns, requires a first cladding thickness (d_1) of $0.12N$ microns (where $N = 0, 1, 2, 3, \dots$) and a second cladding thickness (d_2) of $2.05N$ microns (where $N = 0, 1, 2, 3, \dots$). If the anti-resonant condition is met, the refractive index of the external medium has

minimal effect on the propagating light wave. However, by changing the cladding thicknesses to the resonant condition, the evanescent interaction with the external medium is increased, and as such the propagating wave intensity decreases. By measuring the strength of the transmitted wave, the refractive index can be determined. This sensor has a similar sensitivity and measurement range (1.33-1.47) to the interferometry set-ups, however, the output signal is simpler to obtain, as it is a direct modulation of output intensity, as opposed to conventional interferometry set-ups, which need to transform phase change data into light intensity variation[89].

A hollow core waveguide has been developed using anti-resonant reflection[89].

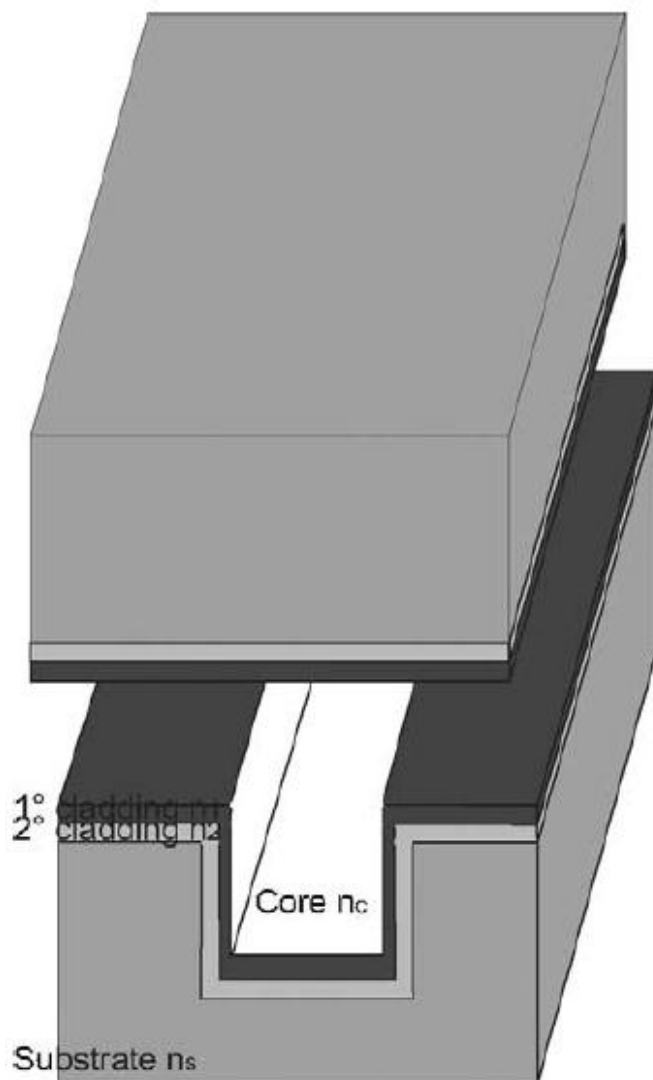


Figure 3-3 Redrawn from *ARROW optical waveguides based sensors*[89]. Hollow core ARROW waveguide structure, n refers to refractive index.

The guide, shown in Figure 3-3, is made from two structures combined together. The guide is set-up according to the anti-resonant conditions described above i.e. $n_c = n_2$, $n_1 \gg n_c$ and n_s is much greater than all the other layers and $d_c = 4 \mu\text{m}$, $d_1 = 0.12N \mu\text{m}$ and $d_2 = 2.05N$. In this condition, all light is confined to inside the waveguide and any attenuation in the waveguide is dependent on the core refractive index, so the core can be filled with a fluid analyte, and the refractive index can be determined by intensity modulation. Of course, this can be problematic, as absorption could become a problem with some analytes[89]. The waveguide also features a fluid input and output system which feeds fluid to the core and an in-coupling and out-coupling waveguide at each end[87, 89]. Anti-resonant waveguides are attractive for the construction of hollow core waveguides, as they are simple to produce. Other hollow core waveguides not based on anti-resonant reflection have also been demonstrated, Figure 3-4.

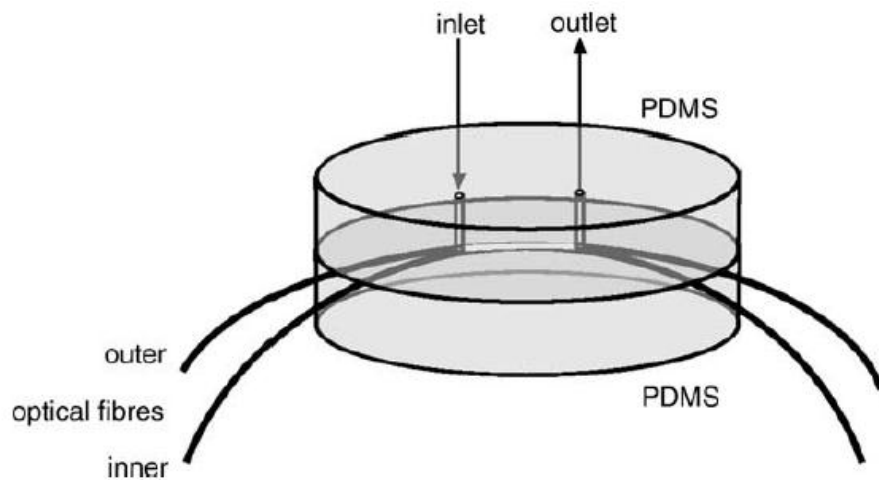


Figure 3-4 Redrawn from *An intrinsic fibre optic chemical sensor based on light coupling phenomenon*[87]. The schematic diagram of hollow core waveguide.

The hollow core waveguide is made using a polymer with unclad fibre optics inserted. The polymer contains a microchannel with a fluid inflow and outflow. The channel has fibre optics on its sides, with light entering the channel from one, moving through the channel and coupling with the output fibre, from which measurements are taken[87]. The positive features are that this sensor has a low cost, is relatively easy to fabricate, and is not solely limited to refractometric measurements (absorption and fluorescence spectroscopy has also been demonstrated), however, the non-reproducible methods (i.e. mechanical polishing) are used on the polymer during construction.

Looped waveguides have been used for sensors, as they have most of their modes propagating in the cladding layers. This makes them more sensitive than the waveguides mentioned above and more like the microsphere/micro ring which will be discussed below. These are attractive as there is less coupling loss, compared with microspheres/rings[82].

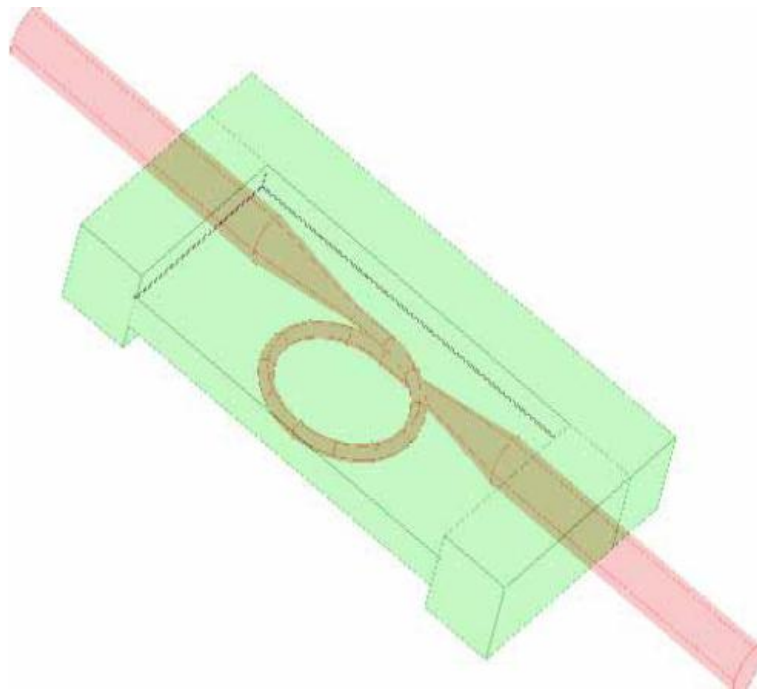


Figure 3-5 Redrawn from *An embedded optical nanowire loop resonator refractometric sensor*[75].The structure of an embedded optical nanowire loop resonator (ENLR) refractometric sensor.

One of these sensors, Figure 3-5, involved the loop of the waveguide being encased in low-loss/low refractive index polymer, with the loop close to the surface, while the polymer around the input/output waveguide was thicker, with the core in the middle. The mechanism of the sensor is the same as the previously discussed waveguides - the analyte fluid covers the polymer surface, causing a change in external refractive index and the external modes are shifted, which is seen in the resulting transmission spectrum[75, 76].

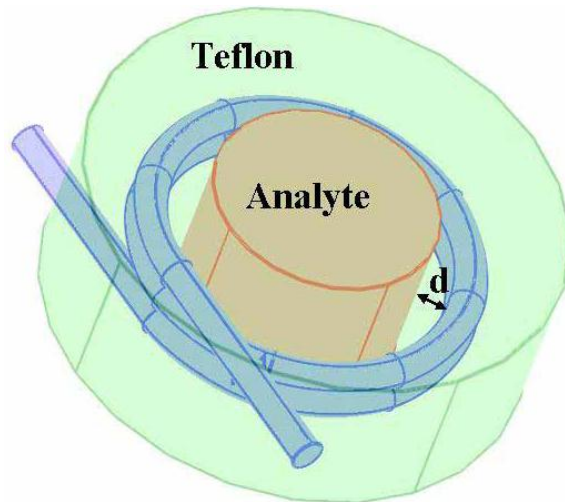


Figure 3-6 Redrawn from *Optical microfiber coil resonator refractometric sensor*[82]. The structure of the coated all-coupling nanowire microcoil resonator (CANMR).

A variation on this is the optical-fibre-nanowire microcoil (coated all-coupling nanowire microcoil resonator or CANMR), shown in Figure 3-6. To construct this sensor, a rod was coated with a layer of low-loss polymer. The optical fibre nanowire is wrapped around the rod and the whole construction is coated with the same low-loss polymer. The rod is then removed from the centre, which creates a chamber for the analyte to flow through. Again, as light moves through the loop, the external modes react with the changing refractive index, causing the transmission spectrum to shift. In both cases, the radius of the waveguide loop and the distance to the edge (d in Figure 3-6) of the surface has an effect on the sensitivity of the sensor, allowing tunability[82]. These loop resonators are predicted to have higher sensitivities and lower detection limits than most of the schemes put forward in this section, excluding LSPR. Of course assumptions on propagation and loss are made which are difficult to realise in a practical setting. Neither geometry is easier to manufacture than the other, however the ENLR is expected to be advantageous due to the added protection[75].

Waveguides have also used interferometry and fibre gratings to determine concentration from refractive index.

Interferometry has been used to establish concentration of an analyte based on a refractive index change due to the analyte. This is achieved by splitting a beam of light and passing one part through a region with the refractive index to be measured and the other through a control region. When the waves are recombined, a phase shift can be extracted from the interference pattern, and the change of phase is related to the

refractive index detected[79]. Young[79, 91] and Michelson interferometer[90] configurations have both shown success at measuring a refractive index change.

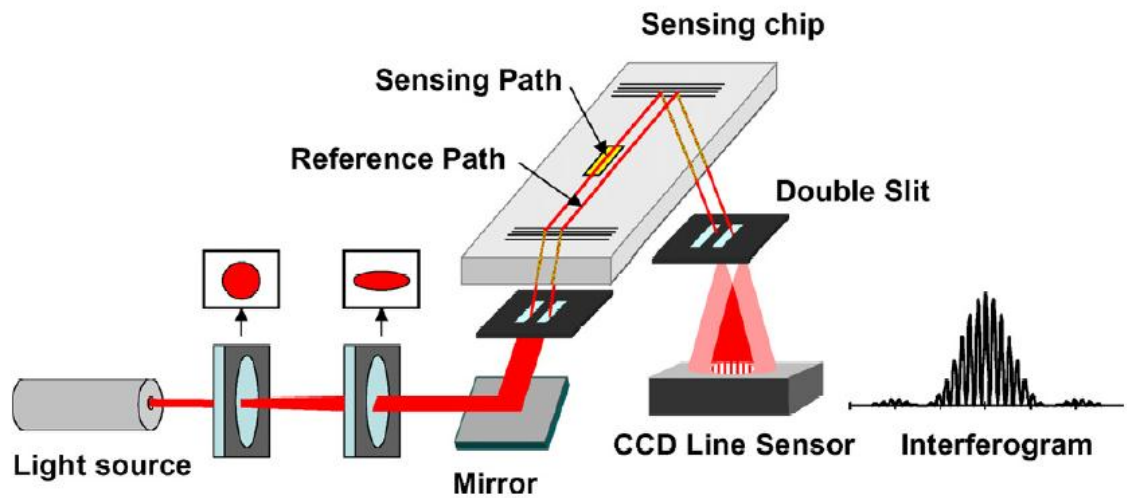


Figure 3-7 Redrawn from *Interferometric biosensor based on planar optical waveguide sensor chips for label-free detection of surface bound bioreactions*[79]. The set-up of a Young interferometer refractive index sensor, and an example of the resultant interferogram.

In the Young interferometer configuration, Figure 3-7, a beam is split (using a double slit) into two beams before each is coupled to a waveguide. One beam runs over a sample of the chemical (sensing path) and the other runs over nothing (reference path), before the beams are outcoupled and pass through another double slit, producing an analysable interference pattern. Refractive index is determined by the phase shift of the interference pattern[79].

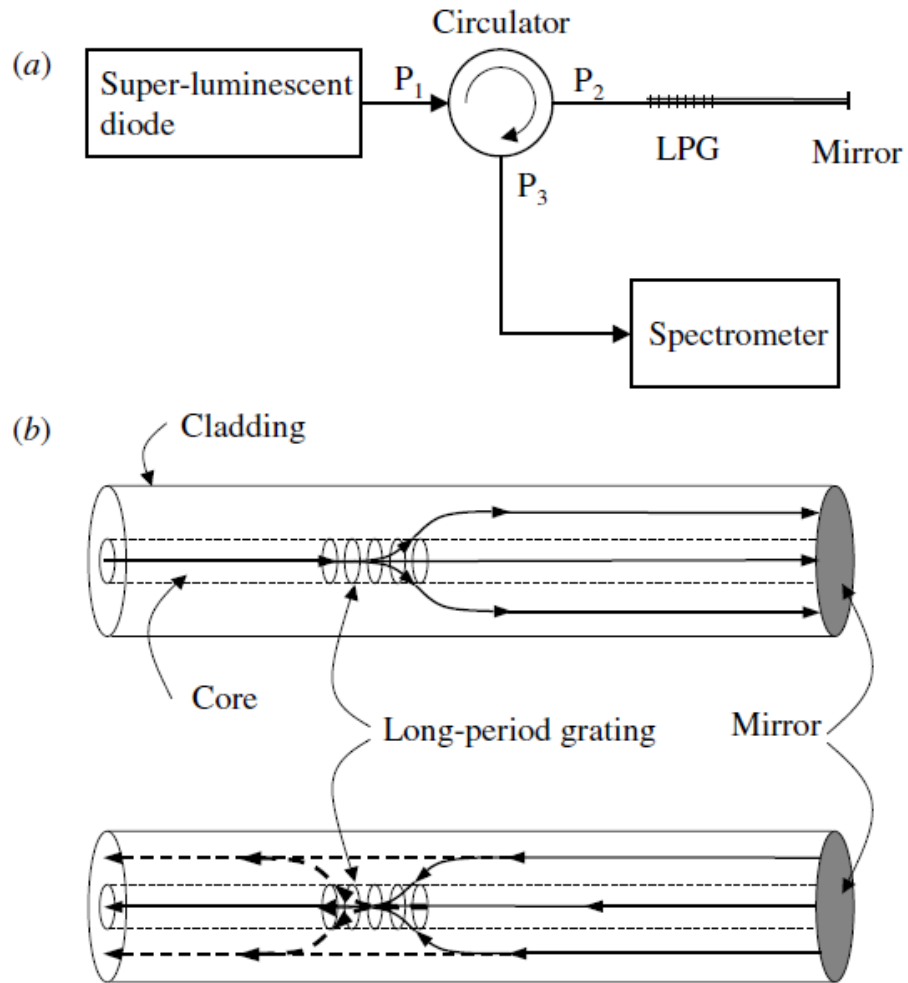


Figure 3-8 Redrawn from *Long-period grating Michelson refractometric sensor*[90]. The a) complete set-up of the sensor and b) the structure of the Michelson interferometer.

Michelson interferometry, Figure 3-8, has also been used to determine concentration[90]. A wave of light is coupled into an optical fibre containing a long-period grating (LPG) which splits the wave into a mode that travels through the core and one that travels through the cladding. At the end of the fibre, a mirror reflects the modes back, and when they reach the LPG some of the cladding mode combines with the core mode, and vice-versa[90]. The mode in the cladding is lost but the core mode decouples from the optical fibre and its interference pattern is analysed. A change in refractive index of the medium that the fibre is in alters the mode in the cladding which can be analysed by the phase shift of the recombined beam[90].

Both of these interference sensors have been practically tested and have a similar effectiveness as the ARROW sensors when used in its resonant condition, however, as described above, the ARROW sensor has a simpler output. The Young interferometer

does have a more complicated set-up than the Michelson interferometer. The complete Michelson sensor itself is compact, as the actual interferometer is 45 mm, and it has been suggested that it can be reduced to 10 mm[90]. In addition, the Michelson interferometer does not require as many parts as the Young interferometer, making the set-up somewhat simpler.

Other interferometric setups have been used such as the wavelength interrogated optical sensor (WIOS), Figure 3-9. This sensor consists of a waveguide with two corrugated grating regions, each with a different period or different thickness, on the surface[91].

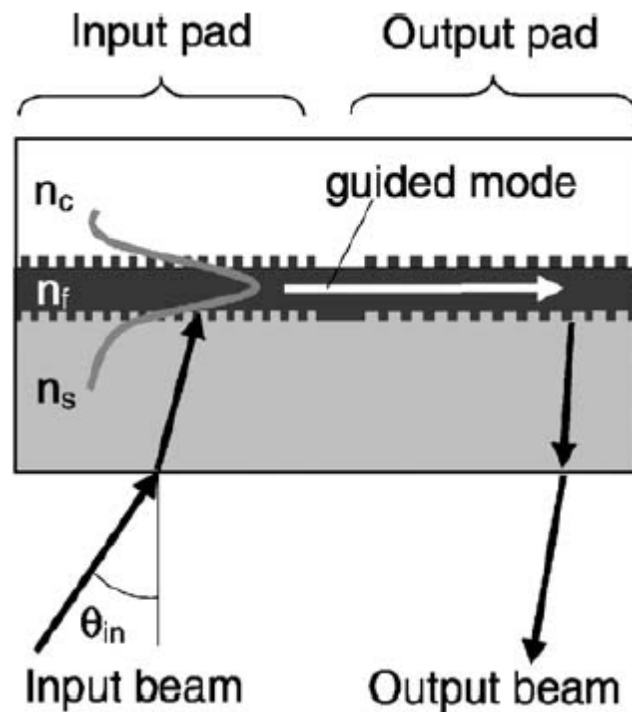


Figure 3-9 Redrawn from *Label-free highly sensitive detection of (small) molecules by wavelength interrogation of integrated optical chips*[91]. The basic structure of the wavelength interrogated optical sensor (WIOS). The refractive index being measured is n_c .

One of these is the in-coupling grating and the other is the out-coupling grating. When an incident beam from a tuneable laser diode strikes the in-coupling grating, a guided mode in the waveguide is excited, provided the wavelength of light is a resonant wavelength, which travels along the guide until it reaches the out-coupling grating and is out-coupled on the detector. The analyte forms the top cladding, (in-coupled wave comes from the bottom cladding, a substrate) and its refractive index determines the resonant wavelength, i.e. a shift in refractive index means a shift in resonant

wavelength. The out-coupled wave interferes with the in-coupled wave before it reaches a photo detector, and by comparing the reference beam (input beam) to the output, the resonant wavelength can be determined[91]. This sensor has a limit of detection of 10^{-6} , refractive index units (RIU) which is in line with most of the other interferometric sensors, and less than the theoretically possible looped waveguides. The sensor has reported parasitic effects on the resonance peak which was solved by using a motorised deflection mirror to recalibrate. The sensor itself has more of a focus on detection of biomolecule concentrations, and while it can be used on bulk liquids, the increased complexity of the device for comparatively little gain makes this an unattractive option compared to some of the other refractometric sensors.

Diffraction has also been used to make refractometric measurements[83].

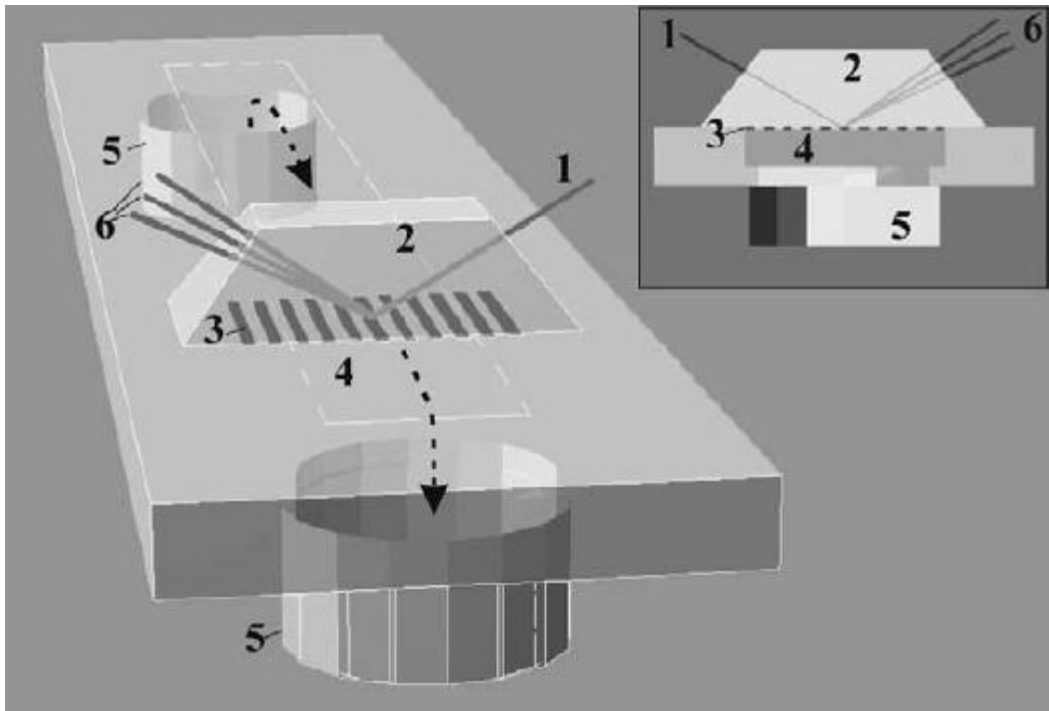


Figure 3-10 Redrawn from *Micro-fluidic analysis based on total internal light reflection*[83]. The schematic of a micro-fluidic analysis system based on total internal light reflection (TIR), with the following aspects highlighted 1-incident light beam, 2-TIR prism, 3-diffraction grating, 4-micro-fluidic channel, 5-inlet and outlet nozzles to the channel and 6-diffraction orders.

A metal grating is deposited on top of a glass liquid cell, which allows liquid to flow underneath. A prism is then attached to the top of the grating. Measurements are taken by shining a light source at a fixed angle which will allow for the total internal reflection of light (critical angle). The light is reflected off the grating and diffracted back out of the prism[83]. The different analytes being measured do not change the

diffraction direction, only the diffraction efficiency, calculated as the intensity of diffracted light divided by the intensity of the incident light[83]. This sensor had a lower sensitivity than most of the others described in this chapter at 1.7×10^{-3} refractive index units. Its main advantage is the fact that it is based on micro-fluidic analysis, and so is useful in diagnostics where not much analyte is available. Of course, microfluidics are not very useful in this context.

3.1.3 Standing Wave Resonators

Standing wave resonators are objects in which light resonates at a certain frequency. Sensors have been constructed which guide light to a resonator, where it resonates based on the intrinsic properties of the resonator (size, shape, material) and the surrounding medium. Therefore, the refractive index (and hence concentration) of the surrounding medium can be ascertained by monitoring the resonator's output. This section focuses mainly on whispering gallery mode (WGM) and localised surface plasmon resonance sensors, however, there are some other resonators which may possibly be used as sensors.

WGM sensors are becoming increasingly popular, particularly those based on microrings[81] and microspheres[78, 81, 86]. WGMs are the resonating modes found in dielectric rings, disks and spheres that allow light to continually propagate around the ring through total internal reflection[78, 81, 84, 86]. These modes have wavelengths dependent on the radius, angular momentum and effective refractive index. WGMs in these objects have been shown to have quality factors (Q-factors) up to 10^9 , due to the fact that the surface area of the object is increased in these objects so that more light interacts with the surface[81]. Q-factors are dimensionless parameters which describe how sharp a spectral feature is (sharpness of a feature is how close the central or peak wavelength is to the edge of the spectral feature (bandwidth)), in this case high Q-factors relate to sharp spectral features which provide very high sensitivity to change. Of course the size of the desired Q-factor is very much based on the concentration range of the sensor. If, for example, a sensor is designed to measure concentrated analytes, then a high Q-factor will be too sensitive to unambiguously determine a concentration. Similarly, a low concentration measured with a low Q-factor might not even register a signal.

Microrings are versatile and can be used in different ways[73, 81]. The simplest conformation of a microring sensor is a microring and fibre bus of similar height in the pedestal type conformation[73], Figure 3-11.

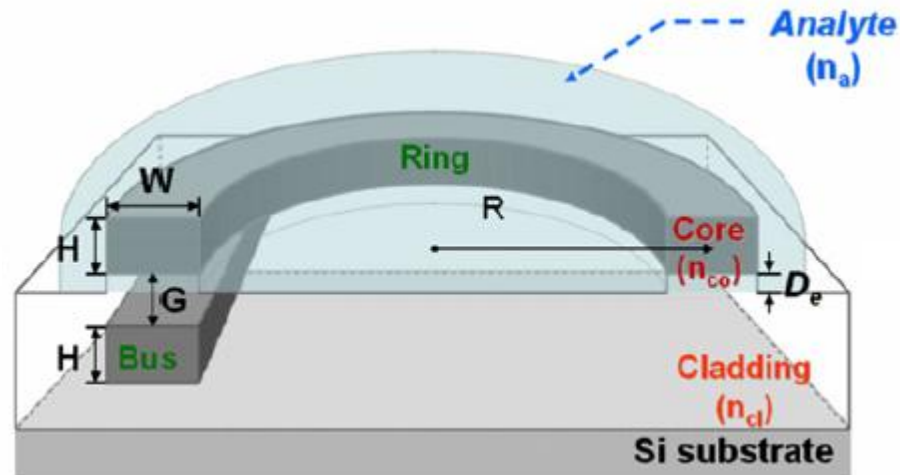


Figure 3-11 Redrawn from *Integrated photonic glucose biosensor using a vertically coupled microring resonator in polymers*[73]. A cross section of a schematic of a microring and bus in the pedestal type conformation.

In this, the fibre bus is enclosed in a cladding and the microring is attached to the cladding on top of the bus, and is itself immersed in an analyte. This configuration is the preferred configuration as it reduces the effect of the analyte on the coupling. The bus acts as the light input and output, while the microring acts as a resonator. Light is coupled to the ring from the bus and is internally reflected around the ring at the resonant wavelength, before being coupled back into the bus causing interference with the output light. A periodic band-stop filtering characteristic can be attained from this output, in this case the free spectral range and resonant wavelength of the ring[73]. The resonant wavelength is determined by the effective refractive index of the ring's guided mode, and it has been shown that the resonant wavelength varied linearly with the effective refractive index. It has been determined that this configuration has a sensitivity of 200 nm/RIU and a detection limit of 5×10^{-6} RIU, which is better than most waveguide and interferometric sensors, but lower than the theoretical values for the looped waveguides. One problem for determining large changes in refractive index is that the sensitivity of the sensor is higher when the refractive index of the analyte and waveguide is similar[73]. Other issues have arisen with inefficiencies in the sensor due to the assembling due to etching leaving rough surfaces and the need to assemble the waveguide separately before integrating it[81]. A possible solution to this is silicon-on-

insulator (SOI) deposition, which has been shown to improve surface roughness, and consequently reduce loss[139]. The waveguide is constructed by depositing silicon onto an insulating oxide, before the silicon is masked and etched. This leaves top and bottom faces of typical SOI wafers atomically flat[139], which reduces loss in the transverse electric propagation direction, while it is suggested that oxidation smoothing could reduce surface roughness on the side walls, and therefore, a reduction in loss in transverse magnetic propagation direction[139].

While the microring described above is useful for small samples, another type of microring resonator has been developed which is useful for measuring the refractive index of flowing fluids[70, 74, 77, 80], Figure 3-12.

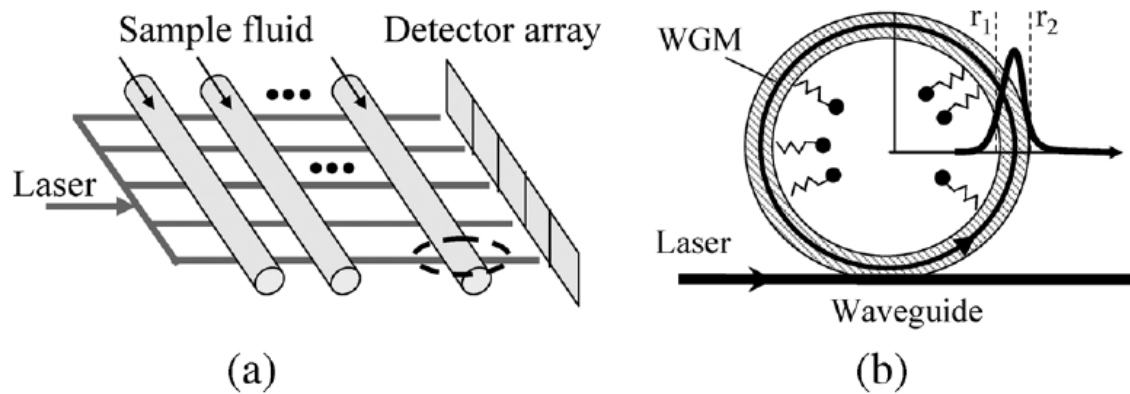


Figure 3-12 Redrawn from *Refractometric sensors for Lab-on-a-Chip based on optical ring resonators*[81]. Schematic of liquid core optical ring resonator (LCORR) a) the set-up of capillaries and fibres and b) the inside of a capillary that has been functionalised for sensing biomolecules.

The liquid core optical ring resonator[70, 77, 80] (LCORR) and the opto-fluidic ring resonator[74] (OFRR) are two such sensors which use the WGMs of glass capillaries to detect refractive index changes in a nanolitre flow. Both sensors are constructed in similar ways, and have similar properties, the glass capillaries are overlaid perpendicularly on a fibre taper[70, 74, 77, 80]. The operation of the sensors is similar to the above sensor; the analyte flow through the capillary causes changes in the effective refractive index of the resonator, and the light which propagates through the tapered fibre couples to the WGMs of the capillary, before coupling back into the fibre and interfering with the output light. From this again, the resonant wavelength is ascertained and the shift of this wavelength is linearly proportional to the refractive index change[70, 74, 77, 80]. LCORR sensors have been shown to reduce noise from

temperature changes through increasing the capillary thickness[80], however, this decreases the sensitivity[81], meaning a balance must be found.

All these have one overriding disadvantage, they are based on liquid not mist. They may be useable by condensing the liquid onto a microfluidic sensor. However, this is an unnecessary complication, and a WGM geometry does exist which can possibly be used in-situ in a mist, microsphere resonators.

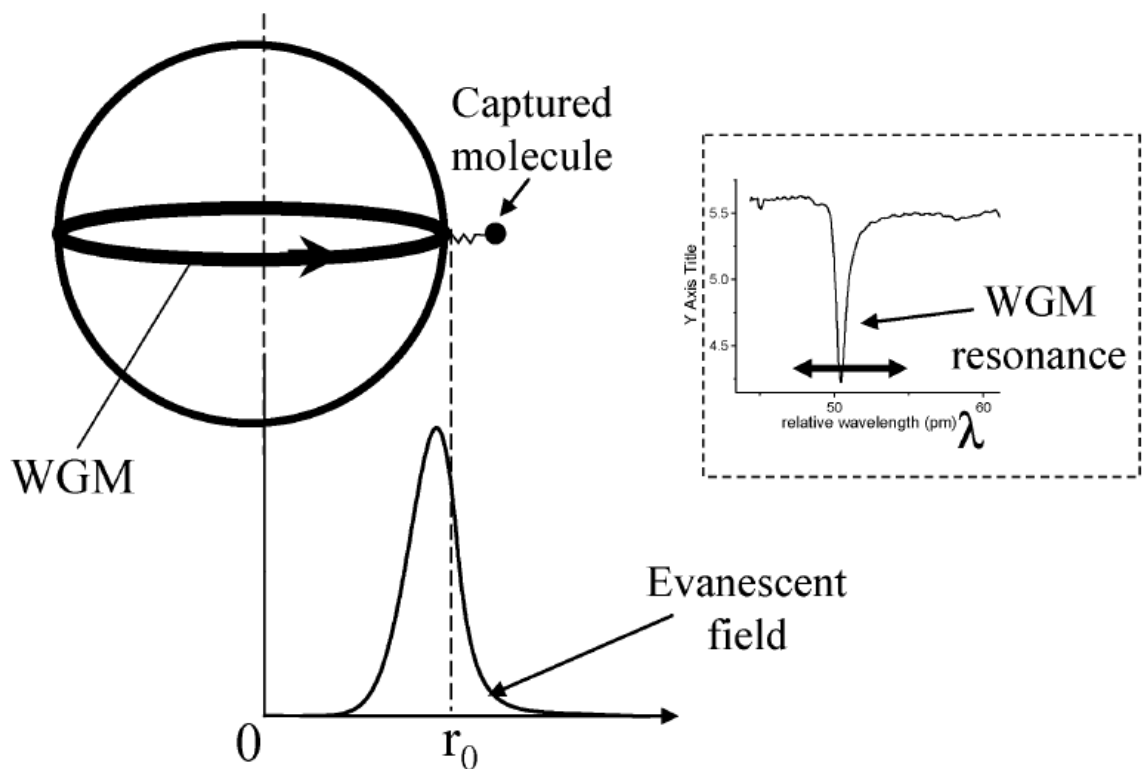


Figure 3-13 Redrawn from *Refractometric sensors for Lab-on-a-Chip based on optical ring resonators*[81]. A schematic of a microsphere WGM resonator functionalised as a sensor for biomolecules.

Microsphere WGMs resonators have been shown to have even higher Q-factors than microdisks and microrings, due to having more surface area[72, 81]. Because of this, the sensitivity of the sphere is inversely proportional to the radius of the sphere[81], Figure 3-13.

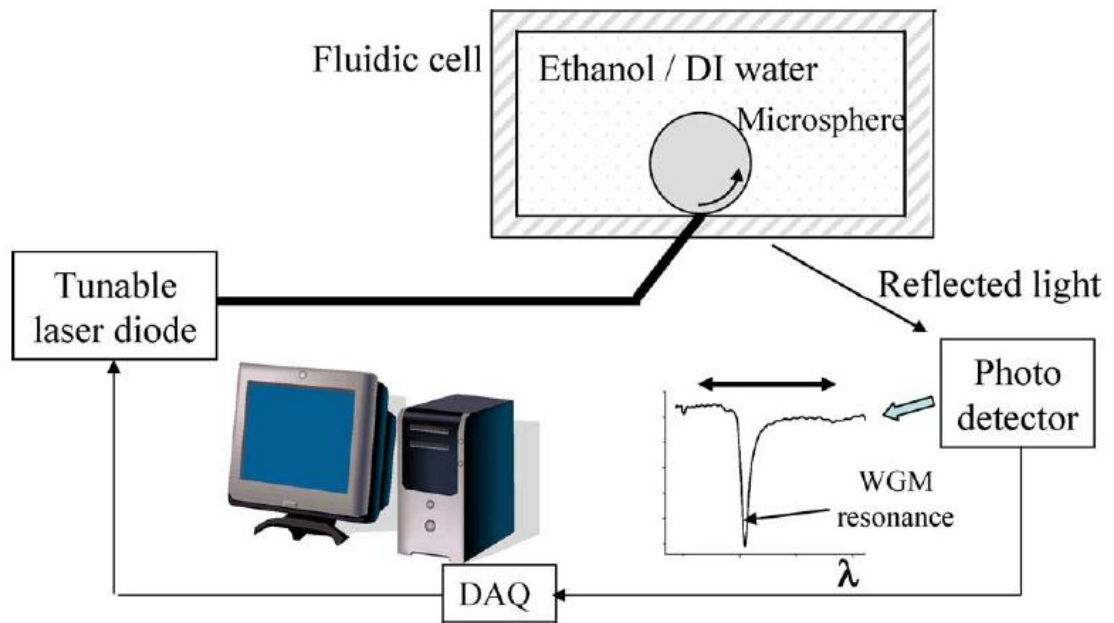


Figure 3-14 Redrawn from *Refractometric sensors for Lab-on-a-Chip based on optical ring resonators*[81]. The set-up of a sensor based on microsphere WGM resonators.

Microspheres are another option, and most experimental sensors based on this geometry have a similar set-up[78, 81, 84, 86]. Rather than a waveguide running next to the microsphere, a prism is used to couple light to the sphere and then reflect the output light to a photo-detector using total internal reflection[78, 84, 86], Figure 3-14. This is an issue with the sensors as it requires a non-trivial solution, which in any fluid flow is currently problematic[81]. As with the microrings and disks, the signal that the photo detector receives is a signal which is the result of the input wave and the resonant wave from the microsphere, from which a resonant wavelength can be detected. Any change to the effective refractive index of the sphere and its surrounding (i.e. changing concentrations) shifts the resonant wavelength as with previous WGM sensors[78, 81, 84, 86].

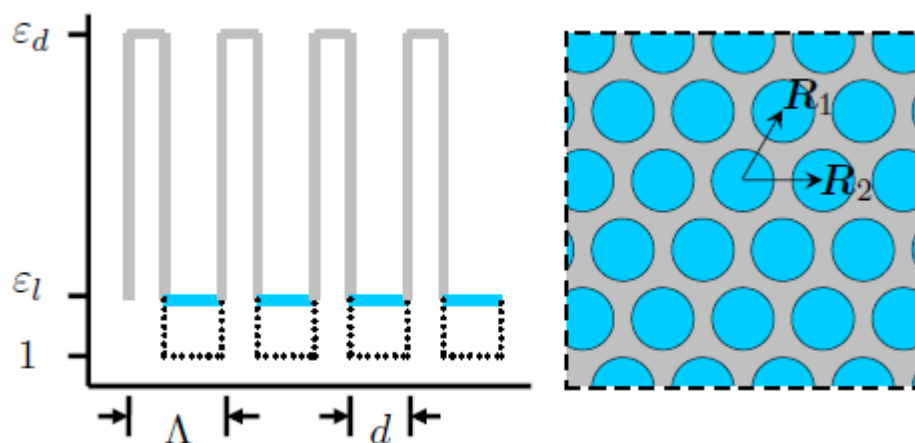


Figure 3-15 Redrawn from *Liquid-infiltrated photonic crystals-enhanced light-matter interactions for lab-on-a-chip applications*[69]. Schematic of the dielectric function variations in a photonic crystal. High refractive index material is labelled as ϵ_d (grey) and the liquid analyte is labelled as ϵ_l (blue).

Photonic crystals have also been suggested as refractometric sensors in similar applications to microspheres[69, 71, 85]. Photonic crystals are multilayered structures with different photonic band gaps, where propagation of certain wavelengths is prohibited. The band gap is determined by parameters such as incident angle, filling fraction and refractive index (related to dielectric function)[69, 71, 85], Figure 3-15. Therefore, if the other parameters are kept constant, the refractive index should be measurable by determining the propagating wavelengths using a photodetector, which should allow the refractive index to be determined[69, 71, 85]. While these crystals have theoretically similar limits to microspheres, and are seen as having a future in the creation of lab-on-a-chips, there is a challenge in designing photonic crystals that have a strong optical proximity from the crystal structure, in addition to having a decent optical overlap with the liquid[69].

Photonic crystals have also been suggested to form sensors based on the anti-waveguide principle[68]. Modelling was done on a photonic crystal fibre (PCF) waveguide which had a hole cut out of the core for the analyte. The analyte in the core needs to have a refractive index below the background PCF, to form a depressed index core. Wavelengths of light will travel through the waveguide until a cut-off wavelength, where all wavelengths shorter than that will not undergo total internal reflection, and thus not propagate. The cut-off wavelength is dependent on refractive index, so by determining the cut-off wavelength, the refractive index can be found[68]. These sensors are reported to have a theoretical sensitivity of 107 nm/RIU, however, this remains a model rather than an actual sensor.

Surface plasmon polariton resonances can occur under some conditions by the interaction of photons of light with the surface electrons of metallic layers. The wavelength of light at which the resonance occurs is determined by the electron structure of the metal, angle of incidence and the refractive index of the medium that the metal is in. Assuming that the metal and photon energy is kept constant, the concentration of a chemical can be determined by the resonance change which is directly related to the changing refractive index[101, 113, 128, 140].

A localised surface plasmon resonance (LSPR) also follows this principle, however, rather than occurring in bulk metal, it appears in nanostructures of the metal. The size and shape of these nanostructures affects the resonance peaks of the material, allowing the peak to be “tuned” to a certain wavelength[101, 106, 118, 119, 124, 128, 129]. In addition, the LSPR phenomenon can be used to amplify the measurement detected through another optical method[125]. For example, U-bend waveguides have been coated with nanoparticles to produce a stronger resonance signal[100]. Similarly, layering nanoparticles on top of one another can amplify the LSPR reading[113].

Various sensors have been described which utilise the LSPR phenomenon. Many use colloidal solutions of nanospheres and rods[31, 114, 133-137]. However, these generally fall into the chemical sensor category as a chemical reaction or adsorption with the metal causes the refractive index change. Examples of hydrogen peroxide sensors were given in the previous Chapter 2. Other sensors for a reducing analyte can have nanoparticle seed solution added. The more concentrated the analyte, the higher the red shift due to larger particles formed by electrochemical reduction[31, 133, 134, 137]. Another type of LSPR-based sensor binds particles together, with the analyte acting to form or break these interparticle bonds causing a colour change[135, 136]. It is worth noting that gold nanoparticles have been shown to catalyse reactions with hydrogen peroxide[141], which may be problematic with an LSPR sensor.

Nanoparticles have been immobilised or deposited on substrates to form the basis for physical sensors which determine concentration by the refractive index change from the analyte[98-132]. This setup has been used to make sensors ranging from simple slides onto which the analyte is deposited to lab-on-a-chip devices and waveguides which are used as flow sensors.

Preparation of these devices by immobilisation involves first the growing of nanorods[112, 117, 134], nanospheres[105, 115, 120, 122, 125, 130] or nanoshells[118, 122] in colloidal suspension, followed by their immobilisation on a substrate[105, 115, 117, 118, 120, 122, 125, 130, 134]. (A nanoshell is a nanoparticle which has a “core” of one type of nanoparticle and “shell” of another. For example, gold nanoshells can be made by addition of chlorauric acid to a solution of silver nanoparticles. The gold ions displace silver ion on the surface of the silver particle to form a gold coating[118].) The material used to immobilise the nanoparticles depends on the nature of the substrate and the nanoparticle [112, 115, 117, 120, 122, 125, 130, 134] but, for example, amine- or thiol-terminated organosilanes are generally used to anchor silver or gold nanoparticles onto quartz or glass substrates[125, 130, 134].

In contrast, chemical deposition of nanostructures on a surface includes nanoparticles being formed on organosilanes seeded with 10 nm gold nanoparticles by electrolysis of chlorauric acid and potassium chloride[103, 107]. Photocatalytic deposition is similar, in which the chlorauric ions are photoreduced into gold nanoparticles (in the presence of ethylene glycol), in this case onto glass coated with titanium oxide[114]. The major advantage of chemical deposition over immobilisation is that it reduces the chances of the anchoring organosilanes being stripped from the surface[114].

Physical deposition of nanoparticles is generally accomplished through evaporation[110, 116, 121, 123, 132], sputtering[102, 106, 109, 110, 119, 126], and ion milling methods[110, 127, 131]. Evaporation is a deposition process where the material is heated until vaporisation, at which point the material moves towards the substrate and condenses on it. Magnetron sputtering is similar, however, it uses an argon plasma to dislodge the material atom-by-atom from a “target”. These atoms move towards the substrate, colliding and binding with it. Over time these atoms nucleate together to form shapes on the substrates. Both have been used in the deposition of nanoislands[132], nanoarrays (spherical[102, 110, 123], pyramidal[102, 110], disks[104, 106, 110, 116], cylinders[110, 121]), triangles[106], rhombi[109], nanocrescents[126], nanoholes[104, 106, 110, 116, 131] and nanoparticles in nanoholes[110, 127], which have also been created using ion milling.

Another possibility is to have two plasmonic nanostructures separated by a nanoscale dielectric gap. These are sometime called antenna-enhanced plasmonic sensors because the nanostructures collect the light and focus its oscillating electric field in the dielectric gap, where interaction with the analyte can occur. Alternatively one part of the nanostructure may chemically absorb the analyte, changing its volume, and hence changing the dielectric gap. The change in gap refractive index or spacing can be seen in the form of a red-shift of the plasmonic peak[142]. The feasibility of antenna-enhanced plasmonic sensors has been demonstrated with simulations for hydrogen[142]. This is useful in Surface Enhanced Raman Scattering cases where the particles of interest are too small to have scattering or the inherent damping of the metal prevents a strong plasmonic resonance[142].

Work has also been done on a single wavelength plasmonic sensor[143]. The response of a variety of gold nanoparticles was simulated, including nano-spheres, nano-rods, nano-triangles and nano-bowties, over a range of refractive indices. It was found that nano-rods were the best geometry to use as a refractometric sensor based on gold nanoparticles, as both the plasmon wavelength shift, and peak sharpness were far superior to the nano-spheres, nano-triangles and nano-bowties[143].

3.2 Electroluminescence Sensors

Electroluminescence has also been utilised for hydrogen peroxide sensors[144]. These sensors are based on optical measurements of a thin film semiconductor, such as titanium oxide, which is part of an electric circuit. When hydrogen peroxide is present on the film, it is reduced. This produces OH⁻ radicals, which injects holes into the semiconductors valence band, which causes a negative polarisation in the film. This polarisation can be detected by a change in the electroluminescence intensity. This method is useful as there is little interference (the wavelength of luminescence is based on the potential applied, so a sensor can be “tuned” to hydrogen peroxide) so it can be used in mixtures, and can it can also be used in on-line monitoring. However, there is low detection range of 10^{-3} - 5×10^{-1} M[144].

3.3 Spectroscopic Sensors

Optical spectroscopy is an analysis technique quantifying the interaction between a material and different frequencies of light [145]. The main concept of

spectroscopy is resonance and the resonant frequency[145]. Matter, or more accurately the electrons or atomic bonds within it, is excited by light typically of different wavelengths/frequencies[145], to an extent that depends on details in the material itself. Those frequencies that do cause a large oscillation of the electrons or bonds within the matter are the resonant frequencies and can be displayed as a spectrum, which is a graph effectively displaying the amplitude of oscillation vs. the frequency of the light[146].

There are many spectroscopic techniques to analyse light/matter interactions but the main ones are ultraviolet-visible (UV-Vis) spectroscopy[147], infrared spectroscopy [148], rotational spectroscopy[148] and Raman spectroscopy[148, 149].

UV-Vis spectroscopy utilises light in the ultraviolet, visible and near infrared (NIR) parts of the spectrum[147]. The basic set-up of the device is that there is a light source which emits light which travels through the sample in a straight line and is then detected by a photo detector. The wavelengths in the light are separated by a monochromator or prism before entering the sample or before entering the detector to ensure that only one wavelength is measured at a time and from here a spectrum can be determined. This technique can be used to measure the absorbance or reflection (the set-up is different with the light source and photo detector offset at angles to measure the light reflected by the chemical) spectrum of a substance[147]. The absorbance spectrum of a chemical has long been used as a determination of concentration. Light interacts with the molecules within the sample, causing the molecules to be excited to a virtual state, before the molecules relaxes again and returns to its ground state [145, 147]. This reduces the intensity of the light which reaches the detector at each frequency of light studied. Maximum absorbance indicates that the frequency of the light matches the resonant frequency of the molecule[145]. Absorbance is generally measured against a reference which becomes zero absorbance, either a baseline in single beam or separate reference and sensor beams split from the light source, and is often expressed as the fraction of light that passes through the sample to a detector for each particular wavelength. The Beer-Lambert law describes the relationship between light and its absorption by substances the light is travelling through[147]. In a sample in which the path length (the distance the light travels through the sample) is fixed, the absorbance of a sample is linearly proportional to the concentration of the sample, at a specific wavelength in the spectrum[147].

The absorbance spectrum for hydrogen peroxide has been studied, however there is difficulty in using it to determine concentration[146, 150-152] because of overlapping absorption bands with ordinary water in the visible range while use of ultraviolet light (below 300 nm) causes hydrogen peroxide to decompose[151]. The best differentiation between the water[153, 154] and hydrogen peroxide signals appears to be in the infrared part of the spectrum, specifically in the vicinity of 7 and 15 microns[150, 152]. However, these wavelengths are not very practical to measure within the parameters of the present project because the 15 micron peak only appears at cryogenic temperatures [150, 152], while this project is looking for a sensor for room temperature conditions. In addition, this region of the spectrum suffers from excessive background noise at room temperature due to ambient thermal radiation. Thermal radiation is the emission of infrared radiation from an object, if that object is at any temperature above absolute zero. When at room temperature, objects are capable of emitting detectable radiation in the high-mid to long wavelength infrared (centred around 10 microns). The detector used for the spectrum will be therefore picking up radiation from around the room in addition to the sample spectrum, making an accurate reading more complicated. There are sensors for hydrogen peroxide vapour streams which use this region (approximately 7.5-8.4 micron[155]) for the detection of hydrogen peroxide. The sensor uses three sources of light for absorption, one for water (low hydrogen peroxide absorption), one for hydrogen peroxide (low water absorption) and one for a background signal (low water and hydrogen peroxide absorption)[155]. These sensors are calibrated to known hydrogen peroxide and water concentrations. This allows the concentration of both water and hydrogen peroxide to be monitored. In addition, it is possible to measure the infrared spectrum at lower temperatures, however, this adds complexity to the sensor design, and is not practical in this project. One area in the spectrum where it appears practical in this case to measure a signal distinct from water is around the 3.5 micron range [146, 152]. This area has been used for a hydrogen peroxide liquid sensor using attenuated total reflectance (ATR)[156]. This type of spectroscopy uses an ATR crystal, with a higher refractive index than the analyte, to internally reflect light at least once off the crystals walls. The crystal is in contact with the analyte (hydrogen peroxide in this case) and when a beam of light (in this case infrared radiation) is passed into the crystal, it reflects off the walls, causing an evanescent wave to extend into the sample (the depth it extends to depends on the

wavelength of light used, the angle of incidence and the refractive indices of the crystal and analyte). The attenuated energy of the evanescent wave is then passed back into the beam, and the beam is then collected by a detector as it leaves the sample and a spectrum of the analyte can be determined[157].

Infrared (IR) spectroscopy can be performed at wavelength ranges where hydrogen peroxide has resonant wavelengths (i.e. 3.5 microns). IR spectroscopy can be as simple as absorption spectroscopy described above, where a beam of monochromatic light is passed through the sample before the light hits a detector, allowing a measurement of how much was transmitted or absorbed by the sample[148]. There is also Fourier Transform IR (FTIR) spectroscopy in which all wavelengths are measured at once, by converting the raw interference data into a Fourier transform which represents the spectrum[148].

One problem with absorbance measurements in a practical sense is that this project is attempting to measure the concentration within mist phase droplets. This will cause a large amount of scattering of the light. Nevertheless, there have been spectroscopic sensors reported as useful in the measurement of gas concentrations within mist or other particulates [158-160], particularly in respect of the tuneable diode laser absorption spectroscopy (TDLAS) method. These technique uses diode lasers which emit light over a narrow range of frequencies (generally a few nanometers[159]), which can be altered through the temperature and current applied to the device[159]. This method has been shown to cope with detecting concentrations of gases even if 99.99% of the transmission is lost, in this case through scattering from a mist[158]. This is achieved using the high speed wavelength tuning capabilities of laser diodes. During measurements, the laser is scanned rapidly compared to the characteristic transmission fluctuations, which means that transmission can be assumed as constant during scan periods. A reconstructed baseline (which is simply the baseline signal with no molecular absorber, in this case oxygen) can be divided through the transmission to then remove the fluctuations[158]. A major advantage of this method is that the signal has been measured directly, which allows the sensor to extract the absolute density without calibration.

TDLAS has also made use of multiple diodes to determine different vapours within mist streams[159]. In this case, each diode is chosen to scan over a frequency

range which resonates with the molecule which is being measured. This sensor has been shown to function in a sub-10 μm mist stream with an optical density of 5.5[159].

Another useful measurement technique when dealing with scattering is Raman spectroscopy. Most photons scattered by the molecule or atom have the same energy as the incident photons (Rayleigh scattering), however, a small percentage are scattered with a lower energy (Stokes shift) and in some occasions a higher frequency (anti-Stokes shift). This is Raman scattering, and by observing these scattered photons (it is possible to ascertain the vibrational, rotational and other low-frequency modes of an atom or molecule which caused this scattering[145, 148]. Atoms and molecules can be identified and analysed by their Raman spectra. However, due to the fact that Raman scattering is very weak, Raman spectroscopy requires specialised equipment for detection.[149]. The typical set up for Raman spectroscopy is a monochromatic light source such as a laser, the sample, a photodetector, and a filter of some kind to reduce the amount of light from the source reaching the detector and preventing the Raman scattered light from being observed[161]. The filter is generally a holographic grating and multiple dispersion stages[161]. Hydrogen peroxide has three Raman active modes at 880 cm^{-1} , 1400 cm^{-1} and 3140 cm^{-1} [162]. The 3140 cm^{-1} mode would be the easiest to use from a technical standpoint, and this mode does show variation between concentrations of hydrogen peroxide as the mode corresponds to the O-H bonds in the molecule[162]. In addition to this information, analysing the polarisation of the scattered light can provide information on the molecule's shape. This could be useful to differentiate between mist and vapour in the sample, and therefore how much hydrogen peroxide is mist and how much is vapour[163]. However, Raman spectroscopy is beyond the scope of this project as the equipment required is expensive and somewhat complex, making it unsuitable for a sensor device in a sterilisation unit intended for widespread service.

The optical platforms which will be covered in this thesis are refractometric LSPR and mid-infrared absorption spectroscopy. The LSPR-based sensor was chosen as it is simple to assemble and has desirable properties, such as tunability, high Q-factors and high sensitivity. An LSPR may be corroded by hydrogen peroxide, however, this experiment will use gold in the hopes that it is non-reactive (gold is also a very strong resonator). The other refractometric sensors have greater issues, such as some being

theoretical, a complex set-up (interferometric) or are based on micro-fluidics. In this case, it may be possible to make an addition to the test rig, to take up liquid, however, the goal of the project is to determine concentration of hydrogen peroxide in a mist. Some of these sensors could have their basic principles adjusted to a larger scale, and in this way alter the test rig to a large resonating chamber (hollow core ARROW, LCORR or looped optical fibre), but the original brief for the project is to develop a simple sensor to use in the decontamination unit, not re-engineering the decontamination unit. In addition, these other techniques for the most part are not recorded as having the sensitivity of the LSPR sensors.

Absorbance of hydrogen peroxide in the mid infrared range will also be studied, as the hydrogen peroxide has some spectral features in this range that may be interrogated. The main reason for using absorption spectroscopy is that it is well understood and cheaper than alternative spectroscopies (specifically Raman).

The next Chapter will detail some general experimental procedures used throughout the whole thesis. The more specific procedures are documented in the individual chapters.

Chapter 4 General Experimental

This chapter will describe some of the experimental techniques which are common to more than one part of the project. These sections of the chapter will be referenced in later chapters as required. In addition this chapter will describe the construction of the calorimetric sensors, in addition to some general characterisation of the sensors.

4.1 Data Analysis

Most data was recorded in comma separated values (.csv) or text files (.txt), and subsequently opened for analysis in Microsoft Excel 2007.

4.1.1 Linear Regression

Microsoft Excel was used to fit single linear regressions, using the statistical function LINEST. This method applied least squares regression to the data which was being analysed and could be used to determine the best relationship between the dependent and independent data (i.e. $y=mx+c$), how well this relationship defines the data (coefficient of determination, r^2), and how precise the relationship between the data is (using the root means squared error (R.M.S.E) of the relationship, shown in Equation 4-1, to create a confidence interval).

$$R.M.S.E = \sqrt{\frac{1}{N} \sum_{i=1}^N (\hat{y}_i - y_i)^2} \quad \text{Equation 4-1}$$

For Equation 4-1, N is the number of values in the population, \hat{y} is the outcome predicted by the regression and y is the actual value of the data point. In some cases standard deviation was calculated mathematically for individual data sets. This was done using Equation 4-2.

$$\sigma = \sqrt{\frac{1}{N} \sum_{i=1}^N (x_i - \mu)^2} \quad \text{Equation 4-2}$$

Equation 4-2 describes the calculation of the population standard deviation, σ . N is the number of values in the population, μ is the mean of the population and x_i refers to each value in the population. The construction of error bars or a confidence interval was performed by the simple addition and subtraction of the R.M.S.E or standard deviation from regression. Using one standard deviation or standard error produces a confidence interval of approximately 66%, while using two standard deviations or standard errors produces a confidence interval of 95%. Any data in the following chapters which uses error bars and confidence intervals will specify how many standard errors or deviations was used in its creation.

4.1.2 Non-Linear Regression

Non-linear regressions were performed using CurveExpert 1.4. As in Chapter 4.1.1, this program fitted a regression using the least squares method. CurveExpert contains a number of different statistical models, and has a 'curve finder' feature that attempts to find the best fit. Coefficient of determination was found by squaring the coefficient of correlation, while the regression and confidence interval were implemented in the same manner as described in Chapter 4.1.1.

4.1.3 Multiple Linear Regression

Two-variable quadratic surfaces were fitted were fitted using a legacy TurboBASIC program, QUADFIT, based on a program found in Science and Engineering Programs Apple II® Edition, written by J. Heilborn[164]. Like the methods in Chapters 4.1.1 and 4.1.2, the program uses the least squares method to determine the best regression. The program was able to output the equation describing the regression and the standard deviation of the regression. Again, confidence intervals were constructed in the same manner as Chapter 4.1.1.

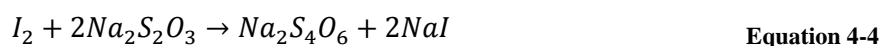
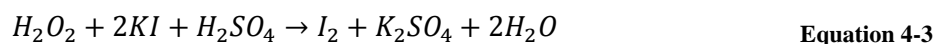
4.1.4 Analysis of Variance

An analysis of variance was performed on regressions calculated using the multiple linear regression to determine whether the increase in terms in the regression had a significant increase in variation compared to the individual residual errors of each independent variable in the regression. This was done by determining the residual error of each independent variable (which was the difference between the regression calculated value and the measured value), the variance of the regression (which is the

standard deviation squared) and the variance of each of the residuals (calculated using the variance function in Microsoft Excel). An F-value was calculated for each independent variable by dividing the variance of the regression by the variance of each independent variable. The *p*-value (probability that F-value is lower than the critical F-value) was calculated, using the calculated F-values, the degrees of freedom of the regression and the degrees of freedom of the residual error, and if this value was greater than 0.05 (which is the general value given to significance), then the higher number of terms in the regression did not significantly affect the variation for that independent variable.

4.2 Determination of Concentration of Hydrogen Peroxide

It is imperative to know the concentrations of hydrogen peroxide used to test the sensors. The concentration of hydrogen peroxide solutions was determined using iodometric titration. The principle of this titration is that hydrogen peroxide oxidises iodide to iodine in the presence of acid and molybdate catalysts. The iodine formed was then titrated against 0.1 normality sodium thiosulfate (0.1N), which reduced the iodine back to an iodide. This reaction was monitored using a starch indicator.



An aliquot of hydrogen peroxide was taken, with its mass being recorded. The mass of the aliquot taken was in the range 0.05-0.2 g, as this required less than 50 mL of 0.1 N sodium thiosulfate solution for titration. 100 mL of 5% (w/w) sulphuric acid was then added to the hydrogen peroxide. 10 mL 1% potassium iodide (w/v) was added to this mixture, followed by 1-2 drops of 3% ammonium molybdate (w/w), which turned the liquid dark brown. This mixture was then titrated against 0.1N sodium thiosulfate using a standard 50 mL burette, while the mixture was continuously swirled. As the titrated continued, the solution turned pale yellow, and at this point, a few drops of 1% starch indicator was added, which turned the mixture blue, and titration was continued until all the blue colour was gone. The volume of sodium thiosulphate was recorded along with the mass of hydrogen peroxide used to calculate the concentration of

hydrogen peroxide, in terms of mass of hydrogen peroxide to mass of the total solution (w/w), using Equation 4-5.

$$Conc.H_2O_2 = \frac{\text{volume of } Na_2S_2O_3(mL) \times \text{Normality of } Na_2S_2O_3 \times 1.7}{\text{Weight of hydrogen peroxide (g)}} \quad \text{Equation 4-5}$$

The 1.7 is the product of the equivalents of hydrogen peroxide and the molar and molar mass ratios between sodium thiosulfate and hydrogen peroxide.

4.3 Porous Platinum Films

One type of catalyst proposed for the calorimetric sensor was a porous platinum catalyst. As detailed in Chapter 2.5, it is possible to create porous thin films on substrates[65] via magnetron sputtering of a precious metal and aluminium. It was theorised that the porosity of the thin film could be controlled by varying conditions in the deposition chamber during sputtering, as the precursor's structure or aluminium content was controlled by these conditions. It was decided not to pursue too many variables as the focus on the project was to develop a calorimetric sensor, and so the most attention was paid to the amount of aluminium deposited on the sample.

4.3.1 Method of Deposition and Analysis

The magnetron sputterer was set up with two targets equidistant from the sample stage at 15 cm. The stage itself was a block heater with a thermocouple connected to it so that it could be set to a constant temperature. The sputtering chamber was typically pumped down for 1-2 hours at least before each deposition, until chamber pressure was below 10^{-5} Torr. The gas used for sputtering was argon, which was constantly flowed into the chamber to produce a constant pressure of 10^{-3} Torr. All depositions were run for 30 minutes. These settings were kept constant for all depositions; the only variations were in the temperature and the applied voltage.

Each target was supplied by an independent DC power supply set in constant current mode. The current was varied to keep the power relatively constant. The platinum was deposited in all but one instance by supplying a constant power of 15 W, using a current of 0.05 A and a voltage of 300 V (The sole exception was sample ALPT13, deposited at 0.05 A and 350 V, i.e. 17.5 W.). The power supplied to the Al target is listed in Table 4-1 for instances when the substrate was held at 400°C. Samples ALPT12, ALPT13, ALPT14, ALPT15, and ALPT16 were deposited on a microscope

slide which was split in two. One of these slides was de-alloyed by submersing the slide in 0.2 M NaOH at room temperature. After 2-3 minutes, the bubbles stopped evolving from the surface, and the film was blackened, indicating that the process was finished. The sample was then withdrawn and rinsed with MilliQ water. Sample ALPT21 was deposited on a single slide and de-alloyed using the same process.

All depositions were done on glass microscope slides. Prior to deposition, these slides were cleaned by sonication in detergent for 10 minutes. Once the slide was removed, it was rinsed thoroughly using tap water, before being rinsed with MilliQ water. The slide was then blow dried under a nitrogen stream.

Table 4-1 Power applied to Al target with substrate temperature fixed at 400°C

Sample Name	Current Applied (A)	Target Potential (V)	Power (W)
ALPT12	0.10	275	27.5
ALPT13	0.15	300	45
ALPT14	0.20	350	70
ALPT15	0.25	350	87.5
ALPT16	0.30	350	105
ALPT21	0.15	300	45

The alloyed slide for samples ALPT12, ALPT13, ALPT14, ALPT15, and ALPT16 were used to determine the X-ray patterns for each alloy. This was done to elucidate the crystal structure and therefore identify the compound. Analysis was performed using grazing incidence X-ray diffraction with a Siemens D5000 Diffractometer, with tilt angle of 0.5°. The X-ray radiation used was CuK α , with a wavelength of 1.5406 Å. The samples were set to measure a two-theta range of 8° to 90°, in steps of 0.02°, with each step being recorded over 5 seconds. These measurements were run at room temperature.

The de-alloyed slides for samples ALPT12, ALPT14, ALPT15 and ALPT16 as well as ALPT21 were imaged in a scanning electron microscope (SEM) to determine their surface topography. The instrument used was the Zeiss Supra 55VP SEM, with an in-lens detector for higher magnification images.

Table 4-2 Al-Pt samples deposited with varying substrate temperature and power fixed at 27.5 W

Sample Name	Temperature of Substrate (°C)
ALPT17	200
ALPT18	250
ALPT20	350
ALPT2	400

Table 4-2 describes the samples of alloys which have been deposited under differing temperature conditions. All the samples are deposited with the same power applied to both targets, 15 W applied to the platinum target and 27.5 W applied to the aluminium target.

The de-alloyed samples ALPT12, ALPT14, ALPT16 and ALPT21, and the alloyed samples ALPT17, ALPT18, ALPT19 and ALPT20 were analysed at the Australian Synchrotron using a non-standard sample holder (normally the particular beam-line uses capillary samples). This was done because the porous samples were expected to be too amorphous and have too little mass to determine a diffraction pattern using laboratory CuK α radiation. A 9 keV beam, equivalent to wavelength of 1.378 Å, was applied. An ordinary sputter coating of Pt made at room temperature was used to establish the best position and tilt angles for the non-standard stage, so that the peak profiles could be optimized relative to the background signal. It was noted that the angle of tilt and the height of the sample strongly influenced peak position, shape and height. A tilt angle of 0.6° was selected. The peaks are broad, in part due to inefficiencies in the geometry used but the patterns can certainly be used to identify the phases present.

4.3.2 Results of Platinum Alloy and Porous Platinum Analysis

The X-ray diffraction patterns of samples ALPT12, ALPT13, ALPT14, ALPT15 and ALPT 16 are shown in Figure 4-1.

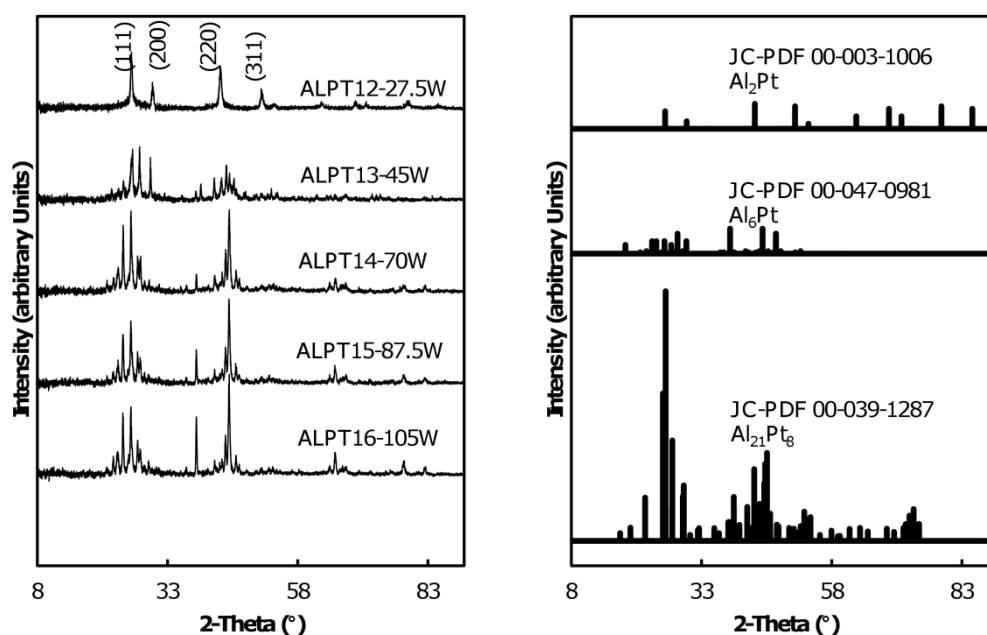


Figure 4-1 The X-ray diffraction patterns of alloyed samples with differing power applied to the aluminium target. Also shown are the known or calculated JC-PDF cards that appear to match up with some parts of the patterns. CuK α radiation was used for this data. Data obtained with assistance of Mr Mark Berkahn, UTS.

Figure 4-1 shows the X-ray diffraction patterns of the various samples and also three of the JC-PDS cards which show the best correspondence to the samples. The samples themselves had very little material in them, so the X-ray count rate was low.

Sample ALPT12 was believed to be Al₂Pt after deposition due to its yellow colour. XRD confirmed this as there was a match for JC-PDS card 00-003-1006. The other samples are somewhat more complex. There is a possibility of peak broadening due to these being thin films which are not perfectly crystalline, and it would also appear that there are multiple phases present in these samples. These two factors make accurate identification of phases in the samples difficult, however, there are some features which may be of interest.

Some of the peaks of sample ALPT13 appear to correspond to Al₂Pt, especially for the (111), (200), (220) and (311) positions, but Al₂₁Pt₈ and/or the meta-stable Al₆Pt could also possibly be present. There are also peaks which are associated with elemental aluminium possibly present (the Al JC-PDS 00-004-0787 has peaks around 38.5°, 44.5°, 65° and 78°). Samples ALPT14, ALPT15 and ALPT16 are similarly difficult to identify, however, all appear to have the same phase. There is a single peak which gets larger from ALPT14, to ALPT16 (as the power applied to the aluminium

tagret increases during deposition), and appears to be present in ALPT13. The fact that it increases with samples may be due to the increasing aluminium in each of the samples.

Figure 4-2 shows SEM micrographs of the de-alloyed samples. ALPT13 was not included as the samples collapsed and was washed off during de-alloying. ALPT21 was included instead, which should be similar, except for having slightly less platinum. The samples are shown at low magnification and high magnification to show the pattern of pores and the shape of the pores.

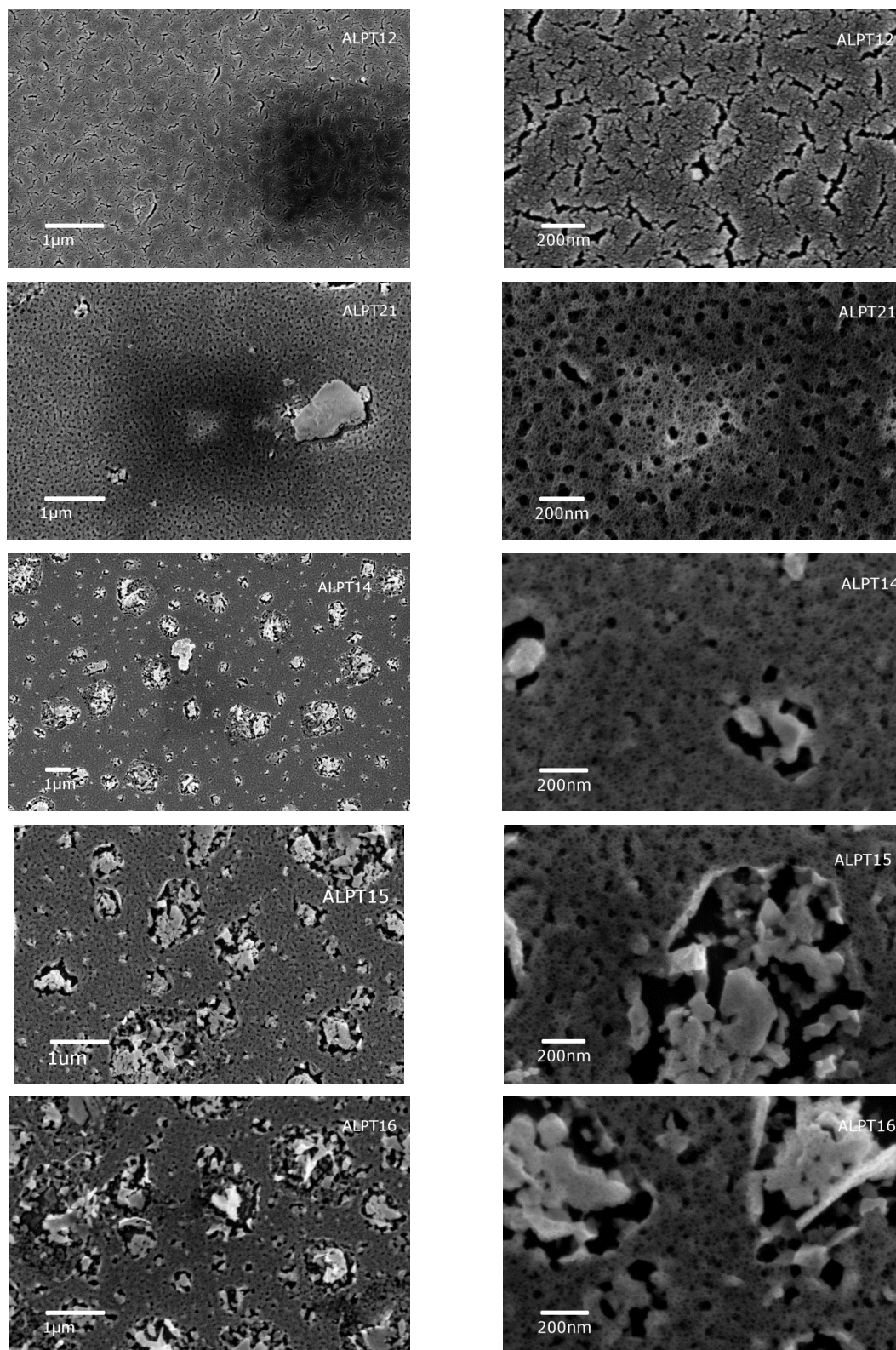


Figure 4-2 SEM micrographs of porous platinum samples. The left column is a view of the surface structure while the right hand column is a close-up on the pores of the sample.

The morphology of de-alloyed ALPT12, identified as Al_2Pt , was unlike that of the other samples. It had pore formations which appear to be long cracks, rather than a sponge-like surface. This is due to the fact that the alloy precursor had the lowest

content of aluminium of those examined (about 70% at.), seen in Figure 4-3. It is unlikely that the platinum aluminides with even less aluminium (for example Al_3Pt_2 or AlPt) would be of use in making porous films. In contrast, the higher aluminium content ALPT21 shows a sponge-like surface, with a distribution of small pores in-between a distribution of large pores. Samples ALPT14, ALPT15 and ALPT16, show something similar, however, the distribution of their ‘large’ pores is more random. Two possible reasons are that these samples are multiple phase, with different phases de-alloying to form different pore structures, or the alloy featured areas of high concentrations of aluminium, which when de-alloyed caused the larger holes to form.

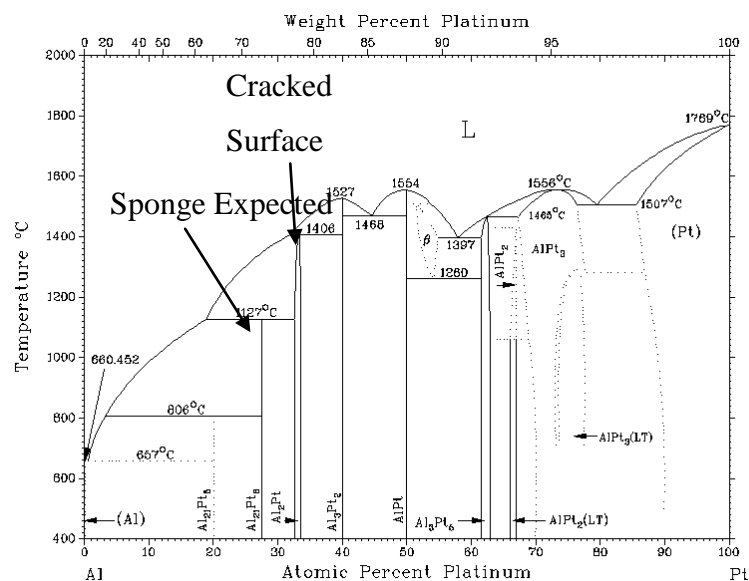


Figure 4-3 Phase diagram of Pt-Al. Diagram is from Building a thermodynamic database for platinum-based superalloys: Part I, in *Platinum Metals Rev.*, by L.A. Cornish et. al.[165]

The XRD patterns of the de-alloyed porous platinum made from samples ALPT12, ALPT21, ALPT14 and ALPT16 (samples have an increasing aluminium content due to a higher power applied to the target during deposition) are shown in Figure 4-4, along with a X-ray pattern of ordinary sputtered platinum and the expected platinum XRD pattern. It can be seen that as the amount of aluminium in the alloy is increased, the sample becomes less and less crystalline when de-alloyed, which is seen by the peak broadening in the samples (the peaks start separated and then begin to merge due to the broadening). The peaks of the XRD patterns of the de-alloyed films are significantly broader than those of the sputtered platinum film.

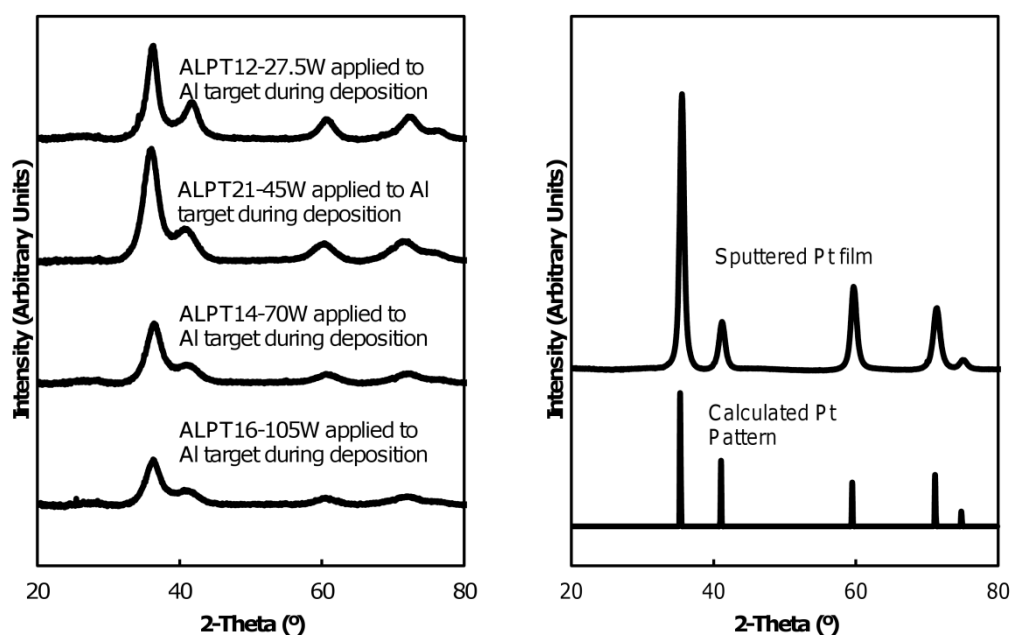


Figure 4-4 The X-ray diffraction patterns taken by the synchrotron of porous Pt from alloy samples. Power applied to aluminium target during deposition is shown. Synchrotron radiation was used for this data. Data obtained with the assistance of the Dr Catherine Kealley and Dr Annette Dowd, UTS.

Figure 4-5 shows the X-ray patterns of another series of samples. These were all made using the same ratio of platinum to aluminium, the same as that found previously to form Al_2Pt , however, they were deposited at different substrate temperatures ranging from 250°C to 400°C . Samples ALPT2 (made under the same conditions as ALPT12) and ALPT18 showed similar patterns, that of Al_2Pt . The X-ray patterns of samples ALPT17 (200°C) and ALPT20 (350°C) were similar to each other, but nothing like the other two patterns. The close-up of the patterns of samples ALPT17 and ALPT20, show that they are different to just a glass substrate, however, whether these are real or an error is not determined. The fact the peaks are so small is compared to the other alloys suggests error, however, the peaks could just be the result of broadened peaks due to a lack of crystallinity. This would suggest that for samples made with substrate temperatures less than 400°C , there is less chance of a crystalline Al_2Pt sample forming.

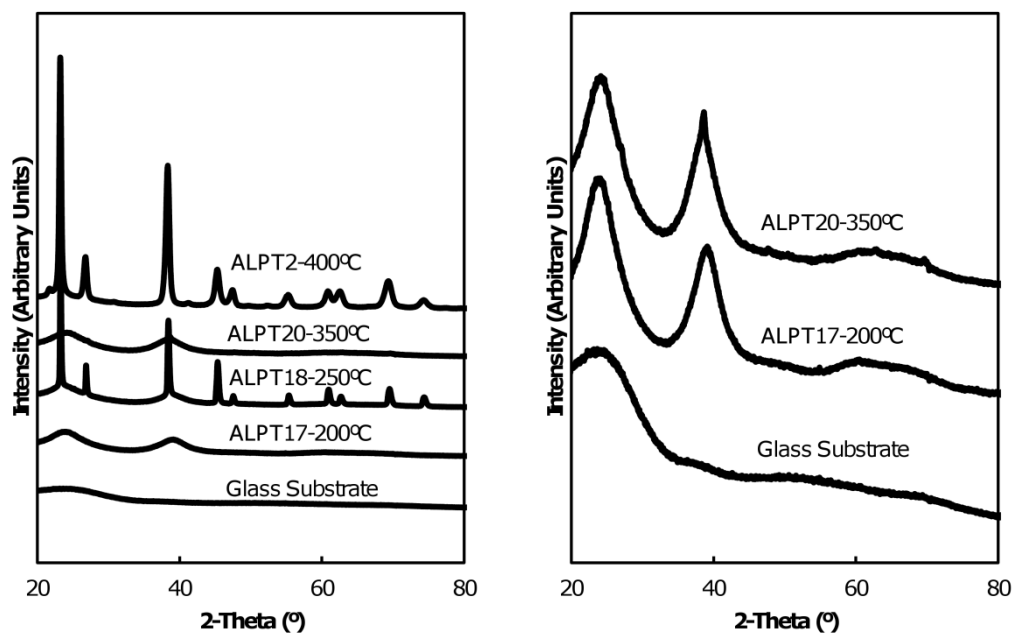


Figure 4-5 The X-ray diffraction patterns taken by the synchrotron of alloy samples made at different substrate temperatures, which are shown with label. ALPT20, ALPT17 and the glass substrate are also shown together in a “zoomed” comparison in the figure on the right. Data obtained with the assistance of the Dr Catherine Kealley and Dr Annette Dowd, UTS.

Figure 4-6 shows the X-ray diffraction pattern of the porous platinum de-alloyed from samples ALPT17, ALPT18, ALPT20 and ALPT12. It can be seen that the alloys which had sharper peaks produced a porous structure which appears to be more crystalline, which is seen by the peaks “narrowing” with respect to each other, which confirms the previous data.

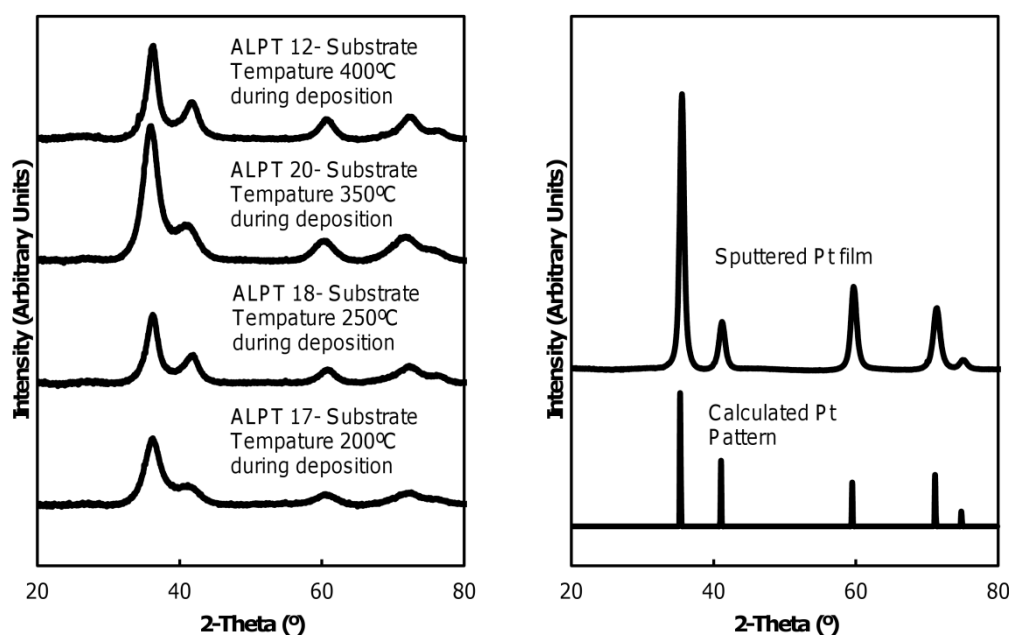


Figure 4-6 The X-ray diffraction patterns taken by the synchrotron of porous Pt from alloy samples made at different substrate temperatures which are shown in the figure. Data obtained with the assistance of the Dr Catherine Kealley and Dr Annette Dowd, UTS.

4.3.3 Summary of Porous Platinum Films

Porous platinum films were made from Al-Pt precursor alloys of different phases. It was found that different phases of the alloy produced different sized and shaped pores in the sample upon de-alloying. As the aluminium content in the alloys increased relative to the Pt, it was seen that the structure of the porous platinum derived from these alloys became less and less crystalline. In addition altering the temperature of the substrate during deposition of the alloy had an effect on the alloy. The more the precursor alloy resembled a crystalline structure, the more crystalline the porous Pt structure became.

For the purposes of this project, porous platinum from an alloy of Al₂Pt should be used for sensors, as it is the most crystalline and best understood at this stage. This may not be the optimal structure for catalysis, but it should be the most stable for longer periods. Further optimisation of the catalyst could be carried out at a later time if required.

4.4 Construction of Calorimetric Sensors

Two different calorimetric sensors were constructed for this project. Both types of sensor share the same design, which is based on using two RTDs, one coated with a catalyst to act as an active sensor and one uncoated to act as a control sensor [38, 166, 167]. The difference between types lay in the size and shape of the RTDs, and the type of catalyst used.

4.4.1 Porous Pt-coated RTD Construction

The porous Pt-coated sensor was constructed using a round 16mm PT100 RTD obtained from Labfacility Ltd. The accuracy of these RTDs was class B under the IEC 751 standard, which is $\pm 0.3^{\circ}\text{C}$ at room temperature.

A radiant heater was installed in the magnetron sputtering deposition chamber, along with a rotor and sample holder as seen in Figure 4-7.

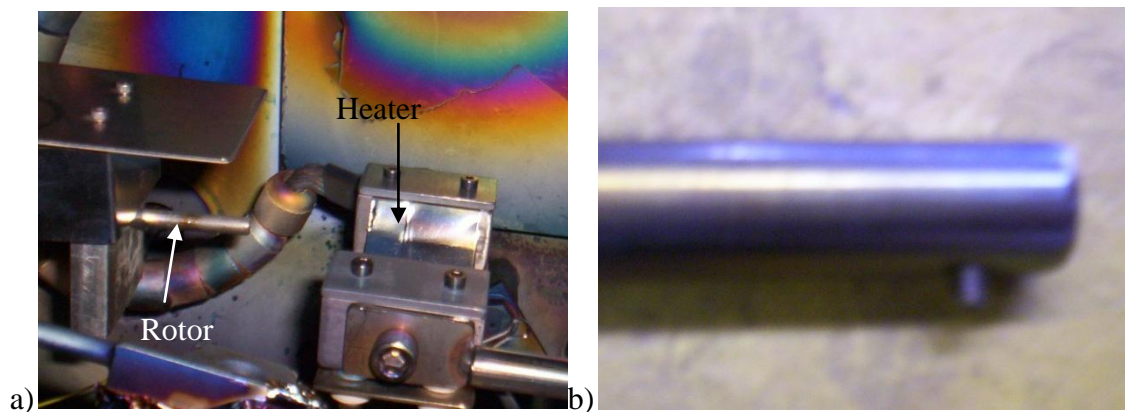


Figure 4-7 A picture of a) the rotor and the radiant heater and b) a close-up of the sample holder

Figure 4-7 b) shows the sample holder, which is simply a circular piece of metal with a hollow core. This hollow core is the same size as the rod on the rotor, seen in Figure 4-7 a), and the holder slides onto the rotor, and is tightened with a screw. The leads of the RTD were put into the hollow core at the other end, and it was again tightened in place by screw. In this way the whole surface of the RTD (but not the wire) was exposed to the targets. The holder was placed on the rotor in such a way that the sample was positioned in the centre of the hot zone produced by the radiant heater.

The conditions of deposition were the same as those previously used to produce Al₂Pt:

- The Pt target was set to 0.05 A, which produced a voltage of 300 V.
- The Al target was set to 0.1 A, which produced a voltage of 275 V.
- The temperature was set to 400°C.
- The deposition was run for 30 minutes.
- The rotor was set to a constant speed of 6 revolutions per minute.

The coated RTD was then immersed in a solution of 0.2 M NaOH, at room temperature, until there were no more bubbles generated by the coating, which took approximately three minutes. The RTD was then rinsed with MilliQ water and dried with in a stream of nitrogen. The RTD leads were soldered to wires, and these wires were run through a stainless steel/aluminium composite housing (which was inert in hydrogen peroxide), for protection during operation in the test rig. Examples are shown in Figure 4-8.

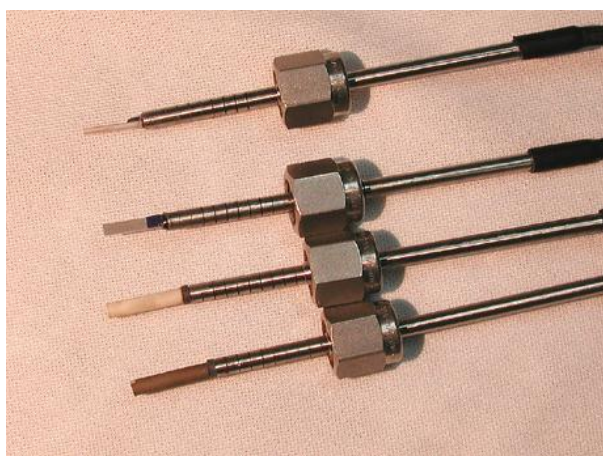


Figure 4-8 RTDs in metal housing

SEM micrographs of the RTD were taken and can be seen in Figure 4-9. It can be seen that there is not much visible difference between the alloyed Al₂Pt coating and the porous Pt coating. It was experimentally observed to be Al₂Pt due to the yellow colour, and the coating was seen to react in the same manner as other de-alloying samples in the alkali bath. Upon being de-alloyed, the sample was capable of causing catalysis of hydrogen peroxide decomposition, something that the Al₂Pt alloy is unable

to do. This seems to suggest that there are pores present on the coated RTD, but they are just too small to observe with an SEM.

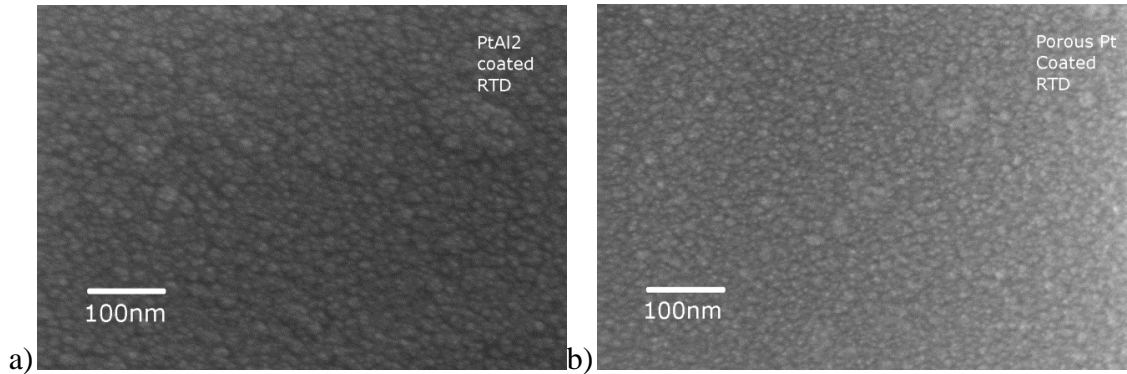


Figure 4-9 SEM micrograph of the Coated RTD that covered in a) Al₂Pt and b) porous-Pt

4.4.2 MnO₂-coated RTD Construction

The MnO₂-coated sensor was constructed on a flat 5 mm PT100 RTD obtained from Labfacility Ltd. The accuracy of these RTDs was class B under the IEC 751 standard.

The coating was made from powdered MnO₂ used in chemically pure form as supplied by May and Baker LTD. A slurry of MnO₂ was prepared by mixing powdered MnO₂ with ethanol. The RTD, which in this case had been mounted in a metal housing prior to coating, was then dip-coated in slurry until the sensor was covered in coating. The sensor was then just left to dry at room temperature suspended in the air. The reason for using ethanol was that it was more volatile than water, which meant the sensor dried faster. The mass of MnO₂ catalyst on the sensor was of the order of 50 mg.

An X-ray diffraction pattern of the MnO₂ powder was taken. Readings were taken on the Siemens D5000 Diffractometer, using CuK α radiation, from 2-theta angles 15° to 80° in increments of 0.02°, at room temperature.

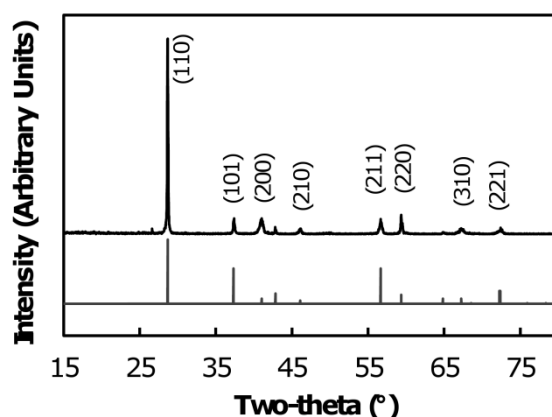


Figure 4-10 The XRD pattern of MnO₂ powder and the lines for the JC-PDF card 00-024-0735 β-MnO₂ (‘pyrolusite’). CuKα radiation was used. Data obtained with assistance of Mr Mark Berkahn, UTS.

As can be seen from Figure 4-10, the powdered MnO₂ used was β-MnO₂ (‘pyrolusite’) which has the rutile crystal structure. However, the broad nature of the (200), (210) and (310) peaks indicates that the material is not completely crystallized.

4.4.3 Uncoated RTD Construction

Uncoated RTDS were constructed by connecting the leads on an RTD to wires, and then mounting the RTD and wires into the stainless steel/aluminium housings mentioned earlier. The uncoated RTDs used were a round 16 mm PT100 RTD and a flat 10 mm PT100 RTD, both obtained from Labfacility Ltd. The accuracy of these RTDs was class B under the IEC 751 standard.

4.4.4 Summary of Sensor Construction

The calorimetric sensor consisted of two RTDs, one “active” RTD which is coated in catalyst and which will react to create a calorimetric response, and a “control” RTD which determines the temperature of the surroundings. The different types of RTDs used for the sensor are summarised below:

Table 4-3 Summary of RTDs used for calorimetric sensors

RTD Size and Shape (PT100)	Catalyst	Accuracy IEC 751 standard	Label
16mm Round	Pt	Class B	A
16mm Round	None	Class B	B
5mm Flat	MnO ₂	Class B	C
10mm Flat	None	Class B	D

4.5 Measurement of Pt-coated, MnO₂-coated and uncoated RTD behaviour in air, liquid water and water mist

It is important to understand the basic thermal properties of the sensor, specifically, how well heat transfers away from the RTD in a specific medium. The convective heat transfer coefficients of the Pt and MnO₂-coated and uncoated RTDs were estimated in air, mist and water. To do this, the temperature of RTDs was measured as a heat pulse was injected into them via electrical heating. This was achieved by connecting each RTD to a Yokogawa power supply YK7651, and multimeter YK7562. The accuracy of the measurement when performing the experiments in this chapter are 0.023%, which equates to 0.07K at room temperature. A LabVIEW program was used to control the parameters of the experiment, and to monitor the temperature of the RTDs. The experiment was set up with three measurement periods, in the first (ambient) period; the RTDs were run with a low applied voltage, and acted as an ambient temperature sensor, in the second (heating) period, a higher voltage was applied to the RTDs, causing them to heat up, and in the third period, the voltage applied to the RTDs was reduced back to the same level as the first period. The pulsed approach was used as it was able to determine transient properties. The time of each period and voltage applied to the RTDs during the ambient and heating periods were controlled through the LabVIEW program. The RTDs were held horizontally in a test rig for the air measurements and vertically in the water, with a measurement period of 240 seconds for air (both still and flowing), 90 seconds in mist and 60 seconds in water, as this was the length of time before the sensor temperature reached a steady state during heating. Heating period powers of 9 mW, 75 mW, 180 mW and 310 mW were tested and the ambient period power used was 0.4 mW. This ambient test power represents a compromise to maintain electronic accuracy (which is better at a high voltage) while reducing the self-heating of the sensor (thermal accuracy, which is better at low voltages). Each power pulse was repeated 5 times.

This data can also be used to estimate the heat transfer coefficient, h (W.m⁻².K⁻¹), of the RTD in air and water, using Equation 4-6:

$$h = \frac{P_{RTD}}{(A \times \Delta T)} \quad \text{Equation 4-6}$$

Where P_{RTD} is the power applied to the RTD in watts, A is the area of the RTD and wire housing exposed to the water in meters squared, and ΔT is the difference in temperature of the RTD in the heated steady state and the first ambient period in °C.

4.5.1 Heat Transfer in Air

The area of the RTDs A and B is about $1.08 \times 10^{-4} \text{ m}^2$, while there is about $1.13 \times 10^{-4} \text{ m}^2$ of wire housing exposed to the fluid. RTDs C and D, on the other hand, had surface areas of $3.64 \times 10^{-5} \text{ m}^2$ and $7.04 \times 10^{-5} \text{ m}^2$, and had an exposed housing of $7.54 \times 10^{-5} \text{ m}^2$ and $1.13 \times 10^{-4} \text{ m}^2$ respectively. These areas were summed to determine the total area from which heat could transfer into the surrounding medium. The value of h for air and water was calculated by focusing on a data point where the temperature was at steady state during the heating period. The point taken was 400 seconds for air as the different heating pulses, and therefore heat transfer coefficient, had reached a steady state by then, as seen in the example calculations in Figure 4-11.

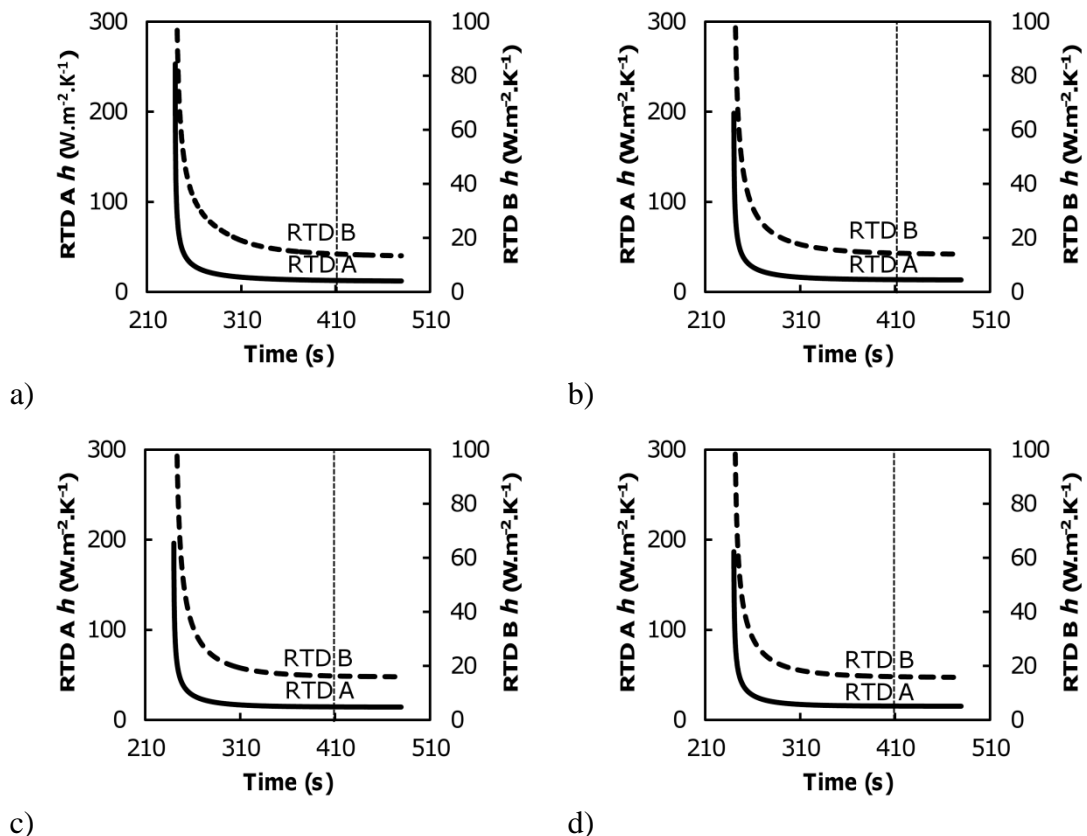


Figure 4-11 An example of the calculation heat transfer coefficient, h , for RTDs A and B in still air. The dotted line represents the point at which the RTD temperature was stable and is the point that h is taken from. Each chart represents a different input power of a) 9 mW b) 75 mW c) 180 mW and d) 310 mW.

By taking the h values of the RTDs at the dotted line, Figure 4-12 can be drawn. The figure represents the average heat transfer coefficient for the RTD against the temperature of the RTD for each applied power (9 mW, 75 mW, 180 mW and 310 mW correspond to RTD temperatures of 29°C, 52°C, 82°C and 120°C).

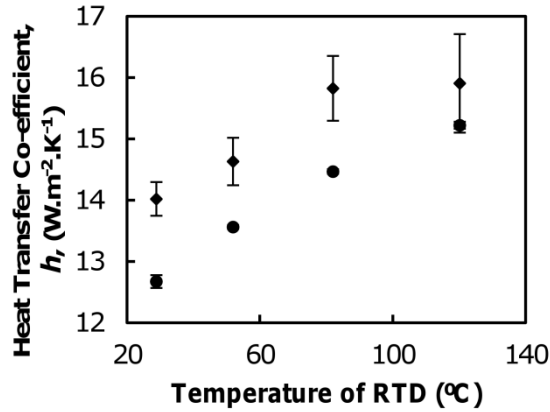


Figure 4-12 The average heat transfer coefficient of RTD A (●) and RTD B (◆) for different temperatures of the RTD in air. Error bars represent 1 standard deviation.

It can be seen that with increasing temperature, the heat transfer coefficient increases, as would be expected due to increasing convection. The h value for RTD A is consistently lower than the h value of RTD B, which would indicate that the RTD is slightly insulated by the porous Pt coating. This trend is clearer in RTD A, than in RTD B where there is much more variability, which could also suggest that RTD A has slightly more insulation, preventing the random fluctuations that appear with the bare sensor. The trend appears to be best described using an expression which will not have any maxima or minima, as the h value is expected to continue to increase with temperature, in this case an empirical exponential function was ascertained using the method described in Chapter 4.1.2 and is described for RTD A in Equation 4-7 and RTD B in Equation 4-8. There is no intrinsic reason for selecting these equations, other than that they fit the data well, and do not have any maxima or minima; they are just used here to interpolate h for different temperatures.

$$h \text{ of RTD A} = 5.56(3.00 - e^{-1.10 \times 10^{-2}x}) \quad \text{Equation 4-7}$$

$$h \text{ of RTD B} = 4.4(3.73 - e^{-2.00 \times 10^{-2}x}) \quad \text{Equation 4-8}$$

The exponential association expression calculated for RTD A shows an $r^2 \approx 1$, and has a 2-sigma confidence interval of $\pm 3.35 \times 10^{-2} \text{ W.m}^{-2}.\text{K}^{-1}$, which is an excellent correlation, whereas the exponential association expression for RTD B shows an $r^2 = 0.95$, with a 2-sigma confidence interval of $\pm 0.74 \text{ W.m}^{-2}.\text{K}^{-1}$.

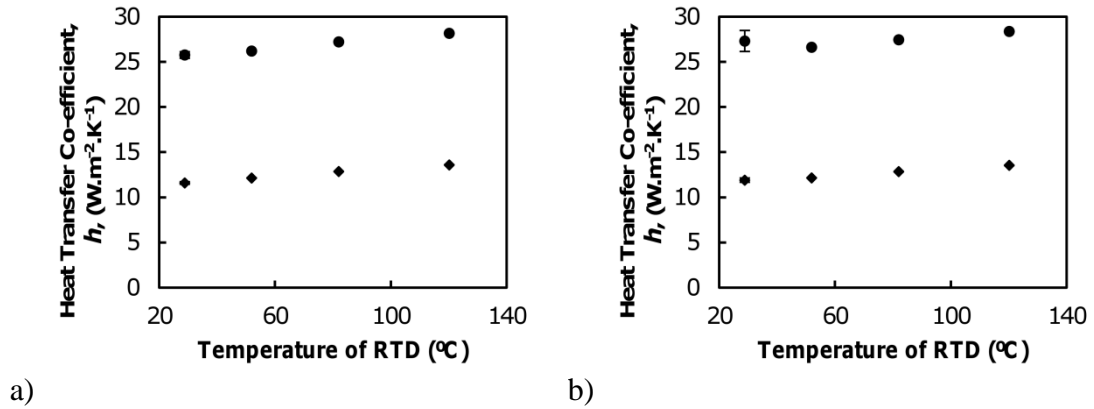


Figure 4-13 The average heat transfer coefficient of RTD C (●) and RTD D (◆) for different temperatures of the RTD in a) still air and b) in flowing air. Error bars represent one standard deviation.

Figure 4-13 a) shows the average h values for RTD C and D in still air, at various temperatures. Both RTDs appear to have strong trends with much lower uncertainty. In this case a linear trend was fitted to these data points as empirical observation showed that a linear set would fit better, which was confirmed when comparing a linear trend to an associated exponential expression for this data. This difference in housing dimensions put the RTDs in different positions from the edge of the of the test rig, which is the likely cause of the difference in h , as it was observed that the RTDs were affected by flowing air at the edges of the test rig more than at the centre. Figure 4-13 a) shows the average h values of RTDs C and D in 7.5 L/min flowing air. The obvious conclusion from this figure is that the 7.5 L/min airflow has no significant effect on the heat transfer of these RTDs. The main difference between this and Figure 4-13 b) is that there is slightly more error in the 29°C temperature measurement. This negatively affects a linear trend, however, all empirical data still points to a linear trend being the trend of the data.

The h value for RTD D is similar to the values of h for RTDs A and B. This is likely due to the similar size of the RTDs. On the other hand, RTD C has a h value of approximately double the value of the other RTDs, which appears appropriate given the RTD is about half the size, and thus thermal mass, of the other RTDs. It is also possible

that since the difference in housing dimensions put the RTDs in different positions from the edge of the of the test rig, it is another possible and this is cause of the difference in h , as it was observed that the RTDs were affected by flowing air at the edges of the test rig more than at the centre.

While the porous Pt coating appeared to have a genuine affect in decreasing the h value, the MnO_2 coating effect is harder to ascertain. The coatings themselves are different, the Pt is a thin film and likely suffers discontinuity in conduction, likely exacerbated by the porous nature of the film, while MnO_2 is simply a powder. If it does reduce heat transfer it is more likely due to increasing the thermal mass of the sensor.

4.5.2 Heat Transfer in Other Fluids

The heat transfer coefficients were also calculated for still water for RTD A and B and water mist for RTD C and D. Most work in this project was done with RTD C and D in mist, so RTD A and B were not tested in the mist as it was not priority. In addition, RTD C and D were not tested in water as the coating was not robust enough to be used as a sensor in liquid (the MnO_2 dispersed in the liquid leaving a nearly bare RTD). The graphs used to calculate these values and the equations which were fitted to them are shown in the Appendix of this thesis.

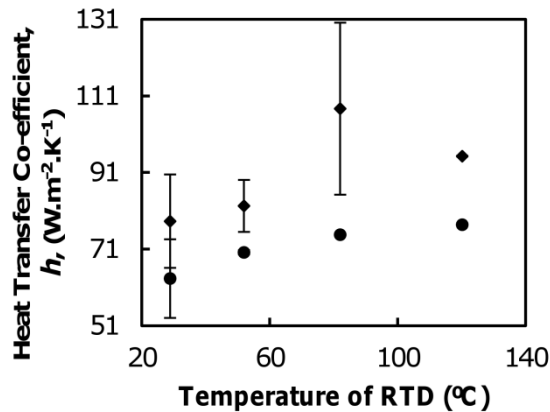


Figure 4-14 The average heat transfer coefficient of RTD A (●) and RTD B (◆) for different temperatures of the RTD in water. Error bars represent 1 standard deviation.

Figure 4-14 shows the average h values of RTDs A and B in water, along with the uncertainties measured. Although the values of h are much higher than for air (as expected), the nature of the trend appears to be similar to that of the RTDs in air, i.e. suitable for fitting with an exponential, however, there is a very high uncertainty in the

h value at 82°C for RTD B. The higher temperatures produced boiling on the surface of the sensor. It appears that the coated sensor has more consistent transfer, however, for boiling temperatures, both RTDs show a fairly consistent transfer. It could be that the bubbling associated with the boiling water stirred the surrounding water producing more consistent transfer. This is positive, since this environment is similar to what the RTDs will encounter in hydrogen peroxide.

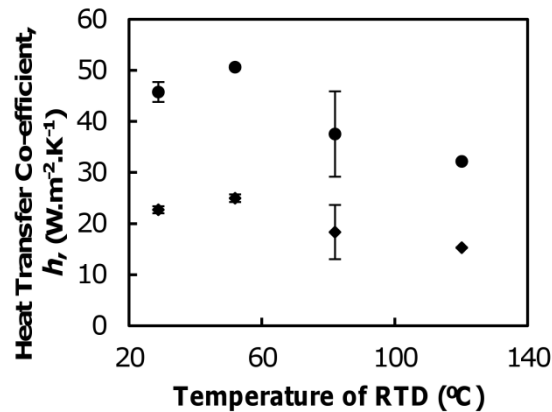


Figure 4-15 The average heat transfer coefficient of RTD C (●) and RTD D (◆) for different temperatures of the RTD in 20% duty cycle water mist with an air flow of 7.5L/min. Error bars represent one standard deviation.

Figure 4-15 shows the average h values for a 20% duty cycle mist and air flow of 7.5 L/min using RTDs C and D. Finding a trend in this data is very difficult due to uncertainty and a decrease in h with increasing temperature, unlike the previous measurements. The comparatively low temperature measurements show an increase in h , however at the high temperatures h values decrease. It is theorised that this is due to an increase in vaporisation at higher temperatures. This means that there is less liquid on the RTDs surface, which reduces evaporative cooling and thus decreases heat conduction from the RTDs. This explains the larger uncertainty at 82°C as the temperature is not enough to quickly vaporise the liquid on the surface and therefore there is a randomness as to how wet the RTD is and subsequently how much cooling is present. An example of this can be seen in Figure 4-16, as there is a decrease in RTD C and also in RTD D. This dip is believed to be due to the RTD being cleared of liquid, and subsequently, lower h . Comparing this with an RTD of higher temperature (120°C, which can be found in the Appendix as Figure A-4 d)), its clear that the deviation at the start of the curve is due to vaporisation, which produces a much more constant h value.

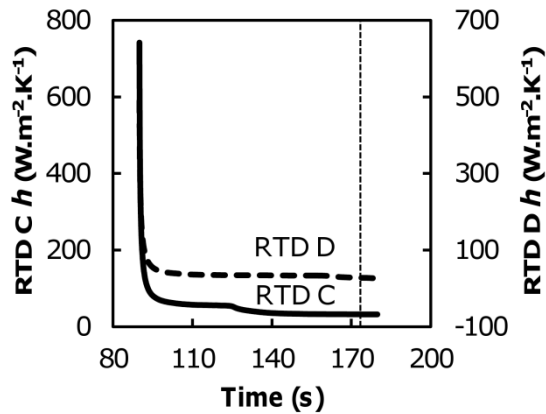


Figure 4-16 Example of mist experiment at 82°C showing drop of h during period that is typically stable

In conclusion, the results show that an RTD in air, no matter which RTD, produces the lowest h values, and is thus best able to determine a temperature, as most of the heat energy transferred to the RTD rather than the surrounding medium, as in water. The size of the RTD appears to be the biggest factor in h value, with the smallest RTD having the highest h value, which is expected with the lowest thermal mass to contain heat. It is possible that this RTD would be the best to use in air as the lower thermal mass will allow the RTD to heat up faster. It was also observed that the 7.5 L/min flow rate does not significantly increase the h values of the RTDs. In liquids and air-liquid environments, all RTDs show an increase in h values, which is expected as water is a better conductor of heat than air. Whether this is problematic for the sensor is discussed further along in this document in the appropriate chapter. The nature of heat transfer in mist is also complicated as temperature changes. The mist will either condense on the RTD or vaporise based on the temperature of the RTD. The mist transfer is dependent on this making it much more complex than the other fluid phases. Individual results for h values can be seen in the appendix of this document (Table A-1 through to Table A-7).

Table 4-4 A summary of the heat transfer coefficients of RTDs A, B, C and D at a temperature of 29°C. The uncertainty given is one standard deviation.

Fluid	RTD A (W.m ⁻² .K ⁻¹)	RTD B (W.m ⁻² .K ⁻¹)	RTD C (W.m ⁻² .K ⁻¹)	RTD D (W.m ⁻² .K ⁻¹)
Unforced Air	12.7±0.1	14.0±0.3	25.8±0.4	11.6±0.3
Forced Air			27.3±1.2	11.9±0.2
Water	63±10	78±12		
Mist			45.8±2.0	22.7±0.7

Chapter 5 Response of the Calorimetric Sensor in Bulk Liquids and Non-mist Droplets

The sensors were tested in a variety of ways to determine their effectiveness: by immersion in aqueous solutions of hydrogen peroxide, by deposition of hydrogen peroxide droplets onto their tips, and by exposure to H₂O₂/H₂O mist flux. This chapter examines the effectiveness of the sensor at determining hydrogen peroxide concentration in liquid, and confirms the hypothesis that calorimetric sensors follow a linear relationship between hydrogen peroxide concentration and decomposition activity, which is measured in terms of temperature. This is covered in Chapter 5.1. Results from this section have been published in *Sensors Letters*[168] and were presented at the 13th *International Chemical Sensors Conference in Perth, Australia 2010*. From this base of understanding, we aim to test whether this relationship remains in more complex systems, such as having smaller quantities of hydrogen peroxide, exposing the reaction to vaporisation, and forced convection. Finally, I wish to determine how a heated RTD affects this system and whether this can also be exploited further in a sensor design.

5.1 Sensor Behaviour during Immersion in Aqueous Hydrogen Peroxide

All immersion testing was done using RTDs A and B as described in Table 4-3 as the coated and uncoated sensor respectively. The aim of this part of the part experiment was to determine whether there was a linear relationship between temperature change in an RTD and the concentration of hydrogen peroxide, and whether this relationship showed a big enough signal to be detected when the RTD was immersed in a liquid.

5.1.1 Method

Before the sensor was tested in aqueous solution, a basic calculation was performed to estimate how large a calorimetric signal could be expected from it when it is immersed in the aqueous solution. This calculation required some estimated values, such as the heat generated by hydrogen peroxide decomposition and the heat transfer coefficient of the RTDs immersed in liquid. To obtain an estimate of the heat generated by hydrogen peroxide decomposition, the mass loss was measured when RTD A was

immersed in 10%, 20% and 35% (w/w) hydrogen peroxide solutions. These concentrations were used to gain an overview of how much hydrogen peroxide reaction increases with concentration. During measurements, more points were used to confirm any relationship. A single beaker of hydrogen peroxide and the immersed RTD A was put on a scale and tared, so mass loss was recorded from 0 g. The mass was recorded approximately every 30 seconds for around 700 seconds. From this data, it was possible to determine the rate of mass lost, and from there, estimate the rate of decomposition of hydrogen peroxide on the Pt-coated RTD. The majority of mass loss occurred due to decomposition (rather than evaporation): as it is expected that oxygen bubbles escape as hydrogen peroxide decomposes via the reaction shown in Equation 5-1:



For every mole of hydrogen peroxide decomposed, $\frac{1}{2}$ a mole of oxygen is produced. It was therefore possible to calculate the rate of decomposition of hydrogen peroxide in moles per second by Equation 5-2:

$$\text{mol}_{\text{H}_2\text{O}_2} = \frac{m_{\text{O}_2} \times 2}{m.\text{mol}_{\text{O}_2}}, \quad \text{Equation 5-2}$$

where m_{O_2} is the mass of oxygen lost in grams per second, $m.\text{mol}_{\text{O}_2}$ is the molar mass of oxygen in grams per mole (32 g/mol) and $\text{mol}_{\text{H}_2\text{O}_2}$ is the number of moles of hydrogen peroxide lost per second.

It is possible to determine the power expected from this decomposition using Equation 5-3:

$$P_{\text{Decomp}} = \text{mol}_{\text{H}_2\text{O}_2} \times \Delta H_{\text{H}_2\text{O}_2}, \quad \text{Equation 5-3}$$

where $\Delta H_{\text{H}_2\text{O}_2}$ is the enthalpy of the decomposition of hydrogen peroxide, which is 98.2 kJ/mol, and P_{Decomp} is the power released by decomposition in watts.

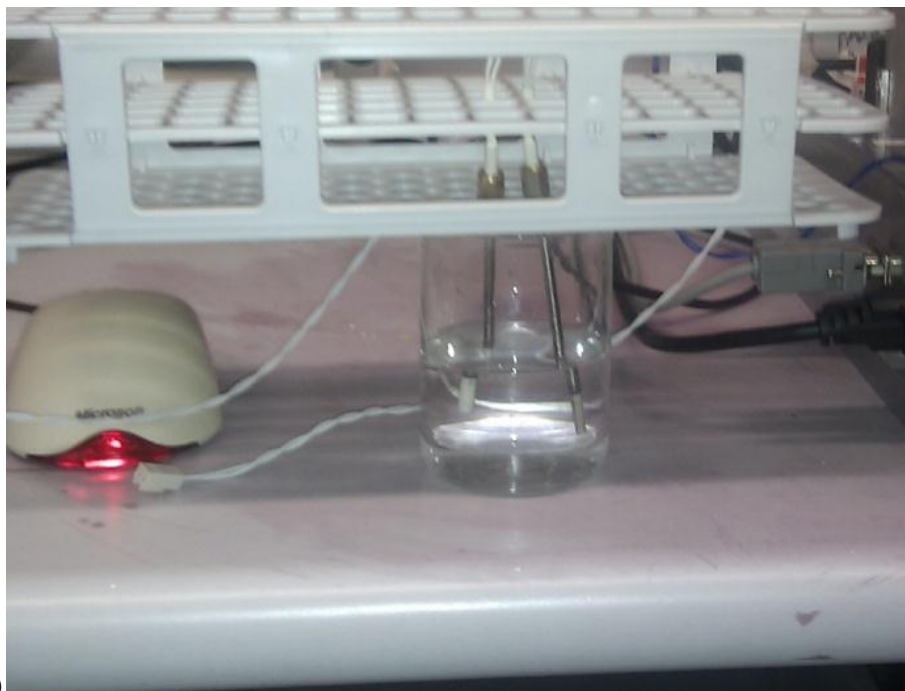
It is then possible to estimate whether the sensor can produce a signal based on temperature difference by using the power determined by Equation 5-3, and rearranging Equation 4-6 to make ΔT the subject:

$$\Delta T = \frac{P_{Decomp}}{A \times h}. \quad \text{Equation 5-4}$$

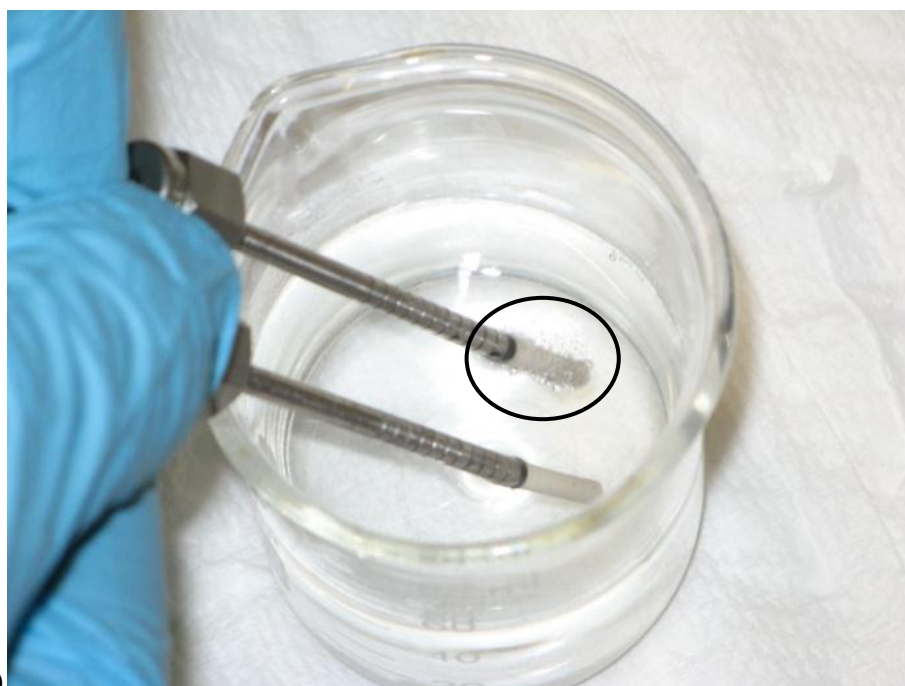
The assumption is made here that all the heat generated is transferred from the boundary layer to the sensor. This provides an upper limit of ΔT . These calculations were carried out for 10, 25, 35, 42 and 50% hydrogen peroxide (w/w), using the measured mass-loss-rate per weight percentage of hydrogen peroxide. These results were then used to determine whether a signal was possible from a calorimetric sensor in aqueous solution.

The actual temperature rise due to decomposition was then measured by using a bare RTD and a coated RTD both immersed in liquid. The bare sensor provided a background reference of the aqueous solution's temperature, while the coated sensor reacted with the aqueous solution causing the RTD to heat up. The sensor signal could then be derived by determining the difference between the coated and uncoated RTD temperatures.

The testing was conducted in MilliQ water (18.2 M Ω), 10, 25, 35, 42 and 50% hydrogen peroxide (w/w). The concentration of the solutions was confirmed using iodometric titration, which is described in Chapter 4.2. To ensure repeatability, the RTDs were suspended in the solution using a test tube rack to keep the sensors consistently separated and at the same height in the liquid, which is demonstrated in Figure 5-1.



a)



b)

Figure 5-1 a) Picture of the sensor set-up showing the test tube rack holding the sensors in place; b) Picture showing the sensors in hydrogen peroxide. Bubbles are visible on the Pt coated RTD (top, circled), while there is no reaction on the uncoated (bottom).

The RTDs were connected to Yokogawa YK 7562 data acquisition hardware controlled by a LabVIEW program on a computer. Under room temperature conditions, these instruments typically have a 0.014% accuracy, which equates to ± 0.04 K. A constant 1 mA current, which ensures minimal self-heating in the sensors, was supplied

to the RTDs and the system recorded the change in resistance of the sensor. The LabVIEW program was able to convert the recorded resistance to the temperature using Equation 5-5:

$$T = \frac{r-100}{0.385}, \quad \text{Equation 5-5}$$

where r is the resistance of the RTD in ohms, and T is the temperature in degrees Celsius.

The sensor was first pre-conditioned by immersing both bare and coated RTDs in MilliQ water. This was to ensure that the sensor was not contaminated between measurements and to start both RTDs from a similar temperature. The hydrogen peroxide and MilliQ water used were set out on the laboratory bench overnight to achieve the ambient temperature. Hydrogen peroxide concentration measurement was then made by immersing the pair of RTDs in the hydrogen peroxide analyte for 60 seconds, which was then followed with withdrawal into air. While the sensor was in air, the measurement cycle continued for 60 to 240 seconds to allow equilibration (the length of time was largely dependent on the concentration of hydrogen peroxide, and the subsequent length of time the reaction occurred for in the air), before the sensor was re-immersed in MilliQ for 20 seconds. At this point the measurement cycle was ended. This produced two separate sources of data as to how the sensor reacted: the first in the solution and the second in open atmosphere.

Each experiment was run multiple (5 or more) times to determine the variability of the results.

5.1.2 Results and Discussion

The mass loss of oxygen was different for each concentration of hydrogen peroxide, which confirms that the concentration affects the rate of reaction, and that up until 35% hydrogen peroxide, the catalyst was not saturated by hydrogen peroxide. The resulting mass losses are shown in Figure 5-2.

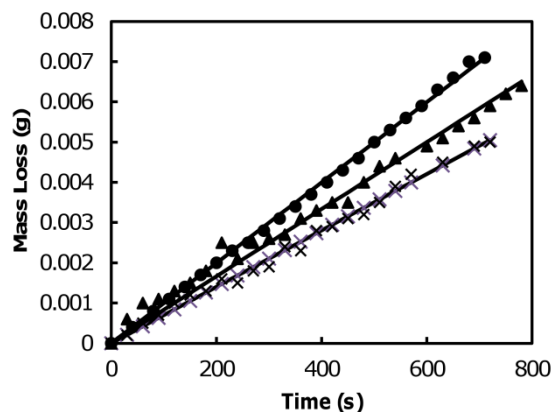


Figure 5-2 The mass of hydrogen peroxide loss due to decomposition using Pt-coated catalyst over time for 10% (x), 20% (▲) and 35% (●) hydrogen peroxide.

Evaporation was estimated by placing an RTD in water and measuring the mass loss over a period of 1650 seconds. In this time, 0.0065 g of mass was lost, indicating a mass loss of 3.87×10^{-6} g/s, compared to a mass loss rate of 7.01×10^{-6} and greater for peroxide. Dissolution of oxygen back into the solution was considered, but ultimately disregarded as the solutions were near or at the saturation solubility, and the release of heat from the reaction will only reduce the solubility of oxygen (countered by an increase in water concentration so that the naturally dissolved oxygen is also not likely a source of error). A more likely cause of uncertainty was vaporised water, however, it is unlikely to be high due to the low reaction rate and relatively large quantity of hydrogen peroxide.

Figure 5-2 also shows linear regressions obtained using the methods outlined in Chapter 4.1.1. All these regressions were constrained to pass through zero. The regressions statistics and the estimated mass loss rate for each concentration of hydrogen peroxide are described in Table 5-1.

Table 5-1 The regression statistics of the mass loss curves and the subsequently calculated mass loss rates

Hydrogen Peroxide Concentration (%(w/w))	Coefficient of Determination (r^2)	2-Sigma Confidence Interval (g)	Mass Loss Rate from Curve (g/s)	Mass Loss Rate Corrected Against Estimated Evaporation (g/s)
10	0.998	$\pm 2.44 \times 10^{-4}$	7.01×10^{-6}	3.14×10^{-6}
20	0.996	$\pm 5.03 \times 10^{-4}$	8.34×10^{-6}	4.47×10^{-6}
35	0.9997	$\pm 1.56 \times 10^{-4}$	9.99×10^{-6}	6.12×10^{-6}

By using Equation 5-2, it was possible to estimate the moles of hydrogen peroxide that were reacted. From this, Equation 5-3 was used to estimate the power that was generated by the hydrogen peroxide decomposition, the results of which can be seen in Figure 5-3.

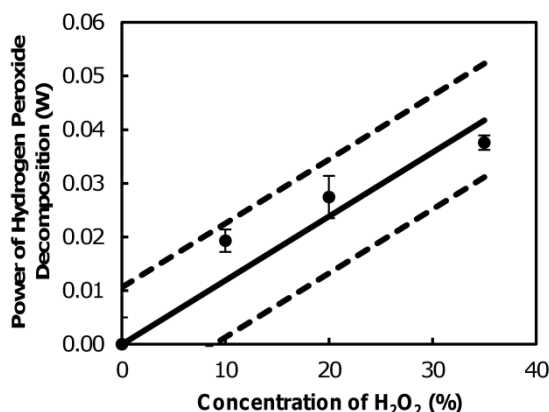


Figure 5-3 The power of hydrogen peroxide decomposition from a Pt coated RTD vs the concentration of hydrogen peroxide with regression line. Dotted lines are upper and lower limits of 2-sigma confidence interval. Note that the regression is constrained to pass through (0,0).

Figure 5-3 has a coefficient of determination of 0.97 and a gradient of 1.2×10^{-3} W/((w/w)%). This gradient will be used to estimate the power of hydrogen peroxide decomposition for a given concentration. The 2-sigma confidence interval of the gradient was $\pm 2.6 \times 10^{-4}$ W/((w/w)%). While the data is fairly described with that relationship, it appears to have some non-linearity. Without further data it cannot be said unequivocally, but it is likely that this non-linearity is only due to forcing the trend through 0, when the data is just peroxide it has a strong linear relationship. What is

likely is a changing rate of decomposition between 0 and 10% hydrogen peroxide before it reaches linear decomposition. The reason for this calculation in this study is to determine whether hydrogen peroxide could produce a linear signal in bulk liquid so assuming a linear trend at this point between 0 and 10% hydrogen peroxide is seen as justified especially as the range of real interest is 25 to 35%, and the only issue with this is that the response calculated with this data will be slightly overstated. In Chapter 6, the 0-10% hydrogen peroxide section will be examined more closely.

Knowing the power released by the decomposition of hydrogen peroxide and the estimated heat transfer coefficient ($46.9 \pm 0.04 \text{ W}\cdot\text{m}^{-2}\cdot\text{K}^{-1}$ from Equation A-1 with temperature 22.5°C), it is possible to determine the maximum expected temperature difference due to decomposition for hydrogen peroxide using Equation 5-4. This can be used to estimate a relationship between hydrogen peroxide concentration and the maximum potential difference in temperature due to the heat of hydrogen peroxide decomposition, as seen in Figure 5-4.

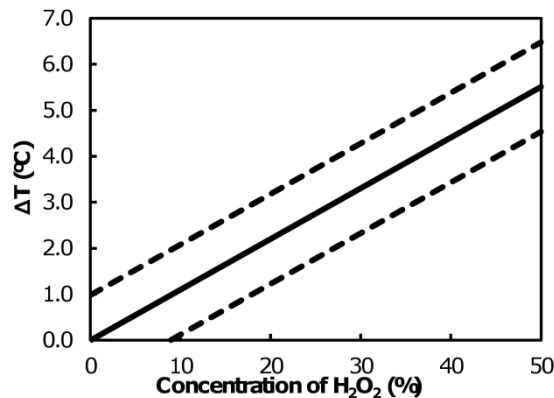


Figure 5-4 The calculated maximum change in temperature of the coated sensor based on the empirically calculated h for water and the calculated heat of decomposition of hydrogen peroxide assuming all heat generated in the boundary layer goes into the sensor. The dotted lines represent the calculation of temperature change using a sigma confidence interval for h .

The graph shows that if the heat-transfer coefficient of hydrogen peroxide is close to that of still water, it is likely that there will be a significant change in temperature relative to the concentration of hydrogen peroxide. While it is reasonable to assume that the coefficient would be similar, it should be noted that hydrogen peroxide conceivably has a higher heat transfer coefficient as the reaction produces effervescence, which could facilitate an increase in heat transfer away from the sensor.

Figure 5-5 shows the results of the first run from each experiment:

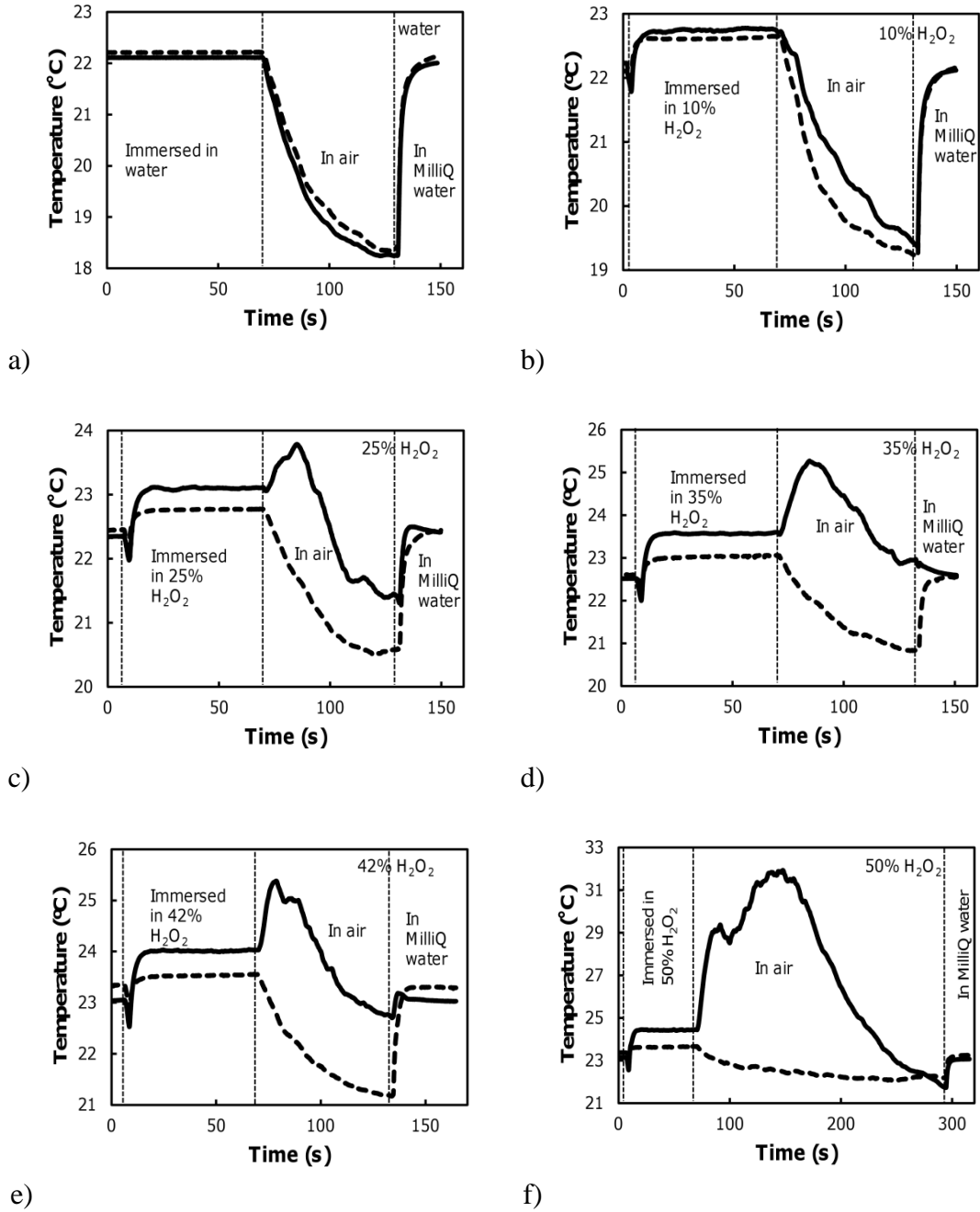


Figure 5-5 Recorded temperature of the coated (solid line) and uncoated (dotted line) RTDs plotted against time for, a) MilliQ water, b) 10% hydrogen peroxide, c) 25% hydrogen peroxide, d) 35% hydrogen peroxide, e) 42% hydrogen peroxide and f) 50% hydrogen peroxide.

All figures show a similar shape. The first 1 or 2 seconds show a period where both RTDs are settled in MilliQ water before there is a drop and subsequent increase in the temperature of the RTDs. This is due to the RTDs being removed from MilliQ water and being placed in the aqueous hydrogen peroxide solution. This effect is not seen in Figure 5-5a), as the RTDs were kept constantly in the same MilliQ water. The figures

then show a steady temperature for both RTDs for the next 60 seconds while they are both stably immersed in the hydrogen peroxide solution. There is a noticeable temperature difference between uncoated and coated sensors above 10% concentration. After this, the sensors are removed from peroxide solution into air, and the coated RTDs show a sharp increase in temperature for 25%, 35%, 42% and 50% hydrogen peroxide solutions; in contrast the coated RTDs in the MilliQ water and 10% hydrogen peroxide, as well as the uncoated RTDs, show a decrease. It should be noted that, despite being withdrawn, the sensors retain a film of solution on the surface. The uncoated RTDs do not exothermically react with the MilliQ water or hydrogen peroxide so the RTD records cooling due to evaporation. This is true for the MilliQ water on the coated RTD too, confirming that the main difference between the sensor signals is the response to hydrogen peroxide. The 10% hydrogen peroxide shows a similar decrease in temperature, however, the coated temperature is recorded as higher than the uncoated RTD, indicating that the hydrogen peroxide is reacting, however the reaction is not able to increase the temperature above ambient due to the dominance of evaporation. From these results, two different methods were used to determine hydrogen peroxide concentration. One focused on the direct difference between the coated and uncoated RTD while it was immersed in solution and the other focused on the peak temperature the coated RTD reached in air.

5.1.3 Concentration determination during the immersion period

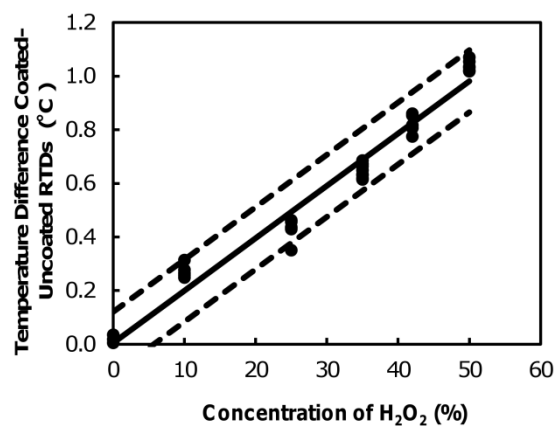


Figure 5-6 The difference in temperature between the Pt-coated and uncoated RTDs. The line represents the linear regression, while the dotted lines represent the upper and lower values of the 2-sigma confidence interval.

Figure 5-6 shows the temperature difference between the Pt-coated and uncoated RTDs while immersed. The difference is significant and shows a linear relationship between the concentration of hydrogen peroxide and the difference recorded by the RTDs when immersed. The ΔT produced are about 20% of that shown in Figure 5-4, indicating that only one fifth of the heat generated is actually transferred to the sensor body itself, while the balance is convected to the solution. The RTD detects $(1.1 \pm 0.1) \times 10^{-2}$ W of the 0.0596 ± 0.01 W of energy (decomposition per mass percentage (%w/w)) possible, suggesting that four fifths of the energy produced by the reaction is not crossing the boundary between the catalyst and the RTD or is being removed by a hitherto unconsidered process. One possible process that may take up extra energy is bubble formation. This can affect the RTD by insulating it when bubbles get stuck on the surface, or by increasing heat transfer through the removal of energy when the bubble bursts. The linear regression was obtained using the method outlined in Chapter 4.1.1. The slope of the line was determined as being 0.02, suggesting that a rise of 0.02°C indicates an increase of 1% (w/w) increase in hydrogen peroxide concentration. The coefficient of determination was 0.97.

By taking a linear regression where the temperature is the independent variable (T) and concentration is the dependent variable ($conc$), the Equation 5-6 can be used to describe an approximation of the relationship between temperature recorded and the concentration of the hydrogen peroxide concentration.

$$conc = 49.77T + 0.55 \qquad \text{Equation 5-6}$$

Equation 5-6 produces the curve shown in Figure 5-7.

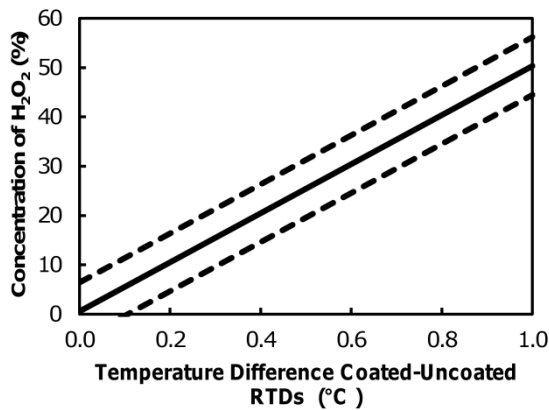


Figure 5-7 The expected concentration from measured temperature difference in temperature between Pt-coated and uncoated RTDs during immersion vs the concentration of hydrogen peroxide (%(w/w)). The dotted lines indicated a 2-sigma confidence interval.

Figure 5-7 shows the estimated prediction of the sensor based on the temperature measured. The sensor is accurate and repeatable over the range 0-50%, however from a practical position, a limit of detection (lowest hydrogen peroxide concentration) has not been established. This sensor is capable of detecting 35% hydrogen peroxide, however in terms of precision, the 2-sigma confidence interval was $\pm 5.8\%$ hydrogen peroxide (w/w). This indicates that a reading of 35% can be between 29% and 41%. This may be acceptable depending on what level of precision is needed in the sterilizing system.

5.1.4 Concentration determination during the post immersion period

The behaviour of hydrogen peroxide on the sensor in the air is more complex and constantly changing due to the heats of vaporisation of water and hydrogen peroxide and the heat of decomposition of hydrogen peroxide. Figure 5-8 shows the energy of water and hydrogen peroxide vaporisation, as well as the decomposition energy of hydrogen peroxide for each concentration of hydrogen peroxide.

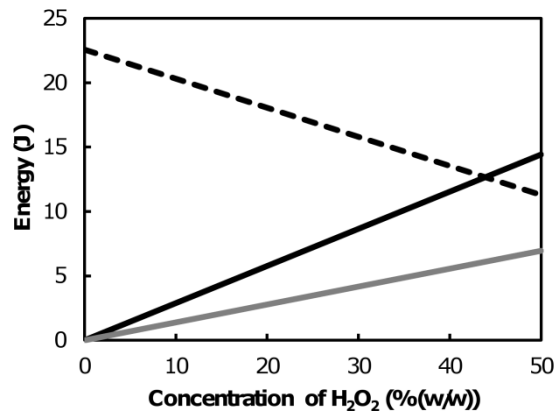


Figure 5-8 The heat energy of decomposition of hydrogen peroxide (solid black line) and vaporisation of water (dotted black line) and hydrogen peroxide (solid grey line) for each concentration of hydrogen peroxide from 0% to 50% (w/w). These values were determined from hydrogen peroxide’s molar heat of decomposition (shown in Equation 1-1) and the boiling point heat of vaporisation for hydrogen peroxide and water from Table 1-1.

From this a basic qualitative model can be inferred. Firstly, it is assumed that the amount of fluid on the surface is the same, or near enough as to not be a significant difference, especially since an increase in temperature will increase hydrogen peroxide decomposition. Figure 5-8, shows that as the percentage of hydrogen peroxide increases, the energy of decomposition of hydrogen peroxide and the energy of vaporisation increases. In addition, the energy of vaporisation of water decreases. As the amount of hydrogen peroxide increases, the longer the decomposition reaction can go for and thus the more energy can be produced. At some point in time the reaction then slows as there is less hydrogen peroxide reacting, and more water on the surface, which causes heat energy to be transferred from the surface via vaporisation. This can be seen as the “peaks” in Figure 5-5 when the RTD is “in air”. It can also be seen that the peaks for 42% hydrogen peroxide and 50% hydrogen peroxide are different from the ones that come before it. Figure 5-8 shows that relatively speaking, from approximately 42-43% hydrogen peroxide upwards more energy is produced from decomposition than from vaporisation of the water. In this case the hydrogen peroxide is able to react so fast that it boils the water from the surface. This can be seen in the 42% data as the plateau after the peak. This means that the peak is not as high as previous peaks and the temperature it reaches is not as high. However, this result was repeatable, where that of the 50% peak is not. This is because at 50% there is more decomposition energy than vaporisation energy from water, which results in vigorous boiling of the water and increasing the relative concentration of hydrogen peroxide and a longer lasting reaction

since there is less vaporisation to oppose it. This is represented graphically in Figure 5-9. As can be seen, an increase in hydrogen peroxide concentration means that there is less heat lost through vaporisation of water and more mass lost due to decomposition and vaporisation. Overall, more heat crosses the boundary into the sensor.

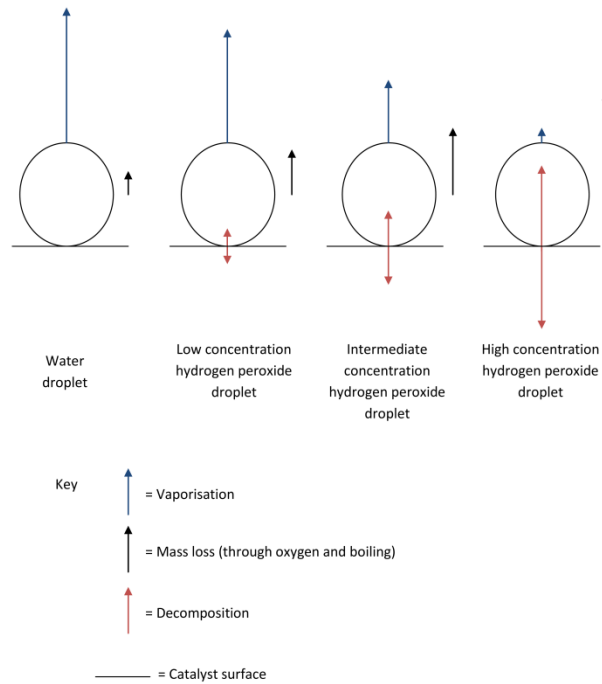


Figure 5-9 Graphical representation of heat flows of catalyst surface and hydrogen peroxide droplets. This graph is not to any scale, just a qualitative representation of the magnitude of heat flows during decomposition. The size of the arrow describes the magnitude of the heat flow.

Given this it seems reasonable that the temperature the peak reaches and the time that the peak reaches it should relate to concentration.

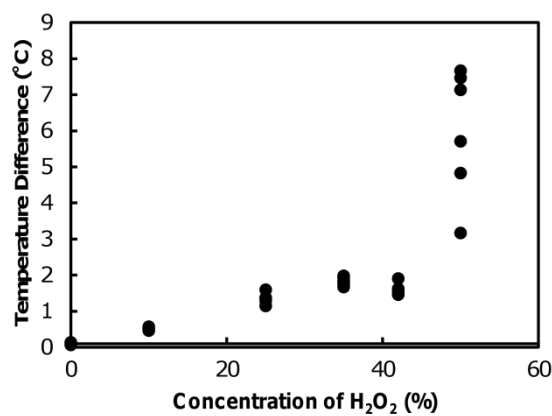


Figure 5-10 The difference between temperature of the Pt-coated RTD at its “peak” post-immersion and the Pt-coated sensor during immersion.

Figure 5-10 shows the difference between the “peak” temperature of the Pt-coated RTD after withdrawal from the solution and the corresponding stable temperature while the sensor was immersed. This figure shows that there is a larger difference between temperatures when the sensor is removed from the aqueous solution.

Another analysis of the raw data showed the relationship between the time that the temperature was at this “peak” value and the concentration of hydrogen peroxide. The results, shown in Figure 5-11, show a similar pattern to Figure 5-10, however it appears to be less reliable than the peak temperature.

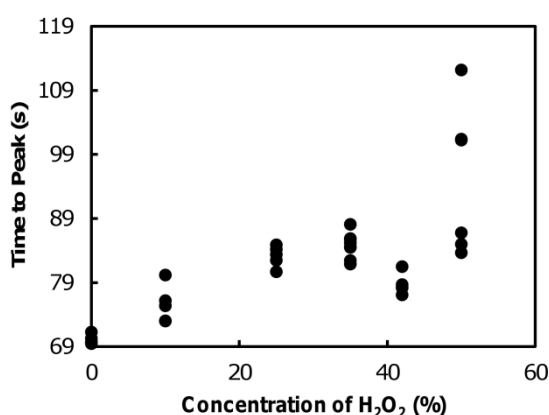


Figure 5-11 The time the taken for the reaction to reach a maximum temperature for each concentration of hydrogen peroxide (time started from 0)

As expected from the experiments and Figure 5-8, both these sets of data suggest that the 50% hydrogen peroxide measurement is unreliable due to a large uncertainty. As the model states above, when hydrogen peroxide is at a concentration of 50% is decomposing, it is capable of boiling water in the mixture, which results in a relative increase in hydrogen peroxide concentration. Under these conditions, where there is very little hydrogen peroxide and water on the sensor, it would be very easy for the peroxide to up-concentrate and thus produce variable readings. Since it is not confirmed what actual concentration the droplet is in this case, the data will not be used in further analysis.

The data from 0% to 42% appears to have a polynomial correlation. The non-linear regression method described in Chapter 4.1.2 was used to fit a curve to the 0-42% data peak temperature and time to peak temperature data. This regression used the independent variable (*conc*) concentration of hydrogen peroxide and the dependent

variable (T) was the peak temperature or the time to peak temperature. This produced Equation 5-7 for the relationship between peak temperature and hydrogen peroxide concentration and Equation 5-8 for the relationship between the time to peak temperature and hydrogen peroxide concentration.

$$T = -7.64 \times 10^{-4} \text{conc}^2 + 0.0742 \text{conc} - 0.088 \quad \text{Equation 5-7}$$

$$t = -0.0176 \text{conc}^2 + 1.015 \text{conc} + 69.05 \quad \text{Equation 5-8}$$

The regression that Equation 5-7 is based on has a coefficient of determination of 0.93 and a 2-sigma confidence interval of $\pm 0.36^\circ\text{C}$ or $\pm 5.3\%$ hydrogen peroxide. This relationship has been represented on Figure 5-12, with confidence interval. This is best case as the confidence intervals increase at higher concentrations.

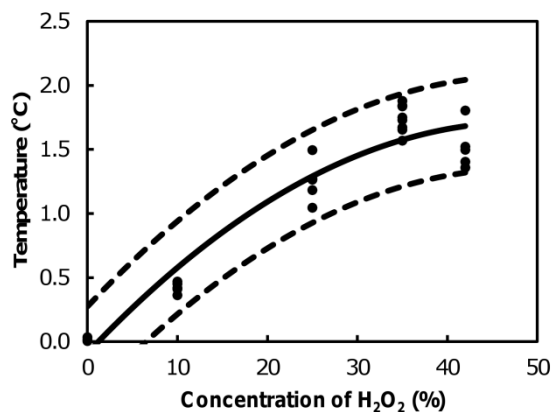


Figure 5-12 The regression line of the peak temperature vs the concentration of hydrogen peroxide, with 2-sigma confidence interval shown as the dotted line. Raw data points (\bullet) are also shown.

Similarly, the regression that Equation 5-8 is based on has a coefficient of determination of 0.83 and a 2-sigma confidence interval of ± 5 s or $\pm 6\%$ hydrogen peroxide, again in the best case. This relationship has been represented on Figure 5-13, with confidence interval. The relationship shows a maximum value between 25% and 35% hydrogen peroxide, which means that as a useable sensor alone, it would have a much smaller range than the temperature sensors.

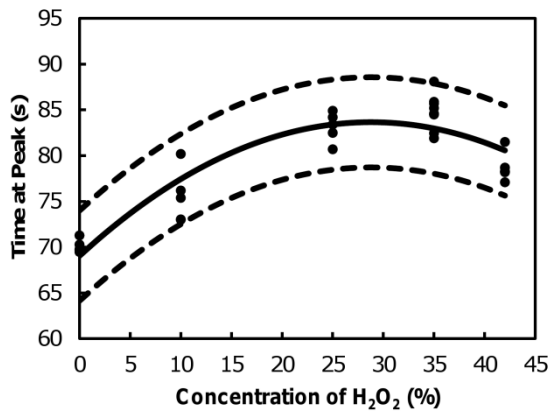


Figure 5-13 The regression line of the time to peak temperature vs the concentration of hydrogen peroxide, with 2-sigma confidence interval shown as a dotted line. Raw data points (•) are also shown.

Comparing Figure 5-12 with Figure 5-13, it can be seen that both graphs have a different shape. Figure 5-12 is the better fit to the data however, Figure 5-13 is still reasonable. However, it may be possible to gain a more accurate and precise regression by combining both the peak temperature and time to peak temperature data sets and performing a two variable quadratic regression. This was performed using the method for multiple linear regression, which is described in Chapter 4.1.3. By running the program with concentration as the dependent variable (*conc*), the relationship described by Equation 5-9 was determined.

$$\begin{aligned}
 conc = & 307.1 + 376.9T + 620.9T^2 - 8.700t + 0.062t^2 - 8.668Tt \\
 & - 13.83T^2t + 0.051Tt^2 + 0.077T^2t^2
 \end{aligned}
 \tag{Equation 5-9}$$

The standard deviation of this regression is 1.8, which equates to a variance of 3.2, while there were 26 degrees of freedom in the regression. Table 5-2 shows the calculated *p*-value for each concentration. It appears that the only concentration that has a significant increase in variation from the regression is water ($p > 0.05$), which is not problematic and to be expected since water has the less causes of uncertainty (no decomposition, only vaporisation).

Table 5-2 Analysis of variance of concentration

Concentration (%) (w/w))	Variance of residual error	F-values of each concentration	<i>p</i> -value of each concentration
0	0.21	15	8.6×10^{-3}
10	1.4	2.3	0.22
25	5.3	0.61	0.81
35	4.1	0.80	0.69
42	6.1	0.53	0.86

To determine how suitable this regression was, the concentration (*conc*) was calculated using the peak temperature data (*T*) and the time to peak temperature data (*t*) from the experiment. The calculated concentration of hydrogen peroxide was then plotted against the actual recorded concentration of hydrogen peroxide and a regression was taken again using the methods outlined in Chapter 4.1.1.

This regression has a coefficient of determination of 0.99 and a 2-sigma confidence interval of $\pm 3.7\%$ hydrogen peroxide, far better than either data set being used alone. This represents a higher accuracy and precision than the immersion sensor described above. This relationship has been plotted in Figure 5-14.

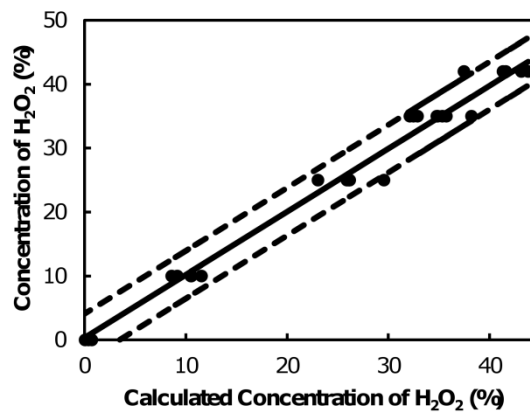


Figure 5-14 The calculated concentration from the regression vs the experimental concentration used, with raw data (•) shown

5.1.5 Summary of immersion testing

The RTDs coated with porous Pt decompose hydrogen peroxide from 10%-35% without becoming saturated, and will produce enough energy of decomposition to produce a significant temperature change (up to 1 K) in a PT100 RTD when it is immersed in liquid hydrogen peroxide. The subsequent response was shown to vary with hydrogen peroxide concentration in a relationship which can be described by a linear regression with a high accuracy ($r^2=0.97$) and reasonable precision ($\pm 6\%$). Furthermore, when a Pt-coated RTD is withdrawn from a liquid hydrogen peroxide sample, the peak temperature it reaches and the time it takes to reach the peak vary in relation to the concentration of hydrogen peroxide on the RTD. The best results are gained from a two-variable quadratic regression which produces higher accuracy ($r^2=0.99$) and precision ($\pm 4\%$), though the range of the measurement is limited to $<42\%$ due to the high decomposition energy and lower vaporisation energy of higher concentration hydrogen peroxide. In addition it was noticed that temperature change due to hydrogen peroxide decomposition in liquid has a linear relationship, whereas in air higher concentration (40-50%) peroxide behaves differently, due probably to the effect of vaporisation.

While this appears to be a strong basis for a sensor, in a practical sense improvements will need to be made, or further study will be needed. The measurements for the immersion sensor and the post immersion sensor both take a reasonable amount of time, which is not practical in a sensing capacity. The initial immersion response appears to happen reasonably quickly, with the rest of the minute period providing more data to improve accuracy, so determining exactly how long the sensor is needed to be in solution to determine a consistent temperature may prove useful. The post immersion response is trickier in that for the best measurement it relies on time. The best way to make improvements to this would be to reduce the thermal mass of the sensor, and/or an improvement of catalytic activity. Decreasing thermal mass should improve the responsiveness of the system since less there is less mass to physically heat up to for a signal, and increasing the catalytic activity, increases the reaction rate, decreasing the time needed for the signal to be fully produced.

5.2 Sensor Behaviour Due to Hydrogen Peroxide Droplets on the Sensor in the Test Rig

Experiments performed with droplets were done using RTD C and RTD B (Table 4-3) as the coated and uncoated RTDs respectively because these were flat rather than cylindrical. The catalysts were changed as there were some questions regarding the Pt-coated sensors ability to generate enough reaction for a measurement, and the flat sensor was also the easiest one to apply the MnO_2 catalyst to.

The behaviour of the RTDs when a droplet was placed on their tips was investigated under two main conditions: The RTDs acting as a temperature detector through the same set-up as described in Chapter 5.1.1, and also with the RTD being heated to maintain a constant temperature. The purpose of this work was to determine what effect airflow and having smaller quantities of hydrogen peroxide would have on the sensors' ability to function. In this case and in the subsequent mist work, evaporation has an important effect on the functioning of the sensor, and this experiment provided an understanding of the different competing heat flows.

In addition, it was also thought to be worthwhile to perform an investigation on how the RTDs performed when they were heated to a constant temperature, as the aim of the project in the early stages was to have a heated sensor to prevent catalyst poisoning.

5.2.1 Method for Ambient Investigation

The energy released by the decomposition of hydrogen peroxide on the MnO_2 catalyst was estimated in a similar investigation to that described for the Pt-coated sensor (Chapter 5.1.1). A 5mm flat MnO_2 coated sensor was dropped into a beaker of 10, 20 and 35% hydrogen peroxide, which was tared on a scale, and the resulting weight loss was recorded over 240 seconds. Equation 5-2 was used to determine the amount of hydrogen peroxide reacted, and Equation 5-3 was used to determine how much energy this released. During testing RTDs were mounted in the test rig that would be used for mist sensing, Figure 5-15.

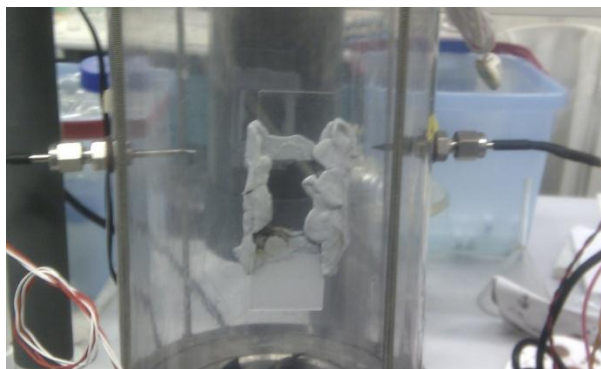


Figure 5-15 Picture of the mist test rig focused on the test chamber

The RTDs were connected to the same Yokogawa data acquisition system that was used for the immersion sensor, and the same LabVIEW program was used to record the output. To determine the effect of airflow on the liquid droplets on the sensor, 200 μL of MilliQ water was deposited on a sensor, as this was the minimum size that could be reasonably dispensed with the available equipment, and the temperature response was observed for 100 seconds. This was repeated 5 times under three different conditions without airflow, and with airflows of 7.5 L/min and 12.5 L/min. Once the effect of airflow was determined, droplets of different concentration hydrogen peroxide (10, 22.5, 35 and 45 (w/w) %) (concentrations confirmed by iodometric titration described in Chapter 4.2) and MilliQ water were deposited on the RTDs using a micropipette containing approximately 200 μL of liquid. Since some liquid fell off the sensor, the drop was only as large as could be physically supported. This means that droplets were not necessarily of uniform size and the results of this experiment are only qualitatively indicative not quantitatively accurate. The temperature of the RTDs was then monitored over the course of 10 minutes. This was repeated a minimum of five times for each concentration.

5.2.2 Results from Ambient Investigation

As detailed in Chapter 5.1.2, the mass loss of water due to vaporisation is 0.0065 g over 1650 seconds. This mass loss is insignificant compared to the mass loss of oxygen due to hydrogen peroxide decomposition, as displayed in Figure 5-16.

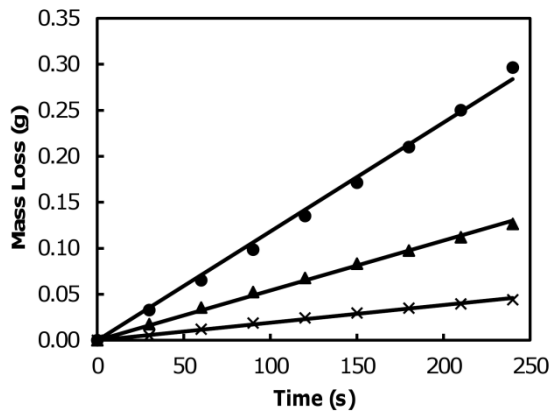


Figure 5-16 The mass loss of hydrogen peroxide due to decomposition using MnO₂ catalyst over time for 10% (×), 20% (▲) and 35% (●) hydrogen peroxide.

It should be noted that some of the MnO₂ was removed from the RTD by the hydrogen peroxide, and thus the actual performance of the MnO₂-coated RTD may be lower due to difference surface area. In addition, the catalyst dispersed into the solution resulting in a fierce reaction, which may have led to more loss through vaporisation (reaction produced more heat). This means that this data should be regarded as an upper limit of the mass loss rate.

Figure 5-16 shows a linear regression obtained using the method outlined in Chapter 4.1.1, which is forced through zero. The regressions statistics and the estimated mass loss rate for each concentration of hydrogen peroxide are described in Table 5-3.

Table 5-3 The regression statistics of the mass loss curves and the subsequently calculated mass loss rates

Hydrogen Peroxide Concentration (%(w/w))	Coefficient of Determination (r ²)	2-Sigma Confidence Interval (g)	Mass Loss Rate from Curve (g/s)	Mass Loss Rate (mol/s)
10	0.999	±2.23x10 ⁻³	1.91x10 ⁻⁴	4.06x10 ⁻⁴
20	0.999	±5.03x10 ⁻³	5.42x10 ⁻⁴	1.15x10 ⁻³
35	0.999	±1.34x10 ⁻²	1.18x10 ⁻³	2.51x10 ⁻³

Again, using Equation 5-2, it was possible to estimate the moles of hydrogen peroxide that were reacted (which can be seen in Table 5-3), and from this, Equation

5-3 was used to estimate the power that was generated by the hydrogen peroxide decomposition, the results of which can be seen in Figure 5-17.

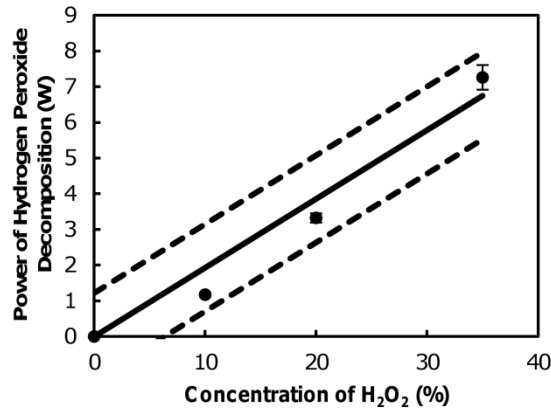


Figure 5-17 The power of hydrogen peroxide decomposition from a MnO₂ coated RTD vs the concentration of hydrogen peroxide with regression line. Dotted lines are upper and lower limits of 2-sigma confidence interval.

By taking a regression of the 0, 10, 20 and 35% data points, a linear regression can be found using the method in Chapter 4.1.1. The relationship has a high coefficient of determination of 0.98, with a 2-sigma confidence interval of ± 1.22 W. The regression calculates that the power per percent of hydrogen peroxide as 0.19 W/%, which is 2 orders of magnitude larger than the Pt-coated sensor. Given the larger catalytic response of RTD C, it should make a more sensitive sensor.

As previously established (Table 4-4), the heat transfer coefficients of the dry sensors in still air and 7.5 L/min airflow are effectively the same. This is due to the fact that, while the flow is large, the volume of the chamber reduces that air velocity to 1 cm/s. Indeed, the maximum flow rate which could be used was 12.2 L/min, which has a velocity of only 1.61 cm/s in the chamber. However, the situation when water droplets are added is expected to be different, as the different velocities may affect the vaporisation of water droplets.

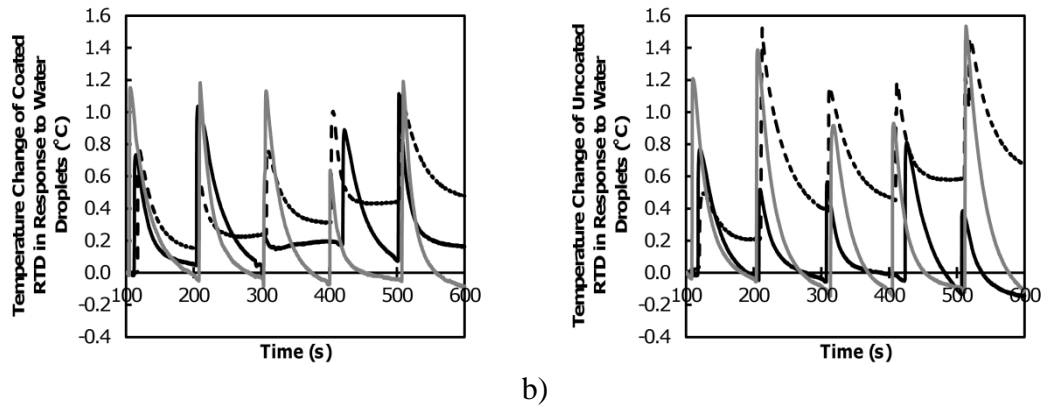


Figure 5-18 The change in temperature of the a) MnO_2 coated RTD and the b) uncoated RTD in response to droplets of MilliQ water deposited on the RTDs in the presence of no airflow (dotted lines), 7.5 L/min airflow (solid black line) and 12.2 L/min airflow (solid grey line). Droplets were deposited every 100 seconds.

Figure 5-18 shows the a) coated RTD response and the b) uncoated RTD response to a droplet of water under different airflow conditions. A single droplet of water, which had a slightly higher temperature than the RTDs, was deposited on both RTDs and the RTDs response was observed for 100 seconds (until the temperature stabilised), before another droplet was added, and the process was repeated. This whole process was done under no airflow, 7.5 L/min airflow and 12.2 L/min. Here the results are presented as the difference relative to the temperature at 100 seconds, in order to exclude the first droplet that was significantly different due to the initially dry surface of the RTD. These results show that RTDs with no flow are cooled less than RTDs surrounded by flowing air. Thus the airflow does have an effect on vaporisation, however, there does not appear to be a drastic difference between the level of cooling and the 7.5 L/min and 12.2 L/min air flows. In Figure 5-18a) there appears to be a difference in the data at 300 s, however, this was due to a malformed droplet.

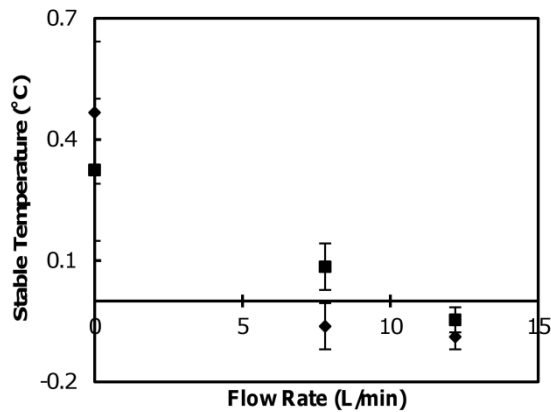


Figure 5-19 Average final temperature of each water droplet run for coated (■) and uncoated (●). Error bars represent 1 standard deviation

Figure 5-19 shows the average temperature the RTD reaches before the next droplet is deposited. Therefore it could not be confidently said that there is a difference in response between the coated and uncoated RTDs under any of the conditions, however, there is a clear difference between the response of the RTDs to droplets of water in still air and flowing air. There is however, less of a difference in RTD response between 7.5 L/min and 12.2 L/min.

Figure 5-20 shows the zeroed difference in temperature response between the coated RTD and the uncoated RTD with airflow of 7.5 L/min. The difference signal is used as it shows the effects of decomposition on the sensor, since the uncoated RTD acts as a control (the only effects on the uncoated RTD are vaporisation and convection). The first run was omitted from all graphs as its behaviour was not typical, due to the fact that in all other runs the RTDs started wet.

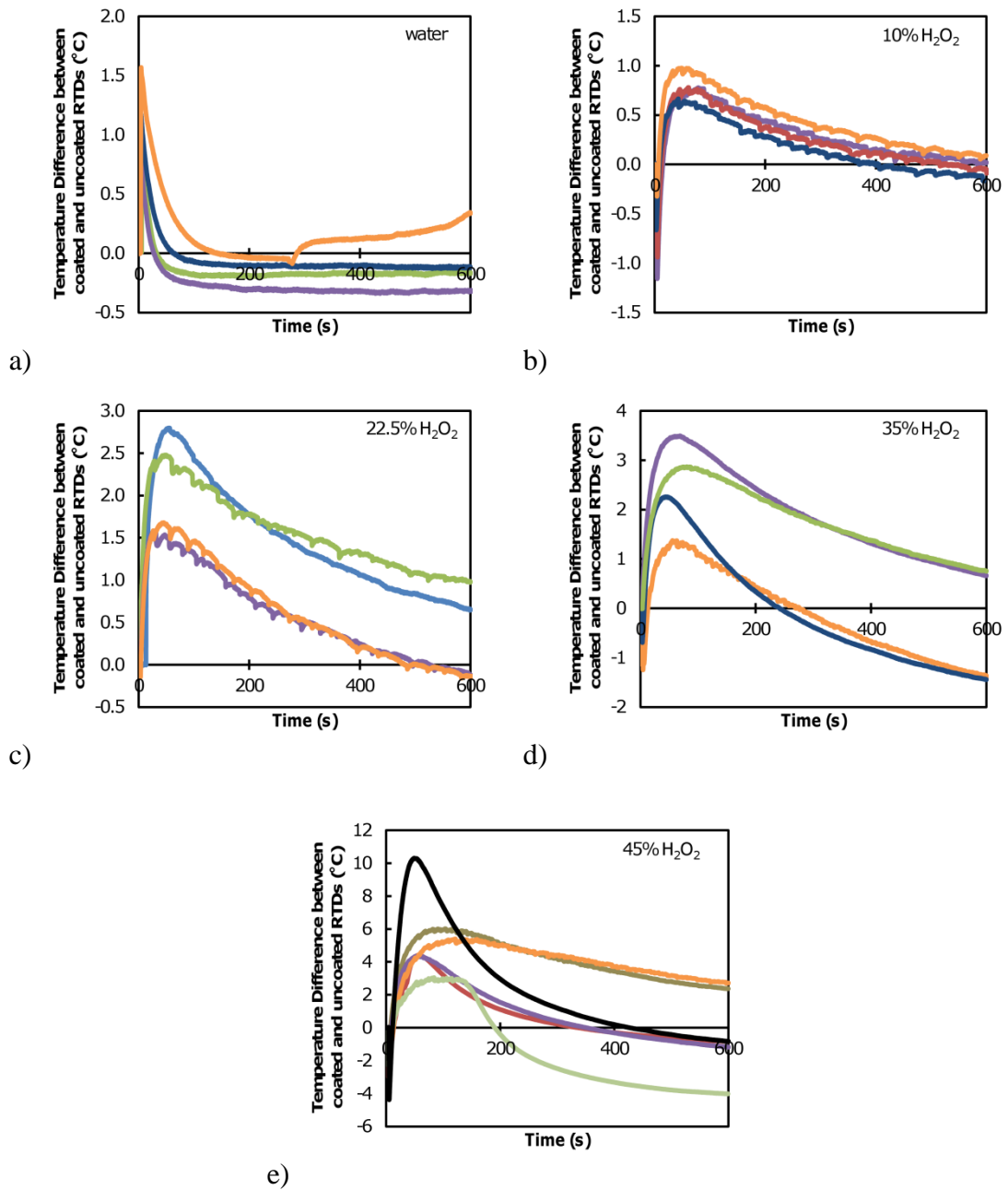


Figure 5-20 The temperature difference between RTDs over time for each droplet of a) MilliQ water b) 10% hydrogen peroxide c) 22.5% hydrogen peroxide d) 35% hydrogen peroxide and e) 45% hydrogen peroxide. The different colours are different runs and all first runs have been omitted. All graphs are zeroed, however, there is a negative temperature spike when the droplet is added which overwhelms this.

The response of the sensors to hydrogen peroxide droplets matches qualitatively with the post immersion stage Pt-coated catalyst data in Chapter 5.1.2, in that the temperature increases until it reaches a maximum, and then cools back to below the start temperature. In comparison the response of the sensor in Figure 5-20, shows a higher sensitivity to temperature, which is expected given the higher activity of the MnO₂ catalyst. The water, 10% and 22.5% hydrogen peroxide data shows a fairly consistent

response. Some responses appear different but it can be likely be traced back to the droplet's mass and shape as the reaction occurs (primarily due to effervescence). The 35% and 45% droplets show the most scatter in response. Effervescence appeared to be the most problematic issue, as it displaces liquid from the RTD. It also insulates that catalyst and RTD from the reaction, causing the reaction to run longer at lower temperature. Lack of a clear peak is generally the result of this phenomenon. This also occasionally affected subsequent runs, and was problematic enough to require the droplet to be rinsed off the sensor before the next run was started.

There are many possible sources of experimental error in this investigation and two prominent systematic ones are the droplet mass on the sensor (which cannot be accurately known since it is unclear how much stays on the sensor), and the erosion of catalyst over subsequent runs. The droplets are sizeable enough to cause the partial removal of catalyst which can affect the response, mostly in the post peak/cooling stage. This may cause the reaction to run longer due to having less catalyst. This was rectified by recoating the RTD if the degradation was evident. Finally error may have been increased by evaporative cooling. Figure 5-17 has shown that the MnO_2 coating is a more powerful catalyst than Pt, which should increase not only the decomposition but also vaporisation, which creates additional uncertainty particularly at the higher concentrations.

Figure 5-21 shows the average peak responses for each run (determined by taking the difference between the peak temperature and the temperature before the droplet was deposited), along with the corresponding uncoated RTD average response which was close to 0°C for all measurements. The times taken for the RTDs to reach a peak were also recorded however they do not show a consistent trend. The "peak" used for water was the first stable temperature the RTD cooled to. It can be clearly seen that the temperature of the uncoated RTD does not significantly change, suggesting that there is no major evaporative cooling present due to the air flow. This is possible since the droplets were a similar temperature to that the RTDs were recording, and as Figure 5-19 shows, the relative stable temperature in an air flow is approximately 0°C .

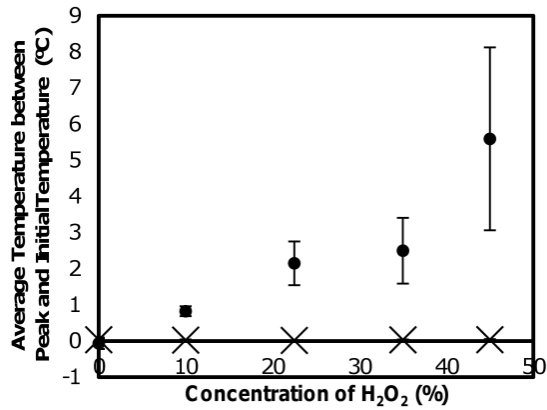


Figure 5-21 The average temperature difference between the peak-initial temperature (temperature change) of the MnO₂-coated (●) and the uncoated (×) RTDs. Error bars represent 1 standard deviation.

The lower values show better repeatability than the higher concentration droplets. There appears to be a relationship between the temperature of the peak and the concentration of hydrogen peroxide. The uncertainty in the measurements at hydrogen peroxide concentrations 35% and 45%, makes identifying the relationship difficult. It may be similar to the Pt-coated RTD post-immersion response where there is a maximum value between 35% and 42% hydrogen peroxide before there is an unstable measurement due to possible catalytic up concentration of the hydrogen peroxide.

A linear relationship was fitted with a reasonably high coefficient of determination and can be seen in Equation 5-10 ($r^2=0.89$, 2-sigma confidence interval $\pm 1.7^\circ\text{C}$), while the relationship between concentration and temperature can be seen in Figure 5-21.

$$y = 0.1128x - 0.3254$$

Equation 5-10

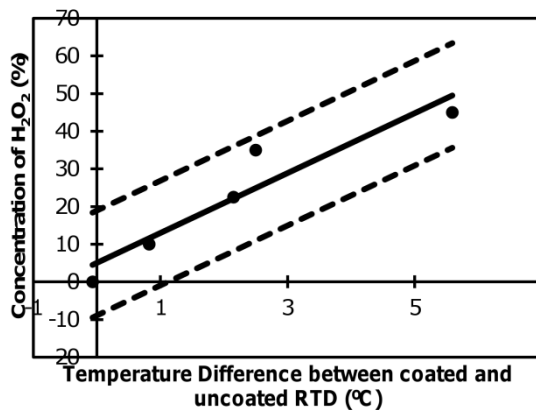


Figure 5-22 Concentration of hydrogen peroxide against the difference between peak temperature with linear regression line and 2-sigma confidence interval (dotted lines)

5.2.3 Ambient Droplet Investigation Summary

The investigation demonstrated that MnO₂ coated flat 5mm RTD was a more active catalyst than the round 15 mm Pt-coated catalyst used in the immersion investigation. Indeed increased cooling power due to forced convection does not seem to overwhelm the decomposition signal.

It was shown that while different air velocities did not affect heat transfer in Figure 4-13 (heat transfer coefficient for RTD C and RTD D in unforced and forced air), flowing air on a moist sensor produces a greater cooling event than still air, though given the dimensions of the test rig, the different flow rates only equate to a small absolute difference in air velocity, with a maximum of approximately 1.61 cm/s.

Application of the sensor to low and mid-range concentrations of hydrogen peroxide show good reproducibility and a large signal, however, the higher concentrations show much more variation. The two main proposed causes of this are differences in the amount of droplet deposited, and the increased effervescence, which creates more turbulence and can lead to the dispersion of the droplet, or perhaps it increases cooling through the release of mechanical energy in bursting bubbles, which may lead to the lower peaks with longer elevated temperatures seen in Figure 5-20 d) and e).

It would appear, without more investigation, a linear relationship between peak temperature and hydrogen peroxide concentration is the most defensible. Improvements to be made in such an experiment are to reduce the size of the droplet of hydrogen

peroxide deposited onto the sensor, and to improve the adhesion of catalyst to the RTD. For now, the experiment provided the necessary confirmation that the decomposition of a hydrogen peroxide droplet on a sensor in airflow shows a trend of increasing temperature with increasing hydrogen peroxide concentration.

5.2.4 Method for Heated Investigation

The heated investigation used the same RTDs C and B, but measured the power drawn by the RTD to remain at a constant temperature. Resistance is kept constant to maintain the desired temperature (resistance and temperature are related through Equation 5-5), while the voltage used to ensure a constant temperature was recorded by a LabVIEW program. Using this data, it was possible to determine the power required to keep the sensor at a constant temperature using

$$P_{sensor} = \frac{V^2}{r} \quad \text{Equation 5-11}$$

Where V is the voltage required in volts, r is the resistance in ohms and P_{sensor} is the power drawn by the sensor in watts. The power drawn by the sensor is dependent on the external conditions, in this case being vaporisation and decomposition (also air flow, however, as shown in Figure 4-13 and Chapter 5.2.2, airflow itself has no significant effect on the power of the RTDs, it just increases vaporisation), and thus the relationship

$$P_{sensor} = P_{initial\ sensor} + P_{Decomp} - P_{Vaporisation} \quad \text{Equation 5-12}$$

Where $P_{initial\ sensor}$ is the power required for a sensor to maintain a constant temperature (in this case 80°C, 105°C or 130°C) without droplets, P_{Decomp} and $P_{Vaporisation}$ are the powers released during decomposition and lost by vaporisation of water and hydrogen peroxide respectively, and P_{sensor} is the power required to maintain a constant temperature during water and peroxide decomposition and vaporisation. All values are in watts. The prediction from this is that a coated RTD heated by decomposition should require less power than an uncoated RTD to remain at constant temperature.

For this investigation, three different temperatures were used, 80°C, 105°C and 130°C. These were chosen as it gave one temperature below the boiling points of hydrogen peroxide and water, one temperature between the boiling points of hydrogen peroxide and water and one temperature with a boiling point above both hydrogen peroxide solution (40% w/w) and water.

This experiment was run in the same rig as Chapter 5.2.1, with an airflow of 7.5 L/min. 12.5 μ L droplets of MilliQ water, 10%, 20%, 30%, 35% and 40% hydrogen peroxide (concentrations were confirmed using iodometric titration described in Chapter 4.2) were deposited on both RTDs, and once again each sample repeated at least 5 times. The droplets were not deposited until the RTDs were dry, which was determined as when the RTDs returned to their baseline power.

5.2.5 Results from Heated Investigation

The raw output of the LabVIEW was a graph of voltage applied against time. An example of the output is given in Figure 5-23, with the voltages converted to power drawn. The droplets have been dropped on after the sensor has returned to its baseline power draw, so each graph shows five separate droplets, one after the other.

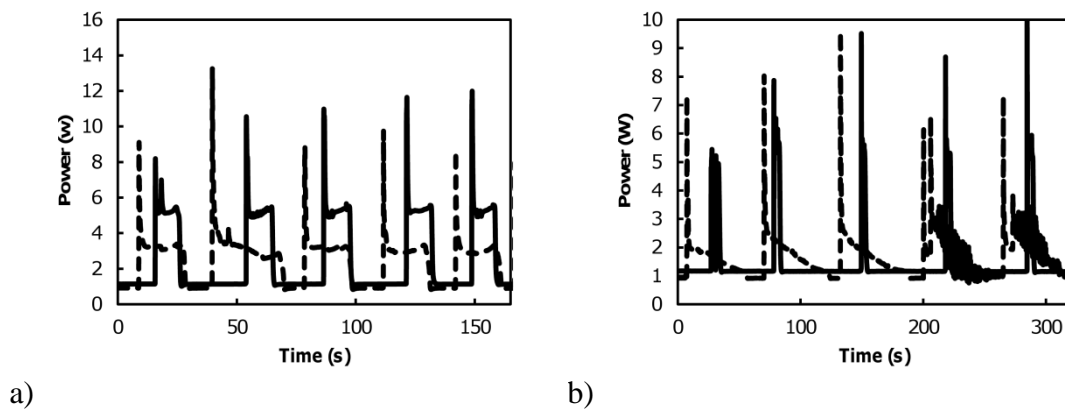


Figure 5-23 An example of the output data converted to watts from the LabVIEW program for the heated RTD experiment. Samples are a) water and b) 30% hydrogen peroxide, with RTDs heated to 105°C. The dotted lines represent the uncoated RTD, while the solid lines represent the coated RTD. The hydrogen peroxide pulses took longer to vaporise, therefore requiring longer runs and later pulses. The droplets were loaded onto each RTD by hand, and the delay between the pulses is the result of the time taken to load each one individually.

There is a clear difference in the shape of each sensor in Figure 5-23 a). It is clear that the coated sensor requires more power over less time until the water is removed, and a similar phenomenon is visible in b) which shows that the coated RTD draws a much higher power while the peroxide droplet is rapidly removed, whereas the

uncoated draws less power over a longer time. The response to hydrogen peroxide of the coated RTD is almost an immediate spike, as the hydrogen peroxide is almost immediately vaporised due to the heated RTD and the decomposition of hydrogen peroxide. The result for water is consistent with the higher heat transfer coefficient of the coated RTD C as noted in Chapter 4.5.1. Although there is an observable difference between the results for water and peroxide, further analysis is required for quantitative comparison.

A quantity of interest is the energy, which was determined by numerical integration of the power against time. The difference between each power and the first recorded power was taken, multiplied by the time interval between measurements and added to the previous measurement, to determine the energy drawn over the course of the experiment.

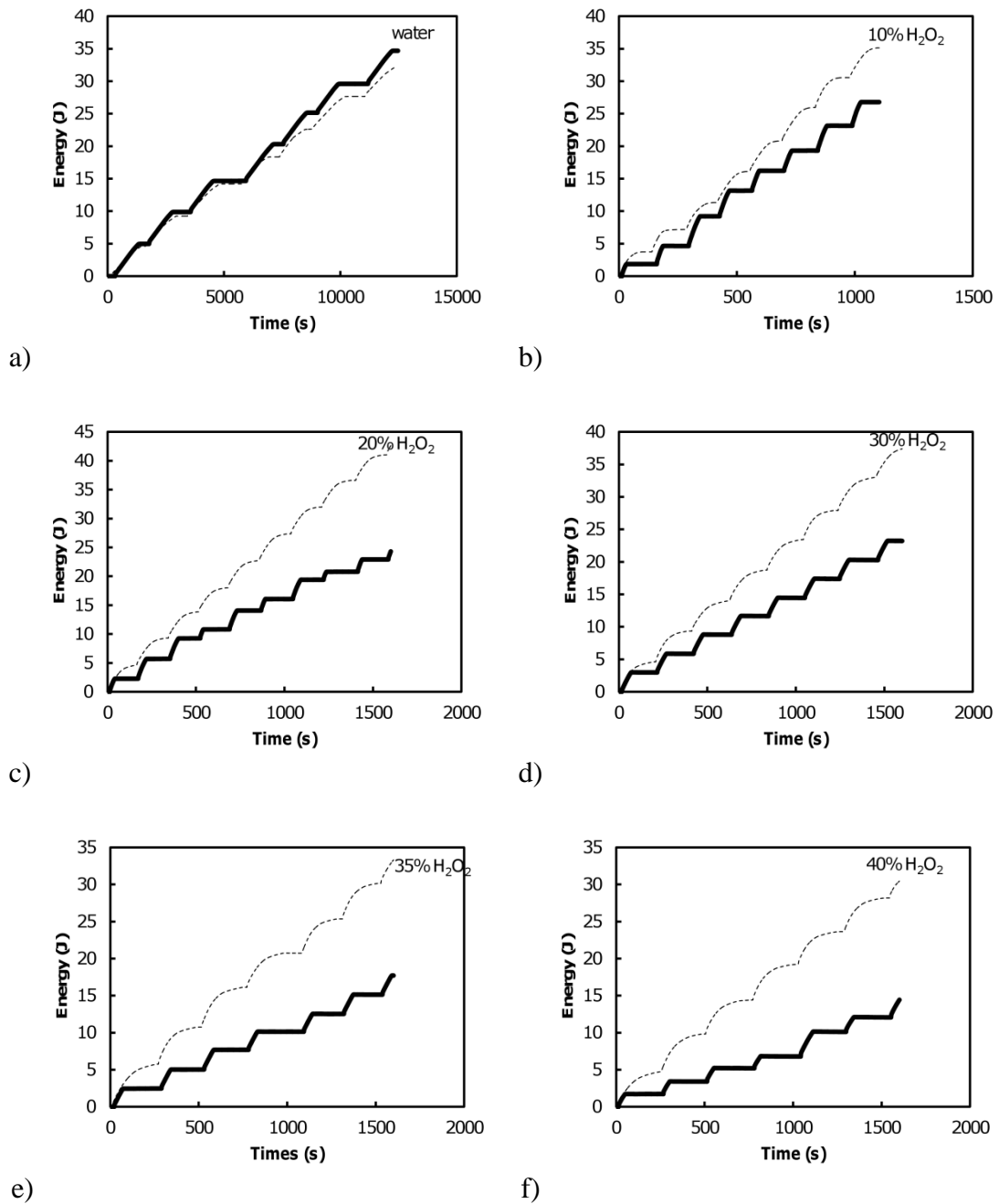


Figure 5-24 The energy drawn over time of experiment when each RTD was set to 80°C. Graphs show a) water, b) 10% hydrogen peroxide, c) 20% hydrogen peroxide, d) 30% hydrogen peroxide, e) 35% hydrogen peroxide and f) 40% hydrogen peroxide. Solid lines are coated RTD, dotted lines are uncoated.

Figure 5-24 shows the cumulative energy drawn over time for each droplet concentration at 80°C. Each step on the graph represents a droplet. The results show that there is an obvious difference between the energy drawn in the coated and uncoated sensors, which is expected from Equation 5-12.

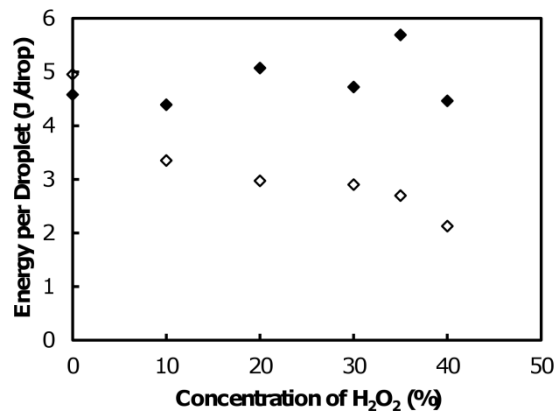


Figure 5-25 The average energy drawn per droplet against concentration for sensors held at 80°C. Symbols represent coated RTD response (◇) and uncoated RTD response (◆)

Figure 5-25 shows the average response to droplets for different concentrations of hydrogen peroxide. The uncoated response shows slight variations but is mostly consistent with that signal being independent of concentration. The response of the coated sensor however shows the energy required decreases as the peroxide content rises to 40%. The difference signal, which should show the effects of decomposition only (Equation 5-12), seems to follow a polynomial relationship between energy drawn ($J/drop$) and concentration ($conc$), which is shown in Equation 5-13:

$$J/drop = -2.158conc^2 + 0.156conc - 0.341 \quad \text{Equation 5-13}$$

Equation 5-13 has a relatively higher coefficient of determination of 0.91, and a 2-sigma confidence interval of ± 0.93 J/drop determined using the method in Chapter 4.1.2. It can also be seen that that until the concentration is 40%, the graph does show linearity. Applying a linear fit for the same variables but only using data until 35% shows a relationship of:

$$J/drop = 0.083conc - 0.057 \quad \text{Equation 5-14}$$

The coefficient of determination for Equation 5-14 was 0.87 and the 2-sigma confidence interval was ± 1.05 J/drop. In this case, a linear relationship is possible but seems unsuitable given that the sensor is only accurate to $\pm 11.8\%$ hydrogen peroxide as a 2-sigma confidence interval.

The same analysis was performed on both the 105°C and 130°C data. The energy drawn over time for each concentration can be found in the Appendix to this document. The average energy drawn per drop for each concentration of hydrogen peroxide is shown in Figure 5-26.

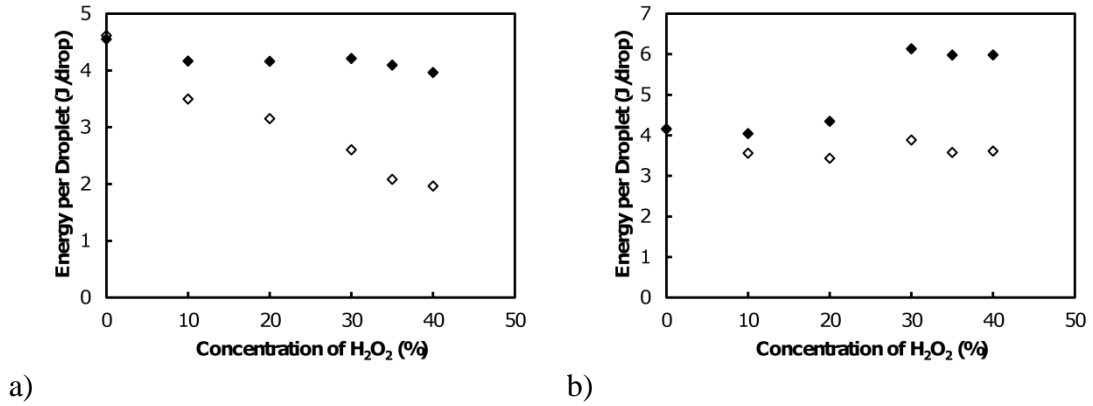


Figure 5-26 The average energy drawn per droplet against concentration for a) 105°C and b) 130°C. Symbols represent coated RTD response (◇) and uncoated RTD response (◆)

First considering the 105°C set-point, Figure 5-26 a) shows that the uncoated RTD response to different concentrations of hydrogen peroxide appears to follow a flatter slope than the coated RTD response to different concentrations of hydrogen peroxide. The difference is that the coated RTD draws much less energy than the uncoated RTD as concentration increases. This time the difference between the RTDs is almost linear until 40%.

$$J/drop = -2.76 \times 10^{-4} conc^2 + 0.064 conc - 0.039 \quad \text{Equation 5-15}$$

Equation 5-15 shows a quadratic relationship fitted using the method from Chapter 4.1.2. It has a coefficient of determination of 0.98 and a 2-sigma confidence interval of ± 0.27 J/drop. In Equation 5-16 we see the linear relationship between 0% and 35% hydrogen peroxide:

$$J/drop = 0.056 conc - 0.021 \quad \text{Equation 5-16}$$

This relationship also has a coefficient of determination of 0.98, with a 2-sigma confidence interval of ± 0.21 J/drop. This is a promising relationship for a sensor, and it

appears due to the more consistent vaporisation on the uncoated RTD. Turning this around, the sensor is accurate for a 2-sigma confidence interval of $\pm 3.8\%$.

Figure 5-26 b) is the response of droplets on the coated and uncoated RTD at 130°C, and shows a different trend. In this case, the coated RTD response is almost constant. The reason for this is that the higher temperature ensured a faster vaporisation rate of the droplet, and thus more energy was lost through vaporisation. The difference between the uncoated and coated RTD shows a linear trend at low values of hydrogen peroxide, however, once vaporisation becomes larger at 30% hydrogen peroxide a jump is observed in the evaporation signal, and from 30% hydrogen peroxide onwards the difference signal levels out. It is possible that this is occurring due to the higher temperature decomposing the hydrogen peroxide, which in turn is increasing the vaporisation (since the higher concentration hydrogen peroxide would release a significant amount of power, more than the lower concentrations, which is why this effect is not seen before). Given the lack of a trend past 30% hydrogen peroxide, and given the ambiguous nature of what is occurring, it was decided that using a temperature around 130°C was not workable in a heated sensor.

5.2.6 Heated RTD Investigation Summary

By heating the RTD and keeping the RTD temperature constant, it was possible to determine how much power it took to offset the power of the decomposition and vaporisation of hydrogen peroxide. Comparison of an RTD coated in porous-Pt and an uncoated RTD did give a signal which was proportional to hydrogen peroxide concentration, and this was observed with the RTDs set at three different temperatures. It was also clear that the best way to process this data was by taking a numerical integration and determining the energy used to stabilise the temperature. While 80°C showed a linear trend, it was not as strong as others. It is theorised that a reason for this is that there is insufficient vaporisation to clear the effects of previous drops, resulting in inconsistency. 130°C shows no usable trend between concentration and energy drawn by the RTD. It is believed that this is because the evaporation rate was increased with the higher temperature, which means that less hydrogen peroxide decomposed and thus a lesser signal was found. 105°C had a linear relationship between 0-35% hydrogen peroxide, with high accuracy. This setup has a more stable vaporisation on the RTDs,

and thus the decomposition signal has more effect on the resulting difference signal, leaving 105°C as the best option if a heated sensor was to be used.

5.3 Summary of Immersion Experiments

Table 5-4 Summary of calorimetric RTD performance as immersion and drop sensor

Sensor	Coefficient of Determination (r^2)	2-Sigma Confidence Interval	Effective Range % H_2O_2
Immersed in Liquid	0.97	±5.8%	0-50
Post Immersion (Peak Temperature)	0.93	±0.36°C or 5.3%	0-42
Post Immersion (Peak Time)	0.83	±4.9s or 5.9%	0-25
Post Immersion (Combined Temperature and Time)	0.99	±3.7%	0-42
Ambient RTD with 7.5L/min Air Flow	0.89	±14%	0-45
80°C Heated RTD with 7.5L/min Air Flow	0.87	±12%	0-35
105°C Heated RTD with 7.5L/min Air Flow	0.98	±3.8%	0-35

Table 5-4 shows a summary of the different immersion and droplet RTD sensor setups and the results with each. Using the sensor as an immersion sensor is accurate, it has the best linear range of measurement and it only decomposes a small amount of hydrogen peroxide, which means it is not overly invasive. However, it has a small signal response, and a large confidence interval because of this. The sensor has utility as it stands right now as a sensor which could determine a rough estimate of hydrogen peroxide concentration. For example in the case of this project, the hydrogen peroxide which is needed is 35%, however, it has been shown that 30% hydrogen peroxide is

capable of sterilising equipment and 40% is more than capable without causing damage to equipment, then a reading of $35 \pm 5\%$ may be adequate. However, as the concentration detected moves down from 35%, the concentration of hydrogen peroxide could be less than 30%, which means it would require a second, more precise measurement to determine whether the concentration of hydrogen peroxide was strong enough. It may be possible to improve this RTD's precision by increasing the catalytic activity of the catalyst in the future.

The post immersion response, both in peak temperature and time can be used individually, however, both are less accurate and have a lower range than the immersion sensor. However, by taking both these responses together in a multiple regression, error can be reduced and the trend becomes slightly more accurate than the immersion sensor, and shows a better confidence interval. In addition, both responses appear to show a highly linear response between 0 to 35%, however more data is required to validate this.

In addition, the RTD post immersion response drops between 30 and 40%, and becomes erratic for the responses over 45%. This is most likely due to the different environment to the immersion sensor. In the immersion sensor, there is no vaporisation component of the reaction as the sensor is buried in a bulk liquid. As the surface area of the hydrogen peroxide is increased (droplet) it is more susceptible to both evaporation and decomposition. We theorise that once the concentration reaches 42% hydrogen peroxide, the decomposition has enough energy to increase evaporation, and once the concentration reaches 50% (perhaps 45%) the decomposition has enough energy to cause enough vaporisation to increase the concentration of hydrogen peroxide in the droplet.

When exposed to droplets the MnO_2 RTD shows a similar response in respect of the post immersion data. However, it is hard to say whether increased uncertainty around 35% and 45% is due to increase in evaporation or other uncontrolled experimental factors. For this reason, the most defensible trend to use is linear, which gives a reasonable trend, of course it is much less accurate than the preceding sensors and has a much larger confidence interval. This sensor is perhaps hampered by not having corresponding time-to-peak data.

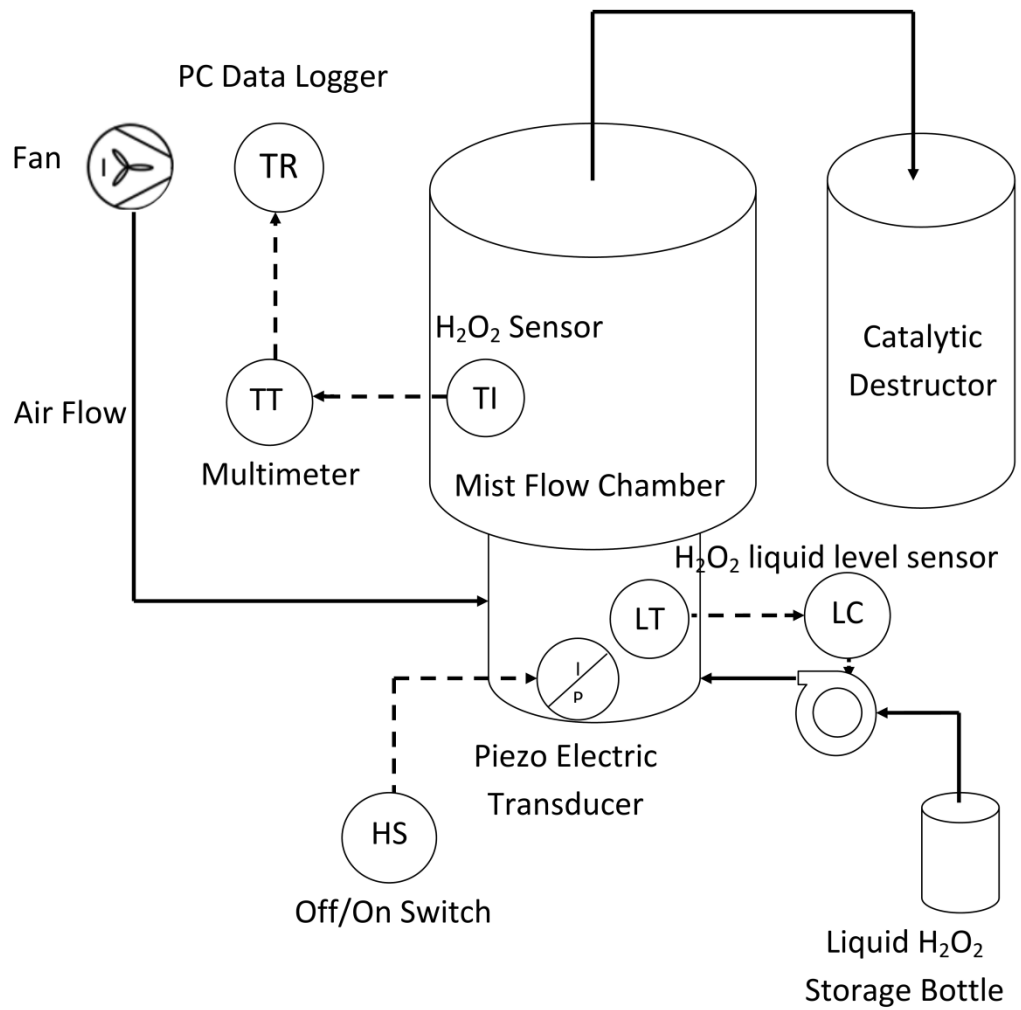
Finally the heated sensors again show that the RTD is only linear from 0-35%. It is clear that using a temperature around 100°C produces the most accurate signal, as it reduces problems due to vaporisation on the RTDs; results show that if temperature is too low then the vaporisation can be more random, while too high produces a reading with too little decomposition response.

Conclusions which can be drawn from this are that hydrogen peroxide concentration can produce a proportional calorimetric response due to hydrogen peroxide. This trend is still apparent in hydrogen peroxide droplets, however here vaporisation becomes important, consistent with the change in behaviour at concentrations of over 40% hydrogen peroxide (signal reduction), and further at concentrations closer to 50% hydrogen peroxide the sensor shows more error due to hydrogen peroxide undergoing up-concentration. These insights are helpful for understanding how the sensors respond to fine mist, which we discuss in the next chapter.

Chapter 6 Testing of the Calorimetric Sensor in Mist

Chapter 5 has provided some important insights into the calorimetric phenomena occurring during the decomposition of hydrogen peroxide solution, particularly the increasing competition between decomposition and vaporisation when the peroxide-air surface is close to the catalyst. This chapter will focus on applying the calorimetric sensor idea to determine the concentration of hydrogen peroxide when it is in the form of a fine mist.

The mist produced by the rig used here is similar to the hydrogen peroxide mist which is used in the Nanosonics disinfection unit as it is generated by a nebuliser which is analogous to the one used in the commercial product. However, in the test rig we are using the mist has reduced turbulence compared to the disinfection unit. In addition, due to the size of our mist flow chamber (where the sensors are located) the flow rate of the mist is lower in our tests than would be the case in the disinfection unit. Figure 6-1 shows the process by which the hydrogen peroxide mist is generated and flowed through the system. The apparatus consists of three chambers, a cup where liquid is converted to mist, the mist chamber which is where the sensor is placed for measurement, and a catalytic destructor to convert all hydrogen peroxide mist into water and oxygen. The mist was generated in the cup by an ultrasonic piezoceramic transducer (Fuji Ceramic Corporation) operated at a frequency of 2.4 MHz, which agitated the liquid, creating a fountain of liquid which was the source of mist droplets. The transducer device oscillated in pulses, and could be controlled using pulse width modulation (%PWM), which increases or decreases the time between oscillations. The cup was connected to an external bottle of liquid which could be automatically pumped into the cup to keep the liquid level constant. The pump was controlled by a sensor in the cup. This ensured constant operating conditions and protected the transducer from running dry and overheating. The droplets were then injected into an airstream which was flowed into the system using a fan. The resulting mist was blended over a baffle and flowed into the mist chamber relatively evenly. From here measurements were taken, while the mist was constantly pushed through this chamber and into the catalytic decomposition chamber.



Legends

TR = Temperature Recorder

TT = Temperature Transmitter

TI = Temperature Indicator

LT = Liquid Level Transmitter

LC = Liquid Level Control

HS= Hand Operated Switch

I/P= Electrical to Physical Transducer

Figure 6-1 Flow process diagram of calorimetric mist sensor test rig

The RTDs in the mist chamber are connected to the same measurement devices that were described in Chapter 5. Figure 6-2 shows the mist chamber itself in operation. Note the mist is rising fairly uniformly indicating a lack of turbulence.

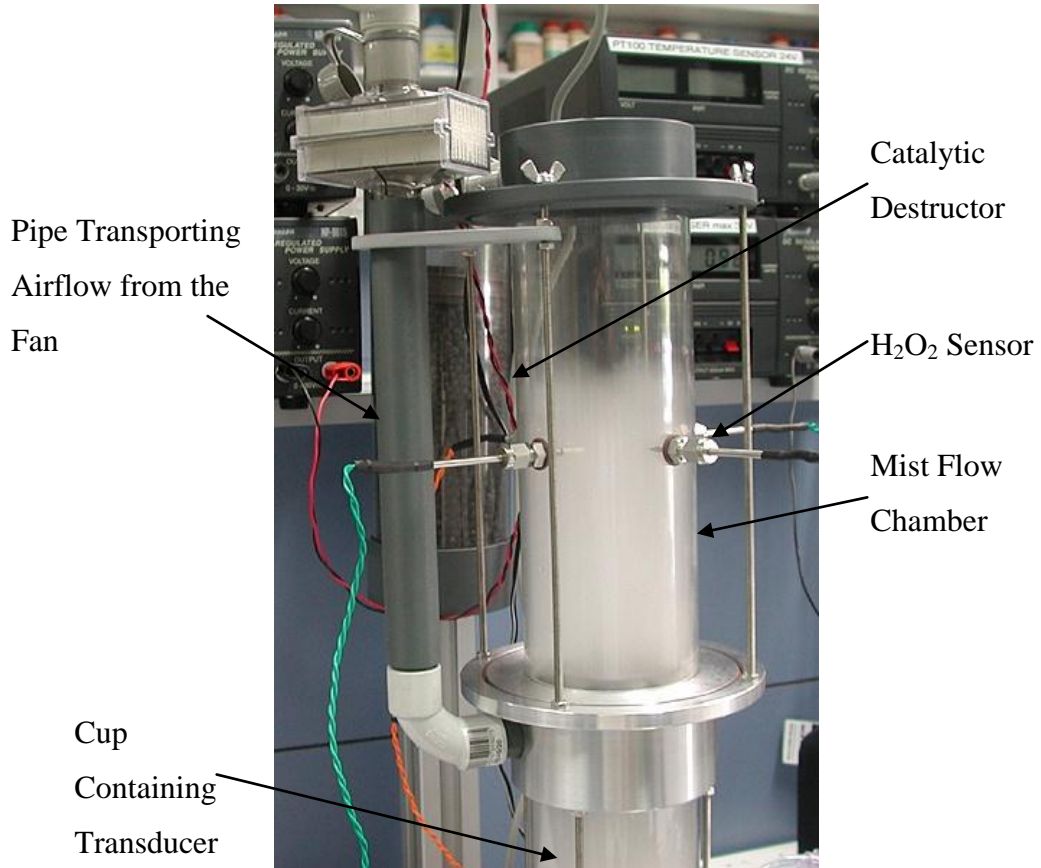


Figure 6-2 Photo of the mist chamber during operation

6.1 Characterisation of the Mist

The production of mist is a function of the voltage applied to the transducer (which in this case was kept constant to 30 V) and the %PWM. Obviously, the higher the duty cycle used, the more mist is created. Mist production is also dependent on some physical characteristics of the liquid such as surface tension. The higher the surface tension of the liquid, the lower the mist production as in this case the height of the fountain formed by the transducer is reduced. The mist density is dependent on the mass of mist produced and the rate of air flow through the sensor. The flow rate in these experiments is at 7.5 L/min of air entering the chamber. The PWM of the transducer can be controlled. However, the surface tension is largely a function of peroxide concentration which is one of the variables to be measured. Hence a calibration curve was created to ensure that the mist flux was known for each mist test.

6.1.1 Method for Determination of Mist Flux

The mist flux was determined as a function of hydrogen peroxide concentration and duty cycle. The cup and bottle were filled with different concentrations of water and hydrogen peroxide (MilliQ water, 35%, 45% and 50% hydrogen peroxide) and the mist was generated over a period of time. Each time the pump refilled the supply in the cup, the nebuliser and timer was stopped (to within a minute) and the mass of the bottle was measured. This was repeated for over 10 minutes to reduce error, and repeated for duty cycles 10%, 15%, 20% and 30%.

The concentrations of hydrogen peroxide were monitored using iodometric titration which was outlined in Chapter 4.2.

6.1.2 Results for the Determination of Mist Flux

The mass of the bottle of hydrogen peroxide after each measurement was recorded and used in a linear regression to determine the rate of mass loss caused by the generation of mist. The average mass loss for each set of conditions was then plotted and a two variable quadratic regression was taken using the method outlined in Chapter 4.1.3. The results are shown in Figure 6-3, and the quadratic regression equation is given as Equation 6-1 where *conc* is the concentration of hydrogen peroxide and *cyc* is the duty cycle.

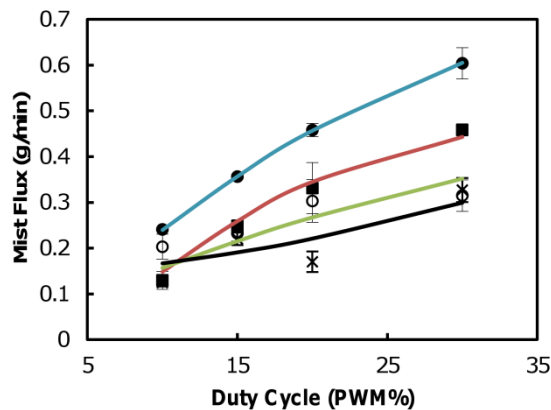


Figure 6-3 The mist flux of water (●), 35% (■), 45% (○) and 50% (×) hydrogen peroxide determined as the slopes of each regression of mass lost from the bottle of hydrogen peroxide, and the quadratic regression calculated values of water (blue), 35%, (red), 45% (green) and 50% (black). The error bars represent the 2-sigma error of the mist flux.

$$\begin{aligned}
\text{mist flux} = & -4.62 \times 10^{-2} + 3.20 \times 10^{-2} \text{conc} - 3.43 \times 10^{-4} \text{conc}^2 \\
& - 1.80 \times 10^{-2} \text{cyc} + 4.34 \times 10^{-4} \text{cyc}^2 + 1.63 \\
& \times 10^{-3} \text{conc. cyc} - 3.57 \times 10^{-5} \text{conc}^2 \text{cyc} - 4.47 \\
& \times 10^{-5} \text{conc. cyc}^2 + 8.99 \times 10^{-7} \text{conc}^2 \text{cyc}^2
\end{aligned}
\tag{Equation 6-1}$$

The variation of the relationship is 7.5×10^{-4} , while the variation in residual error is 5.3×10^{-2} . This has a p -value of 1, which means that variation captured by the higher orders of the relationship did not significantly distort the variation of the individual measurements (p -value > 0.05).

The mist flux predicted from the peroxide concentration and duty cycle was then plotted against the actual mist flux and a linear regression was then taken to check the accuracy of the quadratic regression. The regression of the actual and calculated mist flux had a coefficient of determination of 0.95 and the 2-sigma confidence interval is $\pm 5.70 \times 10^{-2}$ g/min (Figure 6-4).

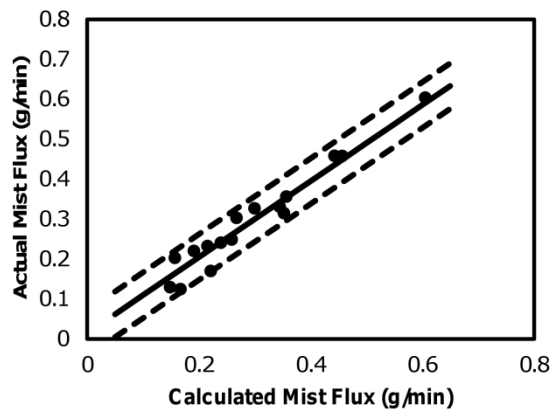


Figure 6-4 The actual mist flux vs the calculated mist flux, with linear regression (solid line) and the 2-sigma confidence interval (dotted lines).

Some of these estimates took 20 minutes for the pump to work for the first time, and the amount of liquid pumped in was smaller than it should have been. This is due to initial over-filling the cup and the formation of a meniscus on the sensor, which causes the sensor to trigger the next pump cycle later than it should. This effect disappears after the first pump cycle, and in this case, that point is taken as the starting time for the remainder of the measurement.

As the concentration increases, the error in the regression increases. This may be due to the increasing viscosity and surface tension of the liquid causing the pump and/or sensor to perform more irregularly.

6.1.3 The Size of Mist Droplets

The size distribution of the droplets was studied by Nanosonics prior to the beginning of my project. This was achieved using a laser diffraction technique with a Malvern analyser MastersizerS. Measurements were conducted by the employment of an analogous mist generation system with an identical Fuji ultrasonic transducer. A 35% H₂O₂ solution was agitated at the same frequency of 2.4 MHz at ambient temperature, as used in my own work, however the transducer voltage used in the sizing experiments was 26 V whereas I used 30 V in the sensing experiments. From data within the sizing experiment, it appears that changing or interrupting the voltage applied does not greatly affect the average droplet size, but can affect the distribution of sizes, which is not a significant difference in this study as the droplets will aggregate to an average for measurement. Droplet size was measured in a mist stream at the volumetric flow rate of 10 L/min.

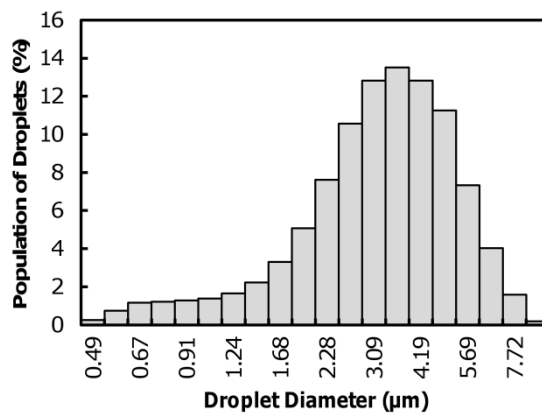


Figure 6-5 The size distribution of 35% hydrogen peroxide mist droplets produced using a voltage of 26V applied to the transducer. Study was commissioned by Nanosonics in collaboration with Sydney University.

As can be seen Figure 6-5 in the ultrasonic transducer produces a distribution of droplet sizes, which range in size from 0.5 µm to 10 µm. However, most particles in this particular experiment are between 3 and 5 µm, with an average size of 3.7 µm. It was calculated that 65% of particles were this size or smaller.

Assuming that the mist particles are spherical, it is possible to estimate that the surface area per gram of the 35% hydrogen peroxide mist is $0.144 \text{ m}^2/\text{g}$. This is much larger than the surface area of the 35% hydrogen peroxide droplets deposited manually as described in the previous chapter (estimated at $0.007 \text{ m}^2/\text{g}$). This suggests that the mist droplets will be much more susceptible to evaporation than the pipetted droplets. In contrast, the bulk solution would have negligible evaporation (however it does cause high rates of heat transfer due to the conductivity of the liquid.)

6.2 Detection of Hydrogen Peroxide Concentration in Mist Using Unheated RTDs

The RTDs used in this sensor were C and D from Table 4-3, and they were set at 10 cm from the edge of the chamber. The aim of studying the response of the RTDs to mists of different hydrogen peroxide concentration and water was to attempt to understand the various energy transfers which occur on the RTD due to the competing processes of decomposition and evaporation. This section has been published in IEEE Sensors Journal article *Calorimetric Sensor for H₂O₂/H₂O Mist Streams*[169].

From the previous chapter it has been observed that, when a coated RTD is placed in air with a droplet of hydrogen peroxide on the surface, the RTD heats until the decomposition energy reaches a peak, at which point the RTD begins to cool due to an increase in vaporisation and a decrease in decomposition (due to a decrease in hydrogen peroxide). The presence of flowing mist changes this. First there is a constant supply of hydrogen peroxide present, which is expected to create a situation more like bulk fluid where the temperature does not peak but increases until it reaches a plateau due to saturation in the amount of hydrogen peroxide in the vicinity of the RTD. It also suggests that the signal will be smaller than in the case of the pipetted droplet due to the cooling effect exerted by continuous arrival of mist particles. Therefore, this section will aim to determine whether a concentration determination is possible by decomposition of hydrogen peroxide on an RTD due to catalyst.

6.2.1 Method for Detection of Hydrogen Peroxide in Mist Using Unheated RTDs

Two data sets were collected, a series of runs in which the mist stream was run for two minutes and a series of runs when the mist stream was run for three minutes.

The data acquisition system used in Chapter 5.1.1 was used here with some modifications. For the two minute runs the system was automated in such a way that the program recorded when the mist was turned on and off. This meant that the number of mist cycles, the length of each mist cycle and the length of time between each mist cycle could be recorded. In these tests, the mist was run for 2 minutes, with 8 minutes between each run and 4 runs overall. Measurements were also taken of the nebuliser cup temperature and the temperature of the air which was being drawn into the fan at the beginning and end of each mist run cycle. These temperatures were taken using two stainless steel sheathed PT100 RTDs from Labfacility Ltd. These were of the same class as the other RTDs used in this project.

This experiment was performed using mists of water and 5%, 10%, 15%, 20%, 25%, 30% and 35% hydrogen peroxide. The samples were all diluted from the 35% hydrogen peroxide. Concentration was confirmed using iodometric titration described in Chapter 4.2. These concentrations were chosen firstly to study more intermediate concentrations (especially between water and 5%) to develop a more complete understanding of the behaviour of a hydrogen peroxide mist on a catalyst. The highest concentration was 35%, since the previous Chapter had shown that hydrogen peroxide droplets behaviour changes between 35% and 40% hydrogen peroxide.

The three minute data was collected using a similar method, however, there was no automation of the mist pulses. The same data acquisition program was used and the same set up was used, however, RTD B was used instead of RTD D and the time that the RTDs were working for was different. This occurred as RTD D was unavailable for this study, however, it was predicted to have little difference as the RTD was just being used as a thermometer of the mist temperature. The RTDs recorded data for 1 minute before the mist was turned on. When the mist was turned on, it was for 3 minutes and following that the RTDs continued to record for another 6 minutes. This provided the RTDs with 7 minutes of recovery time, as the 2 minute data suggested that was all that was necessary to get the signal.

This experiment was performed using mists of water and 4.8%, 8.6%, 11%, 16%, 20%, 25%, 30%, 31.5%, 33%, 34%, 35%, 40%, 45% and 45.7% hydrogen peroxide. All samples below 35% were diluted from 35% hydrogen peroxide stock, while samples above 35% were diluted from 45.7% hydrogen peroxide stock. The

concentrations were confirmed using iodometric titration as described in Chapter 4.2. These concentrations were chosen to determine whether the sensor could determine the difference between small hydrogen peroxide concentration differences. Concentrations above 40% were also tested to observe if there was any strange behaviour above 40% hydrogen peroxide. This data is also anchored to the 2 minute data by the common concentrations (4.8%, 11%, 16% 20%, 25%, 30% and 35%).

In addition to these runs, two additional runs were also performed, one with a mist pulse of 30 seconds and one with a mist pulse of 4 minutes. These runs were only performed for 35% hydrogen peroxide and were for the purpose of checking overall behaviour of the sensor . The runs were performed using the automated method, with a time of 8 minutes between runs, and again each experiment was run 4 times.

The duty cycle used for generation was 20%. This variable is kept constant, however, as shown in Chapter 6.1.2, the mist flux changes with concentration of hydrogen peroxide.

6.2.2 Results for Detection of Hydrogen Peroxide in Mist Using Unheated RTDs for 2 Minute Mist Cycles

The response of the coated and uncoated RTDs to mists of varying concentrations of hydrogen peroxide is shown in Figure 6-6.

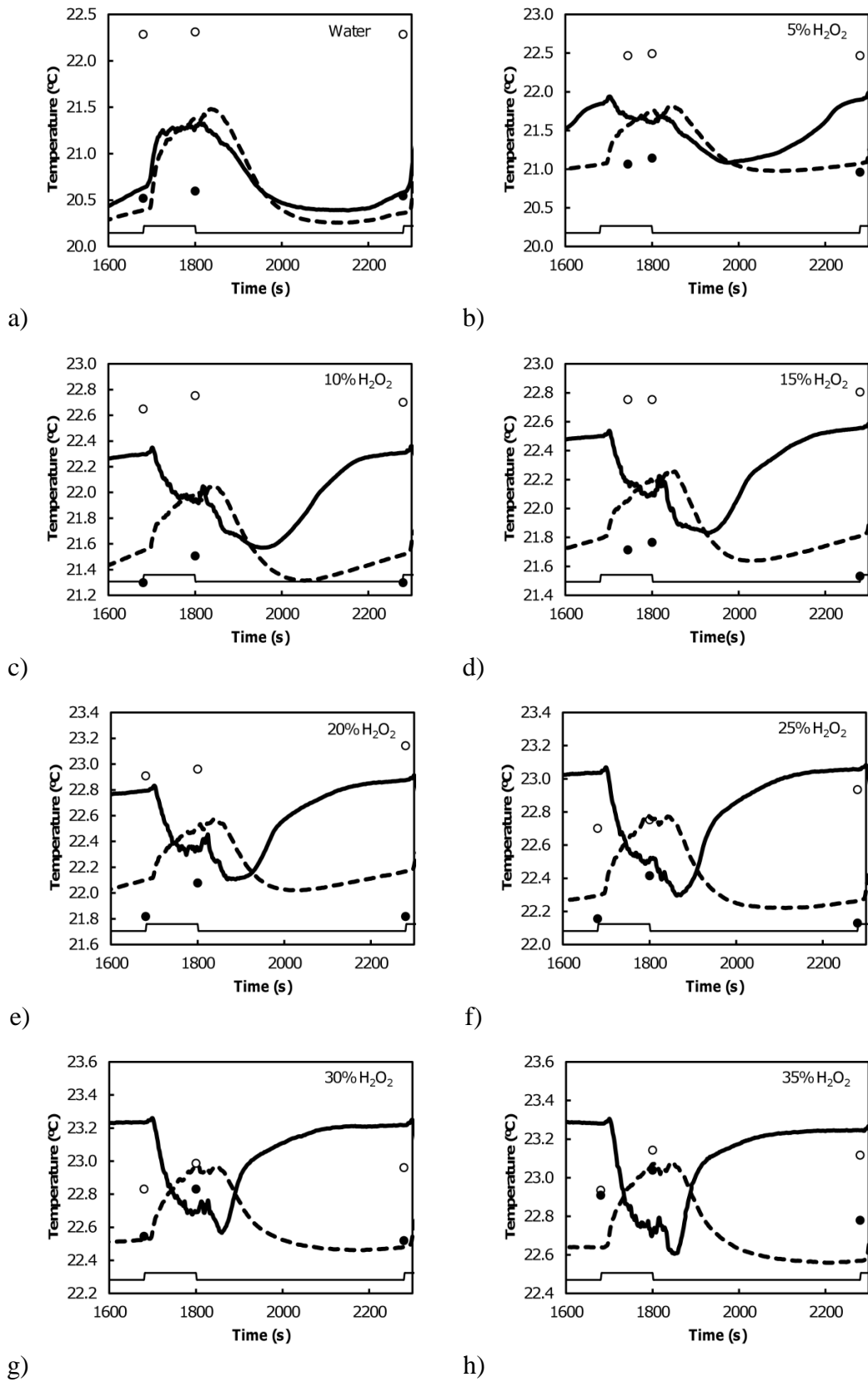


Figure 6-6 An example of the response of the bare (dotted line) and coated (solid line) RTD to hydrogen peroxide of concentrations a) 0%, b) 5%, c) 10%, d) 15%, e) 20%, f) 25%, g) 30% and h) 35%. Temperature measurements of the liquid in the cup (●) and air entering the fan (○) is also presented. Steps in the solid straight line at the bottom of each graph represents the period that the nebuliser was on for.

Each graph shows the third run for each concentration, because this is typical of most runs (apart from the initial run which is different due to the RTDs being dry). It is clear that the uncoated and coated RTDs show a different response to the mists.

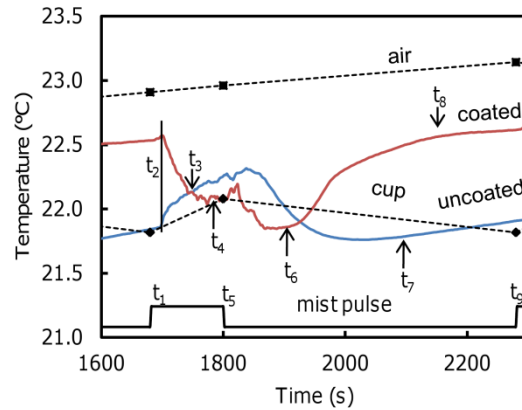


Figure 6-7 A typical response of the coated (red line) and uncoated (blue line) RTDs to mist. The ambient temperature of the air entering the fan (■) and of the liquid in the cup (◆) are also shown connected with a dotted line (this was not measured but is included to show the overall trend of increasing and decreasing ambient temperatures). The solid steps indicate when the mist pulse was on. Specific times are marked on the graph where something important has occurred, t_1 is when the nebuliser is turned on and the mist pulse starts, t_2 is when the mist reaches the RTDs, t_3 is when the temperature of the RTDs reach the temperatures of the RTDs are the same, while t_4 is when the coated RTD begins to reach an thermal equilibrium with the mist, and t_5 is when the nebuliser is turned off and the mist pulse ended. At t_6 the coated RTD reaches a temperature minimum, at which point the energy of vaporisation is overcome by the decomposition of hydrogen peroxide and the temperature of the RTD begins to increase, as the RTD “dries”. At t_7 , the temperature of the uncoated RTD is also slightly increasing, however much slower than the coated as there is no decomposition to drive vaporisation, and at t_8 it can be seen that the coated RTD is almost back to the temperature it was before the mist cycle. Finally, at t_9 the next mist pulse starts, and the process repeats. The example given is from 15% hydrogen peroxide.

As seen in Figure 6-7, both sensors in the figure have started off “wet” due to the previous mist runs. While the uncoated RTD is wet and there is no mist on, the RTD undergoes evaporative cooling due to the mist droplets remaining on the RTD. Once the mist reaches the RTD again, t_2 , the RTD temperature rises which is believed to be due to suppression of evaporation into the saturated air, and the mist coming in being warmer than the RTD consistent with the increase in cup temperature. This increase is due to the transducer heating the liquid in the cup. The uncoated RTD’s temperature remains roughly midway between the air and cup temperature, which is expected in a mixture of liquid droplets and air. Once the mist is turned off again, t_5 , the RTD is left “wet” once more and evaporative cooling again occurs, dropping its temperature.

In a water mist, the coated RTD displays similar behaviour to the uncoated RTD, the main difference is that the rate of the temperature increase of the coated RTD

is lower than that of the uncoated RTD, presumably due to an insulation effect (thermal mass being similar). This is seen in the work done in Chapter 4.5, where the uncoated RTDs generally showed a higher heat transfer coefficient than the coated RTDs. In hydrogen peroxide mists however, the response of the coated RTD is quite different, starting with the readings prior to the mist being turned on. The coated RTD begins with a temperature noticeably higher than the uncoated RTD. When the mist reaches the RTD, t_2 , this temperature actually *decreases* until it is at or below the temperature of the uncoated RTD. This decrease should be expected as, at this point in the measurement cycle, the coated RTD is measuring the temperature of the mist, which is similar to the temperature the uncoated RTD is detecting, t_3 . However, the temperature measured by the coated RTD is always slightly lower than that measured by the uncoated RTD, and the temperature appears to *decrease* relative to the uncoated RTD as the concentration of hydrogen peroxide increases, t_4 , which is surprising. Once the mist is turned off, the temperature of the coated RTD *continues to decrease* until reaching a minimum, t_6 , after which a steep increase in temperature occurs. This increase eventually saturates, returning the sensor to the temperature it had prior to the mist being turned on, t_8 . This effect is consistent and its magnitude depends on the concentration of hydrogen peroxide. As the concentration increases, the minimum temperature is reached sooner and shows a smaller decrease in temperature.

This was somewhat unexpected as previous data had created the expectation that the coated RTD should have a higher temperature than the uncoated sensor due to decomposition of hydrogen peroxide. Instead what appears to be occurring is that (1) prior measurement cycles leave the coated sensor in an elevated temperature condition, which (2) initially leads to cooling when a fresh flow of mist droplets impinges on the sensor, while in addition (3) the effervescence caused by the decomposition of hydrogen peroxide is increasing evaporation, thereby causing more cooling on the coated sensor. Given that the mist droplets have a much larger surface area than the manually pipetted droplets, it would be expected that evaporation would be much higher than for measurements in the previous Chapter. In addition it is believed some of the energy from the decomposition goes into the aiding the vaporisation of droplets from the surface. In contrast, the bare RTD shows a slow temperature rise during the mist-on

period, which is likely caused by the slowly increasing temperature of the mist overriding any evaporation signal.

This effect becomes even clearer after the mist is turned off as the temperature on the coated sensor continues to decrease without the mist to establish pseudo-equilibrium. Although the temperature on the uncoated sensor also decreases after the mist cycle is terminated, the decrease is faster on the coated than the uncoated RTD. After a characteristic time the fall in temperature stops. At this point, I surmise that the energy released by decomposition of the hydrogen peroxide dominates over any cooling from evaporation. The temperature then rises with the decomposition vaporising the remaining droplets until the RTD is back to its “dry” state.

6.2.3 Determining a Signal from Data During the Mist Cycle (‘On-Line’)

There were several ways in which the complex thermal signal described above could be used to generate parameters correlated with concentration of hydrogen peroxide. Particularly useful were the temperatures of the coated RTD before and after the mist was turned on, and the minimum temperature reached by the coated RTD. As noted previously, there is also a slow increase of the mist temperature caused by heating in the cup superimposed on the data. As can be seen from the data in Figure 6-6, the data is rarely flat, and in the cases of most hydrogen peroxide measurements, the data has significant noise, though there does appear to be an overall linear trend present. Temperatures at various stages of the mist pulse were determined by analysis using Fityk 0.9.1. A linear trend was determined for a stable period of approximately 60 seconds on each data set. The equation of this trend was then used to determine the temperature of the RTD before and after the mist using the last time measurement before the mist sensor was turned on and off (i.e. t_1 and t_5), reducing the affect of noise on the data and incorporating more than one data point into the measurement.

The difference between the temperature at the end of the mist cycle and start of the mist cycle for each RTD was determined and is displayed in Figure 6-8 a). The water data is very different from that of the hydrogen peroxide due probably to the proposed mechanism described above. In the case of pure water there is no energy input from decomposition, and therefore the initial temperature of a RTD in water mist is always lower than the final, except in the very first run of a sequence when the sensor

might have been dry and not thermally equilibrated. This data for the uncoated RTD response appears to show a usable trend against peroxide concentration, however, it is unclear what this trend is based on, and it is highly likely based on the cup temperature increasing, as the uncoated RTD will effectively be a measure of the mist temperature. In contrast, the temperature change decreases with increasing hydrogen peroxide concentration from water to 15% hydrogen peroxide as the cooling power of the mist is decreasing due to a decrease in water content (water has a significantly higher heat capacity per gram as it experiences stronger hydrogen bonding between molecules). The temperature increases slightly at the higher concentrations, however this is likely due to the increasing mist temperature. This suggests that it may be possible to determine the concentration of hydrogen peroxide based on only the coated RTD response for a low range of concentrations or if the mist is not varying in temperature highly. Figure 6-8 b) shows the response of only the coated RTD against the concentration of hydrogen peroxide with the data for water excised. The RTD shows a linear response from 5% to 25% hydrogen peroxide. After this the response saturates, which is likely due to the slight increase in temperature of the mist caused by the transducer.

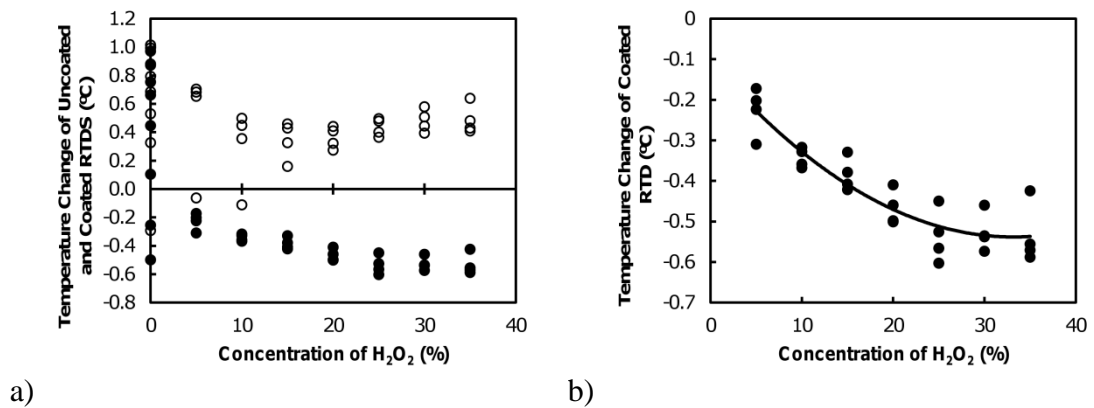


Figure 6-8 The difference in temperature of the a) uncoated (\circ) and coated (\bullet) RTDs from before the mist was turned on to after the mist was turned off and b) is only the hydrogen peroxide measurements on the coated RTD.

The response of the coated RTD is taken as the independent variable (T) and the concentration is taken as the dependent variable ($conc$). Equation 6-2 shows the relationship for 5% to 25% hydrogen peroxide which best describes the data. The regression has coefficient of determination is 0.85, and a 2-sigma confidence interval of $\pm 6\%$. The results are displayed in Figure 6-9.

$$conc = -57.1T - 7.34$$

Equation 6-2

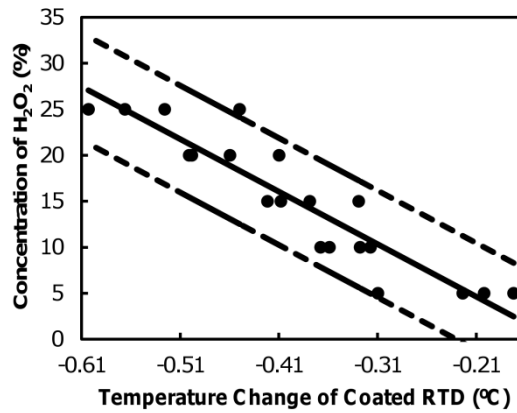


Figure 6-9 The concentration of hydrogen peroxide compared to the temperature response of the RTD. Line of linear regression predicts concentration from temperature response and dotted lines represent 2-sigma confidence interval.

The coefficient of determination and confidence interval both indicate a significant level of noise. One way to reduce this is to take the difference in response between the uncoated and coated sensors, as it has taken into account the changing temperature of the mist, determined by the uncoated RTD temperature response. The results are demonstrated in Figure 6-10. In this case, the temperature response for concentrations of hydrogen peroxide between 10% and 35% appear to show a linear trend.

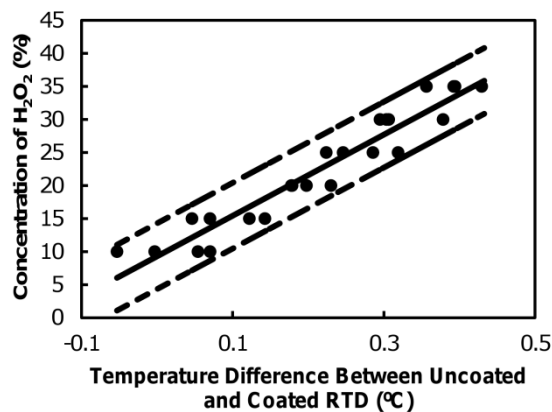


Figure 6-10 The linear section of the concentration of hydrogen peroxide against the difference between uncoated and coated RTD response signal. Solid line represents the linear regression of the data and the dotted lines represent a 2-sigma confidence interval.

Equation 6-3 describes the relationship, which has a coefficient of determination of 0.92, and a 2-sigma confidence interval of $\pm 5\%$. This response is significant upgrade in accuracy, precision and range over using a measurement from just one RTD.

$$conc = 61.4T + 9.30$$

Equation 6-3

The immersion-withdrawal sensor showed that there was a relationship between the time-to-peak and temperature at the peak and the concentration of hydrogen peroxide. The data here also shows a minimum and by applying this principle, it may be possible to utilise a similar concept for this response.

6.2.4 Determining a Signal from Data During the Drying Cycle ('Off-Line')

The minimum temperature that the coated RTD reached after the mist cycle, and the time taken to reach the minimum, was obtained and the results are displayed in Figure 6-11.

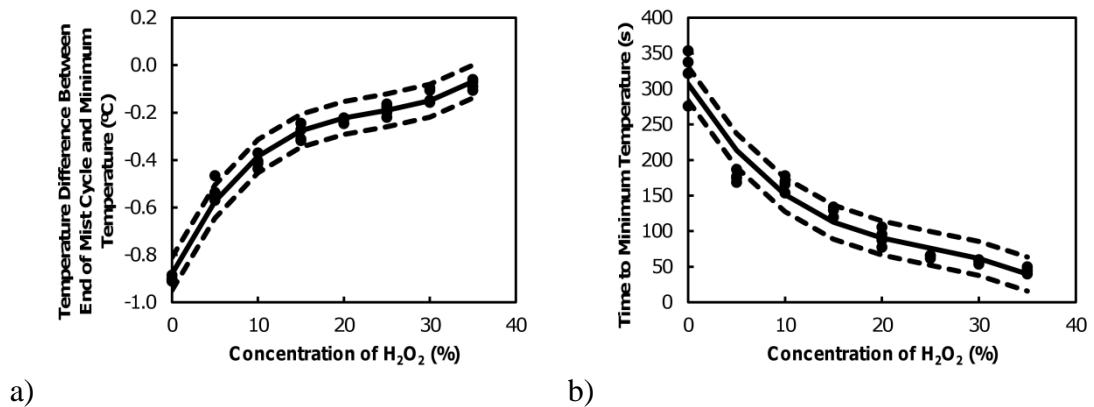


Figure 6-11 a) The difference between the temperature of the coated RTD at the minimum temperature after the mist cycle and the temperature at the end of the mist cycle, b) the time that the coated RTD temperature is at a minimum after the mist cycle. Solid lines are 3rd order polynomial regressions and dotted lines are the 2-sigma confidence intervals.

From a practical standpoint, this sensor is problematic, in that it takes such a long time to determine a concentration. If this sensor is to be used specifically to determine 35% hydrogen peroxide, it would take approximately 50 seconds from the end of a (two minute) cycle to confirm a measurement (if it takes significantly longer, it is likely less than 35% hydrogen peroxide). This is a long time to wait for a

measurement, and it is clear that either this process needs to be optimised or a new process needs to be found for a commercial sensor.

Both data sets show a trend that could be described as a cubic polynomial. This trend was empirical, and cannot be used to predict anything outside of the range measured. The minimum temperature and concentration regression has a coefficient of determination of 0.98, while the 2-sigma confidence interval is $\pm 0.07^\circ\text{C}$ compared to 0.85 and $\pm 0.09^\circ\text{C}$ for the ‘on-line’ measurement. The regression fit to the minimum time and concentration is less accurate with a coefficient of determination of 0.94 and a 2-sigma confidence interval of $\pm 44\text{s}$. Equation 6-4 and Equation 6-5 describe the relationships between the hydrogen peroxide concentrations (*conc*) as a function of the temperature difference at the minimum (*T*) and the time at the minimum (*t*) respectively.

$$\text{conc} = 44.4T^3 + 131T^2 + 131T + 44.2 \quad \text{Equation 6-4}$$

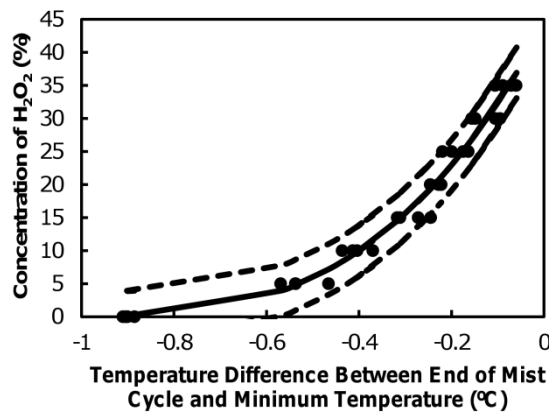


Figure 6-12 Concentration of hydrogen peroxide as a function of temperature difference between the end of the mist cycle and minimum temperature reached after the mist. Solid line represents cubic regression and dotted lines represent 2-sigma confidence interval.

Figure 6-12 shows the concentration of hydrogen peroxide as a function of temperature difference between the end of the mist cycle and the minimum temperature. A cubic regression is fit to it with high accuracy (coefficient of determination 0.98) and a narrow confidence interval of $\pm 4\%$.

$$\text{conc} = -1.15 \times 10^{-6}t^3 + 1.17 \times 10^{-3}t^2 - 0.41t + 49.4 \quad \text{Equation 6-5}$$

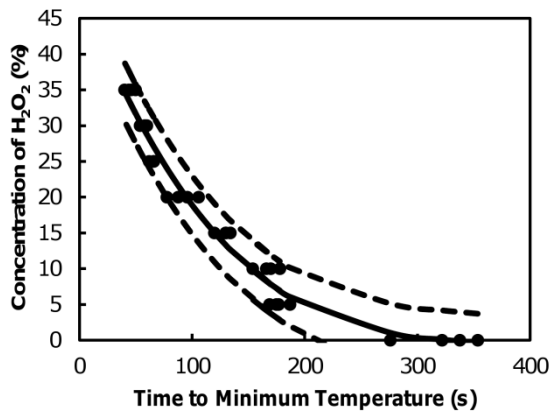


Figure 6-13 Concentration of hydrogen peroxide as a function of the time the minimum temperature was reached. Solid line represents cubic regression and dotted lines represent 2-sigma confidence interval.

Figure 6-13 shows the concentration of hydrogen peroxide as a function of time the temperature reaches a minimum point. The cubic regression also shows high accuracy (coefficient of determination 0.97) and a narrow confidence interval of $\pm 4\%$.

It is possible to improve the accuracy of this measurement by calculating the expected values of hydrogen peroxide using both of these methods and combining the results by averaging. The results are shown in Figure 6-14. The trend between the actual concentration and the calculated concentration appears to be linear. A regression was applied using the method outlined in Chapter 4.1.1. The regression applied is strong with a coefficient of determination of 0.99, and has high precision with a 2-sigma confidence interval of $\pm 3\%$.

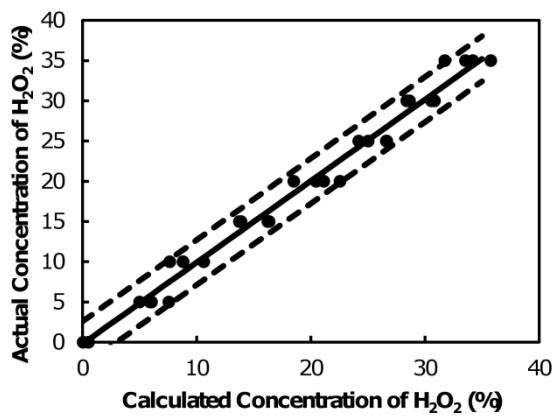


Figure 6-14 The actual concentration of hydrogen peroxide as a function of the average calculated hydrogen peroxide using the regressions for time to minimum temperature and difference between end of cycle temperature and minimum temperature.

This correlation is similar to the correlation in Chapter 5.1.4. In this case it is an inversion to the model described in Figure 5-9, due to the fact that the mist droplets are many orders of magnitude smaller than the droplets in that model, and as Chapter 6.1.3 shows, these have a much higher surface area and are much more susceptible to vaporisation. In this case the vaporisation is so much higher that the decomposition signal is completely overridden, and in, the hydrogen peroxide helps drive the vaporisation by boiling the droplets. This removes the droplets from the surface, and at a certain point, the vaporisation is overridden due to the mass lost due to decomposition and vaporisation (effectively “drying” the sensor), and the temperature of the RTD is then driven back to the temperature before the mist cycle. With increasing hydrogen peroxide concentration, the hydrogen peroxide should dry faster, and drop to a lower temperature (as the decomposition is working against it). Additionally, this would be highly sensitive to the amount of hydrogen peroxide on the sensor. A longer mist cycle would mean more mass to dry, but this would be balanced again having more energy to dry the RTD. Additionally, having a quicker mist cycle would have less energy to dry, but balanced against less mass to dry. Duty cycle should have a similar relationship, i.e. lower duty cycle less mass on the sensor, higher duty cycle more mass on the sensor. Therefore, it is important to find a time or duty cycle in which this drying period can be seen.

6.2.5 Results for Detection of Hydrogen Peroxide in Mist Using Unheated RTDs for 3 Minute Mist Cycles

The experiment was performed again, this time with a mist pulse period of three minutes. A large number of mists (0%, 4.8%, 8.6%, 11%, 16%, 20%, 25%, 30%, 31.5%, 33%, 34%, 35%, 40%, 45% and 45.7% hydrogen peroxide) were used for this part of the investigation. The detailed results of the experiment are provided in the Appendix.

In summary, these three-minute pulses show similarity to the two minute data above, with the uncoated RTD heating up slowly during the mist cycle due to the increasing temperature of the mist, and cooling occurring after mist is terminated, due to the evaporative cooling by the droplets left behind. The coated RTD meanwhile decreases in temperature during the mist cycle, due to the three reasons given previously

in Chapter 6.2.2, before reaching a minimum temperature and increasing in temperature again.

There is a slight difference in the results of the 4.8%, 8.6% and 11% hydrogen peroxide from the similar results in the two minute data, in that the temperature increases after mist rather than decreases. This appears to be due to the fact that the six minute resting time after the mist pulse is not long enough for the hydrogen peroxide to burn off and the RTD to return to “dry” temperature, and so when the mist pulse is repeated for the next run, it is then measured as an increase rather than a decrease in temperature.

6.2.6 Determining a Signal from Data During the Mist Cycle (‘On-Line’)

Given that the curves have similar shape it should be possible to apply the same analysis to this data as to the two minute data. The temperature difference recorded by both RTDs between the end of the mist cycle and the start of the mist cycle are shown in Figure 6-15. All data from the first runs have been omitted due to the fact that the first run was performed under ‘dry’ conditions.

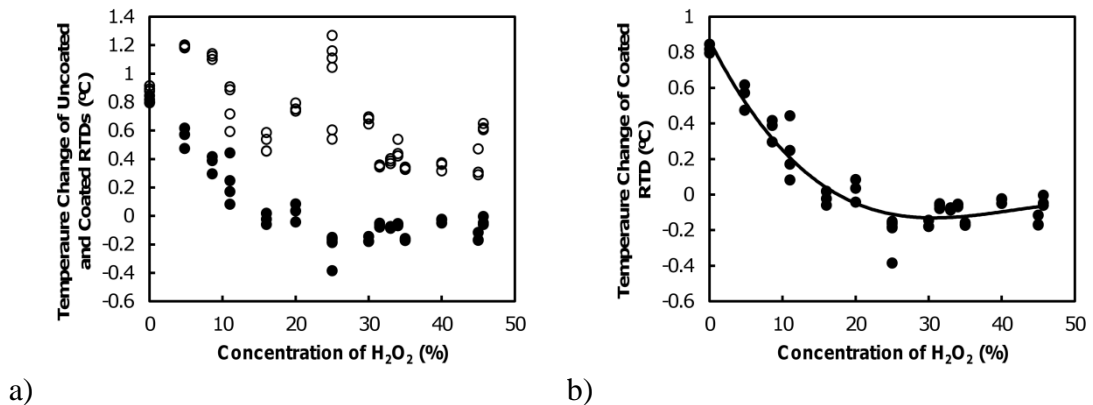


Figure 6-15 The difference in temperature of the a) uncoated (\circ) and coated (\bullet) RTDs from before the mist was turned on to after the mist was turned off and b) is only the hydrogen peroxide measurements on the coated RTD, for three-minute mist pulses.

The figure shows that parameter for the uncoated RTD has no real trend, while the coated RTD has a similar trend as in the two minute data, linear between 0 and 25% hydrogen peroxide before the response flattens out, and temperature change is no longer affected by concentration. A linear regression was taken by the temperature change (T) as a function of concentration of hydrogen peroxide ($conc$). The regression is described in Equation 6-6 and shown in Figure 6-16, and shows good accuracy with a coefficient

longer time between mist runs, to determine whether the same relationship between coated and uncoated temperatures is possible for the three minute data.

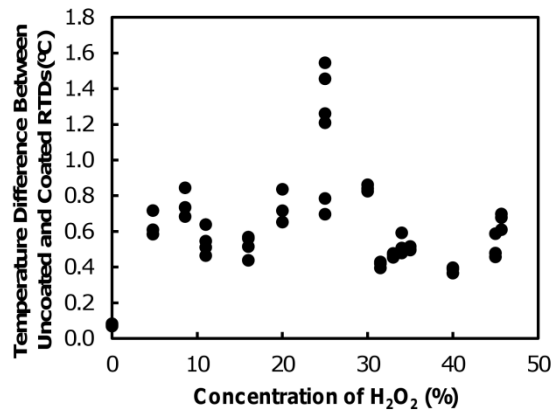


Figure 6-17 The difference between uncoated and coated RTD temperatures for different concentrations of hydrogen peroxide exposed to three minute mist pulses.

6.2.7 Determining a Signal from Data During the Drying Cycle ('Off-Line')

As with the two minute data, it was possible to estimate concentration by the time taken for the temperature of the coated RTD to reach a minimum post mist pulse, and from the difference between the minimum temperature reached and the temperature at the end of the mist cycle. The data are displayed in Figure 6-18. The water data was not included as the RTDs never reached a minimum temperature during these tests. The method described in Chapter 4.1.2 was used to determine a relationship between hydrogen peroxide concentration and the temperature difference and time at the minimum. A cubic regression was found to have the best accuracy describing both curves, with a coefficient of determination of 0.90 and a 2-sigma confidence interval of $\pm 0.14^{\circ}\text{C}$ for the minimum temperature, and a coefficient of determination of 0.92 and 2-sigma confidence interval of ± 43 s for the minimum time. The time to minimum regression is similar to the two minute data in both shape and accuracy and precision. On the other hand, while the minimum temperature data has a similar shape, it is less accurate and less precise than the two minute data.

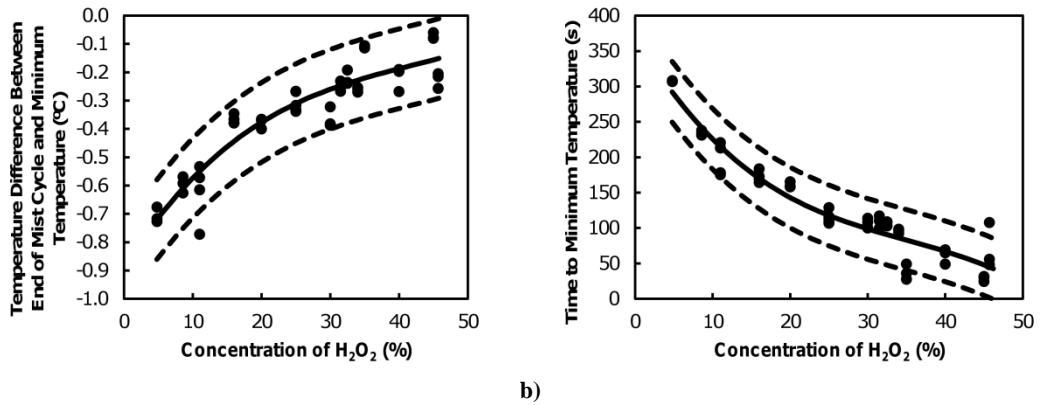


Figure 6-18 a) The difference between the temperature of the coated RTD at the minimum temperature after the mist cycle and the temperature at the end of the mist cycle, b) the time that the coated RTD temperature is at a minimum after a 3 minute mist cycle. Solid lines are 3rd order polynomial regressions and dotted lines are the 2-sigma confidence intervals.

The data appears to flatten out after 35% hydrogen peroxide, which suggests that this is the limit of the sensor's range. A simple calculation shows that a possible cause of this could be the reduction in mist flux observed with increasing concentration of hydrogen peroxide in the cup (mist flux reduces as concentration increases as described in Chapter 6.1.2). Figure 6-19 shows the reduction of decomposition energy (which is assumed to all be used in vaporisation of droplets) as the mist flux drops. By 35-40% hydrogen peroxide, the signal begins to flatten as the reduction of mass of hydrogen peroxide results in a reduction of power available to vaporise the water. For the purposes of this sensor it has an effective range of 0 to 35% hydrogen peroxide.

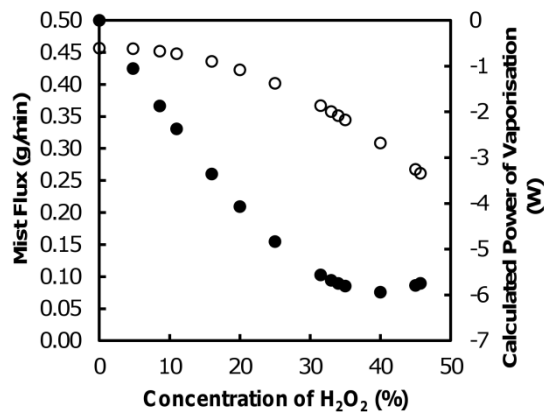


Figure 6-19 The mist flux of the hydrogen peroxide calculated from the calibration curve (○) and the corresponding calculated power predicted to be released due to vaporisation of mist droplets (●). Decomposition of hydrogen peroxide is assumed to increase vaporisation of droplets.

A regression was then performed where the concentration of hydrogen peroxide was taken as the dependent variable (*conc*) and temperature difference between end of mist cycle and the minimum temperature following the mist cycle as the independent variable (*T*). This regression is described in Equation 6-7 and shown in Figure 6-20. The regression has a coefficient of determination of 0.87 and 2-sigma confidence interval of $\pm 7.4\%$ hydrogen peroxide.

$$conc = -289T^3 - 334T^2 - 54.4T + 33.3 \quad \text{Equation 6-7}$$

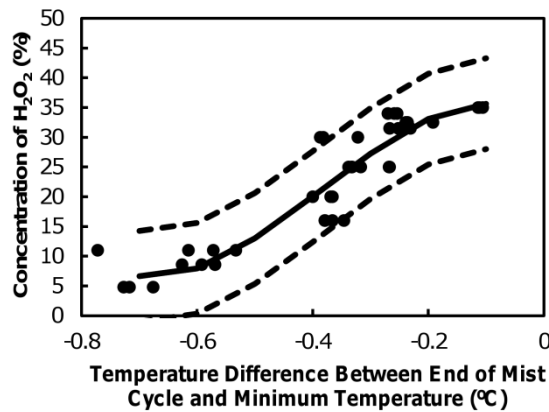


Figure 6-20 Concentration of hydrogen peroxide as a function of the time the minimum temperature was reached for 3 minute mist cycle. Solid line represents cubic regression and dotted lines represent 2-sigma confidence interval.

The same procedure was applied to the time to minimum data. The regression is described in Equation 6-8 and shown in Figure 6-21. The regression is more accurate with a coefficient of determination of 0.94 and a 2-sigma confidence interval of $\pm 5.4\%$ hydrogen peroxide.

$$conc = 4.52 \times 10^{-6}t^3 - 2.14 \times 10^{-3}t^2 + 1.39 \times 10^{-1}t + 33.5 \quad \text{Equation 6-8}$$

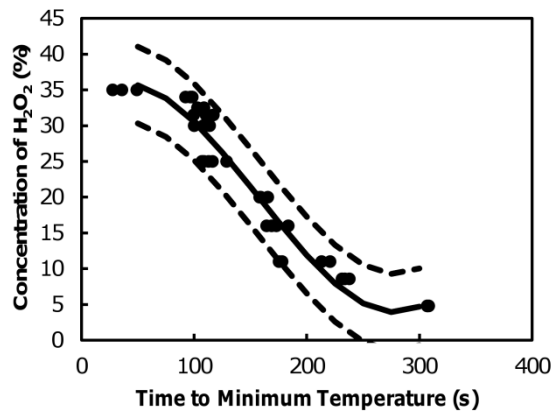


Figure 6-21 Concentration of hydrogen peroxide as a function of temperature difference between the end of the mist cycle and minimum temperature reached after 3 minute mist cycle. Solid line represents cubic regression and dotted lines represent 2-sigma confidence interval.

As with the two minute data, the concentration of hydrogen peroxide could also be calculated by combining the minimum temperature regression and the time to minimum regression, with the results being averaged. The calculated hydrogen peroxide concentration (*conc*) was regressed against actual hydrogen peroxide concentration (*T*) to determine how accurately the averaged data predicts hydrogen peroxide concentration. The regression described in Equation 6-9, and shown in Figure 6-22, is linear and predicts that the actual and calculated concentrations are approximately equal. The relationship has a coefficient of determination of 0.93, which is the same as the time to minimum, and the 2-sigma confidence interval of $\pm 5.3\%$ hydrogen peroxide, which is slightly less than the time-to-minimum regression. This suggests that while combining measurements for the three minute data greatly improves on the temperature at minimum data, there is no real improvement over the time-to-minimum data. This result would also suggest that concentration determination is more effective with a shorter mist cycle (for example two minutes).

$$conc = 1.03T - 0.76$$

Equation 6-9

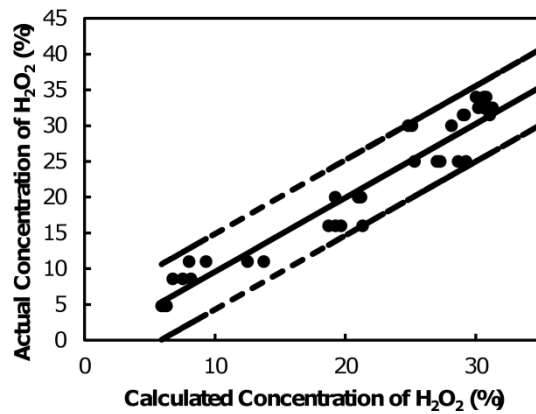


Figure 6-22 The actual concentration of hydrogen peroxide as a function of the average calculated hydrogen peroxide using the regressions for time to minimum temperature and difference between end of cycle temperature and minimum temperature for 3 minute mist cycles.

6.2.8 Comparison of 2 and 3 Minute Cycles to Shorter and Longer Cycles

The sensor was also run in 35% hydrogen peroxide in mist cycles which were 30 seconds long and 4 minutes long, Figure 6-23. The 30 second mist cycle is not long enough for the sensor to reach the equilibrium, and due to the relatively small quantity of hydrogen peroxide from the mist cycle, the sensor reaches a minimum within seconds of the mist cycle being turned off. The 4 minute data does reach equilibrium, however, the minimum after the mist pulse is not clear. It is possible that since there is more hydrogen peroxide, relatively, on the RTD, it is able to produce enough energy from decomposition to overwhelm the evaporation signal.

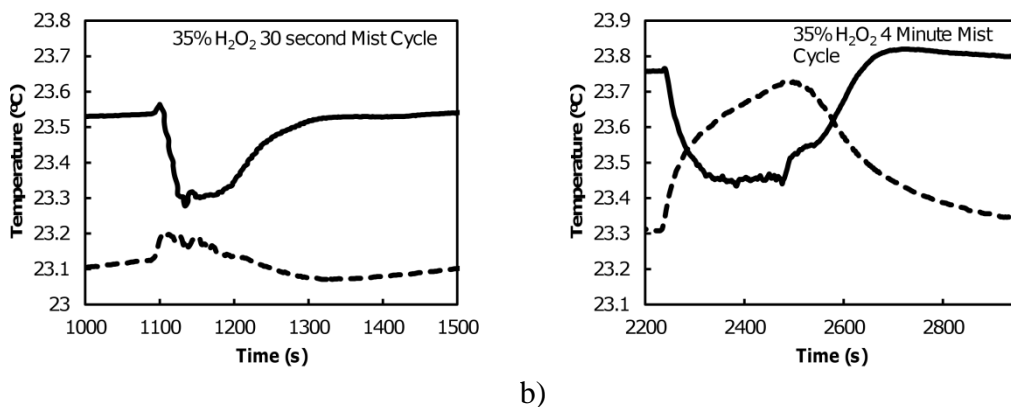


Figure 6-23 The RTD response to 20% mist cycle for 35% hydrogen peroxide with mist cycle length lasting a) 30 seconds and b) 4 minutes. Solid lines denote coated RTD and dotted lines denote uncoated RTD.

Figure 6-24 compares the difference in temperature between the uncoated and coated RTDs for the 30 second, 2, 3 and 4 minute data at 35% hydrogen peroxide. It can be seen that the temperature difference is similar for both 2 and 3 minutes, which is due

to the three minute data not having enough time between mist pulses to complete the evaporation, while the 30 second response is lower and 4 minute is higher. This is because the RTD does not reach equilibrium at 30 seconds.

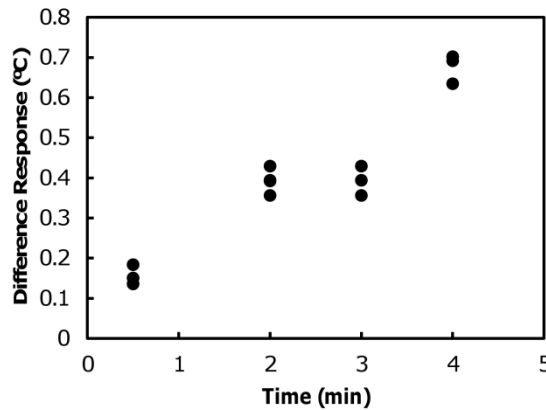


Figure 6-24 The difference in response between uncoated and coated RTDs at the end of the mist cycle for 35% hydrogen peroxide for different mist cycle times.

It may be possible to perform online measurements with 30 seconds or less, without the equilibrium, however, as the work stands now, two and three minute mist pulses appear to be best for determination of concentration of hydrogen peroxide in the mist. The four minute data acquisition is probably too slow for the proposed application. In addition, there is no evidence that a more accurate measurement could be made using a four minute mist pulse anyway.

6.2.9 Summary of Experiments Using Unheated RTDs

It was found in these experiments that an uncoated RTD heated up slowly in a mist flow, due to the slowly increasing temperature of the mist, whereas a coated RTD initially experienced a strong *decrease* in temperature under the same mist conditions. It is theorised that the decomposition energy produced by the hydrogen peroxide is enough to vaporise the high surface area droplets, and this vaporisation is enough to absorb all the decomposition energy and even to cool the sample. This continues after the mist is turned off, until the heat evolved by decomposition of the remaining hydrogen peroxide is sufficient to overcome the cooling effect due to vaporization. This then drives the RTD back to its starting temperature.

By simultaneously utilising an unheated coated and uncoated RTD, it was possible to ascertain several relationships between RTD response and concentration of

hydrogen peroxide in a mist pulse. Use of a coated RTD alone provided a linear relationship between hydrogen peroxide concentration and the difference in temperature of the RTD before and after mist pulses of two and three minutes duration for hydrogen peroxide concentrations of 5% to 25% hydrogen peroxide. The coefficient of determination in the case of a two minute mist pulse was 0.85 with a 2-sigma confidence interval of $\pm 6\%$. Similarly, in the case of the three minute pulse, a linear relationship was obtained between 0 and 25% hydrogen peroxide with a coefficient of determination of 0.91 and a 2-sigma confidence interval of $\pm 5\%$.

Another source of information was the difference signal obtained from the response of the uncoated and coated RTDs before and after the mist pulse. This response was linear from 10% to 35% hydrogen peroxide and had a coefficient of determination of 0.92 and a 2-sigma confidence interval of $\pm 5\%$, for a mist pulse of 2 minutes. This was a significant improvement over using just a coated RTD as it reduced uncertainty by almost 1% hydrogen peroxide concentration, and improved the range so that it could detect the hydrogen peroxide concentrations necessary in this project. No similar response could be found with the three minute data. It is theorised that this was due to the three minute measurement cycle having insufficient rest time between measurement cycles to reset the sensor temperatures to ambient.

In the phase after the mist pulse, other effects were found which showed correlation to hydrogen peroxide concentration. For example, by taking the time the coated RTD takes to reach a minimum (decomposition begins to overcome evaporation) and the temperature the RTD reaches at this point, it is possible to estimate hydrogen peroxide concentration. Individually, these two relationships are best described as 3rd order polynomials, with coefficient of determination of 0.97 and 0.98 respectively. The time to minimum data has 2-sigma confidence interval of $\pm 4.1\%$ while the temperature difference at the minimum has a 2-sigma confidence interval of $\pm 3.8\%$. Both these are improvements over the measurements during the mist pulse, however, by combining both sets of data it is possible to improve the estimate to within 2.8% hydrogen peroxide. In addition this sensor can be used to determine concentration from 0 to 35% hydrogen peroxide.

A similar method was applied to the three minute data. The data did not include water as the sensor temperature did not reach ambient in-between those test cycles,

unlike the case for the two minute data. The three minute data has less robust 3rd degree polynomial trends for time to minimum (0.94 coefficient of determination) and minimum temperature (0.87). The trends also have more error with confidence intervals of $\pm 5.4\%$ and $\pm 7.4\%$ hydrogen peroxide respectively. By combining the data sets the concentration can be estimated to within $\pm 5.3\%$ hydrogen peroxide. This is only slightly more precise than using the time data alone, in this case. It is unclear whether this increase in error for the three minute data is down to methodology or something intrinsic to the three minute mist run. In principle, that question could be answered by repeating the experiment using the automated test method developed for the two minute data and/or increasing the length of the measurement cycle to ensure that the sensors returned to ambient, but this is not necessary as use of the two minute mist pulse has the advantage of superior accuracy and speed.

A simple calculation showed that the response of the sensor will begin to flatten out at 35% hydrogen peroxide anyway, due to the reduction in rate of mist production at higher concentrations. This means that the sensor has an effective range from 0% to 35% hydrogen peroxide, which the mist response data appears to support.

The 35% hydrogen peroxide was also run with mist pulses of 30 seconds and 4 minutes. The 30 second data showed no equilibrium during the mist pulse but it may nevertheless be possible to use this data to determine concentration. This could be carried out as future work to determine how crucial it is for the hydrogen peroxide to reach equilibrium. The 4 minute data does reach equilibrium, however the post mist behaviour is different with a small minimum directly after the pulse. It is theorised that the extra mass of liquid deposited on the sensor tip is able to suppress the evaporation signal by having larger and harder to evaporate droplets of hydrogen peroxide. Using 4 minute mist pulses is not feasible in practice, however, as the project brief required a faster measurement cycle in any case. The only reason to investigate this would be if it gave a significant accuracy improvement.

A complete summary of the unheated mist sensors accuracy and precision can be found in Chapter 6.4.

6.3 Detection of Hydrogen Peroxide Concentration in Mist Using Heated RTDs

The above techniques for detection, though functional, are not ideal. They are slow, require the accurate measurement of small temperature differences on the order of 0.1K, and will require some means of refreshing the sensor to provide a reliable starting condition. A possible solution to these problems is to use a heated sensor which should provide a stable reading relatively quickly and prevent build up of hydrogen peroxide. The theory is that if an uncoated RTD and coated RTD are put into a mist flow, and connected to an electrical circuit that maintains them at a constant temperature, then the coated RTD will draw less power, as the decomposition on the surface is producing energy to vaporise the mist droplets, as was demonstrated in Chapter 5.2.5.

The RTDs used for this section were RTDs A and B, and they were set to a constant temperature of 105°C. RTD A was used as the coating was superior to the coating on C in a repeatable manufacturing sense, and RTD B was used as it was the same RTD that A was based on, making a better control sensor.

6.3.1 Method of Detection of Hydrogen Peroxide Concentration in Mist Using Heated RTDs

The RTDs were configured into the same set-up used in Chapter 5.2.4, with the temperature of the RTD (and therefore resistance of the RTD) being set. In this case, the temperature is set at 105°C which corresponds to a resistance of 140.43 Ω . The RTD supply was measured in millivolts and converted to watts and joules in processing. This represented the voltage (and subsequently power and energy) which needed to be drawn to keep the RTD at this temperature.

The air flow rate was set to 7.5 L/min, and as with the previous experiments, the air flow was kept on and constant the whole time. The program began recording for several seconds before the mist was turned on, so that the RTD response was relatively stable. The mist was then turned on for 3 minutes before being turned off. The data was recorded until the RTDs began to approach the initial readings. Experiments were run using 18.2M Ω MilliQ water, 10%, 20%, 30%, 35% and 40% hydrogen peroxide, and all of these experiments were run using transducer duty cycles of 7.5%, 10%, 15%, 20%,

25% and 30%. The hydrogen peroxide concentration was confirmed using iodometric titration, the method of which is described in Chapter 4.2.

These experiments were run ten times each.

6.3.2 Results of Detection of Hydrogen Peroxide Concentration in Mist Using Heated RTDs

The response for both coated and uncoated heated RTDs is similar in shape, and there are no major differences in the shape of the responses between water and hydrogen peroxide as seen in Figure 6-25.

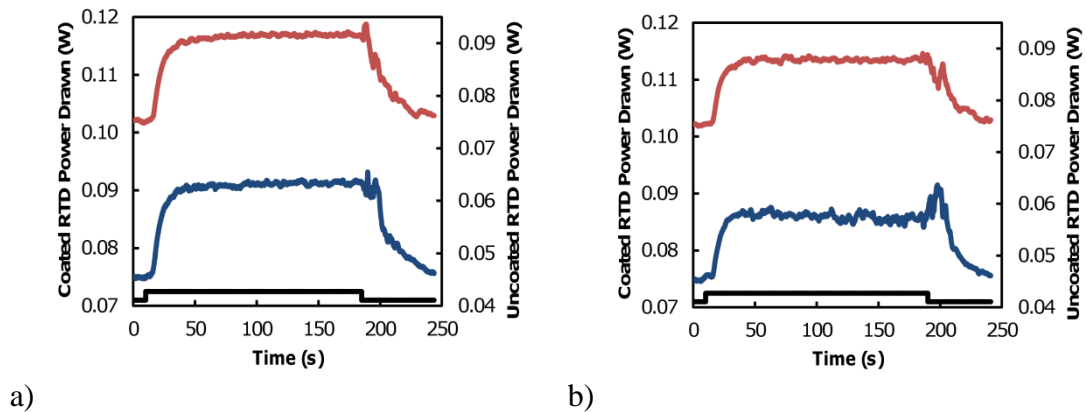


Figure 6-25 The response of coated (blue line) and uncoated (red line) RTDs in a mist of a) water and b) 40% hydrogen peroxide. The black line shows the mist pulse (the step is when the mist is on). The mist duty cycle is set to 20%.

The energy was calculated by using the LABView program to determine the average stable power draw before the mist is turned on and the average power draw from the time it stabilises after the mist hits the RTD until the nebuliser is turned off. This time period was taken as a nominal 120 seconds as the time was slightly different for each measurement due to the different mist densities. Using this it was possible to determine the energy drawn by the RTD. Figure 6-26 shows the average energy drawn by both the uncoated and coated RTDs during the time that the mist is on.

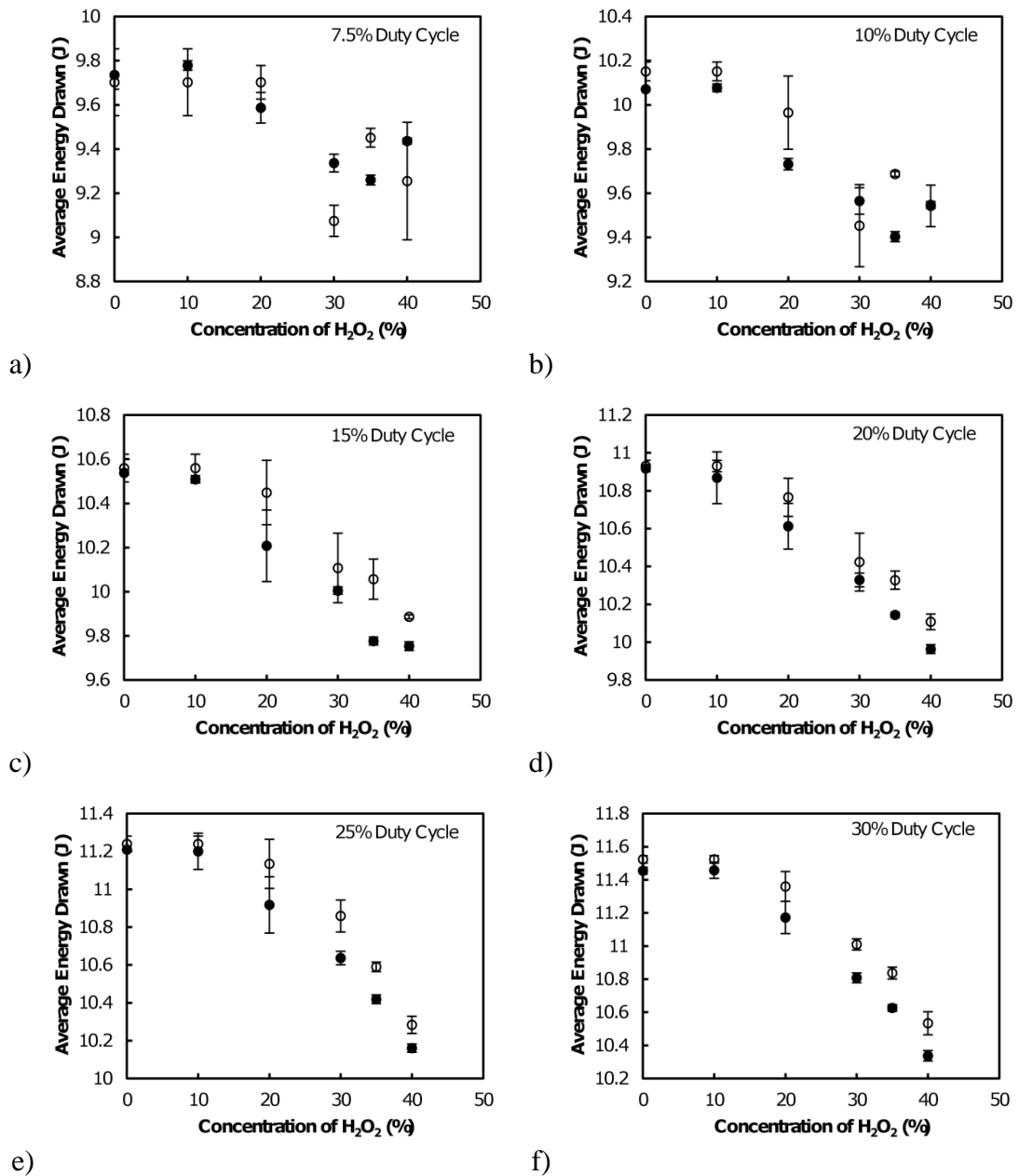


Figure 6-26 The average response of the uncoated (○) and coated (●) RTDs to different concentrations of hydrogen peroxide at duty cycles a) 7.5, b) 10%, c) 15%, d) 20%, e) 25% and f) 30%. Error bars represent 1 standard deviation.

There is insufficient difference in power drawn at the lower concentrations of hydrogen peroxide (below 10%) to provide a usable signal. However, there is a clear trend for concentrations of greater than 10% hydrogen peroxide. This indicates that insufficient decomposition energy is produced by 0 to 10% hydrogen peroxide mists to make a real difference signal. At low duty cycles (7.5% and 10%) the trend is unclear, as the response decreases to 35% hydrogen peroxide before increasing at 40%, though there is significant error in these measurements. This is because the mist itself is not as

dense, which may introduce more randomness, which will be seen as an increase in error. The error reduces as the duty cycle increases (at least in the higher concentrations), which seems to support that the mist increasing in density decreases randomness and provides a better equilibrium. In addition, as the duty cycle increases, the difference between the coated and uncoated RTDs increases as the error begins to become reduced by the better equilibrium.

The data suggests that both the coated and uncoated heated RTD are, in the first instance, most sensitive to mist flux. Figure 6-27 shows the average response of the uncoated and coated RTDs to mist flux, which is determined by the calibration curve seen in Figure 6-3.

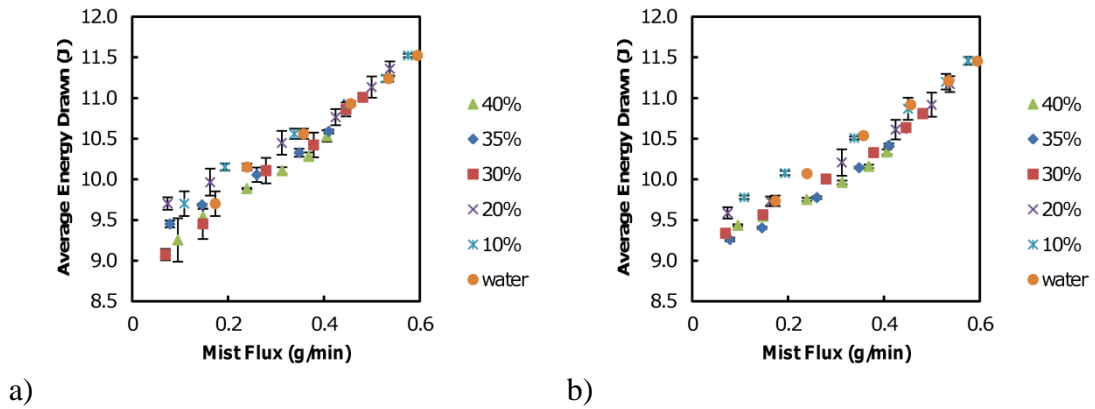


Figure 6-27 The average energy drawn against the mist flux by the a) uncoated and b) coated RTDs at different concentrations of hydrogen peroxide. The error bars represent 1 standard deviation.

The data shows that as mist flux increases, the response becomes less scattered. The data appears to have a slight inflection and so quadratic regression was applied (as described in Chapter 4.1.3). The mist flux was taken as the independent variable while concentration was taken to be $conc$ and the energy response was denoted as Q . The regression for the uncoated RTD and coated RTDs can be seen in Equation 6-10 and Equation 6-11 respectively.

$$\begin{aligned}
 \text{Mist Flux} = & -0.685 + 0.101conc - 9.96 \times 10^{-4}Q - 5.89 \times 10^{-2}conc^2 \\
 & + 1.44 \times 10^{-2}Q^2 - 1.95 \times 10^{-2}conc \cdot Q + 1.77 \\
 & \times 10^{-4}conc^2Q + 9.03 \times 10^{-4}conc \cdot Q^2 - 6.57 \\
 & \times 10^{-6}conc^2Q^2
 \end{aligned}
 \tag{Equation 6-10}$$

$$\begin{aligned}
 \text{Mist Flux} = & -3.17 - 0.117\text{conc} + 1.79 \times 10^{-4}Q + 4.03 \times 10^{-1}\text{conc}^2 \\
 & - 6.50 \times 10^{-3}Q^2 + 2.28 \times 10^{-2}\text{conc} \cdot Q - 2.31 \\
 & \times 10^{-5}\text{conc}^2Q - 1.11 \times 10^{-3}\text{conc} \cdot Q^2 \\
 & + 1.18 \times 10^{-6}\text{conc}^2Q^2
 \end{aligned}
 \tag{Equation 6-11}$$

An analysis of variance of both relationships showed that both equations had *p*-values of 0.51 (larger than 0.05) and therefore, the different in the variation that the higher orders of the relationships picked up was not significant compared to the variance of the residuals.

The mist flux was then calculated using these regressions and compared to the actual mist flux. This data was put into a linear regression (as described in Chapter 4.1.1) and the results can be seen in Figure 6-28.

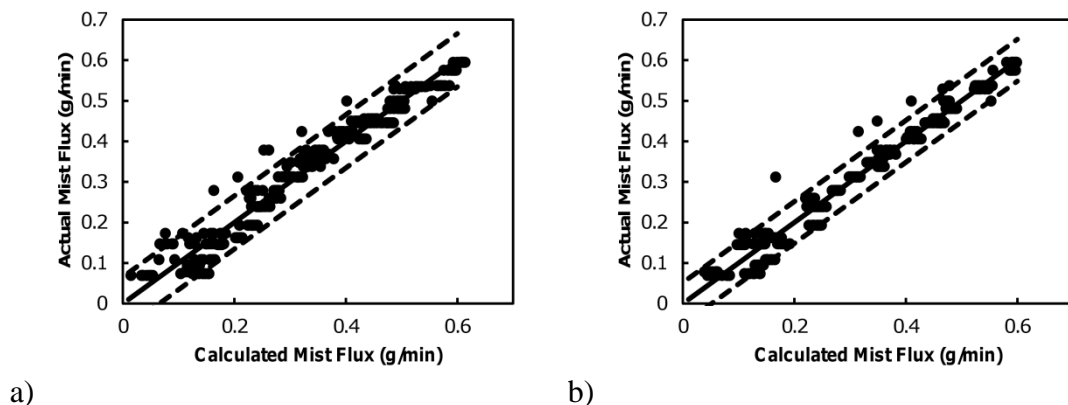


Figure 6-28 The actual mist flux from the calibration against the mist flux calculated from the regression of the energy drawn and hydrogen peroxide concentration for the a) uncoated and b) coated RTDs. Solid line represents the regression and the dotted lines represent a 2-sigma confidence interval.

Both regressions have a gradient of 1 and an intercept of 0, indicating that the calculated data and actual data are the same. Both regressions are strong with that from the uncoated RTD having a coefficient of determination of 0.96, while that of the coated RTD had a coefficient of determination of 0.97. The uncoated RTD has a 2-sigma confidence interval of ± 0.065 g/min and the coated RTD has a 2-sigma confidence interval of ± 0.052 g/min. Under these circumstances it appears that there is no major difference between using the uncoated and coated RTDs to determine the mist flux, however, there is slightly more precision with the coated RTD. This is possibly due to the hydrogen peroxide being constantly decomposed to water, which is easier to vaporise than hydrogen peroxide. This may produce a more constant signal, whereas the

uncoated RTD must vaporize the unaffected mist, which can create more uncertainty as the time taken to vaporise the droplets increases.

It was anticipated that a measure for the concentration of hydrogen peroxide would be obtained by subtracting the uncoated RTD signal from the coated RTD signal. Figure 6-29 shows the average difference of energy between the uncoated and coated RTDs.

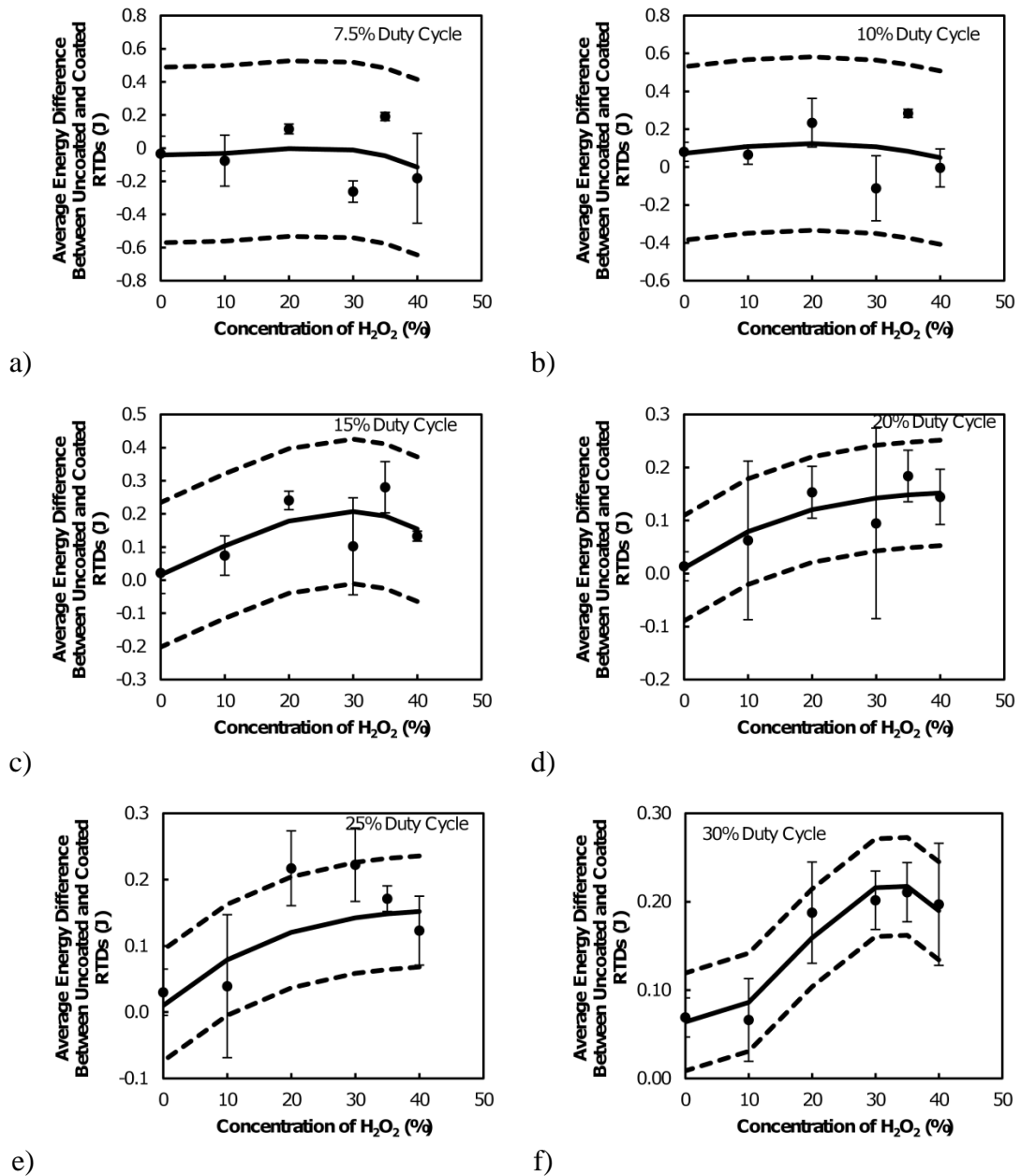


Figure 6-29 The average difference between energy drawn by the uncoated-coated RTDs for different concentrations of hydrogen peroxide for duty cycles of a) 7.5%, b) 10%, c) 15%, d) 20%, e) 25% and f) 30%. The error bars represent 1 standard deviation. Solid lines are the polynomial regressions of the concentration of hydrogen peroxide and difference in energy drawn and the dotted lines represent the 2-sigma confidence interval of the regression.

The data for the 7.5%, 10% and 15% duty cycles show no real trend, due to the errors in the measurement being as big as or bigger than the measurements themselves. The trends become stronger for the 20% (r^2 of 0.76), 25% (r^2 of 0.90) and 30% (r^2 of 0.93) duty cycles, however, the trends displayed are only for the average difference not all the difference points. The standard deviation of the averages cannot all be contained by the 2-sigma confidence intervals of the predicted trends. In addition to this, average data and the standard deviation overlaps for most of the measurements, which suggests that the scheme using heated RTDs is incapable of predicting hydrogen peroxide concentration from the difference signal between a coated and uncoated RTD, best illustrated by Figure 6-30.

Figure 6-30 shows the average difference signal against the mist flux. The difference signal does not respond to the mist flux for mist fluxes of about 0.2 g/min or greater, which suggests that if only the sensor can be improved to increase the signal, the heat mist sensor could in principle be used to determine the mist density and concentration.

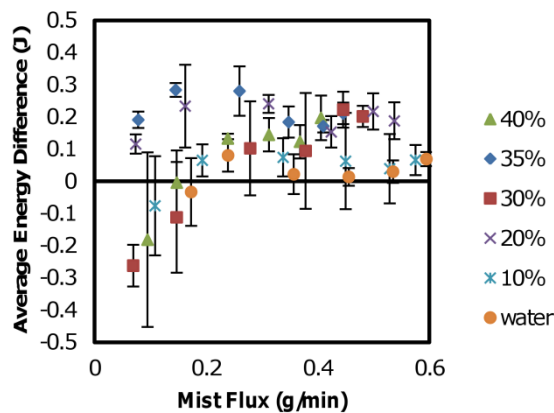


Figure 6-30 The average drawn energy difference between uncoated and coated RTDs against the mist flux at different concentrations of hydrogen peroxide. The error bars represent 1 standard deviation.

A possible improvement which could be made is to use a more active catalyst to improve the decomposition signal from the coated sensor. Two possibilities are MnO_2 powder which has been used at other parts of this study, or porous platinum films of greater porosity. It was shown in Chapter 4.3 that it is possible to deposit a high surface area porous platinum film, which has a sponge-like conformation.

At one point the heated sensor was tried at a lower temperature and a higher temperature to determine what effect that would have (similar to the tests performed on individual droplets in Chapter 5.2.5). The sensor was set to 80°C for one of these and 130°C for another and a 20% duty cycle of 35% mist was run past the sensor. The 80°C sensor had an average difference between the RTDs of 4 mV, while the 130°C had a difference between readings of 2 mV both of which were smaller than the 105°C data seen above. This suggests that there is probably an optimum temperature somewhere between 80 and 130 °C.

6.3.3 Summary of experiments using Heated RTDs

It was not possible to determine the concentration of a stream of hydrogen peroxide mist using heated uncoated and coated RTDs. There were differences between the RTDs, however, the differences were too small and the error was too high, which produced a response which was neither precise, nor accurate.

It may be possible to obtain a signal by using a more active catalyst, such as MnO₂ powder (deposited in a consistent manner) or a higher surface area sponge of porous platinum. There was an attempt to determine whether using a lower or higher set point temperature for the RTD would improve the signal, however, it was shown to yield no improvement on the difference between the signals.

Despite the heated sensor having little utility as a concentration sensor in this current configuration, it has shown a response to mist flux using just the response of the uncoated or coated RTD to different concentrations of hydrogen peroxide during different duty cycles. By applying a multiple quadratic regression to the data, the mist flux could be determined by knowing the concentration of hydrogen peroxide and energy response. It was determined that there was a linear relationship between the actual mist flux and the calculated mist flux, indicating that the calculated response was very similar to the actual response. The trend was very strong with a coefficient of determination of 0.96 for the uncoated RTD and 0.97 for the coated RTD. The coated RTD was found to have a better precision with a 2-sigma confidence interval of ± 0.052 g/min compared to ± 0.065 g/min. It was believed that this improvement in precision was due to less error in the coated RTD measurement as predominantly water was being

vaporised after decomposition as opposed to the uncoated sensor which had minimal decomposition and was vaporising different concentrations of hydrogen peroxide.

It may be possible to combine both the mist density sensor and concentration sensor into one by measuring using a RTD with a much smaller thermal mass to measure concentration while the mist is flowing, before increasing the temperature to enable the mist density sensing, and to burn off the droplets during the rest cycle. This would require much more work. It is also unlikely as the experiments in Chapter 4.5 (not included in the thesis as they are not relevant) revealed that even RTD C took approximately 4 minutes to cool back to the starting temperature after it was heated by increasing applied voltage.

6.4 Overall Summary of Mist Sensor Experiment

Table 6-1 Summary of calorimetric RTD performance as a mist sensor

Sensor	Coefficient of Determination (r^2)	2-Sigma Confidence Interval	Effective Range
Single Coated RTD 2 Minutes	0.85	$\pm 5.8\%$	5% hydrogen peroxide to 35% hydrogen peroxide
Single Coated RTD 3 Minutes	0.91	$\pm 5.2\%$	Water to 25% hydrogen peroxide
Difference Between RTDs During Mist 2 minutes	0.92	$\pm 5.0\%$	10% hydrogen peroxide to 35% hydrogen peroxide
Time To Minimum 2 Minutes	0.97	$\pm 4.1\%$	Water to 35% hydrogen peroxide
Temperature Difference To Minimum 2 Minutes	0.98	$\pm 3.8\%$	Water to 35% hydrogen peroxide
Combined Time and Temperature 2 Minutes	0.99	$\pm 2.8\%$	Water to 35% hydrogen peroxide
Time To Minimum 3 Minutes	0.94	$\pm 5.4\%$	4.8% hydrogen peroxide to 40% hydrogen peroxide
Temperature Difference To Minimum 3 Minutes	0.87	$\pm 7.4\%$	4.8% hydrogen peroxide to 40% hydrogen peroxide
Combined Time and Temperature 3 Minutes	0.93	$\pm 5.3\%$	4.8% hydrogen peroxide to 40% hydrogen peroxide
Mist Flux Sensor- Uncoated	0.96	± 0.065 g/min	0 g/min to 0.6 g/min
Mist Flux Sensor- Coated	0.97	± 0.052 g/min	0 g/min to 0.6 g/min

Utilising uncoated and coated RTDs without heating, it was possible to estimate the concentration of hydrogen peroxide to about $\pm 3\%$. This investigation demonstrated that the hydrogen peroxide and water vaporises on the surface of the coated RTD, while the uncoated RTD slowly increases in temperature due to heating in the mist from the nebuliser. This was somewhat counterintuitive from the previous data as it was expected that the coated RTD would heat up. The explanation for this phenomenon was that the mist droplets were so much smaller and had such greater surface area than the previous liquids studied, and due to this the droplet was much more susceptible to vaporisation. When the decomposition occurs, the energy produced is overridden by the energy used for vaporisation of droplets. This is kept somewhat constant during the mist pulse by the stream of incoming mist particles, enabling a type of pseudo-equilibrium to occur. When the mist is turned off, the vaporisation continues until enough of the liquid is gone to allow the decomposition to heat the RTD back to its starting temperature.

During the mist pulse, it was possible to determine the concentration of hydrogen peroxide between 5% and 25%, during a two minute mist pulse, and water and 25% during a three minute mist pulse by determining how much the temperature of the coated RTD dropped during the mist pulse. The two minute data could be improved upon by taking a difference signal between both RTDs. This provided a signal with a greater accuracy, precision and range as it allowed the detection of hydrogen peroxide from 10% to 35%. This signal could not be reliably extracted from the three minute data, which may be due to the measurement cycle having terminated before the sensors has returned to a dry state.

After the mist pulse, it was determined that the length of time that the coated RTD took to reach a minimum temperature and the difference between that minimum temperature and the temperature just before the mist was turned off could both be related to hydrogen peroxide concentration through a polynomial regression. For two minute data both data sets show excellent accuracy and precision, while the three minute data shows a relationship that is less accurate and precise than the three minute data, probably due to the issue mentioned above. The two minute data was combined into a single linear regression which was highly accurate ($r^2=0.99$) and precise to within 2.8% hydrogen peroxide, which was better than any of the other calorimetric sensors attempted in this project. The two minute data had a predictive range for between 0 and

35% hydrogen peroxide while the three minute data had a predictive range from 5% to 40% hydrogen peroxide.

In general, the calorimetric sensor saturated at about 35 to 40% hydrogen peroxide. This was shown to be due to the fact that the flux of the hydrogen peroxide mist decreased at high concentrations (due probably to the increase in surface tension and density of the fluid). The reduced flux caused an associated reduced enthalpy of the decomposition reaction.

It has been determined that hydrogen peroxide mist flux can be connected to two main variables, hydrogen peroxide concentration and the duty cycle of the nebuliser. Temperature in the cup should also have an effect, however in this case, temperature does not vary enough to make a significant effect on the flux of mist. An increase in duty cycle, increases the mist flux, while an increase in concentration of hydrogen peroxide, causes a decrease in mist flux as the surface tension and density of the hydrogen peroxide increase with concentration. In the tests of unheated sensors the duty cycle was fixed, as a device which uses this sensor would be expected to operate at a fixed duty cycle. This means that as the concentration of hydrogen peroxide increases, the mist flux will decrease and the response of the sensor will decrease, as described above.

Thirty second and 4 minute data was also trialled. Four minute data has no minimum in temperature for the measurement cycle used as too much liquid is deposited on the sensor tip to evaporate and/or react in the available time. A longer drying cycle would no doubt have solved this problem but would have been impractical as the sensor needs to respond quickly. The 30 second data shows no equilibrium, just a straight drop in temperature until the sensor begins to burn off liquid. It may be possible to use this length of mist pulse in a sensor, and it should not be ruled out yet.

Actually, the mist pulse used in Nanosonic's commercial product is 14 seconds, so none of the schemes described above is suitable for industrial implementation. One possible option to increase the speed of response is to heat the RTDs and calculate a temperature difference between the two. This was performed at several duty cycles for several hydrogen peroxide concentrations. The low duty cycles showed more error, which was believed to be because the mist was not in equilibrium. It was not until 20%

to 30% duty cycles were applied that both sensors showed a reasonable response. However, the difference signal was not strong and showed no clear trend due to the high noise of the data. It is postulated that the sensor could be improved using a more active catalyst such as MnO_2 or the sponge like porous platinum described in Chapter 4.3. Decreasing and increasing the temperature of the heated RTDs did nothing to improve the signal. Nevertheless, this type of sensor has promise as a means of determining mist flux. The coated RTD was more slightly more accurate and had less error in this regard, which was believed to be due to the decomposition improving evaporation of droplets, leaving less random evaporation.

Chapter 7 Physical Optical Sensor

The hydrogen peroxide mist is quantifiable using calorimetric means, however, there are some drawbacks to those techniques, such as the time it takes to make a measurement. In addition, the calorimetric sensor is highly susceptible to fluctuations in the mist flux. It may be possible to improve upon this using an optical sensor based on the different physical characteristics of hydrogen peroxide and water. Two such properties in which there is difference between hydrogen peroxide and water are refractive index and absorption of light.

This chapter will discuss an investigation into the feasibility of using one or both of these properties to quantify the concentration of hydrogen peroxide.

7.1 Refractometric Sensor

Precious metal nanoparticles have been used in refractometric sensors due to their higher Q-factors (see Chapter 3.1.3) and ability to tune their resonant wavelength. Gold nanoparticles were chosen here due to their optical properties and gold's chemical inertness. However, it has been observed that gold nanoparticles do interact with hydrogen peroxide, and this is something which must also be tested.

7.1.1 Theoretical Refractometric Nanoparticle LSPR Response to Hydrogen Peroxide

As explained in Chapter 3, the surface plasmon resonance of nanoparticles can be used to determine changes to the refractive index of a medium. This is due to the fact that the total resonance of a particle is based upon the properties of both the particle and the surrounding medium. Notably, changing the refractive index of the medium should result in a change in resonance of the particle (since the particles' properties are kept constant in this circumstance). It is then possible to determine a change in refractive index due to a resonance change, and from here determine the concentration of a material based on its refractive index.

Work was done together with colleagues to determine the best geometry for a refractive index sensor. The results have been published in *Sensors based on monochromatic interrogation of a localised surface plasmon resonance* by Kealley et al. [143] with the conclusion of that work being that gold nanorods were the best choice

of a refractometric sensor when using a single wavelength to determine refractive index changes. The advantage of using a single wavelength sensor is simplicity, whereas previously sensors were generally required to measure over a range of wavelengths to determine how much the peak shifted [143]. Gold nanorods were determined to be a good shape as the shift, and hence change in intensity at a single wavelength, was larger than the other geometries and the peak was also sharper, providing more sensitivity was larger than the other geometries measured and the peak was sharper, providing more sensitivity[143].

This approach was then tried as a hydrogen peroxide concentration sensor, first by testing the response to well-known substances, and then to hydrogen peroxide.

7.1.2 Method of Investigation of Refractometric Nanoparticle Sensor

The principle of the refractometric sensor was tested using gold nanorods in a colloidal suspension, stabilised by CTAB. The ability of the rods to function as a refractometric sensor was characterised in solutions of sucrose and glycerol, before being tested in hydrogen peroxide.

Gold nanorods were obtained from a previous PhD project *Selective targeting and thermal destruction of live cells using antibody functionalised gold nanoparticles* [170] and their absorbance between 200 and 1100 nm was characterised using a Shimadzu UV Mini 1240 spectrophotometer. All following absorbance measurements were measured in this range. The gold nanorods were loaded into a plastic cuvette with a 1 cm path length for the measurement. 0.5 mL of gold nanorods was diluted by 3.5 mL of MilliQ water to prevent absorbance from exceeding the absorption limits of the spectrophotometer. All measurements were conducted in the same plastic cuvette. In addition, the absorbance of a 35% (w/w) hydrogen peroxide (diluted 1:3 by MilliQ water), CTAB mixture and a gold seed solution were also taken.

To test the potential for gold nanoparticles as a refractometric sensor, various concentrations of sucrose and glycerol were added to the gold nanoparticles and the absorbance of the resulting solution was recorded, with the peak absorbance of the different concentrations of sucrose and glycerol being compared to each other.

Sucrose was prepared by dissolving 100 g of sucrose in 100 g of MilliQ water, with 10 g of sucrose added at a time and agitated until sucrose was dissolved, leaving a stock solution of 50% (w/w). Sucrose/gold nanorod solutions were made using 0.875 mL, 1.75 mL, 2.625 mL and 3.5 mL of sucrose. Each solution contained 0.5 mL of gold nanorods and any remainder of the 4 mL volume was filled with MilliQ water.

Glycerol was taken from a stock of 99.5% (w/v). On the recommendation of a colleague, ammonium bromide powder was added only to the glycerol/gold nanorod solutions to allow the two solutions to mix. The effect of the ammonium bromide on the refractive index was negligible due to the low mass used (0.3% (w/w)), and in addition, all solutions would have been similarly affected. Glycerol concentrations were made using the same volumes as described in the previous paragraph.

All sucrose and glycerol absorbance measurements were base-lined against the plastic cuvette filled with MilliQ water. The concentrations of sucrose and glycerol were determined by obtaining the density of each stock (in the case of glycerol it was given) and using this, determining the mass of sucrose or glycerol in each volume added. The remainder of the volume was water and was taken as 1 mL being equal to 1 g. The weight of the nanorods is discounted since there are so few, with the neglected figure being in the nanograms range.

The effect of hydrogen peroxide on the gold nanorods was tested by combining 0.5 mL of gold nanorods with, 0.5 mL of 35% (w/w) hydrogen peroxide, and diluting this mixture with 3 mL of MilliQ water, and taking the absorbance of the resulting mixture.

7.1.3 Results of Investigation of Refractometric Nanoparticle Sensor

In this study, the actual magnitude of the absorbance was disregarded, as only the wavelength at which the absorbance is at a maximum is necessary.

Figure 7-1 shows the absorbance of the nanorods used. There are 3 peaks, at wavelengths 292 nm, 534 nm and 589 nm. The 292 nm peak is most likely due to ascorbic acid used to make the rods or to absorption of the ultraviolet by the cuvette used, while the 534 nm and 589 nm peaks are the transverse and longitudinal plasmon

peaks of the nanorods respectively. The main peak of interest (due to its higher sensitivity) is the longitudinal peak, which is initially at 589 nm.

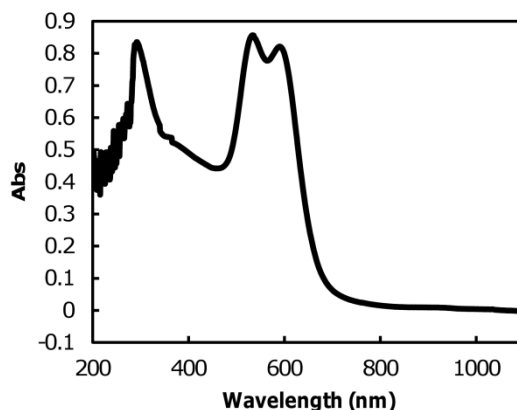


Figure 7-1 The absorbance spectrum of the gold nanorods used.

The shift in the longitudinal peak can be seen in Figure 7-2, which shows the absorbance of the nanorods in different concentrations of sucrose and glycerol solutions and MilliQ water.

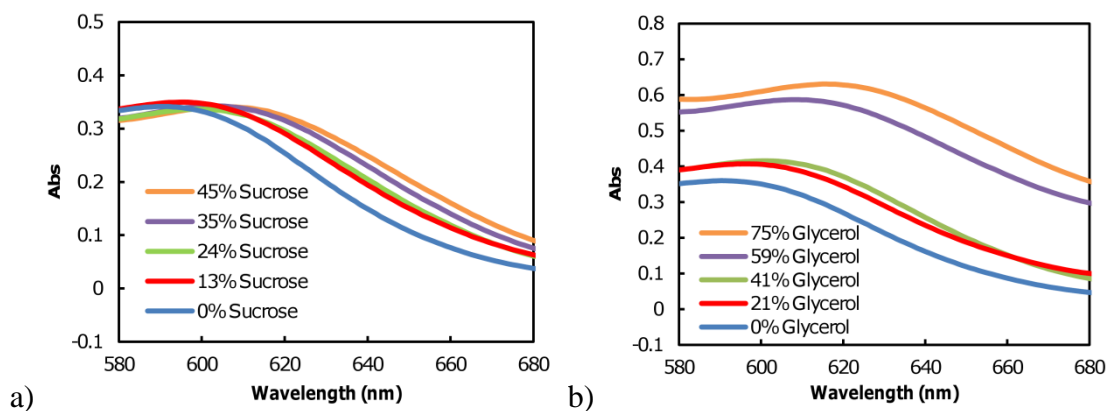


Figure 7-2 The absorbance spectra of gold nanorods transverse peak (589) and surrounding area in different concentrations of a) sucrose and b) glycerol.

By plotting the wavelength that the peak occurs at for each concentration of sucrose and glycerol, a linear relationship can be determined, which can be seen in Figure 7-3.

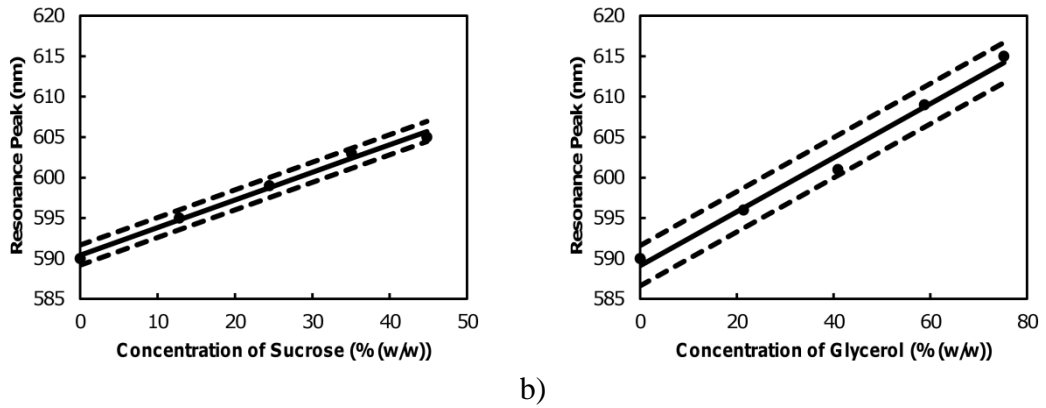


Figure 7-3 The relationship between the position of the gold nanorods' longitudinal peak and the concentration of a) sucrose and b) glycerol. Solid line denotes linear regression while 2-sigma confidence interval is described by the dotted lines.

The linear regression was performed using the method outlined in Chapter 4.1.1. Both the position of the peak against the concentration of sucrose and glycerol showed linear relationships, which are very similarly accurate, however the sucrose relationship showed a greater precision (coefficient of determination 0.99 for both, and a 2-sigma confidence interval of 1.24 nm for sucrose as opposed to 2.5 nm for glycerol. This equates to an error of $\pm 3.6\%$ and 7.4% respectively).

By taking the concentration (C) of sucrose and glycerol together, Equation 7-1 and Equation 7-2, as the function of the resonance peak position (λ_{res}) it is possible to determine the gold nanorods' response as a sensor in both liquids:

$$C = 2.91\lambda_{res} - 1716 \quad \text{Equation 7-1}$$

$$C = 2.96\lambda_{res} - 1743 \quad \text{Equation 7-2}$$

This indicates that the gold nanorods have a resolution of 2.9%/nm and 3.0%/nm in sucrose and glycerol respectively. This shows that the concentration of an analyte can be measured using refractive index as an intermediate measurement. Given that the refractive indices of sucrose and glycerol are known, the sensor's overall response and sensitivity to refractive index (RI) can be determined with response to the position of the resonance peak (λ_{res}), seen in Equation 7-3.

$$RI = 4.2 \times 10^{-3}\lambda_{res} - 1.2 \quad \text{Equation 7-3}$$

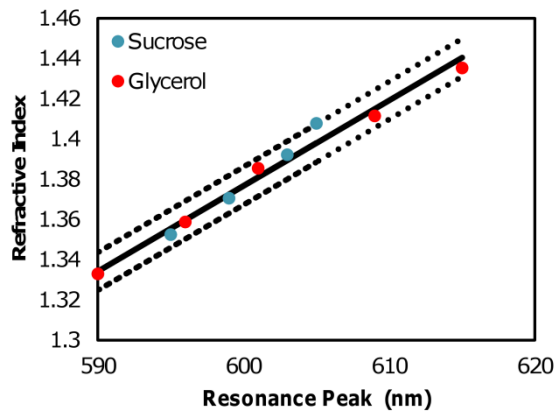


Figure 7-4 The recorded peak shift for different refractive indices of both sucrose and glycerol. Solid line represents linear regression, while dotted lines represent 2-sigma confidence interval.

Figure 7-4 shows the refractive index measured as a function of peak shift. The resulting curve displays high linearity, with a coefficient of determination of 0.98, and a small 2-sigma confidence interval of ± 0.0095 RIU. The sensitivity of the gold nanorods as a sensor is 0.0042 RIU/nm. This sensitivity should be more than adequate to determine the concentration difference between water and 35% hydrogen peroxide, however, it may lack sufficient precision to determine the exact concentration.

The sensor was tested as a single wavelength sensor against both concentration and refractive index at a wavelength of 621 nm (this was the wavelength with the most change between absorbances for different concentrations) for sucrose and glycerol. In this case, since these measurements were base-lined against water, glycerol showed more absorbance across the range (as shown in Figure 7-2 b). A crude estimate was made to normalise the glycerol measurements to water around the peak area. The relationship between absorbance and concentration for sucrose and glycerol can be seen in Figure 7-5.

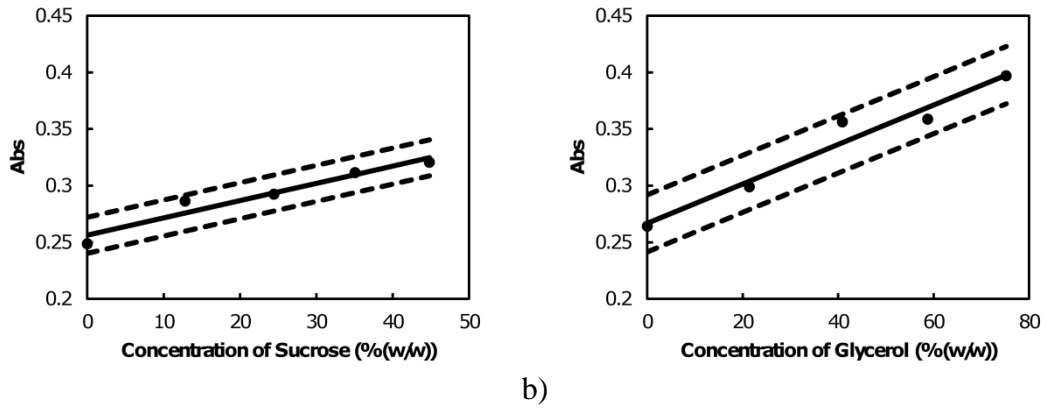


Figure 7-5 The absorbance measured at a wavelength of 621 nm for differing concentrations of a) sucrose and b) glycerol.

These relationships are strong with a co-efficient of determination of 0.94 for sucrose and 0.96 for glycerol. However, these are much less precise than using the peak wavelengths, with 2-sigma confidence intervals of $\pm 10\%$ and $\pm 14\%$ respectively.

Following from this, the data was combined to determine the response to refractive index, Figure 7-6.

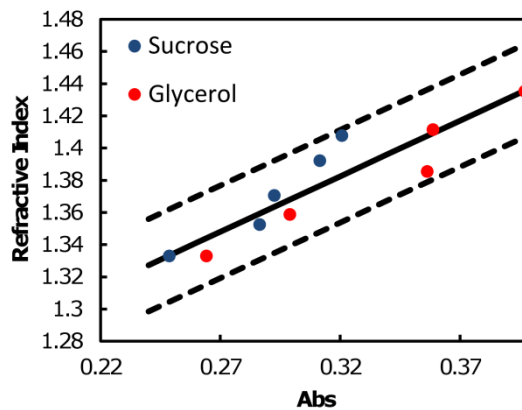


Figure 7-6 The recorded absorbance for different refractive indices of both sucrose and glycerol at a wavelength of 621 nm. Solid line represents linear regression, while dotted lines represent 2-sigma confidence interval.

This relationship is much weaker than the resonance peak data (co-efficient of determination 0.85 and 2-sigma error of $\pm 2.9 \times 10^{-2}$ RIU). A possible source of this problem is errors from the base-lining of glycerol (base-lining is less of an issue in using this in a water hydrogen peroxide mixture, and both datasets show strong linearity independently). However, another larger issue is that the peaks need to be sharpened by optimising the nanorods, and this is likely causing the increase in error, and loss of

sensitivity. This is something to be considered when creating the sensor, but for now it is just a confirmation of principles.

With the characterisation of the nanorods response done, it was possible to use the nanorods to determine whether hydrogen peroxide concentration could be determined in the same manner. However, when 0.5 mL of 35% (w/w) hydrogen peroxide was added to 0.5 mL of the gold nanorod solution, the colour noticeably changed to a lighter purple. The solution was diluted and allowed to sit for a time, and eventually turned to a yellow colour. The solution was checked for absorbance and the result can be seen in Figure 7-7.

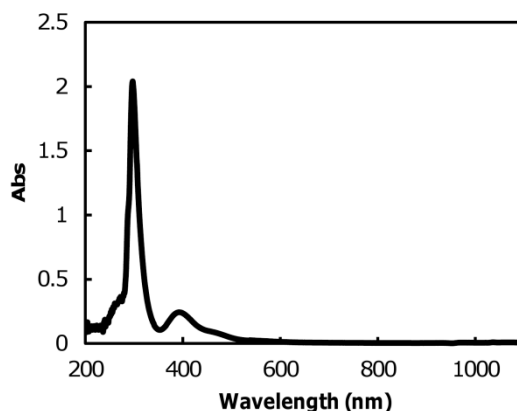


Figure 7-7 The absorbance spectrum of gold nanorods and 35% hydrogen peroxide in 1:1 ratio.

There are two main peaks at a position of 297 nm and 393 nm. The peak at 297 nm is most likely due to hydrogen peroxide in the mixture. The spectrum of hydrogen peroxide alone with no rods was recorded, as was the spectra of hydrogen peroxide in CTAB with no rods, and these can be seen in Figure 7-8. Figure 7-8 a) shows that there is a large absorbance peak at approximately 301 nm, while when CTAB is added to the solution (as seen in Figure 7-8 b) the peak shifts slightly to 297 nm and in addition, the 947 nm peak, which is likely due to water in hydrogen peroxide, is also no longer present (this peak is also missing in the nanorods spectra, Figure 7-1, which are suspended in MilliQ water).

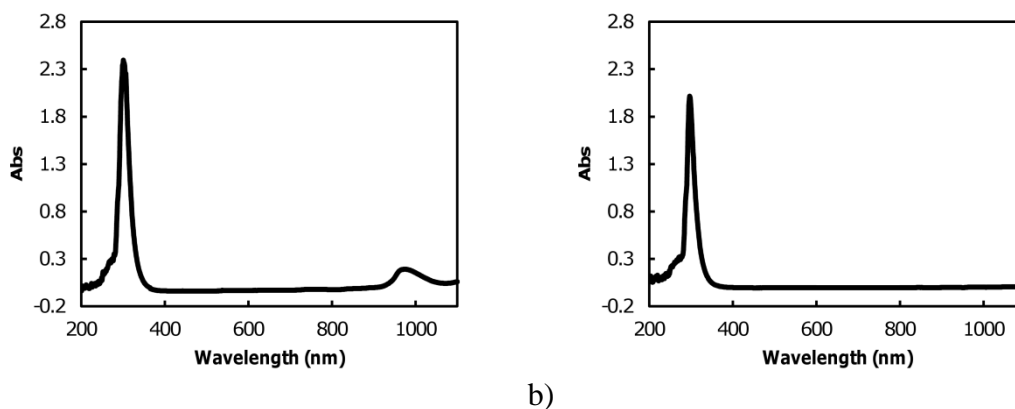


Figure 7-8 The absorbance spectra of a) 35% hydrogen peroxide b) 35% hydrogen peroxide and CTAB in a ratio of 1:1.

The peak at 393 nm is in a similar position to the 394 nm peak in the gold seed solution, Figure 7-9 (The 287 nm peak in this spectrum is due to ascorbic acid). This would indicate that the hydrogen peroxide has oxidised the gold nanorods, leading to the rods dissolving back into gold ions. Due to the presence of CTAB, it is theorised that gold is dissolved as gold bromide.

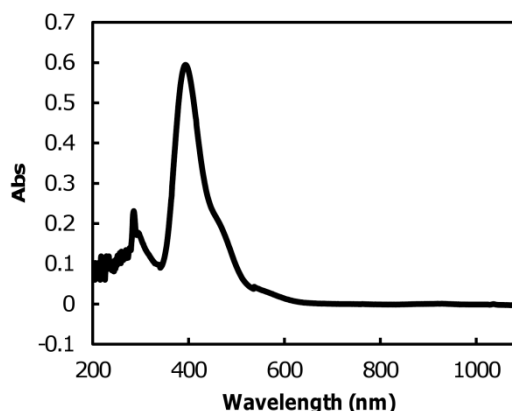


Figure 7-9 The absorbance of gold seed solution.

This presents a major problem since the design of this sensor requires gold nanorods to be deposited onto a surface, and the hydrogen peroxide flow moving past. If gold nanoparticles are oxidised by hydrogen peroxide then the sensor will fail quickly.

7.1.4 Summary of Refractometric Hydrogen Peroxide Sensor

The LSPR of a nanoparticle is determined by the resonance properties of the particle and the refractive index of the surrounding medium. Changes to the refractive

index cause changes to the particle's resonance, and this phenomenon can be used as the basis of a concentration sensor, in this case the concentration of hydrogen peroxide. Gold nanorods were found to be the most sensitive particles for a sensor based on a single wavelength.

Nanorods in solution were acquired to be used in a sensor for hydrogen peroxide concentration. These rods showed a resonance peak at 589 nm and showed good accuracy and precision when used in sucrose and glycerol. Unfortunately when exposed to hydrogen peroxide, the rods were oxidised back to gold ions, which destroyed the possibility of using them in a refractometric sensor. While dissolution of metal nanoparticles has been used before for hydrogen peroxide detection (see Chapter 2), it is of no value in respect of the design of a re-usable sensor.

For the future in regards to a refractometric sensor, WGM microspheres, which have been discussed in Chapter 3.1.3, are a possibility given they do have high Q-factors and are not likely to be dissolved by hydrogen peroxide. However, this would require more equipment and a rethink of the sensor set-up. As absorption spectroscopy has the potential for better chemical identification it was decided to focus efforts in that direction instead.

7.2 Hydrogen Peroxide Sensor Based on Absorption Spectroscopy

Absorption spectroscopy was chosen as a means of investigation as the technique is well understood and relatively simple, with only a light source and a detector being necessary. In addition, unlike the refractometric sensor, the signal is based on the more specific physical properties of the substance.

Table 7-1 Terms and symbols describing variables related to absorption spectroscopy

Symbol	Variable
A	Absorbance
α'	Absorbance coefficient of the analyte
l	Path length
I	Intensity of light at the detector
I_0	Intensity of light at the source
κ	Imaginary part of the refractive index of the analyte
λ	Wavelength of the light passing through the analyte
c	Volumetric percentage concentration of the analyte
d	Thickness of analyte that light is passing through

The Beer-Lambert law defines ‘absorbance’ as the log of the ratio between the intensity of light transmitted through a substance, I , and the intensity of the incident light source, I_0 , as in Equation 7-4. The natural log was used to avoid unnecessary scaling when inverting the exponential. Some additional variation in perceived absorption can be expected due to the full effect of refractive index, especially reflection, as well as possible scattering, but these effects are ignored here. The Beer-Lambert law describes absorbance as a linear function of the absorbance coefficient and the distance the light travels through the substance (path length), shown in Equation 7-5. The absorbance coefficient is intrinsic to a substance and is defined in terms of the imaginary part of the refractive index of a substance, κ and the wavelength of light being absorbed, λ , described in Equation 7-6. In addition, the effective path length can be expressed as the product of the volumetric concentration of the specific substance, c , and the total thickness, d , as seen in Equation 7-7, which results in the expanded expression for absorbance shown in Equation 7-8.

Therefore, in principle, it will be possible to determine the concentration of hydrogen peroxide in the sample by determining the absorbance of the sample.

$$A = -\text{Log}_e \left(\frac{I}{I_0} \right) \qquad \text{Equation 7-4}$$

$$A = \alpha' l \quad \text{Equation 7-5}$$

$$\alpha' = \frac{4\pi\kappa}{\lambda} \quad \text{Equation 7-6}$$

$$l = cd \quad \text{Equation 7-7}$$

$$A = \sum_{i=1}^n \frac{4\pi\kappa_i c_i d}{\lambda} \quad \text{Equation 7-8}$$

Equation 7-8 assumes a linear summation of the absorbance of each analyte.

An issue which will arise when determining the absorbance of a mist is that the mist has no set thickness, d , since as shown in Chapter 6.1.2, the mist flux changes with concentration and other parameters. This necessitates a need for a way to solve the equation simultaneously, for both concentration and thickness. One way to do this is using matrices*. Equation 7-8 can be expressed as $\mathbf{A}=\mathbf{KC}$, where \mathbf{KC} denotes a vector product of matrices \mathbf{K} (intrinsic parameters) and \mathbf{C} (extrinsic parameters). We write the elements of \mathbf{A} with spectral variation along the row index i , and repeated measurements along the column index j . Following the conventions of matrix multiplication, this means that the elements of \mathbf{K} have spectral variation along i and different analytes along j , while \mathbf{C} has analytes along i and repeated measurements along j . We define:

$$\mathbf{K}_{ij} = \frac{4\pi\kappa_{ij}}{\lambda_i} \quad \text{Equation 7-9}$$

$$\mathbf{C}_i = c_i d \quad \text{Equation 7-10}$$

Calibration to determine the intrinsic parameters of hydrogen peroxide and water mixtures must be performed prior to applying this matrix approach to measurement.

* I am grateful to my co-supervisor, Dr. Matthew Arnold, for the assistance in respect of the matrix algebra in this Chapter.

This linear matrix model assumes that there are two chemicals in the mixtures (water and hydrogen peroxide), and there have been n concentrations measured at m wavelengths, giving an m by n matrix, for \mathbf{A}_{cal} , and 2 by n for \mathbf{C}_{cal} , which can be inverted to find the m by 2 intrinsic matrix $\mathbf{K}=\mathbf{A}_{cal}\mathbf{C}_{cal}^{-1}$. The pseudo-inverse is used to fit Equation 7-9 in a least squares sense. The pseudo-inverse is calculated by first transposing the matrix. If $m>n$, then the initial matrix is multiplied by the transposed matrix, and the inverse of the resulting matrix is then calculated and multiplied by the transposed matrix. If instead $m<n$, then the transposed matrix is multiplied by the initial matrix, and the resulting matrix is inverted. The transposed matrix is then multiplied by this inverted matrix. This is demonstrated in Equation 7-11 and Equation 7-12 for the example matrix \mathbf{X} .

$$\text{if } m > n, \text{ then } \mathbf{X}^{-1} = (\mathbf{X}^T \cdot \mathbf{X})^{-1} \cdot \mathbf{X}^T \quad \text{Equation 7-11}$$

$$\text{if } m < n, \text{ then } \mathbf{X}^{-1} = \mathbf{X}^T \cdot (\mathbf{X} \cdot \mathbf{X}^T)^{-1} \quad \text{Equation 7-12}$$

Once \mathbf{K} is determined by the calibration outlined above, determination of an unknown concentration can be performed by measuring at m wavelengths, creating an m by 1 \mathbf{A} matrix, which is used to calculate the 2 by 1 matrix $\mathbf{C}=\mathbf{K}^{-1}\mathbf{A}$. This provides the information required for determining extrinsic parameters, starting with the total thickness, d .

$$d = \sum_{i=1}^2 \mathbf{C}_i \quad \text{Equation 7-13}$$

This is finally used to determine the chemical concentration of the mixture using Equation 7-14.

$$c = \frac{\mathbf{C}}{d} \quad \text{Equation 7-14}$$

The existing literature has data for the absorbance spectra of water and 10% and 20% hydrogen peroxide using ATR in the mid-infrared range[156]. The absorbance data from the Voraberger paper[156] was used in conjunction with the known water data reported from Hale-Querry[171], to estimate the imaginary part of the refractive index

(κ) of water and 10% and 20% using the Beer-Lambert law, described in equations Equation 7-4 and Equation 7-8.

Using these data it was possible to determine an estimate of the 10% and 20% hydrogen peroxide transmission spectra in addition to the expected water transmission spectra at different thicknesses, in this case for quartz cuvettes of 10 micron and 100 micron thickness, Figure 7-10.

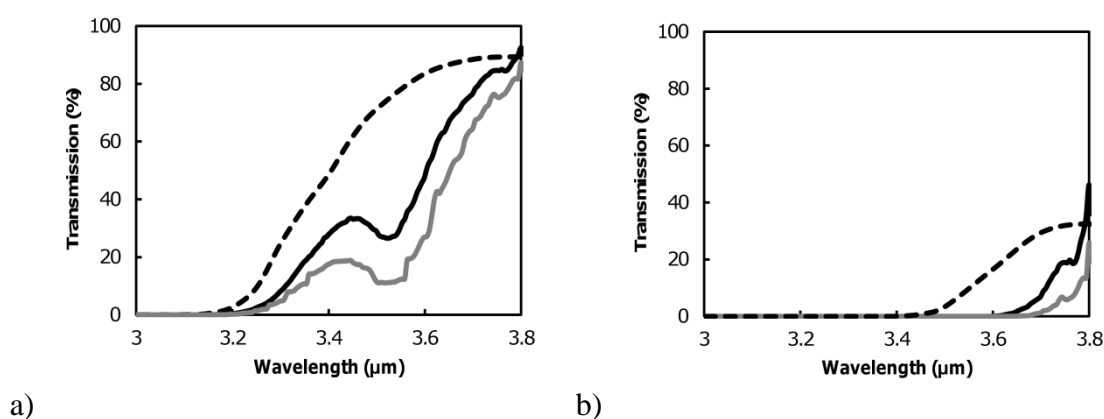


Figure 7-10 The calculated transmission profile of water (dotted line), 10% hydrogen peroxide (solid line) and 20% hydrogen peroxide (grey line) for a thickness of a) 10 μm and b) 100 μm. Water data is calculated using Hale refractive index data while hydrogen peroxide mixtures are calculated from Voraberger data.

Figure 7-10 shows that a 10 micron thick film of hydrogen peroxide should provide a useful absorbance peak around 3.5 microns, which disappears as the thickness is increased to 100 microns due to stronger absorption. The estimate of hydrogen peroxide stops being useful around 3.8 microns, due to the fact that this data is derived from an experiment where the refractive index was not determined (the signal has not had the instrument shape removed and no thickness or normalisation was described in the paper).

While ideally a signal in the 3.5 micron range would be preferable for high sensitivity, as we will see, instrument broadening reduces linearity in this range and therefore other wavelengths must be considered too.

This section will deal with the investigation of the spectra of the water-hydrogen peroxide mixture in the mid infrared (3-4.4 microns) range, with a focus on the 3.7-4.2 micron range where broadening is less severe. This data will be used to solve the matrix *KC*.

7.2.1 Method of Investigation of Hydrogen Peroxide Liquid Absorption

The source used was a Pulsed Broadband Infrared Light Source MIRL17-900, and the detector used was a pyroelectric detector with a tuneable Fabry-Perot filter LFP-3041L-337 (spectral bandwidth of 80nm). Both of these were included in an evaluation kit from Infratec, along with the various computer programs necessary to run the spectrometer. The source and detector were mounted to a steel block (3 cm apart, the light source was partially collimated by a parabolic reflector, with a cone angle of 10°, so care was taken to ensure that this set-up remained constant for all measurements.), with the cuvette holder between them, as displayed in Figure 7-11. This provided a set-up where a hydrogen peroxide-water mixed could be pumped through the flow cell cuvette, and none of the parts had to be moved between measurements, which improved the repeatability of the experiment.

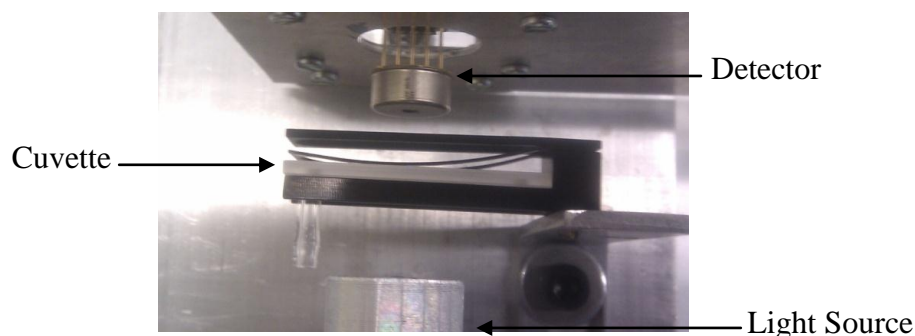


Figure 7-11 The experimental set-up of the IR spectrometer.

Two different flow cell cuvettes were used, a 10 micron path length cuvette made of fused silica and a 100 micron cuvette made of Infrasil, both of which were obtained from Starna Pty. Ltd (“Infrasil” is a trade name given to a type of fused silica with lower water content due to being electrically fused rather than flame fused. This improves the transmission of the quartz in the infrared, at 3.6 microns). For measurements, a 50 mL syringe and short length of hose were used to flow the solution into and out of the cell through the spigots in the cell.

A signal was taken with no cuvette, to ensure that the detector was not saturating, and a dark signal was taken (by unplugging the light source) to ensure that the detector signal was coming from the light source and not the ambient environment. The detector gain was adjusted to maximise signal and avoid saturation (“gain”=1.56), and the light source had a modulated frequency of 10 Hz and was driven with a 135 mA

current. The detector used in the collection of data had a wavelength range of 3000 nm to 4400 nm, with incremental measurement steps set to 20 nm.

Solutions of hydrogen peroxide were prepared by the dilution of 35% hydrogen peroxide by 18.2 MΩ MilliQ water. Water, 5%, 10%, 15%, 20%, 25%, 30% and 35% (w/w) hydrogen peroxide were prepared, which was confirmed using the method detailed in Chapter 4.2.

Before each liquid measurement, the baseline spectrum of the flow cell was taken. This was to ensure the accuracy of the transmission for each reading. The flow cell was then flushed once with the concentration of hydrogen peroxide being measured before the spectrum was taken, and the liquid was flowed through, passing out of the other side of the cell.

Each spectrum was taken three times to confirm repeatability of the measurement. All spectra were base-lined against the cuvette, so that the focus is the transmission and absorbance of the water-hydrogen peroxide mixture. This data was then averaged to determine an average spectrum for each sample, while the standard deviation was used as δI , to calculate the noise in the transmission, δT and absorbance, δA , as shown in Equation 7-15 and Equation 7-16.

$$\delta T = \frac{\delta I}{I_0} \quad \text{Equation 7-15}$$

$$\delta A = \delta I \left(\frac{1}{I_0} + \frac{1}{I} \right) \quad \text{Equation 7-16}$$

The reflection losses in the experiment are assumed to be minimal. The two main types of reflection are air-fused silica and fused silica-water interfaces (in our case hydrogen peroxide was assumed to have a similar real refractive index to water). Using the Fresnel equations and the real refractive index data for water from Hale, and fused silica from Kitamura [172], the reflections at these interfaces were calculated at a normal incidence and are displayed in Figure 7-12.

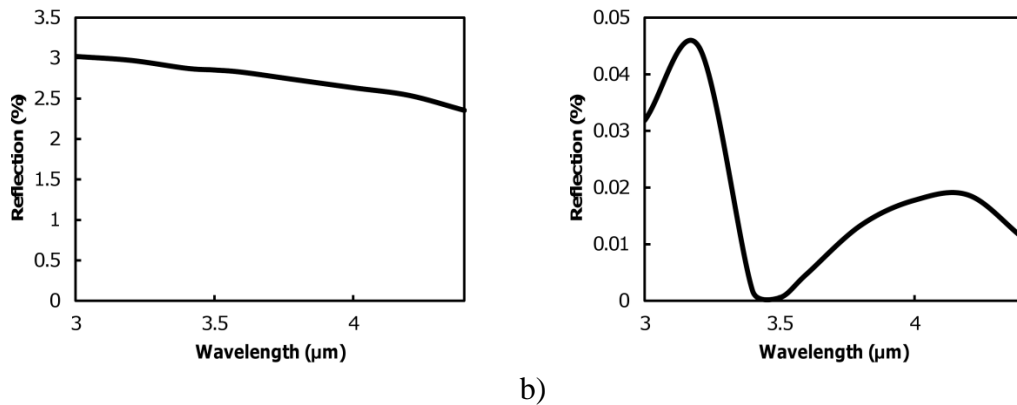


Figure 7-12 The calculated reflection from normal incidence from a) an air-fused silica interface and b) a water-fused silica interface using the Fresnel equations and the real refractive index data for water (hale) and fused silica (Kitamura[172]).

There are 4 main sources of reflection in the cuvette: air-glass, glass-sample cavity, sample cavity-glass and glass-air. Reflection losses at the air-glass interfaces (the front and back of the cuvette) are consistent for all measurements, and were removed by base-lining the spectra against the cuvettes. The internal reflections formed in the glass-sample cavity are a little more complex. The reflections when water and water-hydrogen peroxide mixtures fill the cavity are insignificant, due to the small refractive index differences between water, hydrogen peroxide and the cuvettes. However, when air fills the cavity, reflections off each surface are more significant, although still relatively small (<5%). Of course, since the cavity of the 10 micron cuvette is only a few times the wavelength, it can be treated as a thin film, and interference causes a minor oscillation that is mostly unrelated to absorption. This oscillation is used later in section 7.2.2 to determine the actual sample thickness in the cuvette. Interference in the 100 micron cuvette would result in very short cycle oscillation, but this is averaged out by the comparatively wide spectral bandwidth of the spectrometer. The reflection of the air-glass cavity (both incoherent and coherent reflection) is one contributor to error in determining the true absorption coefficient.

The effect of this error on the base-lined transmission (and subsequently the calculated absorbance) can be estimated from a rough calculation of transmission through the cuvette from first principles, as seen in Equation 7-17 (note this equation is for incoherent reflection only):

$$T \sim (1 - ac)(1 - afs)^2(1 - 2(ra + rc)) \tag{Equation 7-17}$$

Where T is transmission, ac is the absorbance in the cavity, afs is the absorbance of the fused silica, ra is the reflection at the air-fused silica interface and rc is the reflection at the fused silica-cavity interface. The approximate transmission of a cuvette containing an analyte baselined against an empty cuvette can be seen in Equation 7-18:

$$T \sim \frac{(1 - al)(1 - afs)^2(1 - 2(ra + rl))}{(1 - ac)(1 - afs)^2(1 - 2(ra + rc))} \quad \text{Equation 7-18}$$

Where al is the absorbance of the liquid analyte, rl is the reflection at the fused silica-liquid analyte and ac is the absorbance of air in the empty cavity. . It is evident from Equation 7-18 that the term $(1-afs)^2$ is eliminated, however, the reflection is slightly is not easily eliminated to 1 (as can be inferred from Figure 7-12). This means that the transmissions determined will not be $(1-al)/(1-ac)$, but the product of $(1-al)/(1-ac)$ and the reflection term. By using the data in Figure 7-12, it is possible to calculate an estimate of the reflection term, which is shown in Figure 7-13. Ideally the reflection term should be 1, however, as Figure 7-13 shows, in our case it is slightly higher than 1. This error affects primarily the third significant term in the absorbance (absorbance in underestimated) and is therefore not highly significant in this study. The absorbance data shown below is not corrected, as this is only an estimate to show what order of magnitude the error is.

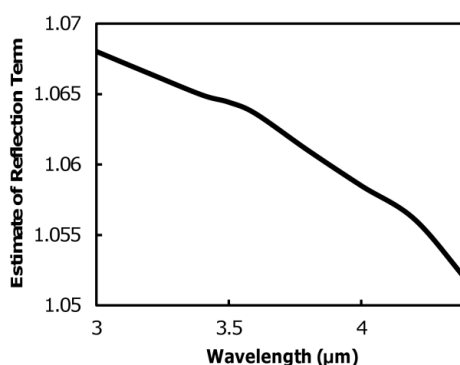


Figure 7-13 The estimated reflection term when a cuvette containing analyte is base-lined against an empty cuvette.

7.2.2 Results of Investigation of Hydrogen Peroxide Liquid Absorption

The transmission of the cuvettes can be seen in Figure 7-14. These transmissions are base-lined against the air signal. The dark signal is effectively zero across the whole

wavelength range, meaning that the signal the detector picks up will be from the source. The cuvette transmissions are similar for the most part, with the 100 micron being slightly more transmissive. These small differences are most likely due to the cuvettes being made of different material (the 100 micron cuvette is made of Infrasil quartz, while the 10 micron cuvette is made of ordinary quartz).

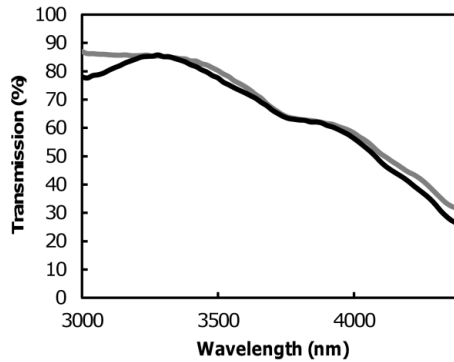
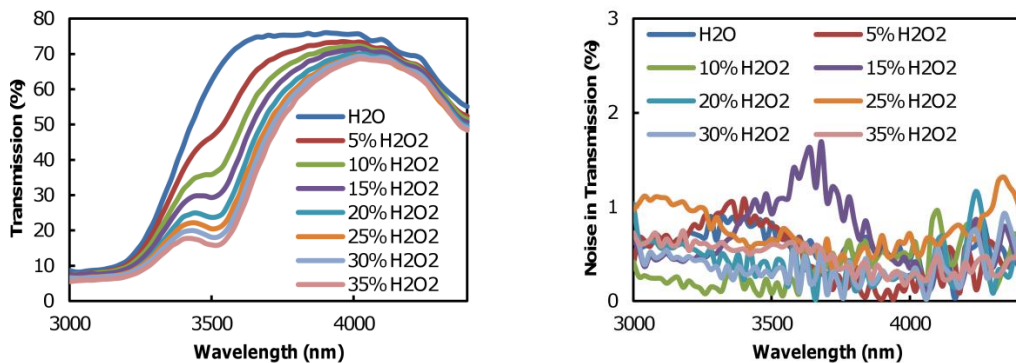


Figure 7-14 The transmission of the 10 micron cuvette (black line) and the 100 micron cuvette (grey line). These spectra are base-lined against air

The transmission spectra of the hydrogen peroxide-water mixtures, over the range of 3 to 4.4 microns, are displayed in Figure 7-15 and Figure 7-16. The transmission has been base-lined to the 10 and 100 micron cuvette respectively. The spectra are similar to the expected values, however there is evidence of broadening, which is expected, given that the transmission is slightly higher than expected close to 3000 nm and slightly lower than expected between 3500 nm and 3800 nm.



a)

b)

Figure 7-15 Raw a) transmission and b) noise in transmission spectra from all runs of water(H₂O)-hydrogen(H₂O₂) peroxide in the 10 micron cuvette. Spectra run from water to 35% hydrogen peroxide.

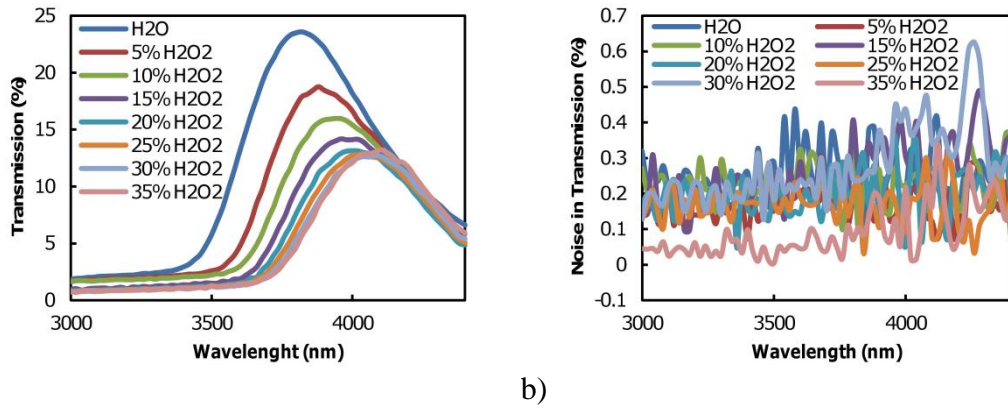


Figure 7-16 Raw a) transmission and b) noise in transmission spectra from all runs of water(H₂O)-hydrogen(H₂O₂) peroxide mixtures in the 100 micron cuvette. Spectra run from water to 35% hydrogen peroxide.

These results demonstrate that it is the “bright” noise and not the dark noise which is significant in this project. To determine the absorbance of the hydrogen peroxide-water mixtures, the natural log of the transmission data was used.

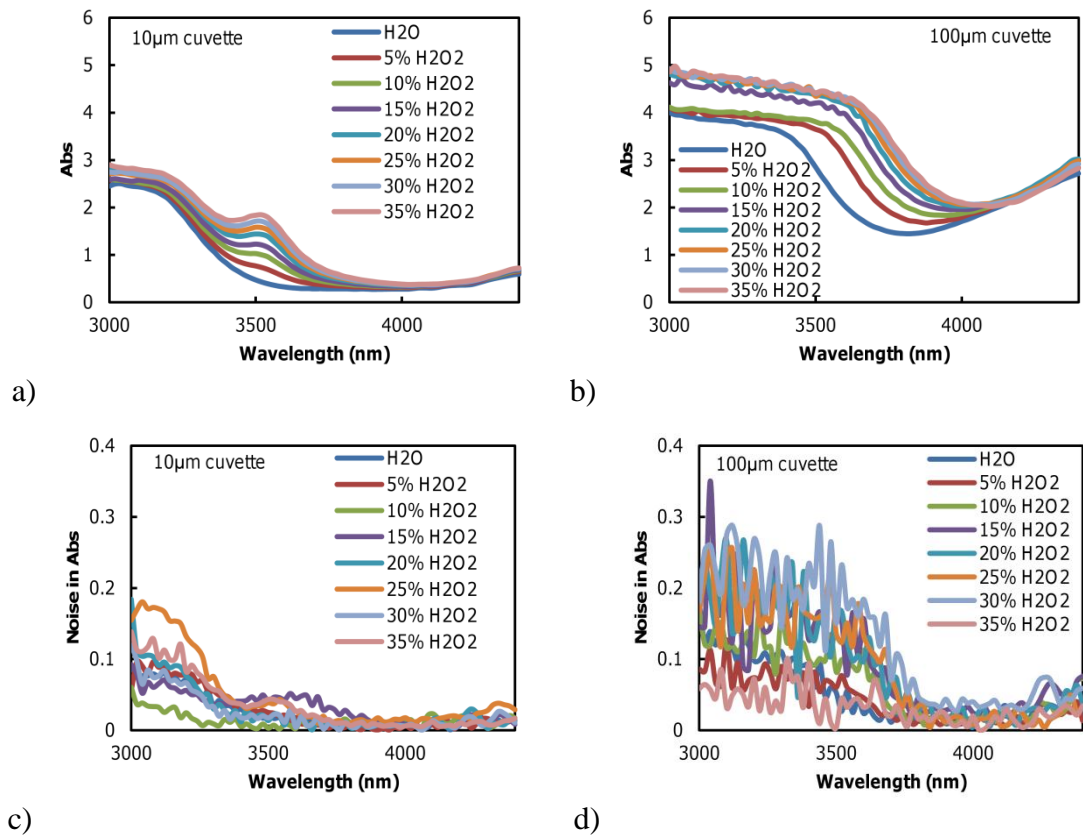


Figure 7-17 Absorbance (natural log) spectra of water-hydrogen peroxide mixtures for a thickness of a) 10 microns and b) 100 microns. Also shown is the noise in the absorbance signal for a thickness of c) 10 microns and d) 100 microns spectra run from 35% hydrogen peroxide to water.

This data, shown in Figure 7-17 represents the absorbances of different concentrations of hydrogen peroxide at 71 different wavelengths between 3000 nm and 4400 nm for each thickness. As expected, the 100 micron thickness results have higher absorbance, which cannot be accurately determined by the spectrometer and overwhelms the characteristic hydrogen peroxide peak at 3500 nm. Fortunately, this peak is visible in the data from the cuvette of 10 micron thickness. The obvious way of using this data to determine the concentration of hydrogen peroxide is to take the data from a single wavelength and plot the concentration against the absorbance, which the Beer-Lambert law states should be linear. In this case, the concentrations were taken as volume percentage (water, 3.5%, 7.1%, 10.9%, 14.7%, 18.7% 22.7% and 27.1% (v/v)).

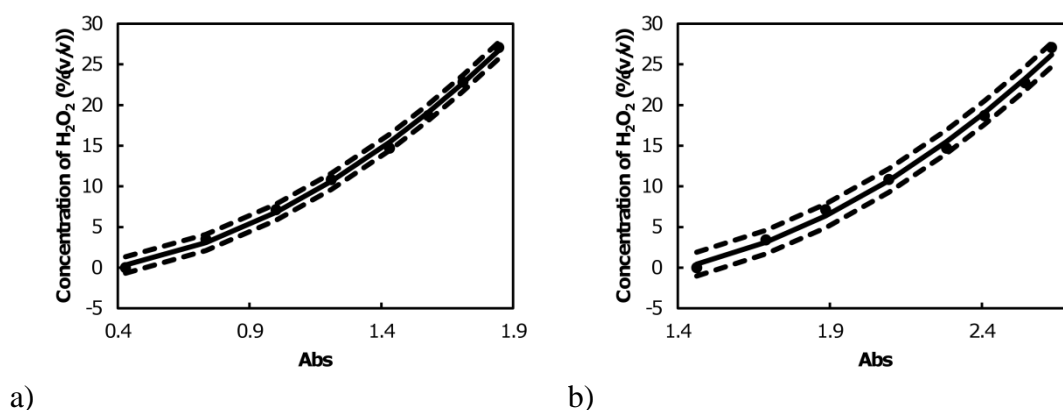


Figure 7-18 The concentration of hydrogen peroxide in solution (v/v) against the optical absorbance of the solution for a) 10 µm thickness at a wavelength of 3520 nm and b) 100 µm thickness at a wavelength of 3860 nm. Solid lines are quadratic regression and dotted lines represent 2-sigma confidence interval.

Figure 7-18 shows these relationships. The 10 micron data was taken around the hydrogen peroxide peak, since the peak is intrinsic to hydrogen peroxide. This peak is not present in the 100 micron thickness data, so the data in that case was taken from a point where the different concentrations registered a larger difference in absorbance. In neither case was the trend linear, which is a consequence of instrument broadening, which will be discussed later in this chapter.

Both data sets had a quadratic fit determined applied using the method outlined in Chapter 4.1.2, and in both cases the fit was highly accurate with coefficient of determinations of 0.998 and 0.996 respectively. The fit were also quite precise with a 2-sigma confidence interval of $\pm 1\%$ (v/v) and $\pm 1.5\%$ (v/v) respectively.

It is therefore theoretically possible to determine the concentration of hydrogen peroxide between 0% and 27% using these simply calibrated trends for the MIR spectrometer used. However, this is predicated on having a fixed thickness of fluid, and in the mist stream, the effective thickness is not constant. It is therefore important to calculate the concentration of hydrogen peroxide simultaneously with the thickness, which may be done using the matrices as described earlier in this chapter.

There were 8 different concentrations producing a 71x8 (wavelength x sample) matrix for A_{cal} . The C_{cal} matrix was formed by multiplication of the cuvette thickness (10 microns and 100 microns respectively) and the concentrations of water and hydrogen peroxide (%v/v) in each sample.

The cuvettes both had a transmission spectrum taken on a Cary Varian 2400 Spectrophotometer, shown in Figure 7-19, to acquire a more accurate physical thickness estimate. This was done by measuring the interference fringes in regions of high transmission (the fringes exist due to the interference of light going into and out of the cavity in the cuvette). The 10 micron cuvette was found to have a cavity thickness of 10.8 microns and the 100 micron cavity had a 104 micron cavity thickness.

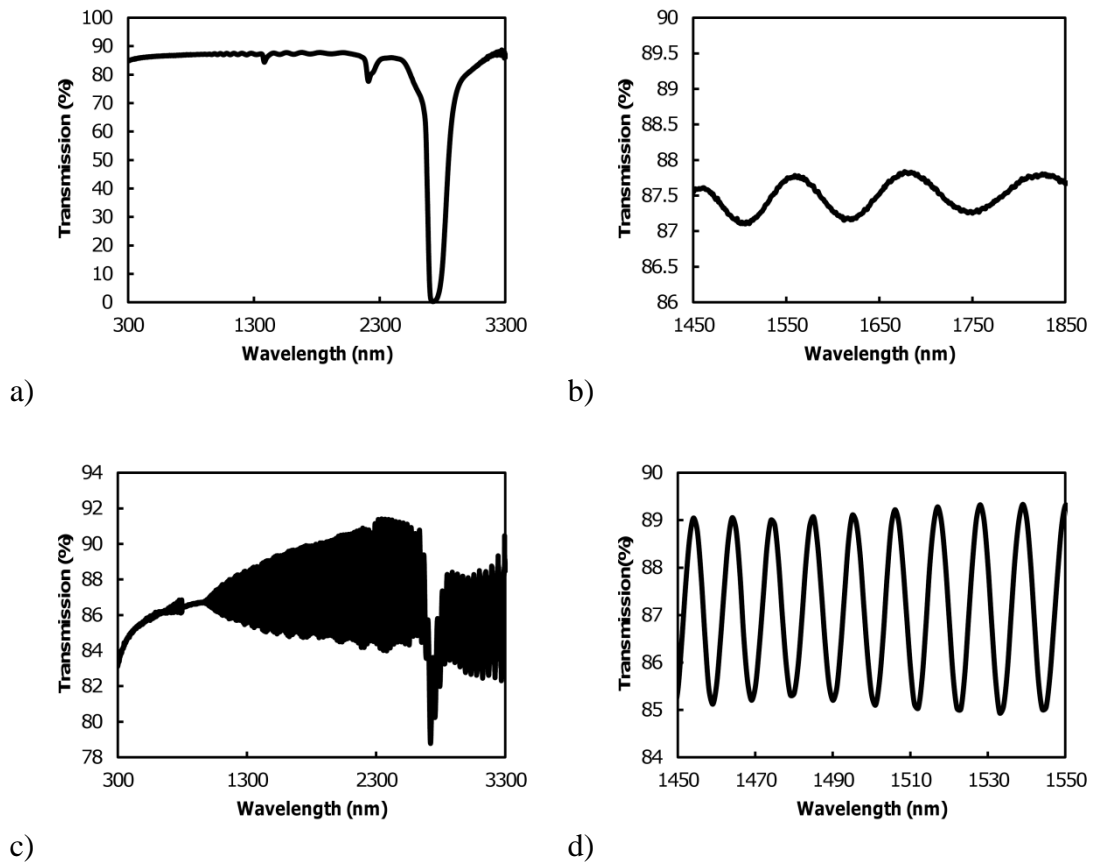


Figure 7-19 The transmission spectra of a) the 10 micron cuvette, b) a close up of 10 micron cuvette spectrum, c) the 100 micron cuvette spectrum and d) a close up of 100 micron cuvette spectrum.

Both matrices (10 micron and 100 micron) contained three of each concentration forming a 2x8 matrix in each case. C_{cal}^{-1} was then calculated in each case and the resulting matrices are presented in the appendix as Figure A-8.

From here, the calibration **K** matrix was generated which will then be used for actual measurements. The **K** matrix for the 10 micron data and the 100 micron data can be seen in the appendix as Table A-8 and Table A-9. This matrix is a 2x71 matrix which contains the calibrated **K** values (the only variable is refractive index, κ) for water and hydrogen peroxide respectively over each wavelength measured.

The imaginary part of the refractive index (which describes the absorbing properties of a species), κ , can be calculated over the wavelength range using Equation 7-9. The results are displayed in Figure 7-20 along with values calculated by Hale-Querry and Voraberger et.al.

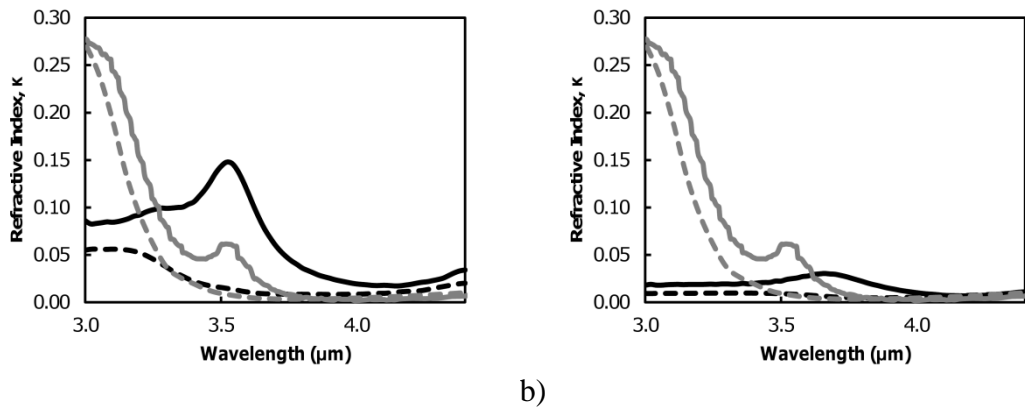


Figure 7-20 The refractive index, κ , of hydrogen peroxide (black solid lines) and water (black dotted lines) calculated from K matrix for a thickness of a) 10 microns and b) 100 microns. Also shown are 20% hydrogen peroxide data (grey solid lines) and water (grey dotted lines) values of refractive index, κ , published in Voraberger and Hale papers respectively.

Figure 7-20 shows that the calculated values of water and hydrogen peroxide from the experiment are rather different from the values obtained in the literature. Most of this difference is likely due to line broadening from the instrument. Broadening is also the expected cause of the apparent “peak shift” in 100 micron refractive index estimate. The peak in this case is not the peak found in the 10 micron data, but a consequence of the cumulative effect of the broadening in each measurement concentration using the 100 micron thickness. The instrument profile suggests a 0.08 micron broadening of the signal. The effect of this broadening on water can be seen in Figure 7-21.

It can be clearly seen that both signals correspond strongly with the expected broadening. There are differences between the experimental and theoretical data, which may be explained by the instrument shape provided by the manufacturer being slightly different to the one used in this experiment as there are additional sources of broadening such as the less collimated beam and order-blocking spectral features.

Hydrogen peroxide also shows a similar effect from 3-3.6 microns, Figure 7-22. Figure 7-20 shows the comparison of 100% hydrogen peroxide, which we have calculated and the 20% Voraberger data. The calculated data is expected to be five times the value of the Voraberger data, but clearly this is not the case, and indeed the 100 micron data shows a weaker absorbance. These differences are due to broadening from the instrument profile. In Figure 7-22, the 20% Voraberger hydrogen peroxide data was compared to the 20% hydrogen peroxide data obtained during

experimentation, however, the Voraberger data has its own difficulties to work with, these being that the normalisation is ambiguous, and the data itself still contains artefacts from its own the instrument profile. Given these facts, and that the broadened water data matches well with the experimentally determined water, we are confident in saying that this broadening is present and the reason for some of the issues to be discussed next.

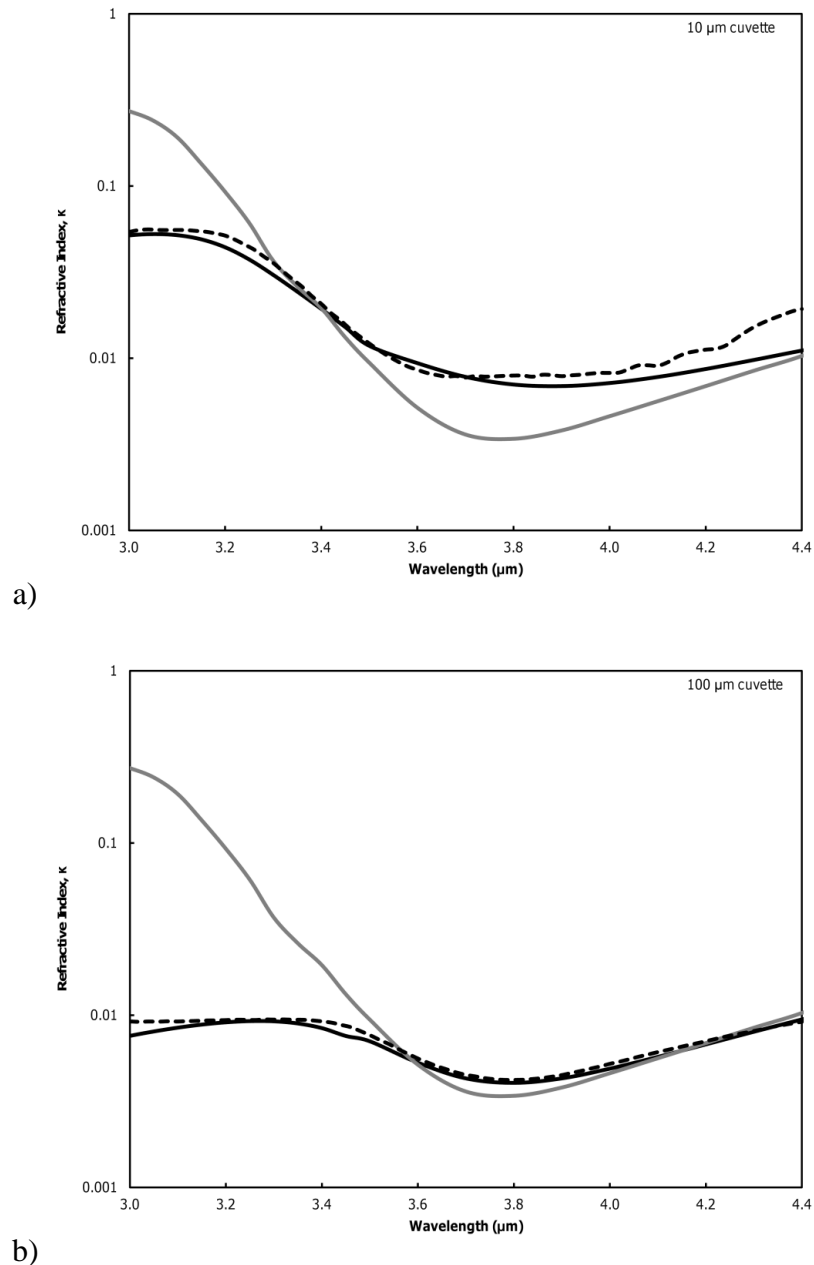
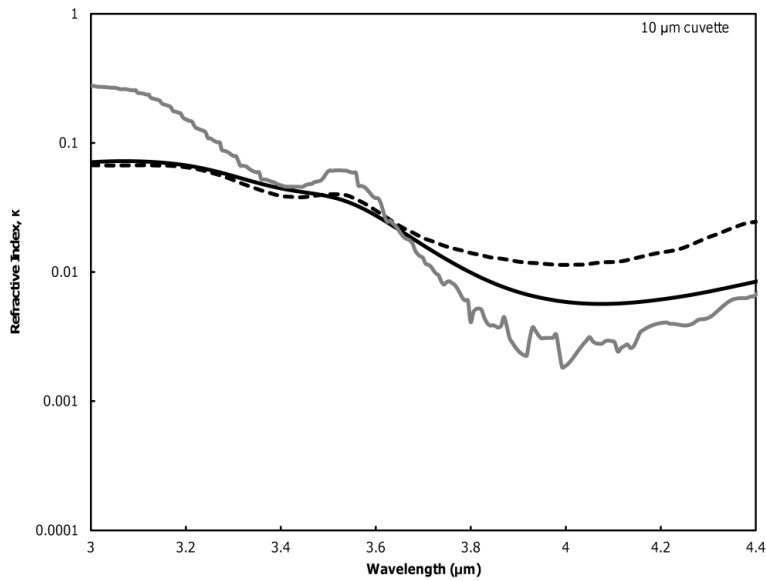
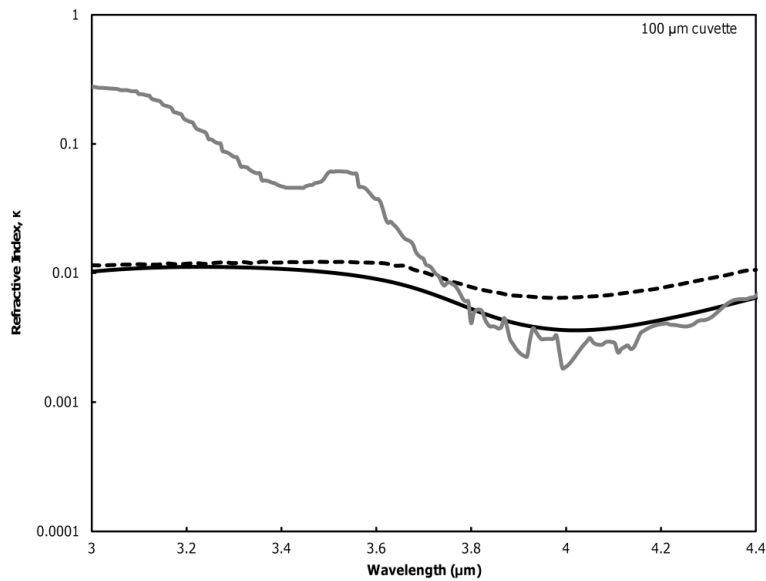


Figure 7-21 The effect of 0.08 micron broadening on the refractive index, κ , of water of thickness a) 10 micron and b) 100 micron The solid grey line represents the tabulated refractive index from Hale, the solid black line is the simulated refractive index with broadening, and the black dotted line represents the calculated refractive index from our experimental water data.



a)



b)

Figure 7-22 The effect of 0.08 micron broadening on the refractive index, κ , of 20% hydrogen peroxide of thickness a) 10 micron and b) 100 micron. The solid grey line represents the tabulated 20% hydrogen peroxide refractive index from Vorabeger , the solid black line is the simulated refractive index with broadening and the black dotted line represents the measured refractive index from 20% hydrogen peroxide.

Deconvolution was considered, however, given that there are absorbance bands on both sides of the data range that was observed, and given that there are other properties of the detector for which we have no good estimate, deconvolution was unlikely to produce a result which was any sharper than what we already had. The solution was to use short ranges of data between 3.6 and 4.2 microns which are less

affected by broadening. The Beer-Lambert law does allow for this off resonance measurement as long as the broadening is intrinsic to the analytes. However, in this case, there is also broadening due to the instrument shape. I was not able to find any relevant literature about off resonance measurement when this broadening is present, but it is expected that the range that linearity has been found in is due to instrument broadening being less apparent in that range. The other possible issue is that off-resonance may be affected by the real refractive index. In absorption spectroscopy it is common to discount this, as the minor reflection component is assumed not to cause significant deviation from the Beer-Lambert law. Thus this is not an issue in this work as earlier this chapter it was shown that reflection has an insignificant effect. Each range contained 10 wavelengths and the pseudoinverse \mathbf{K}^{-1} was determined for each. The range of wavelengths from 3.9 microns to 4.08 microns was used to determine \mathbf{K}^{-1} for the 10 micron cuvette and the wavelengths from 4 to 4.18 microns was used to determine the \mathbf{K}^{-1} for the 100 micron cuvette, as these were the ranges that linearity held in, and which seemingly obeyed the Beer-Lambert law.

Maximum sensitivity would be obtained if the data sets were used as a whole or at least data predominantly around the 3.5 micron peak, however, as the spectra have been affected by broadening, and broadening has specifically occurred around the 3.5 micron peak, using these data sets results in non-linearity in the relationship between the calculated concentration (from the matrix) and the actual concentration, as seen in Figure 7-23.

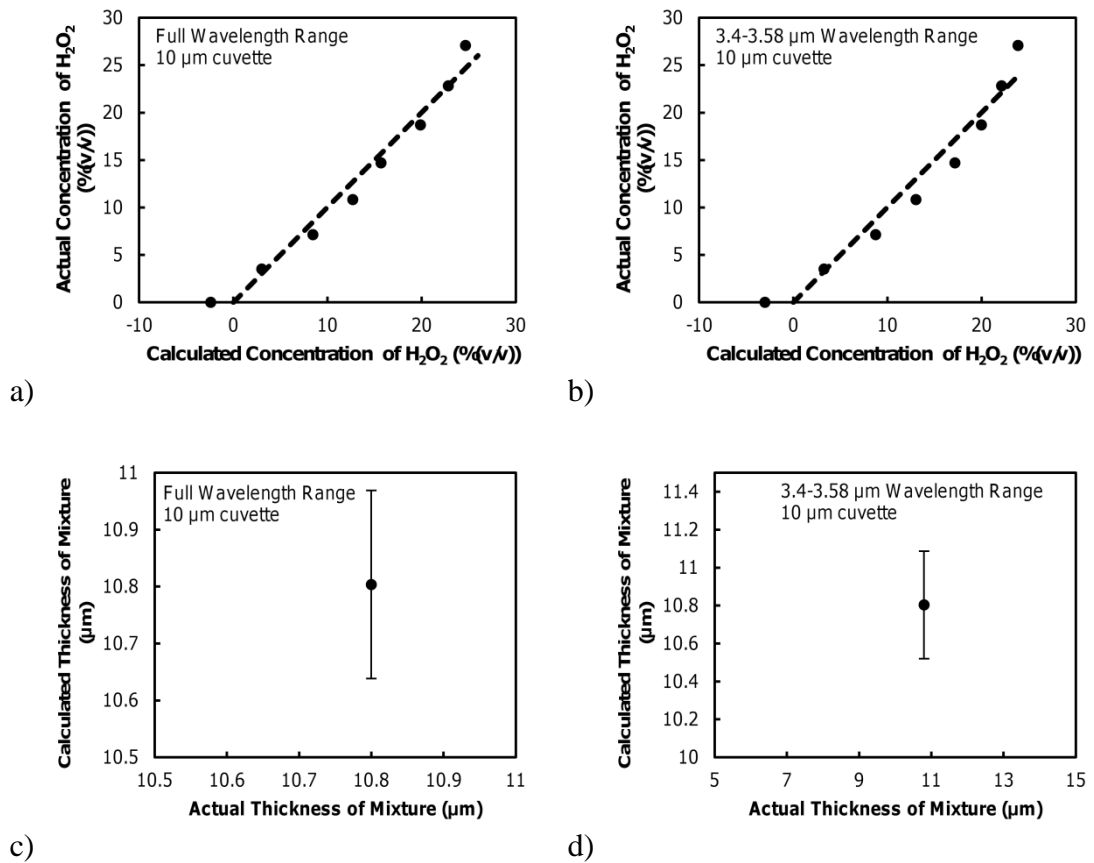


Figure 7-23 The concentration of hydrogen peroxide and the average total cuvette thickness calculated (with error bars of one standard deviation) from the 10 thickness data using a) & c) the full wavelength range and b) & d) the 3.4-3.68 micron range. Dotted line represents a 1:1 linear line.

Figure 7-23 a) and b) shows the trend between actual concentration and calculated concentration for the 10 micron data set using the whole wavelength range and the data around the 3.5 micron peak, respectively. The trend between these values is not linear, which is the expected result of broadening. While the calculated concentration in both cases is not linear (the data points are below and above the dotted line, and can be seen to curve), it could provide a fair linear estimate if a linear regression is applied. In addition, both data sets are also able to fairly accurately determine the total thickness of the mixture of hydrogen peroxide and water, shown in the plots in Figure 7-23 c) and d). The graphs show the average thickness calculated by the matrix, and the error bars show one standard deviation of the average.

A linear regression of the calculated and the actual concentration of hydrogen peroxide was taken and resulted in a coefficient of determination of 0.97 using the whole range and a coefficient of determination of 0.95 for the data around the 3.5 micron peak. The whole range results have slightly more precision, with a 2-sigma error

of $\pm 4\%$ as opposed to $\pm 5\%$. This is to be expected as the broadening effect is greater around the peak, while the taking the whole range may have an effect of slightly reducing the broadening effect on linearity.

To reduce broadening, a data range between 3.9-4.08 microns was chosen to estimate the concentration of hydrogen peroxide. In this range, with no spectral features, there is more possibility of finding a data which is not as affected by broadening. In this case the data was much more linear. The same linear regression method was used to determine the relationship between the calculated and actual hydrogen peroxide concentration, with the results being presented in Figure 7-24, along with the estimated total thickness of the liquid mixture.

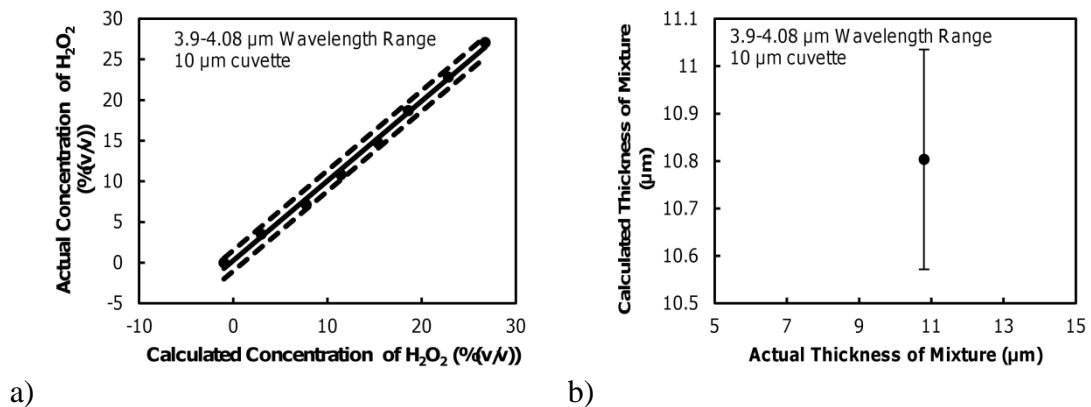


Figure 7-24 The a) concentration of hydrogen peroxide and b) average total cuvette thickness calculated (with error bars of 1 standard deviation) using the data from 3.9-4.08 microns for the 10 thickness mixture. The concentration of hydrogen peroxide includes a linear regression (solid line) with a 2-sigma confidence interval (dotted lines).

The coefficient of determination of the calculated against the actual hydrogen peroxide concentration linear regression is 0.99, which indicates that using the data from this wavelength range results in a highly linear trend between the calculated concentration and the actual concentration, much more so than using the whole range of wavelengths or the wavelength range around the peak (which were detailed above). The regression also shows a higher precision with a 2-sigma error of $\pm 1.3\%$. In addition the data range also provides a more accurate response for the total thickness of the mixture of hydrogen peroxide and water when compared to the thickness estimates from the other data ranges.

The same analysis was applied to the 100 micron data set and using the whole data range and the data around the peak (in this case the peak is around 3.7 microns).

The results can be seen in the Appendix in Figure A-9. In this case the results were similar to the previous data, in so far as using the whole range had provided a more linear response in concentration (This is supported by coefficient of determination for linear regressions of 0.93 and 0.73 respectively, both of which are worse than the 10 micron data, which is to be expected as broadening is much more significant in a thicker mixture.). Once again this shows that using the whole range is less susceptible to broadening than using data from around a peak.

The best linearity in the relationship between calculated and actual hydrogen peroxide concentration was found in the wavelength range of 4-4.18 microns (again where there are fewer spectral features, there is less broadening) for the 100 micron thickness mixture. The results can be seen in Figure 7-25.

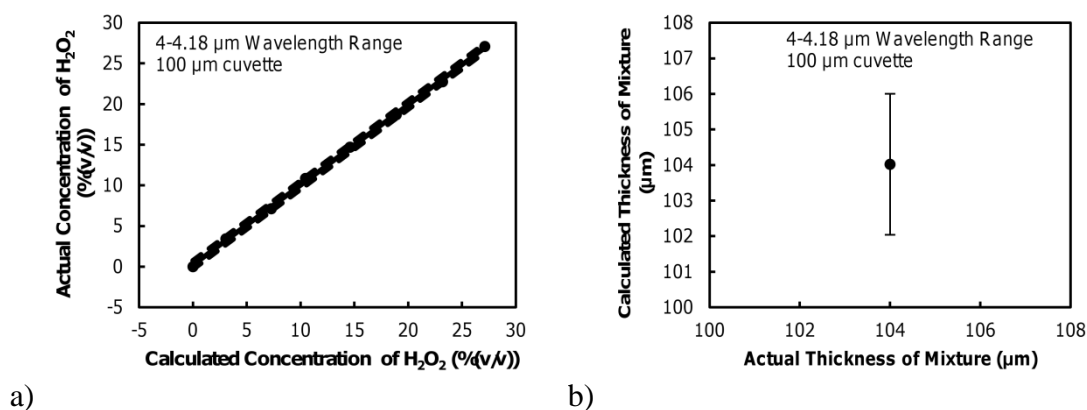


Figure 7-25 The a) concentration of hydrogen peroxide and b) average total cuvette thickness calculated (with error bars of 1 standard deviation) using the data from 4-4.18 microns for the 100 thickness mixture.

The coefficient of determination was 0.999, with a 2-sigma confidence interval of $\pm 0.5\%$. The thickness of the total mixture is also estimated quite accurately, with all estimates being within 5 microns either side, and the majority of the points being within 2 microns. In this case, the certainty of the fit and the error are both slight improvements over the 10 micron data.

The next step was to investigate whether combining the data sets would provide the same accuracy and allow the calculation of hydrogen peroxide based on different thicknesses *between* 10 and 100 microns. In this case both thicknesses and concentrations were combined into the C_{cal} matrix forming a 2×16 matrix. The pseudo-inverse of C_{cal} (C_{cal}^{-1}) was calculated as above and is displayed in the Appendix as Figure A-10.

This was multiplied with the corresponding absorbances to calculate the matrix **K**, seen as Table A-10 in the appendix, and subsequently the refractive index of water and hydrogen peroxide, which can be seen in Figure 7-26.

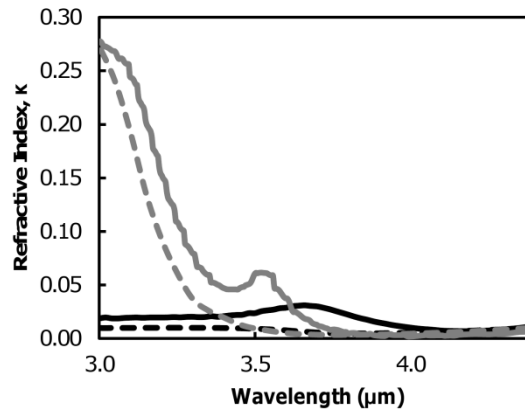


Figure 7-26 The refractive index, κ , of hydrogen peroxide (black solid lines) and water (black dotted lines) calculated from K matrix for both 10 and 100 micron data combined. Also shown are 20% hydrogen peroxide data (grey solid lines) and water (grey dotted lines) values of refractive index, κ , published in Voraberger and Hale papers respectively.

It can be seen from Figure 7-26 that combining the data sets produces a refractive index similar to that calculated with the 100 micron data. This makes sense due to the fact that the measured absorbance of the 100 micron data is larger and would therefore skew the data.

In the case of the combined 10 and 100 micron data set, which can be seen in the appendix Figure A-11, it is clear that neither using the whole wavelength range, nor the data range around a peak (the 10 micron peak or the 100 micron “peak”) is suitable to determine a linear trend for calculated against actual hydrogen peroxide concentration. In addition, this data set is completely unsuitable to determine the total thickness of the mixture: not only is there a lack of linearity, using these ranges with the combined data predicts negative concentrations, which is unphysical. It also appears that the 10 and 100 micron absorbance data provides very different values for concentration, with the 10 micron absorbances predicting the negative concentrations, and also the lower concentrations. The solution was, again, to find a range with no spectral features to use for these calculations, in this case the data range from 3.74 to 3.92 microns.

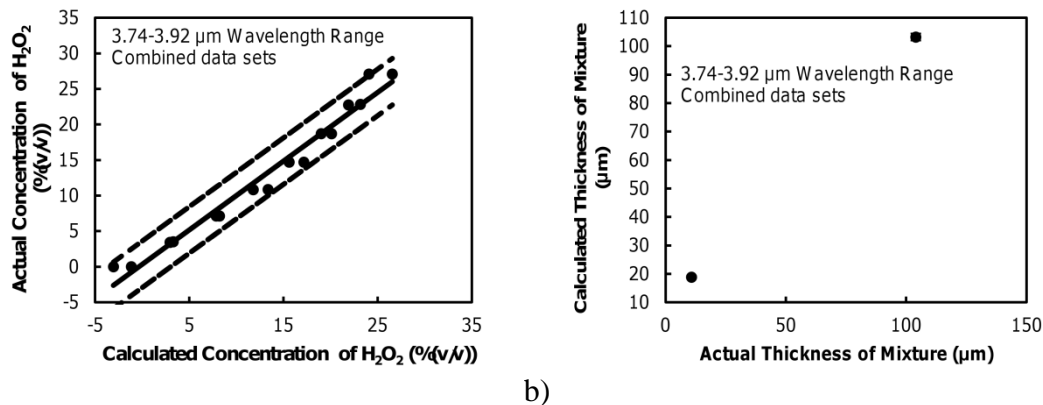


Figure 7-27 The a) concentration of hydrogen peroxide and b) average total cuvette thickness calculated (with error bars of 1 standard deviation) using the data from 3.74-3.92 microns for the combined 10 and 100 micron data set. Solid line represents linear regression, while dotted line represents 2-sigma confidence interval.

Figure 7-27 shows that using a data range between 3.74-3.92 microns produces the most linear relationship. This relationship is not as linear as in the case of the individual data sets.

This region of the spectrum is the closest that the two data sets come to overlapping each other in response. The regression has a coefficient of determination of 0.97 and a 2-sigma confidence interval of $\pm 3.3\%$, which is less accurate and precise than the individual data sets. In addition, the total mixture thickness is calculated more accurately for the 100 micron data than the 10 micron data. This was expected since the calculated concentrations are linear at different parts of the range.

In the future it may be worth performing the experiments over a wider spectral range encompassing the entire group of absorption bands in this study (say 2 – 5 microns) , and then performing a deconvolution, or using an instrument with better resolution. In the present however, it is certainly possible to determine hydrogen peroxide concentration accurately using absorbance spectroscopy as long as there is a fixed thickness being interrogated. It may be possible to determine concentration with a combined data set, however, the accuracy of the thickness is poor as is the precision of the concentration.

7.2.3 Investigation of spectroscopic specificity against other compounds

One reason this sensor approach was initially favoured was due to the fact that it should be somewhat selective to hydrogen peroxide. However, given that the best results here have been found in areas without peaks (due to broadening), there is some

question as to whether good selectivity is actually possible. To test this more rigorously a solution of 95% ethanol and 5% water was measured using the same technique as for the hydrogen peroxide, with the resulting, transmission, absorbance and noise spectra of 95% ethanol for a thickness of 10 and 100 microns displayed in Figure 7-28. Again, reflection was assumed to be insignificant, as the ethanol has similar reflection losses to water.

Both thicknesses transmissions were measured three times to ensure repeatability, before being averaged. The standard deviation of these samples was used to calculate the noise.

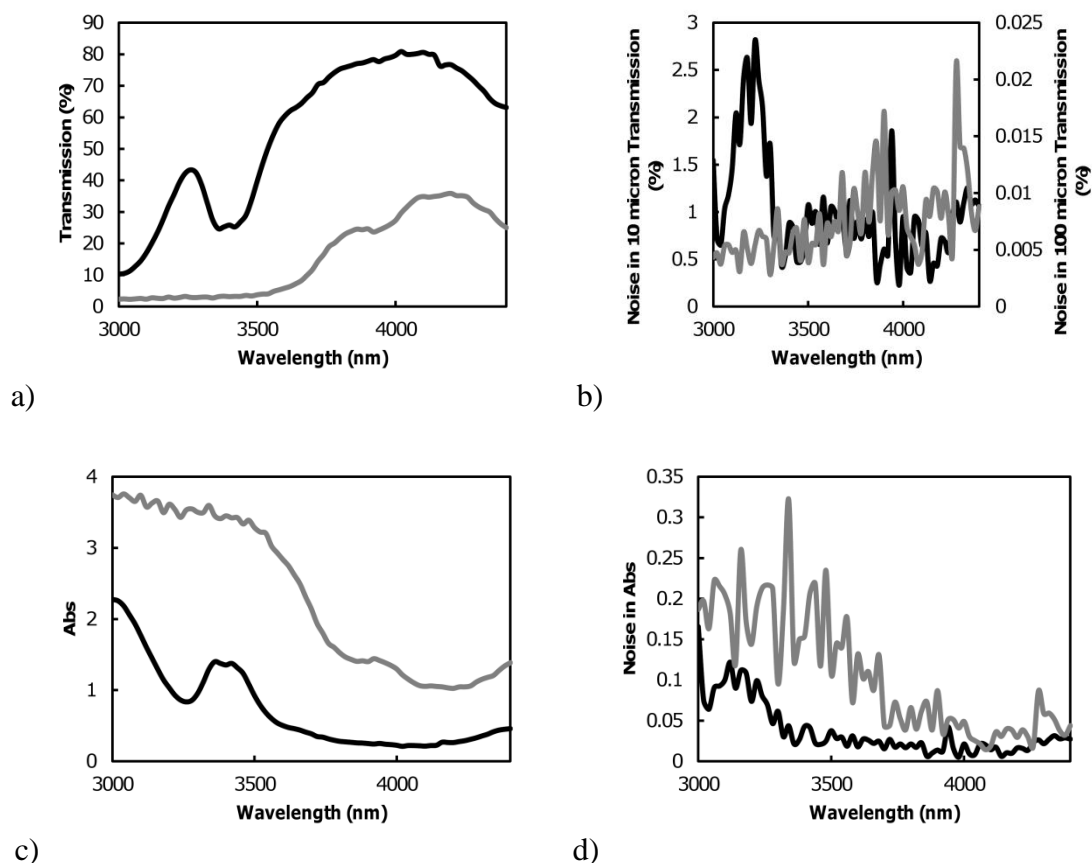


Figure 7-28 The optical a) transmission, b) noise in transmission, c) absorbance (natural log) and d) noise in absorbance of 95% ethanol. The black line describes the 10 micron thickness and the grey line describes the 100 micron thickness.

Figure 7-28 shows that the ethanol solution has a lower absorbance compared to water and hydrogen peroxide mixtures above. The 10 micron thickness absorbance in the range 3.9-4.08 microns (found earlier to be well correlated with hydrogen peroxide concentration) was multiplied by the corresponding range in the \mathbf{K}^{-1} matrix for the 10 micron data to check the extent of any spurious hydrogen peroxide signal.

Table 7-2 The calculated ethanol thickness and concentrations for 10 micron thickness of 95% ethanol/5% water (v/v) (three repeat measurements). The spurious H₂O₂ signal calculated from these spectra using the calibration matrices is also shown.

Thickness (μm)	6.2
Water (%)	72.7
Hydrogen peroxide (%)	27.3

Table 7-2 shows an erroneous matrix calculation of 27% hydrogen peroxide (v/v). At the same time, the calculated thickness is much lower than 10 microns, and is outside the range of data shown in Figure 7-24 b). This suggests that while an erroneous concentration can be calculated, mismatch from the expected thickness would be a useful indicator for the presence of a third compound when using a setup with known or well calibrated thickness.

The same method was applied to the 100 micron thickness ethanol (the absorbance matrix was multiplied by 4-4.18 micron range of \mathbf{K}^{-1} from the 100 micron calibration), and once again, the calculated thickness was much lower than the actual thickness and that shown in Figure 7-25. Once again, the mismatch in calculated thickness versus known thickness gives a way of identifying that there is a non-hydrogen peroxide/water solution present.

Table 7-3 The calculated ethanol thickness and concentrations for 100 micron thickness of 95% ethanol/5% water (v/v) (three repeat measurements). The spurious H₂O₂ signal calculated from these spectra using the calibration matrices is also shown.

Thickness (μm)	50.4
Water (%)	42.8
Hydrogen peroxide (%)	57.2

Finally, this data was put into the combined matrix calculation which produced Table 7-4.

Table 7-4 The calculated ethanol thickness and concentrations for the combined thickness data sets of 95% ethanol/5% water (v/v) (three repeat measurements). The spurious H₂O₂ signal calculated from these spectra using the calibration matrices is also shown.

Actual Thickness (μm)	10	100
Thickness (μm)	12.9	79.5
Water (%)	88.1	93.1
Hydrogen peroxide (%)	11.9	6.9

The erroneously low cuvette thickness calculated for the 100 μm cuvette is a giveaway that the analyte contains substances other than water and hydrogen peroxide.

In addition, it may be possible to qualitatively determine if some other contaminants are present by continuing to observe the spectrum that is measured from the sensor. Given that there is already a calibrated spectrum of what hydrogen peroxide and water should look like using this sensor, any major deviations could give a clue that something is wrong and further investigation is necessary.

A third approach that was considered as a means of achieving selectivity was to generate a combined calibration matrix for solutions of ethanol-in-water and peroxide-in-water, to determine how well this would work for ternary mixtures. However, the technique was relatively inaccurate even when applied to a binary ethanol-water mixture, with a relatively large scatter between measurements, Table 7-5 and Table 7-6. Clearly, the absorption spectra of water and peroxide are sufficiently similar to result in them being confused by this technique.

Table 7-5 The concentrations of hydrogen peroxide, water and ethanol calculated from the 10micron calibration matrix, using a sample containing 95% ethanol and 5% water.

Ethanol (%)	91.8
Water (%)	14.6
Hydrogen peroxide (%)	-6.5

Table 7-6 The concentrations of hydrogen peroxide, water and ethanol calculated from the 100micron calibration matrix, using a sample containing 95% ethanol and 5% water.

Ethanol (%)	92.1
Water (%)	5.3
Hydrogen peroxide (%)	2.6

Given the extra effort, and little reward, expanding the calibration matrix to include additional possible contaminants would be unfeasible. The current set-up lacks the spectral resolution required to cope with increased matrix entries, and there are already issues with that in a two component matrix.

The best way of monitoring the sample for contaminants using the two species data is to check the thickness and possibly qualitatively check the refractive index of the absorbance spectrum collected, as the three (or more) species calculation does not improve the experiment in any meaningful way.

7.2.4 Absorption of Mist

The previous section showed that the concentration of hydrogen peroxides in liquid can be determined using spectroscopy in the mid-infrared (3-4.4 microns). The next step was to determine whether it would be possible to determine the concentration of hydrogen peroxide in a mist consisting of droplets of hydrogen peroxide solution suspended in air. The main issues in adapting the above technique are (1) the increase in

path length that the beam of light must travel, (2) scattering by the mist droplets, and (3) uncertainty regarding what proportion of the beam path is actually liquid phase analyte.

The mist chamber is 12.7 cm wide, which if, it was completely full of water would prevent any transmission in the range of 3-4.4 microns. However, due to the fact that it is a mist, the path length from the point of view of analytical chemistry is not that long. Equation 6-1 in Chapter 6.1.2 describes the mass of mist moving through the mist chamber every minute in terms of hydrogen peroxide/water concentration and the duty cycle of the nebuliser. Given that air flow was 7.5 L/min, it was possible to determine the volume of the water in the mist flow, which is multiplied by the chamber width to estimate an effective path length, shown Table 7-7.

Table 7-7 The estimated effective path length of water for each duty cycle.

Duty Cycle (%)	Mist Flux (g/min)	Mist Flux (L/min)	Volume of Water in Mist Flow (L/L)	Effective Path Length (μm)
5	1.05×10^{-1}	1.05×10^{-4}	1.40×10^{-5}	1.78
7.5	1.75×10^{-1}	1.75×10^{-4}	2.33×10^{-5}	2.95
10	2.40×10^{-1}	2.40×10^{-4}	3.19×10^{-5}	4.06
15	3.57×10^{-1}	3.57×10^{-4}	4.76×10^{-5}	6.04

This of course assumes that the water is distributed uniformly as a mist – the condensation on the windows is ignored. The transmission was calculated from these path lengths using Equation 7-5 that and can be seen in Figure 7-29.

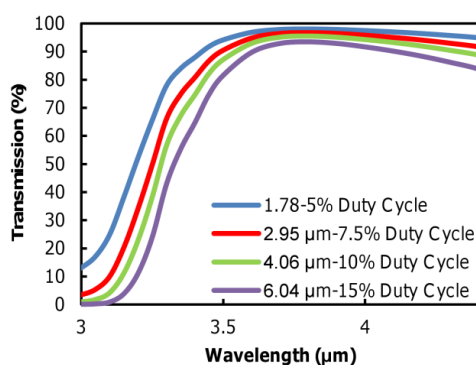


Figure 7-29 The theoretical transmission of water at different effective path lengths.

This leaves the larger problem of scattering light by the mist droplets, the effects of which are shown in Figure 7-30.

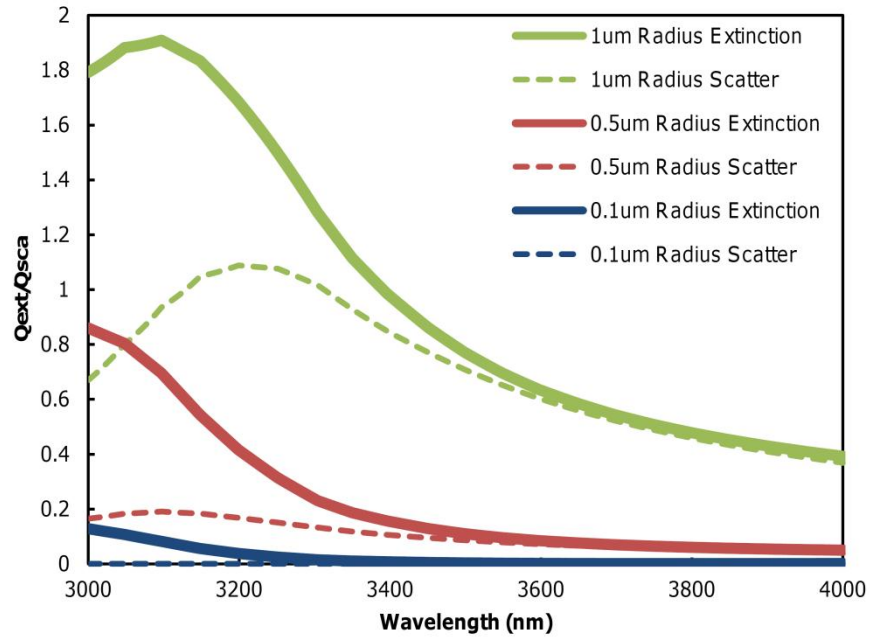


Figure 7-30 The scattering (dotted line) and extinction coefficient (solid line) of different radius spheres of water.

Figure 7-30 was produced using MiePlot v4.1.08 and the Segelstein water data provided with the program. The figure shows that as the radius of the spheres increases, the scattering signal increases until it becomes a significant part of the extinction coefficient, which results in a broadened signal. The estimated hydrogen peroxide mist droplet diameters are described in Chapter 6.1.3, Figure 6-5. The average sphere diameter was 3.69 microns and it is evident that most of the droplets have diameters between 2 and 7 microns. Water droplets were modelled based on this data using the same process as above, but using the two-mode size-dispersion option to produce spheres with the same size distribution as those droplets. Figure 7-31 shows the predicted scattering, absorbance and extinction coefficient using this model, and it can be seen that the scattering seriously broadens the signal, which as seen above causes linearity problems when trying to determine concentration.

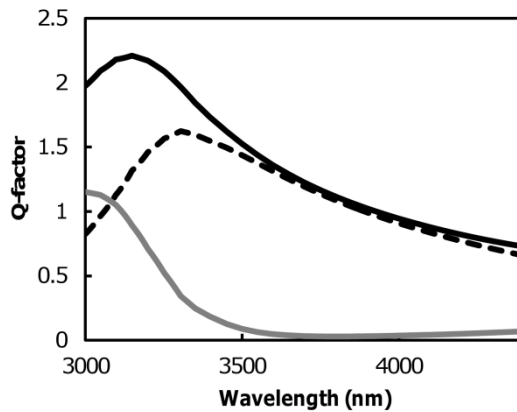


Figure 7-31 The predicted extinction coefficient (solid black line), absorbance (grey line) and scattering (dotted black line) of mist droplets produced by the nebuliser.

An idea to reduce the scattering signal and path length simultaneously was to reduce the mist density of the mist flow when it was being measured. This would be achieved by decreasing the duty cycle of the nebuliser.

The nebuliser test rig had glass windows installed (a hole was cut into the rig on opposite sides of the rig and glass microscope slides were temporarily sealed using Blu-tac). The test rig shown in Figure 7-11 was disassembled and the source and detector were placed on opposite sides of the mist chamber and held using retort stands as can be seen in Figure 7-32. The glass windows gave the rig a flat surface for the beam to enter, reducing the effects the curved surface would have on the light. Importantly the glass is much more transparent to infrared than the plastic wall of the chamber.



Figure 7-32 The detector and source are held outside the mist chamber using retort stands.

A spectrum was taken of the rig with the windows on the mist chamber and airflow of 7.5 L/min in the test rig, which was used as the maximum transmission. This signal was quite low, due to the long path length and plain glass windows, which produced significant noise, however it was not so much as to overwhelm the signal.

Water mist was used first for a proof of concept. Experiments started from a duty cycle of 5%, before being raised to 7.5%, 10% and finally 15%. Lower than 5% was tried, however, the transducer does not work at a duty cycle lower than 2.5% and a proper mist does not begin to form until 5%. The mist was allowed to stabilise before a transmission spectrum was taken, and each run was repeated once to ensure the measurement. The results of the experiment are shown in Figure 7-33.

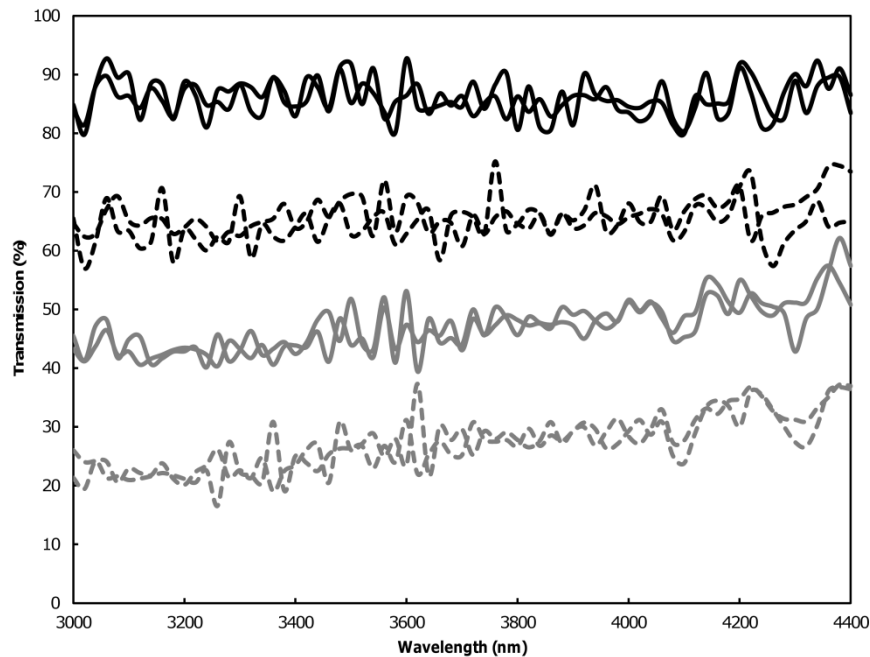


Figure 7-33 The transmission of spectra of water mist at different duty cycles, 5% (black solid lines), 7.5% (black dotted lines), 10% (grey solid lines) and 15% (grey dotted lines).

There is no identifiable spectral feature seen on the spectra shown in Figure 7-33, indicating that even a modest mist density is capable of significant scattering of light. The attenuation of the light was calculated by taking the natural log of the transmission and compared to the expected absorbance spectrum of light for each individual effective path length.

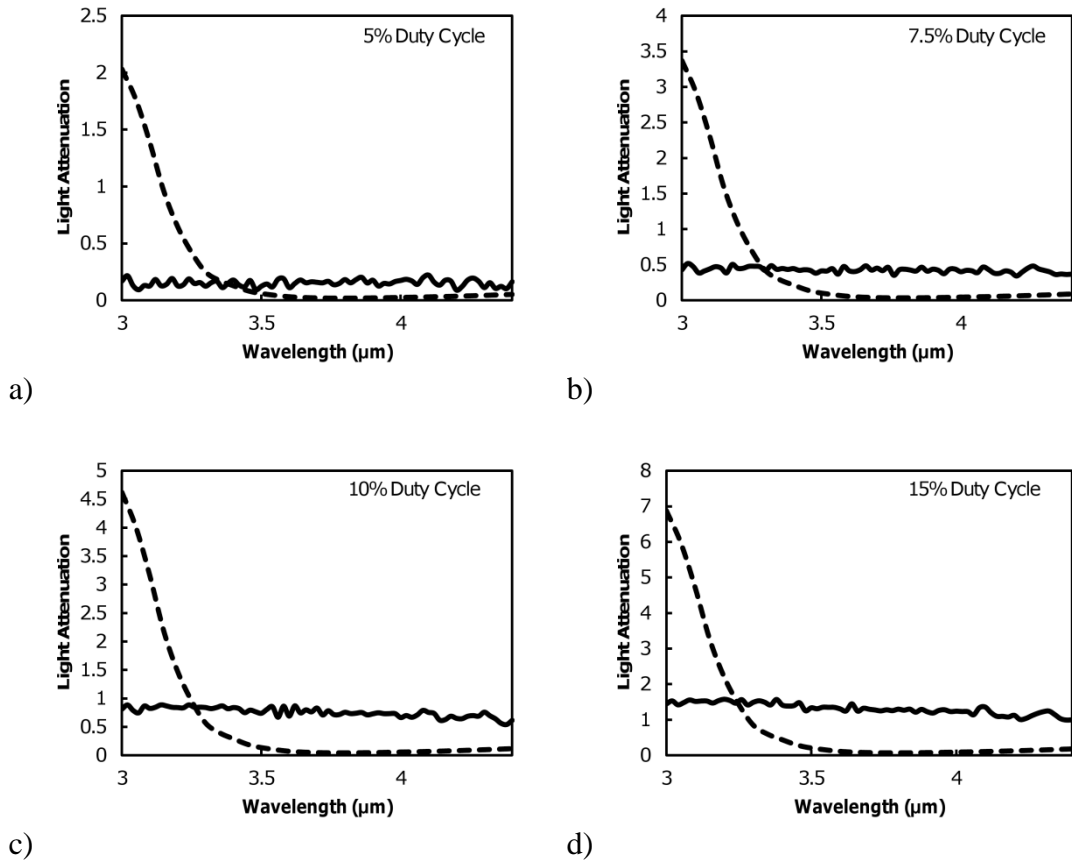


Figure 7-34 The average attenuation of light of the mist (solid line) and the theoretical absorbance of water (dotted line) for a duty cycle of a) 5%, b) 7.5%, c) 10% and d) 15%.

Figure 7-34 shows how much scattering has broadened the signal. Despite this broadening, at 3 microns the linear relationship between attenuation and thickness continues to hold, as shown in Figure 7-35.

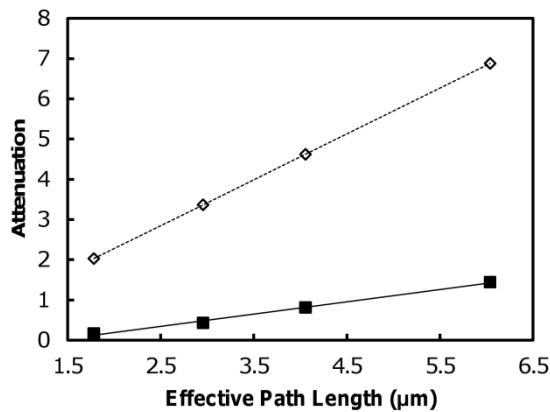


Figure 7-35 The attenuation of light at a wavelength of 3 microns for a theoretical water path length (\diamond) and for the water mist (\blacksquare). Lines show linear regression of each data set.

In this way, the sensor has shown a lower, but still linear (coefficient of determination 0.99), response to the changing concentration of water in the mist flow, with a 2-sigma confidence interval of 0.34 microns. The actual response is 3.25 microns for 1 unit of attenuation, against the theoretical response of 0.88 microns for every attenuation unit.

Given this fact, it may be possible to determine the concentration of a mist stream using the total attenuation of the signal. However, there are still complicating issues to fix before this can be viable. As shown in Chapter 7.2.2, the absorbance sensor has difficulty handling different thicknesses, and in the case of the mist stream, mist density is heavily dependent on not just the duty cycle but also the concentration of hydrogen peroxide (Chapter 6.1.2), meaning changing concentrations of hydrogen peroxide will produce different thicknesses too, even if the duty cycle is not changed. In an empirical sense this can be used for a 35% hydrogen peroxide sensor (assuming the same relationship holds true for hydrogen peroxide) and if the effective path length changes, then this would indicate that something is wrong with either the mist or the nebuliser.

Another possible sensor could be made using TDLAS, as described in Chapter 3. Using this method in the mid-infrared range can be expensive, however taking transmission spectra of MilliQ water and 35% hydrogen peroxide using a 1cm path length quartz cuvette on a Perkin-Elmer Lambda 950 UV/VIS/NIR Spectrometer, I found that there was a difference between the two spectra between 1300 nm and 1440 nm which falls into the range of some commercially available devices.

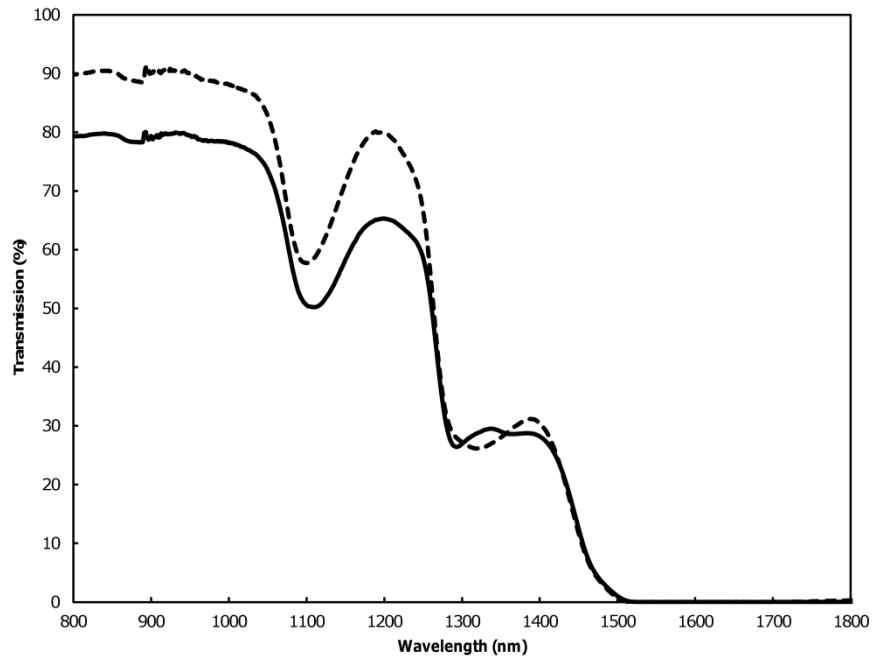


Figure 7-36 The transmission of MilliQ water (dotted line) and the 35% hydrogen peroxide (solid line).

This assumes that a mist could be produced which had a liquid phase path length of approximately 1 cm, which would be a much higher density than that used here.

7.2.5 Summary of Hydrogen Peroxide Absorption

Absorption spectroscopy is an attractive option to determine the concentration of a water/hydrogen peroxide mixture as it is relatively simple and well understood, and the measurement is based on an inherent property of the material. The focus of this study was on the absorbance of water and hydrogen peroxide in the wavelength range from 3 to 4.4 microns. Liquid hydrogen peroxide with a fixed path length (thickness) was shown to be accurately determined using a measurement at a single wavelength. However, since the focus of the study is a sensor for mist, a method for determining concentration with variable thickness was necessary. A database of absorbances was built from numerous concentrations at two different thicknesses for liquid mixtures. Broadening of the absorption peaks by the spectrometer used in these experiments proved to be a problem, which was solved by using smaller samples of the wavelength where the measurements proved to be linear. By using a 10 micron cuvette and a 100 micron cuvette it was possible to determine hydrogen peroxide concentration quite accurately and precisely, however when the data were combined into one data set, it was much less accurate and could not predict the thickness of the mixture accurately. This

would be a huge problem in the case of mist where different concentrations or flow conditions produce different thicknesses of liquid in the optical path.

It was also possible to determine whether ethanol (a proxy for many other ternary solutes) was present using the total computed thickness as a guide. A deviation of the calculated thickness from the known cuvette thickness would indicate the presence of impurity compounds. An attempt was made to determine whether possible ternary additions could be combined into the calibration matrix directly, however, it was apparent that the spectrometer being used lacked the resolution to perform this well, and it only served to make the actual measurements less accurate.

Preliminary efforts were made with applying a binary version of this approach to a mist. It was found that scattering of light by the mist stream of water was more than enough to completely broaden out any specific absorption peaks. However, after measuring the absorbance at four different duty cycles (i.e. mist densities) it was found that the signal between attenuation of the sensor and the effective thickness of the mist was still linear. This may lead to a sensor for the density of hydrogen peroxide mist, however, the chemical concentration of hydrogen peroxide has to be measured in the liquid phase first by some other means.

Another possible method of detection is TDLAS, however, in this range it may be too expensive for the scope of this project. It was found however, that if an effective path length of 1cm can be made using the mist, then a commercially available TDLAS might be suitable in the 1300-1400 nm range.

7.3 Summary of Physical Optical Sensor Investigation

Table 7-8 Summary of Optical Sensor Performance

Sensor	Coefficient of Determination (r^2)	2-Sigma Confidence Interval	Effective Range
Refractometric Gold Nanorods	Did not work	Did not work	Did not work
10 micron Absorbance Calibration	0.998	$\pm 1\%$ (v/v)	0-27.1% (v/v) H_2O_2
100 micron Absorbance Calibration	0.996	$\pm 1.5\%$ (v/v)	0-27.1% (v/v) H_2O_2
10 micron Absorbance Matrix	0.99	$\pm 1.3\%$ (v/v)	0-27.1% (v/v) H_2O_2
100 micron Absorbance Matrix	0.999	$\pm 0.5\%$ (v/v)	0-27.1% (v/v) H_2O_2
Combined 10 and 100 micron Absorbance	0.97	$\pm 3.3\%$ (v/v)	0-27.1% (v/v) H_2O_2
Mist Thickness	0.99	$\pm 0.34 \mu m$	1.78-6.04 μm

The physical optical sensor investigation for hydrogen peroxide was primarily based on two main sensor ideas: a sensor based on the refractive index of a water/hydrogen peroxide solution, and a sensor based on the absorption properties of a water/hydrogen peroxide solution.

The refractometric sensor used gold nanorods, which have been determined to be a most effective geometry in single wavelength refractometric sensors. The gold nanorods were optically characterised and found to have a resonance peak at 589 nm. These rods were then tested as a sensor in sucrose and glycerol before being tested in

hydrogen peroxide. At this point the rods were found to oxidise back to gold ions and it was established that gold was unsuitable for use.

There may be some possibility of another nanoparticle being of use, or perhaps WGM microspheres could be used as a refractometric sensor, and this could be a possible future consideration.

Absorption spectroscopy was performed first on water/hydrogen peroxide mixtures in liquid. It was shown to be possible to determine concentration by directly calibrating the concentration of hydrogen peroxide from the absorbance of a mixture in fixed thicknesses. However, it was necessary to determine concentration with a variable thickness in mist. It was thought that a matrix approach could be utilised to determine concentration and thickness together, which would be advantageous in determining the concentration of hydrogen peroxide in a mist stream. To do this, cuvettes of 10 micron and 100 micron thickness were used to take the absorbance of water and various hydrogen peroxide concentrations to build calibration matrices. The absorbances measured were then multiplied by these matrices to provide estimates of the hydrogen peroxide and water concentrations.

Line broadening was an issue, however it was partially circumvented by taking small samples of the wavelength where less broadening occurred. While there was less accuracy in an overall sense, the accuracy and precision of measurements using both the thicknesses separately was excellent. In addition, both matrices were able to accurately determine the total thickness of the mixture.

Unfortunately, when the calibration matrices of the two cuvettes were combined, the accuracy and precision reduced, and the total thickness of the 10 micron cuvette was no longer accurately determined. This effect is most likely due to the broadening, which has made determining an accurate refractive index difficult (both thicknesses are affected differently causing different refractive indices), and the obvious consequence is a bias to the thicker sample.

The fact that this cannot yet deal with different thicknesses makes a sensor for mist difficult as the effective thickness of the liquid analyte is dependent on concentration of hydrogen peroxide. Still, the sensor was tested in water of different mist densities (effective thicknesses) based on duty cycle, and a linear trend with mist

density observed. However, even at low mist densities broadening of the peaks led to no spectral features being observed. For the future it would be best to optimise this signal to find a stronger trend.

One final possibility for future work is to utilise TDLAS as a mist sensor. Assuming a large enough path length can be created using mist density (corresponding to approximately 1 cm of liquid phase), it may be possible to use commercially available equipment in a sensor in the 1300-1400 nm wavelength range.

Chapter 8 Conclusions and Future Work

This project produced several viable H_2O_2 sensor options, all of which are suitable for industrial implementation. In general, the most promising sensors for the mist streams were the calorimetric ones but, provided contiguous liquid phase is available, absorption spectroscopy also became viable.

Platinum film or MnO_2 powders were used as heterogeneous catalysts for the calorimetric sensor. In general the MnO_2 powder was more effective as a catalyst, however, this could be because there was more of it present than the platinum (the latter was only present at a nanogram level yet still produced a usable signal). The platinum catalyst was produced by co-depositing platinum and aluminium on a heated substrate, and then removing the aluminium by leaching with sodium hydroxide. It was shown in Chapter 4 that increasing the aluminium content in the initial deposition led to a platinum film which looked much more sponge-like, and seemingly had a higher surface area. In contrast, the MnO_2 film was applied simply by dipping the sensor tip into a slurry of MnO_2 powder in ethanol. Some lines of further research would be (1) to investigate the utilisation of platinum films of higher surface area for the calorimetric sensor, (2) to determine how repeatable the production of platinum films is when using sputter deposition and (3) to optimize the adhesion of the MnO_2 powder to the sensor tips by including additives into the slurry. None of these lines of work were pursued here due to time constraints.

The heterogeneous Pt was used for the H_2O_2 immersion sensor (Chapter 5) and produced a consistently useable signal from 0 to 50% H_2O_2 . This sensor could be used as a dip sensor which would be inserted into the nebuliser cup to ensure that the mist will be produced from a suitable concentration of H_2O_2 liquid. In addition, the sensor was found to provide an even better accuracy and precision when it was removed from the liquid and allowed to react/dry out in air. By monitoring the peak temperature that the sensor reached against the time it took to reach that temperature, it was possible to reliably determine the H_2O_2 concentration. The drawbacks to this latter process is that it takes slightly longer to get a reading and the concentration range over which the sensor was accurate is not as extensive. However, it does cover the 30-40% range that this project's industrial sponsor is interested in. This sensor scheme failed at concentrations greater than about 45%, with the signal becoming unrepeatable and unstable. This was

thought to be due to the onset of the phenomenon of self-accelerated decomposition of H_2O_2 , which occurs as the heat produced by decomposition boils the water part of the mixture, which constantly allows more space for H_2O_2 to react with the catalyst.

The mist stream was studied in Chapter 6. It was found that the mist density varied based on the duty cycle of the nebuliser and the concentration of H_2O_2 . In this part of the investigation, duty cycle was fixed to 20% to isolate the interaction of the mist and sensor due to concentration. MnO_2 was used as the catalyst. We were surprised to find that in mists the sensor initially recorded *decreasing* temperature with increasing H_2O_2 concentration. This was explained as being due to the heat of decomposition actually accelerating vaporisation of the H_2O component. This observation inspired a series of different sensing schemes for “online” measurement which could determine H_2O_2 concentration between 5% and 35% in the mist stream. These sensors had relatively low precision, approximately 5%, however they may be useful as a general indication of the concentration during a sterilisation cycle. Presumably a more accurate test could be used later if the concentration seems to be approaching some limiting value, or the supply of hydrogen peroxide could simply be changed to fresh reagent.

A sensing scheme that showed better accuracy was the “after mist sensor” which took into account the details of the thermal transient after the mist pulse had been ended. Both the time taken to reach the lowest temperature, and the actual lowest temperature recorded, were found to be correlated to H_2O_2 concentration. This was because the greater the concentration, the more vigorous the reaction, and the faster the evaporation of the water. The length of time to return to ambient temperature is a function of how long the reaction lasted, during which time it caused the water to evaporate. Although these parameters had a non-linear correlation with H_2O_2 concentration, reasonably accurate estimates could be made by calibrating the system. However, this did require that a full mist pulse of two to four minutes duration pass through the rig first. It may be worth some further work to determine if the same effect occurs earlier with a shorter mist pulse. These measurements were found to be affected by mist density too (as mist density changes due to concentration of H_2O_2 as well). Higher concentrations of H_2O_2 were associated with smaller values of mist density. This may be the reason for the non-linear response at higher concentrations and explained the saturation of some of the sensor schemes at about 35% H_2O_2 .

A heated sensor (sensor with a set-point temperature) was also investigated using Pt as the heterogeneous catalyst. Unlike the previous work, this was performed at various duty cycles. The idea here was to boil off the liquids and detect the H_2O_2 by a decrease in the electrical power required. While the sensor was found to be non-responsive to concentration, it did respond well with regards to variations in mist density. From here there are many avenues to travel. Given that the Pt catalyst used may not be the optimum, a better catalyst may create an even larger signal based on concentration. Another way of proceeding is to take the ambient H_2O_2 sensor described in the above paragraph and include the heated sensor so that the mist density and concentration signals can be used to determine the concentration in tandem.

Finally, Chapter 7 described the work done on possible optical H_2O_2 sensors. The first optical sensor attempted was a refractometric sensor using gold nanorods. The nanorods were tested in sucrose and glycerol to determine the response to refractive index before being tested in H_2O_2 . Unfortunately the nanorods dissolved back into gold ions as soon as they were exposed to H_2O_2 . Using, for example, the WGM microspheres described in Chapter 3, may be viable, however, I did not pursue this line of thought any further.

In addition, the absorbance of light by H_2O_2 was investigated to determine the extent to which a sensor based on that was possible. This would be preferable to a refractometric sensor, since the absorption signal is based on an intrinsic property of the molecule itself. By interrogating the mid-IR spectrum of H_2O_2 at a single wavelength, 3840 nm, a calibration curve could be derived from which concentration could be accurately ($\pm 0.87\%$ (v/v)) measured. While this is relatively straight forward to implement for liquid H_2O_2 , a mist will produce a varying (liquid) path length for the light to travel through. Application of optical absorbance in this case requires a means by which both the thickness of liquid and concentration can be determined simultaneously. A matrix-based numerical method was utilised in an attempt to produce a calibration for 10 and 100 μm thicknesses of H_2O_2 liquid. While the calibration worked fine for each cuvette individually (taking each known thickness into account), the combined calibration matrix was biased towards the data of the larger thicknesses. It appears that inclusion of calibration data from quartz cuvettes of 10 and 50 μm thickness might solve this problem, but such quartz cuvettes could not be sourced.

Measurements performed on water mist of different densities show that a linear response between absorbance and concentration (or path length) still exists despite broadening of the absorption peak due to scattering. Given this, performing measurements on various concentrations of H₂O₂ should be done to determine whether this type of spectroscopy can be done on the mist. If not there are still TD-LAS techniques to be tried.

In summary, at the present time it appears that the two most accurate designs of sensor are the immersion calorimetric sensor (an accuracy of ± 2 to 4% H₂O₂, depending on range covered), or the inclusion of a cuvette between the H₂O₂ source and the cup to perform optical absorption spectroscopy on liquid ($\pm 1\%$ H₂O₂ accuracy). Both of these probe the contiguous liquid phase, such as exists in the reservoir of the system. As far as the actual mist phase is concerned, the calorimetric sensor also shows promise, with an accuracy of ± 3 to 4% H₂O₂, depending on range covered.

References

1. N.A. Klapes and D. Vesley, Vapor-phase hydrogen peroxide as a surface decontaminant and sterilant. *Applied and Environmental Microbiology*, 1990. **56**(2): p. 503-506.
2. B.M. Andersen, M. Rasch, K. Hochlin, F.H. Jensen, P. Wismar, and J.E. Fredriksen, Decontamination of rooms, medical equipment and ambulances using an aerosol of hydrogen peroxide disinfectant. *Journal of Hospital Infection*, 2006. **62**(2): p. 149-155.
3. S.S. Pietrobon, High density liquid rocket boosters for the space shuttle. *Journal of the British Interplanetary Society*, 1999. **52**(5-6): p. 163–168.
4. R. Hage and A. Lienke, Applications of transition-metal catalysts to textile and wood-pulp bleaching. *Angewandte Chemie International Edition*, 2006. **45**(2): p. 206-222.
5. G. Grigoropoulou, J.H. Clark, and J.A. Elings, Recent developments on the epoxidation of alkenes using hydrogen peroxide as an oxidant. *Green Chemistry*, 2003. **5**(1): p. 1-7.
6. C.W. Jones, Chapter 1 Introduction to the preparation and properties of hydrogen peroxide, in *Applications of hydrogen peroxide and derivatives: Rsc clean technology monographs*, J.H. Clark, Editor. 1999, The royal society of chemistry: Cambridge.
7. C. Lei and J. Deng, Hydrogen peroxide sensor based on coimmobilized methylene green and horseradish peroxidase in the same montmorillonite-modified bovine serum albumin glutaraldehyde matrix on a glassy carbon electrode surface. *Analytical Chemistry*, 1996. **68**(19): p. 3344-3349.
8. Y. Liu, J. Qian, X. Fu, H. Liu, J. Deng, and T. Yu, Immobilization of horseradish peroxidase onto a composite membrane of regenerated silkfibroin and polyvinyl alcohol and its application to a new methylene blue-mediating sensor for hydrogen peroxide. *Enzyme and Microbial Technology*, 1997. **21**(3): p. 154-159.
9. S. Uchiyama and Y. Sano, Hydrogen peroxide sensor with bienzyme membrane based on antagonism of reaction to tyrosinase reaction using common substrate. *Electroanalysis*, 2000. **12**(11): p. 817-820.

10. X. Xu, S. Liu, and H. Ju, A novel hydrogen peroxide sensor via the direct electrochemistry of horseradish peroxidase immobilized on colloidal gold modified screen-printed electrode. *Sensors*, 2003. **3**(9): p. 350-360.
11. Y. Song, L. Wang, C. Ren, G. Zhu, and Z. Li, A novel hydrogen peroxide sensor based on horseradish peroxidase immobilized in DNA films on a gold electrode. *Sensors and Actuators B: Chemical*, 2006. **114**(2): p. 1001–1006.
12. C. Fan, I. Suzuki, Q. Chen, G. Li, and J.-i. Anzai, An unmediated hydrogen peroxide sensor based on a hemoglobin-SDS film modified electrode *Analytical Letters*, 2000. **33**(13): p. 2631-2644.
13. X.B. Kang, G.C. Pang, X.Y. Liang, M. Wang, J. Liu, and W.M. Zhu, Study on a hydrogen peroxide biosensor based on horseradish peroxidase/GNPs-thionine/chitosan. *Electrochimica Acta*, 2012. **62**: p. 327-334.
14. J.M. Chapsal, M.M. Bourbigot, and D. Thomas, Oxidation of aromatic compounds by haemoglobin. *Water Research*, 1986. **20**(6): p. 709-713.
15. H. Zhang, X. Zou, and D. Han, Hydrogen peroxide sensor based on hemoglobin immobilized on glassy carbon electrode with SiO₂ nanoparticles/chitosan film as immobilization matrix. *Analytical Letters*, 2007. **40**(4): p. 661-676.
16. X. Zeng, X. Liu, B. Kong, Y. Wang, and W. Wei, A sensitive nonenzymatic hydrogen peroxide sensor based on DNA–Cu²⁺ complex electrodeposition onto glassy carbon electrode. *Sensors and Actuators B: Chemical*, 2008. **133**(2): p. 381-386.
17. G. Li, Y. Wang, and H. Xu, A hydrogen peroxide sensor prepared by electropolymerization of pyrrole based on screen-printed carbon paste electrodes. *Sensors*, 2007. **7**(3): p. 239-250.
18. A. Mehta, S. Patil, H. Bang, H.J. Cho, and S. Seal, A novel multivalent nanomaterial based hydrogen peroxide sensor. *Sensors and Actuators A: Physical*, 2007. **134**(1): p. 146-151.
19. S. Yao, S. Yuan, J. Xu, Y. wang, J. Luo, and S. Hu, A hydrogen peroxide sensor based on colloidal MnO₂/Na-montmorillonite. *Applied Clay Science*, 2006. **33**(1): p. 35-42.
20. Y. Shimizu, H. Komatsu, S. Michishita, N. Miura, and N. Yamazoe, *Hydrogen peroxide sensor based on carbon electrode loaded with perovskite-type oxide*, in

Transducers '95, The 8th International Conference on Solid-state Sensors and Actuators, and Eurosensors IX. 1995, IEEE: Stockholm, Sweden. p. 981 - 984

21. A. Gutes, I. Laboriante, C. Carraro, and R. Maboudian, Palladium nanostructures from galvanic displacement as hydrogen peroxide sensor. *Sensors and Actuators B: Chemical*, 2010. **147**(2): p. 681-686.
22. M.R. Guascito, E. Filippo, C. Malitesta, D. Manno, A. Serra, and A. Turco, A new amperometric nanostructured sensor for the analytical determination of hydrogen peroxide. *Biosensors and Bioelectronics*, 2008. **24**(4): p. 1057-1063.
23. J. Hrbac, V. Halouzka, R. Zboril, K. Papadopoulos, and T. Triantis, Carbon electrodes modified by nanoscopic iron(III) oxides to assemble chemical sensors for the hydrogen peroxide amperometric detection. *Electroanalysis*, 2007. **19**(17): p. 1850-1854.
24. R. Garjonyte and A. Malinauskas, Amperometric sensor for hydrogen peroxide, based on Cu₂O or CuO modified carbon paste electrodes. *Fresenius' Journal of Analytical Chemistry*, 1998. **360**(1): p. 122-123.
25. R. Garjonyte and A. Malinauskas, Operational stability of amperometric hydrogen peroxide sensors, based on ferrous and copper hexacyanoferrates. *Sensors and Actuators B: Chemical*, 1999. **56**(1-2): p. 93-97.
26. D. Ravishankaran, N. Uehara, and T. Kato, A novel hydrogen peroxide sensor based on specifically interacted silver dispersed sol-gel derived ceramic composite electrode. *Analytical Sciences*, 2002. **18**(8): p. 935-937.
27. A. Malinauskas, R. Araminaitė, G. Mickevičiūtė, and R. Garjonytė, Evaluation of operational stability of Prussian blue- and cobalt hexacyanoferrate-based amperometric hydrogen peroxide sensors for biosensing application. *Materials Science and Engineering: C*, 2004. **24**(4): p. 513-519.
28. S.A.G. Evans, J.M. Elliott, L.M. Andrews, P.N. Bartlett, P.J. Doyle, and G. Denuault, Detection of hydrogen peroxide at mesoporous platinum microelectrodes. *Analytical Chemistry*, 2002. **74**(6): p. 1322-1326.
29. D.T.V. Anh, W. Olthuis, and P. Bergveld, A hydrogen peroxide sensor for exhaled breath measurement. *Sensors and Actuators B: Chemical*, 2005. **111-112**(11): p. 494-499.

30. D.T.V. Anh, W. Olthuis, and P. Bergveld, Electroactive gate materials for a hydrogen peroxide sensitive ^EMOSFET. *IEEE Sensors Journal*, 2002. **2**(1): p. 26-33.
31. E. Filippo, A. Serra, and D. Manno, Poly(vinyl alcohol) capped silver nanoparticles as localized surface plasmon resonance-based hydrogen peroxide sensor. *Sensors and Actuators B: Chemical*, 2009. **138**(2): p. 625-630.
32. I.D. Villar, I.R. Matiasa, F.J. Arregui, J. Echeverría, and R.O. Claus, Strategies for fabrication of hydrogen peroxide sensors based on electrostatic self-assembly (ESA) method. *Sensors and Actuators B: Chemical*, 2005. **108**(1-2): p. 751-757.
33. E. Omanovic and K. Kalcher, A new chemiluminescence sensor for hydrogen peroxide determination. *International Journal of Environmental Analytical Chemistry*, 2005. **85**(12-13): p. 853-860.
34. B. Li, Z. Zhang, and L. Zhao, Chemiluminescent flow-through sensor for hydrogen peroxide based on sol-gel immobilized hemoglobin as catalyst. *Analytica Chimica Acta*, 2001. **445**(2): p. 161-167.
35. H.E. Posch and O.S. Wolfbeis, Optical sensor for hydrogen peroxide. *Microchimica Acta*, 1989. **97**(1-2): p. 41-50.
36. H.S. Voraberger, W. Trettnak, and V. Ribitsch, Optochemical hydrogen peroxide sensor based on oxygen detection. *Sensors and Actuators B: Chemical*, 2003. **90**(1-3): p. 324-331.
37. J.F. McAleer, P.t. Moseley, P. Bourke, J.O.W. Norris, and R. Stephan, Tin dioxide gas sensors: use of the seebeck effect. *Sensors and Actuators*, 1985. **8**(3): p. 251-257.
38. P. Kirchner, B. Li, H. Spelthahn, H. Henkel, A. Schneider, P. Friedrich, J. Kolstad, M. Keusgen, and M.J. Schöning, Thin-film calorimetric H₂O₂ gas sensor for the validation of germicidal effectivity in aseptic filling processes. *Procedia Chemistry*, 2009. **1**(1): p. 983-986.
39. V. Casey, J. Cleary, G. D'Arcy, and J.B. McMonagle, Calorimetric combustible gas sensor based on a planar thermopile array: Fabrication, characterisation, and gas response. *Sensors and Actuators B: Chemical*, 2003. **96**(1-2): p. 114-123.
40. M. Merzlyakov, Integrated circuit thermopile as a new type of temperature modulated calorimeter. *Thermochimica Acta*, 2003. **403**(1): p. 65-81.

41. M.L. Antonelli, C. Spadaro, and R.F. Tornelli, A microcalorimetric sensor for food and cosmetic analyses: L-Malic acid determination. *Talanta*, 2008. **74**(5): p. 145-1454.
42. T.D. McGee, Thermistors and semiconductors for temperature measurement, in *Principles and Methods of Temperature Measurement*, T.D. McGee, Editor. 1988, Wiley-Interscience: New York. p. 203-236.
43. Y. Zhang and S. Tadigadapa, Calorimetric biosensors with integrated microfluidic channels. *Biosensors and Bioelectronics*, 2004. **19**(12): p. 1733-1743.
44. D. Neuschäfer, W. Budach, C. Wanke, and S.-D. Chibout, Evanescent resonator chips: a universal platform with superior sensitivity for fluorescence-based microarrays. *Biosens. Bioelectron.*, 2003. **18**(4): p. 489-497.
45. X.-Z. Wu, H. Shindoh, and T. Hobo, Thermo-optical flow-injection determination for hydrogen peroxide based on an enzymic reaction heat-induced optical beam deflection. *Analytica Chimica Acta*, 1995. **299**(3): p. 333-336.
46. S.J. Choquette and L. Locascio-Brown, Thermal detection of enzyme-labelled antigen-antibody complexes using fiber-optic interferometry. *Sensors and Actuators B: Chemical*, 1984. **22**(2): p. 89-96.
47. M.A. Rahman, M.-S. Won, and Y.-B. Shim, Xanthine sensors based on anodic and cathodic detection of enzymatically generated hydrogen peroxide. *Electroanalysis*, 2007. **19**(6): p. 631-637.
48. D.B. Broughton and R.L. Wentworth, Mechanism of decomposition of hydrogen peroxide solutions with manganese dioxide. 1. *Journal of the American Chemical Society*, 1947. **69**(4): p. 741-744.
49. D.W. Mckee, Catalytic decomposition of hydrogen peroxide by metals and alloys of the platinum group. *Journal of Catalysis*, 1969. **14**(4): p. 355-364.
50. G. Bianchi, F. Mazza, and T. Mussini, Catalytic decomposition of acid hydrogen peroxide solutions on platinum, iridium, palladium and gold surfaces. *Electrochimica Acta*, 1962. **7**(4): p. 457-473.
51. J.C. Chaston, Reaction of oxygen with the platinum metals I-the oxidation of platinum. *Platinum Metals Review*, 1964. **8**(2): p. 50-54.

52. J.H. Clark and D.J. Macquarrie, Supported Catalysts, in *Kirk-Othmer Encyclopedia of Chemical Technology, Electronic Release, 4th Edition*, M. Grayson, Editor. 2002, John Wiley & Sons, Inc.: New York. p. 322-344.
53. A. Mills, Platinized platinum, platinum sponge and platinum black. *Bulletin of the Scientific Instrument Society*, 2006(89): p. 35-37.
54. J.W. Hightower and P.H. Emmett, Chemisorption of carbon monoxide on finely divided platinum held in aqueous suspension. *Journal of Colloid and Interface Science*, 1966. **22**(2): p. 158-160.
55. R. Adams, V. Voorhees, and R.L. Shriner, Platinum catalysts for reductions. *Organic Syntheses*, 1928. **8**: p. 92.
56. O. Loew, Representation of very active platinum black. *Journal of the American Chemical Society*, 1890. **23**(1): p. 289-290.
57. R. Willstätter and D.H.D. Hatt, Hydrogenation of aromatic compounds with platinum and hydrogen. *Journal of the American Chemical Society*, 1912. **45**(2): p. 1471-1481.
58. V. Voorhees and R. Adams, The use of the oxides of platinum for the catalytic reduction of organic compounds. *Journal of the American Chemical Society*, 1922. **44**(6): p. 1397-1405.
59. C.W. Scheeren, J.B. Domingos, G. Machado, and J. Dupont, Hydrogen reduction of Adams' Catalyst in ionic liquids: formation and stabilization of Pt(0) nanoparticles. *Journal of Physical Chemistry C*, 2008. **112**(42): p. 16463–16469.
60. L. Maya, G.M. Brown, and T. Thundat, Porous platinum electrodes derived from the reduction of sputtered platinum dioxide films. *Journal of Applied Electrochemistry*, 1999. **29**(7): p. 883-888.
61. M. Raney, Method of producing finely-divided nickel, *United States Patent Office*, 1927, United States
62. A. Mills, Porous platinum morphologies: platinised, sponge and black. *Platinum Metals Review*, 2007. **51**(1): p. 52.
63. J. Wrzyszczyk, H. Grabowska, M. Zawadzki, L. Kepinski, and L. Krajczyk, A method to produce porous platinum film. *Platinum Metals Review*, 2005. **49**(3): p. 138-140.

64. H. Liu, P. He, Z. Li, and J. Li, High surface area nanoporous platinum: facile fabrication and electrocatalytic activity. *Nanotechnology*, 2006. **17**(9): p. 2167-2173.
65. M.B. Cortie, A. Maarooft, G.B. Smith, and P. Ngoepe, Nanoscale coatings of AuAl_x and PtAl_x and their mesoporous elemental derivatives. *Current Applied Physics*, 2006. **6**(3): p. 440-443.
66. E. Hecht, Refraction, in *Optics 4th Edition*, A. Black, Editor. 2002, Addison Wesley: San Francisco. p. 100-106.
67. S. Egashira, The Abbé refractometer as a liquid chromatographic detector using an image sensor for bound location. *Journal of Chromatography A*, 1985. **332**: p. 195-201.
68. A. Banerjee, Enhanced refractometric optical sensing by using one-dimensional ternary photonic crystals. *Progress In Electromagnetics Research*, 2009. **89**: p. 11-22.
69. N.A. Mortensen, S. Xiao, and J. Pedersen, Liquid-infiltrated photonic crystals: enhanced light-matter interactions for lab-on-a-chip applications. *Microfluidics and Nanofluidics*, 2008. **4**(1-2): p. 117-127.
70. J.D. Suter, I.M. White, H. Zhu, H. Shi, C.W. Caldwell, and X. Fan, Label-free quantitative DNA detection using the liquid core optical ring resonator. *Biosensors and Bioelectronics*, 2008. **23**(7): p. 1003-1009.
71. J. Li and T. Zheng, A comparison of chemical sensors based on the different ordered inverse opal films. *Sensors and Actuators B: Chemical*, 2008. **131**(1): p. 190-195.
72. I.M. White and X. Fan, On the performance quantification of resonant refractive index sensors. *Optics Express*, 2008. **16**(2): p. 1020-1028.
73. G.-D. Kim, G.-S. Son, H.-S. Lee, K.-D. Kim, and S.-S. Lee, Integrated photonic glucose biosensor using a vertically coupled microring resonator in polymers. *Optics Communications*, 2008. **281**(18): p. 4644-4647.
74. G. Yang, I.M. White, and X. Fan, An opto-fluidic ring resonator biosensor for the detection of organophosphorus pesticides. *Sensors and Actuators B: Chemical*, 2008. **133**(1): p. 105-112.
75. F. Xu, V. Pruneri, V. Finazzi, and G. Brambilla, An embedded optical nanowire loop resonator refractometric sensor. *Optics Express*, 2008. **16**(2): p. 1062-1067.

76. F. Xu, V. Pruneri, V. Finazzi, and G. Brambilla, *High sensitivity refractometric sensor based on embedded optical microfiber loop resonator*, in *Conference on Lasers and Electro-Optics (CLEO)/Quantum Electronics and Laser Science Conference and Photonic Applications Systems Technologies*. 2008, OSA Technical Digest (CD) (Optical Society of America, 2008), paper CMJ7: San Jose, California.
77. V. Zamora, A. Díez, M.V. Andrés, and B. Gimeno, Refractometric sensor based on whispering-gallery modes of thin capillaries. *Optics Express*, 2007. **15**(19): p. 12011-12016.
78. M. Noto, D. Keng, I. Teraoka, and S. Arnold, Detection of protein orientation on the silica microsphere surface using transverse electric/transverse magnetic whispering gallery modes. *Biophysical Journal*, 2007. **92**(12): p. 4466-4472.
79. K. Schmitt, B. Schirmer, C. Hoffmann, A. Brandenburg, and P. Meyrueis, Interferometric biosensor based on planar optical waveguide sensor chips for label-free detection of surface bound bioreactions. *Biosensors and Bioelectronics*, 2007. **22**(11): p. 2591-2597.
80. J.D. Suter, I.M. White, H. Zhu, and X. Fan, Thermal characterization of liquid core optical ring resonator sensors. *Applied Optics*, 2007. **46**(3): p. 389-396.
81. I.M. White, H. Zhu, J.D. Suter, N.M. Hanumegowda, H. Oveys, M. Zourob, and X. Fan, Refractometric sensors for lab-on-a-chip based on optical ring resonators. *IEEE Sensors Journal*, 2007. **7**(1): p. 28-35.
82. F. Xu, P. Horak, and G. Brambilla, Optical microfiber coil resonator refractometric sensor. *Optics Express*, 2007. **15**(12): p. 7888-7893.
83. Y. Sarov, K. Ivanova, T. Ivanov, B.E. Volland, and I.W. Rangelow, Microfluidic analysis based on total internal light reflection. *Microelectronic Engineering*, 2006. **83**(4-9): p. 1294-1297.
84. N.M. Hanumegowda, I.M. White, and X. Fan, Aqueous mercuric ion detection with microsphere optical ring resonator sensors. *Sensors and Actuators B: Chemical*, 2006. **120**(1): p. 207-212.
85. W.C.L. Hopman, P. Pottier, D. Yudistira, J.v. Lith, P.V. Lambeck, R.M.D.L. Rue, A. Driessen, H.J.W.M. Hoekstra, and R.M.d. Ridder, Quasi-one-dimensional photonic crystal as a compact building-block for refractometric

- optical sensors. *IEEE Journal of Selected Topics in Quantum Electronics*, 2005. **11**(1): p. 11-16.
86. N.M. Hanumegowda, C.J. Stica, B.C. Patel, I. White, and X. Fan, Refractometric sensors based on microsphere resonators. *Applied Physics Letters*, 2005. **87**(201107): p. 201107-1-201107-3.
 87. D. Stadnik and A. Dybko, An intrinsic fibre optic chemical sensor based on light coupling phenomenon. *Sensors and Actuators B: Chemical*, 2005. **107**(1): p. 184-187.
 88. A. Andreev, B. Pantchev, P. Danesh, B. Zafirova, E. Karakoleva, E. Vlaikova, and E. Alipieva, A refractometric sensor using index-sensitive mode resonance between single-mode fiber and thin film amorphous silicon waveguide. *Sensors and Actuators B: Chemical*, 2005. **106**(1): p. 484-488.
 89. R. Bernini, S. Campopiano, L. Zeni, and P.M. Sarro, ARROW optical waveguides based sensors. *Sensors and Actuators B: Chemical*, 2004. **100**(1-2): p. 143-146.
 90. P.L. Swart, Long-period grating Michelson refractometric sensor. *Measurement Science and Technology*, 2004. **15**(8): p. 1576-1580.
 91. K. Cottier, M. Wiki, G. Voirin, H. Gao, and R.E. Kunz, Label-free highly sensitive detection of (small) molecules by wavelength interrogation of integrated optical chips. *Sensors and Actuators B: Chemical*, 2003. **91**(1-3): p. 241-251.
 92. R. Eberl and J. Wilke, NIR spectroscopic application of a refractometric sensor. *Sensors and Actuators B: Chemical*, 1996. **32**(3): p. 203-208.
 93. L.M. Gowman and C.R. Ethier, Concentration and concentration gradient measurements in an ultrafiltration concentration polarization layer Part I: A laser-based refractometric experimental technique. *Journal of Membrane Science*, 1997. **131**(1-2): p. 95-105.
 94. C.R. Ethier and D.C. Lin, Refractometric measurement of polarized layer structure: studies of hyaluronic acid ultrafiltration. *Journal of Membrane Science*, 1992. **68**(3): p. 249-261.
 95. S. Binu, V.P.M. Pillai, V. Pradeepkumar, B.B. Padhy, C.S. Joseph, and N. Chandrasekaran, Fibre optic glucose sensor. *Materials Science and Engineering: C*, 2009. **29**(1): p. 183-186.

96. K. Cherif, S. Hleli, A. Abdelghani, N. Jaffrezic-Renault, and V. Matejec, Chemical detection in liquid media with a refractometric sensor based on a multimode optical fibre. *Sensors*, 2002. **2**(6): p. 195-204.
97. P.A. Giguere and P. Geoffrion, Refractive index of hydrogen peroxide solutions. A revision. *Canadian Journal of Research*, 1949. **27B**(3): p. 168-173.
98. Y. Wang, J. Deng, J. Di, and Y. Tu, Electrodeposition of large size gold nanoparticles on indium tin oxide glass and application as refractive index sensor. *Electrochemistry Communications*, 2009. **11**(5): p. 1034-1037.
99. Y.-S. Shon, H.Y. Choi, M.S. Guerrero, and C. Kwon, Preparation of nanostructured film arrays for transmission localized surface plasmon sensing. *Plasmonics*, 2009. **4**(2): p. 95-105.
100. V.V.R. Sai, T. Kundu, and S. Mukherji, Novel U-bent fiber optic probe for localized surface plasmon resonance based biosensor. *Biosensors and Bioelectronics*, 2009. **24**(9): p. 2804-2809.
101. V. Coello and S.I. Bozhevolnyi, Surface plasmon polariton excitation and manipulation by nanoparticle arrays. *Optics Communications*, 2009. **282**(14): p. 3032-3036.
102. S. Zhu, C. Du, and Y. Fu, Biochemistry nanosensor-based hybrid metallic nanostructures array. *Sensors and Actuators B: Chemical*, 2009. **137**(1): p. 345-349.
103. R.V. Olkhov, J.D. Fowke, and A.M. Shaw, Whole serum BSA antibody screening using a label-free biophotonic nanoparticle array. *Analytical Biochemistry*, 2009. **385**(2): p. 234-241.
104. H.M. Chen, L. Pang, A. Kher, and Y. Fainman, Three-dimensional composite metallodielectric nanostructure for enhanced surface plasmon resonance sensing. *Applied Physics Letters*, 2009. **94**(073117): p. 073117-1-073117-3.
105. C. Huang, K. Bonroy, G. Reekmans, W. Laureyn, K. Verhaegen, I.D. Vlaminc, L. Lagae, and G. Borghs, Localized surface plasmon resonance biosensor integrated with microfluidic chip. *Biomedical Microdevices*, 2009. **11**(4): p. 893-901.
106. Y.B. Zheng and T.J. Huang, Surface plasmons of metal nanostructure arrays: From nanoengineering to active plasmonics. *Journal of Laboratory Automation*, 2008. **13**(4): p. 215-226.

107. V.G. Praig, G. Piret, M. Manesse, X. Castel, R. Boukherroub, and S. Szunerits, Seed-mediated electrochemical growth of gold nanostructures on indium tin oxide thin films. *Electrochimica Acta*, 2008. **53**(27): p. 7838-7844.
108. T. Nakanishi, H. Takada, H. Iida, M. Kajiura, and T. Osaka, Immobilization of gold nanoparticles on optical waveguides with organosilane monolayer. *Colloids and Surfaces A: Physicochemical and Engineering Aspects*, 2008. **313-314**: p. 234-238.
109. S. Zhu, F. Li, C. Du, and Y. Fu, A localized surface plasmon resonance nanosensor based on rhombic Ag nanoparticle array. *Sensors and Actuators B: Chemical*, 2008. **134**(1): p. 193-198.
110. M.E. Stewart, C.R. Anderton, L.B. Thompson, J. Maria, S.K. Gray, J.A. Rogers, and R.G. Nuzzo, Nanostructured plasmonic sensors. *Chemical Review*, 2008. **108**(2): p. 494-521.
111. L. Yang, C. Du, and X. Luo, Numerical study of optical properties of single silver nanobowtie with anisotropic topology. *Applied Physics Letters*, 2008. **92**(1): p. 53-59.
112. K.M. Mayer, S. Lee, H. Liao, B.C. Rostro, A. Fuentes, P.T. Scully, C.L. Nehl, and J.H. Hafner, A label-free immunoassay based upon localized surface plasmon resonance of gold nanorods. *ACS Nano*, 2008. **2**(4): p. 687-692.
113. J. Ye, K. Bonroy, D. Nelis, F. Frederix, J. D'Haen, G. Maes, and G. Borghs, Enhanced localized surface plasmon resonance sensing on three-dimensional gold nanoparticles assemblies. *Colloids and Surfaces A: Physicochemical and Engineering Aspects*, 2008. **321**(1-3): p. 313-317.
114. I. Tanahashi, H. Iwagishi, and G. Chang, Localized surface plasmon resonance sensing properties of photocatalytically prepared Au/TiO₂ films. *Materials Letters*, 2008. **62**(17-18): p. 2714-2716.
115. T.-J. Lin and C.-T. Lou, Reflection-based localized surface plasmon resonance fiber-optic probe for chemical and biochemical sensing at high-pressure conditions. *Journal of Supercritical Fluids*, 2007. **41**(2): p. 317-325.
116. T. Rindzevicius, Y. Alaverdyan, M. Käll, W.A. Murray, and W.L. Barnes, Long-range refractive index sensing using plasmonic nanostructures. *Journal of Physical Chemistry C*, 2007. **111**(32): p. 11806-11810.

117. S.M. Marinakos, S. Chen, and A. Chilkoti, Plasmonic detection of a model analyte in serum by a gold nanorod sensor. *Analytical Chemistry*, 2007. **79**(14): p. 5278-5283.
118. S.M. Wang, J.J. Xiao, and K.W. Yu, Tunable coupled plasmon modes via nanoshell particle chains. *Optics Communications*, 2007. **279**(2): p. 384-389.
119. M.A. Bratescu, N. Saito, H. Mori, and O. Takai, Localized surface plasmon resonance of silicon compounds adsorbed on silver nanoparticles. *Surface Science*, 2007. **601**(18): p. 3886–3891.
120. I. Ruach-Nir, T.A. Bendikov, I. Doron-Mor, Z. Barkay, A. Vaskevich, and I. Rubinstein, Silica-stabilized gold island films for transmission localized surface plasmon sensing. *Journal of the American Chemical Society*, 2007. **129**(1): p. 84-92.
121. G. Barbillon, J.-L. Bijeon, J. Plain, M.L.d.l. Chapelle, P.-M. Adam, and P. Royer, Electron beam lithography designed chemical nanosensors based on localized surface plasmon resonance. *Surface Science*, 2007. **601**(21): p. 5057–5061.
122. C.-S. Cheng, Y.-Q. Chen, and C.-J. Lu, Organic vapour sensing using localized surface plasmon resonance spectrum of metallic nanoparticles self assemble monolayer. *Talanta*, 2007. **73**(2): p. 358-365.
123. N. Hashimoto, T. Hashimoto, T. Teranishi, H. Nasu, and K. Kamiya, Cycle performance of sol–gel optical sensor based on localized surface plasmon resonance of silver particles. *Sensors and Actuators B: Chemical*, 2006. **113**(1): p. 382–388.
124. J. Grand, P.-M. Adam, A.-S. Grimault, A. Vial, M.L.d.l. Chapelle, J.-L. Bijeon, S. Kostcheev, and P. Royer, Optical extinction spectroscopy of oblate, prolate and ellipsoid shaped gold nanoparticles: experiments and theory. *Plasmonics*, 2006. **1**(2-4): p. 135-140.
125. J.-L. Tang, S.-F. Cheng, W.-T. Hsu, T.-Y. Chiang, and L.-K. Chau, Fiber-optic biochemical sensing with a colloidal gold-modified long period fiber grating. *Sensors and Actuators B: Chemical*, 2006. **119**(1): p. 105–109.
126. J. Kim, G.L. Liu, Y. Lu, and L.P. Lee, Spectral tuning of localised surface plasmonpolariton resonance in metallic nano-crescents. *IEE Proceedings Nanobiotechnology*, 2006. **153**(3): p. 42-46.

127. A. Csáki, A. Steinbrück, S. Schröter, and W. Fritzsche, Combination of nanoholes with metal nanoparticles—fabrication and characterization of novel plasmonic nanostructures. *Plasmonics*, 2006. **1**(2-4): p. 147-155.
128. A.J. Haes, S. Zou, J. Zhao, G.C. Schatz, and R.P.V. Duyne, Localized surface plasmon resonance spectroscopy near molecular resonances. *Journal of the American Chemical Society*, 2006. **128**(33): p. 10905-10914.
129. A.K. Sharma and B.D. Gupta, Fiber optic sensor based on surface plasmon resonance with nanoparticle films. *Photonics and Nanostructures: Fundamentals and Applications*, 2005. **3**(1): p. 30-37.
130. E. Hutter and J.H. Fendler, Exploitation of localized surface plasmon resonance. *Advanced Materials*, 2004. **16**(19): p. 1685-1706.
131. A.G. Brolo, R. Gordon, B. Leathem, and K.L. Kavanagh, Surface plasmon sensor based on the enhanced light transmission through arrays of nanoholes in gold films. *Langmuir*, 2004. **20**(12): p. 4813-4815.
132. G. Kalyuzhny, A. Vaskevich, M.A. Schneeweiss, and I. Rubinstein, Transmission surface-plasmon resonance (T-SPR) measurements for monitoring adsorption on ultrathin gold island films. *Chemistry - A European Journal*, 2002. **8**(17): p. 3850-3857.
133. X.W. Shen, C.Z. Huang, and Y.F. Li, Localized surface plasmon resonance sensing detection of glucose in the serum samples of diabetes sufferers based on the redox reaction of chlorauric acid. *Talanta*, 2007. **72**(4): p. 1432-1437.
134. C.-D. Chen, S.-F. Cheng, L.-K. Chau, and C.R.C. Wang, Sensing capability of the localized surface plasmon resonance of gold nanorods. *Biosensors and Bioelectronics*, 2007. **22**(6): p. 926-932.
135. K. Aslan, J.R. Lakowicz, and C.D. Geddes, Tunable plasmonic glucose sensing based on the dissociation of Con A-aggregated dextran-coated gold colloids. *Analytica Chimica Acta*, 2004. **517**(1-2): p. 139-144.
136. K. Aslan, J.R. Lakowicz, and C.D. Geddes, Nanogold-plasmon-resonance-based glucose sensing. *Analytical Biochemistry*, 2004. **330**(1): p. 145-155.
137. Q. Zhang, Y.N. Tan, J. Xie, and J.Y. Lee, Colloidal synthesis of plasmonic metallic nanoparticles. *Plasmonics*, 2009. **4**(1): p. 9-22.
138. E. Hecht, Fibre Optics, in *Optics 4th Edition*, A. Black, Editor. 2002, Addison Wesley: San Francisco. p. 193-201.

139. Y.A. Vlasov and S.J. McNab, Losses in single-mode silicon-on-insulator strip waveguides and bends. *Opt. Express*, 2004. **12**(8): p. 1622-1631.
140. M. Piliarik, P. Kvasnička, N. Galler, J.R. Krenn, and J. Homola, Local refractive index sensitivity of plasmonic nanoparticles. *Optics Express*, 2011. **19**(10): p. 9213-9220.
141. L. Wang, P. Yang, Y. Li, H. Chen, M. Li, and F. Luo, A flow injection chemiluminescence method for the determination of fluoroquinolone derivative using the reaction of luminol and hydrogen peroxide catalyzed by gold nanoparticles. *Talanta*, 2007. **72**(3): p. 1066-1072.
142. A. Tittl, C. Kremers, J. Dorfmueller, D.N. Chigrin, and H. Giessen, Spectral shifts in optical nanoantenna-enhanced hydrogen sensors. *Optical Materials Express*, 2012. **2**(2): p. 111-118.
143. C.S. Kealley, M.D. Arnold, A. Porkovich, and M.B. Cortie, Sensors based on monochromatic interrogation of a localised surface plasmon resonance. *Sensors and Actuators B: Chemical*, 2010. **148**(1): p. 34-40.
144. S.K. Poznyak and A.I. Kulak, An electroluminescence optical sensor system based on TiO₂ film electrodes for continuous measurement of H₂O₂ concentration in solution. *Sensors and Actuators B: Chemical*, 1994. **22**(2): p. 97-100.
145. E. Hecht, Rayleigh Scattering, in *Optics 4th Edition*, A. Black, Editor. 2002, Addison Wesley: San Francisco. p. 85-95.
146. P.A. Giguere, The infrared spectrum of hydrogen peroxide. *Journal of Chemical Physics*, 1950. **18**(1): p. 88-92.
147. T. Chiba, Spectroscopy: Visible spectroscopy and colorimetry, in *Encyclopedia of Food Sciences and Nutrition Second Edition*, Caballero Benjamin, Editor. 2003, Academic Press: Oxford. p. 5454-5459.
148. P. Jacobsson and P. Johansson, Measurement methods: Vibrational Properties: Raman and Infra Red, in *Encyclopedia of Electrochemical Power Sources*, Jürgen Garche, Editor. 2009, Elsevier: Amsterdam. p. 802-812.
149. E. Hecht, The Spontaneous Raman Effect, in *Optics 4th Edition*, A. Black, Editor. 2002, Addison Wesley: San Francisco. p. 603-606.
150. R.C. Taylor, The infrared spectra of hydrogen and deuterium peroxides in condensed phases *Journal of Chemical Physics*, 1950. **18**(6): p. 898-899.

151. W.C. Schumb, C.N. Satterfield, and R.L. Wentworth, Hydrogen Peroxide, A.C.S Monograph No. 128. 1955, New York: Reinhold Publishing Corporation.
152. P.A. Giguère, G. Morissette, A.W. Olmos, and O. Knop, Hydrogen peroxide and its analogues VII. Calorimetric properties of the systems H₂O - H₂O₂ and D₂O - D₂O₂. *Canadian Journal of Chemistry*, 1955. **33**(5): p. 804-820.
153. J.A. Curcio and C.C. Petty, The near infrared absorption spectrum of liquid water. *Journal of the Optical Society of America*, 1951. **41**(5): p. 302.
154. W.M. Irvin and J.B. Pollack, Infrared optical properties of water and ice spheres. *Icarus*, 1968. **8**(1-3): p. 324-360.
155. I.F. McVey, Non-dispersive mid-infrared sensor for vaporized hydrogen peroxide, *USPTO*, 2005, Steris Inc., US
156. H. Voraberger, V. Ribitsch, M. Janotta, and B. Mizaikoff, Application of mid-infrared spectroscopy: Measuring hydrogen peroxide concentrations in bleaching baths. *Applied Spectroscopy*, 2003. **57**(5): p. 574-579.
157. F.M. Mirabella, Principles, Theory and Practice of Internal Reflection Spectroscopy, in *Handbook of Vibrational Spectroscopy*, J.M. Chalmers and P. Griffiths, Editors. 2006, John Wiley & Sons, Ltd.: Chichester, UK.
158. H.E. Schlosser, J. Wolfrum, V. Ebert, B.A. Williams, R.S. Sheinson, and J.W. Fleming, In situ determination of molecular oxygen concentrations in full-scale fire-suppression tests using tunable diode laser absorption spectroscopy. *Proceedings of the Combustion Institute*, 2002. **29**(1): p. 353-360.
159. A.R. Awtry, B.T. Fisher, R.A. Moffatt, V. Ebert, and J.W. Fleming, Simultaneous diode laser based in situ quantification of oxygen, carbon monoxide, water vapor, and liquid water in a dense water mist environment *Proceedings of the Combustion Institute*, 2007. **31**(1): p. 799-806.
160. F. Wang, K.F. Cen, N. Li, Q.X. Huang, X. Chao, J.H. Yan, and Y. Chi, Simultaneous measurement on gas concentration and particle mass concentration by tunable diode laser *Flow Measurement and Instrumentation*, 2010. **21**(3): p. 382-387.
161. J.R. Ferraro, K. Nakamoto, and C.W. Brown, Instrumentation and Experimental Techniques, in *Introductory Raman Spectroscopy (Second Edition)*. 2003, Academic Press: San Diego. p. 95-146.

162. R.C. Taylor and P.C. Cross, Raman spectra of hydrogen peroxide in condensed phases. I. The spectra of the pure liquid and its aqueous solutions. *Journal of Chemical Physics*, 1956. **24**(1): p. 41-44.
163. J.R. Ferraro, K. Nakamoto, and C.W. Brown, Basic Theory, in *Introductory Raman Spectroscopy (Second Edition)*. 2003, Academic Press: San Diego. p. 1-94.
164. J. Heilborn, Multiple Linear Regression, in *Science and Engineering Programs Apple II Edition*. 1981, OSBORNE/McGraw-Hill: Berkeley. p. 28-31.
165. L.A. Cornish, R. Süß, A. Watson, and S.N. Prins, Building a thermodynamic database for platinum-based superalloys: Part I. *Platinum Metals Review*, 2007. **51**(3): p. 104-115.
166. N. Näther, H. Henkel, A. Schneider, and M.J. Schöning, Investigation of different catalytically active and passive materials for realising a hydrogen peroxide gas sensor. *physica status solidi A*, 2009. **206**(3): p. 449– 454.
167. S. Reisert, H. Henkel, A. Schneider, D. Schäfer, P. Friedrich, J. Berger, and M.J. Schöning, Development of a handheld sensor system for the online measurement of hydrogen peroxide in aseptic filling systems. *physica status solidi A*, 2010. **207**(4): p. 913–918.
168. A.J. Porkovich, M.D. Arnold, G. Kouzmina, B. Hingley, A.Dowd, and M.B. Cortie, Calorimetric sensor for use in hydrogen peroxide aqueous solutions. *Sensor Letters*, 2011. **9**(2): p. 695-697.
169. A.J. Porkovich, M.D. Arnold, G. Kouzmina, B. Hingley, and M.B. Cortie, Calorimetric Sensor for H₂O₂/H₂O Mist Streams. *IEEE Sensors Journal*, 2012. **12**(7): p. 2392-2398.
170. D. Pissuwan, *Selective targeting and thermal destruction of live cells using antibody functionalised gold nanoparticles*, in *Faculty of Science*. 2008, University of Technology, Sydney: Sydney. p. 168.
171. G.M. Hale and M.R. Querry, Optical constants of water in the 200-nm to 200- μ m wavelength region. *Applied Optics*, 1973. **12**(3): p. 555-563.
172. R. Kitamura, L. Pilon, and M. Jonasz, Optical constants of silica glass from extreme ultraviolet to far infrared at near room temperature. *Applied Optics*, 2007. **46**(33): p. 8118-8133.

Appendix

Additional data is presented here as additional evidence for conclusions presented in earlier chapters.

The following work is from Chapter 4.5 and includes the calculation of the heat transfer co-efficient, h , for the other fluids and RTDs C and D.

The work below is an example of the raw data used to calculate the heat transfer coefficient of unforced water for the RTDs A and B in Chapter 4.5.2. The equations of the lines fitted are also included. The values are calculated from 110 s.

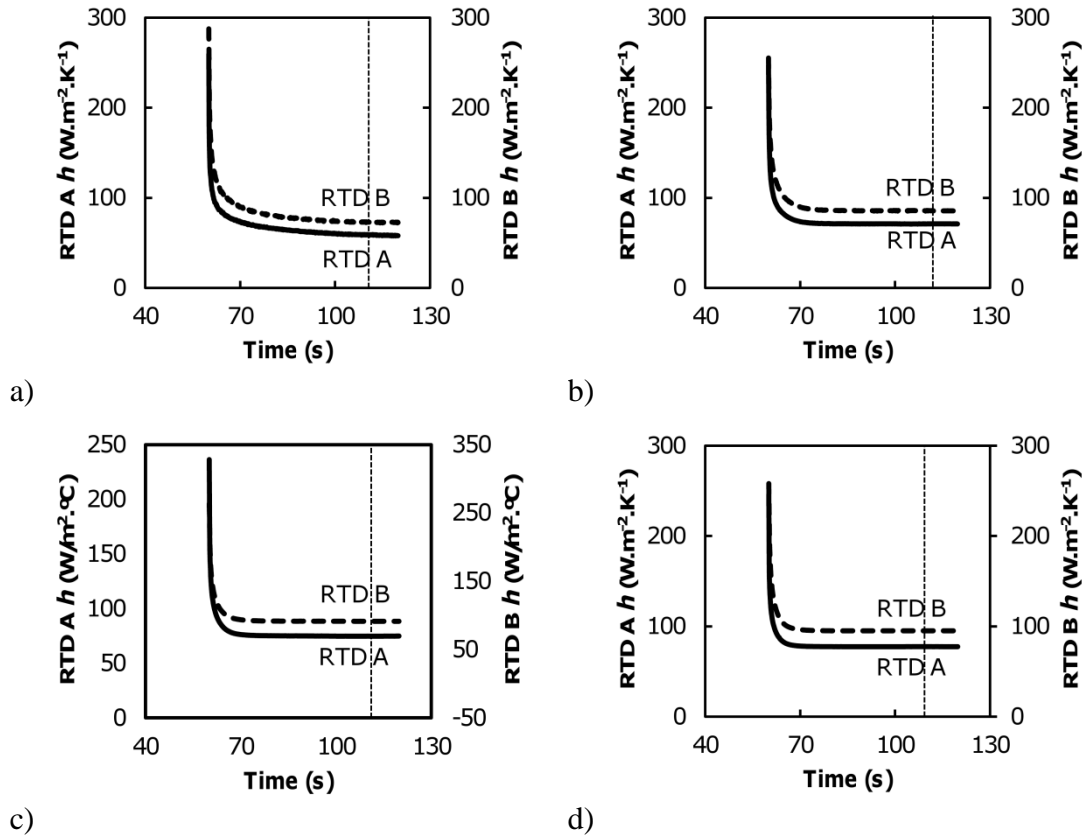


Figure A-1 An example of the calculation heat transfer coefficient, h , for RTDs A and B in still water. The dotted line represents the point at which the RTD temperature was stable and is the point that h is taken from. Each chart represents a different input power of a) 9 mW b) 75 mW c) 180 mW and d) 310 mW.

$$h \text{ of RTD A} = 32.1(2.46 - e^{-2.47 \times 10^{-2}x}) \quad \text{Equation A-1}$$

$$h \text{ of RTD B} = 99.6(1 - e^{-4.80 \times 10^{-2}x}) \quad \text{Equation A-2}$$

Equation A-1 shows a trend which describes the average h values with respect to temperature for RTD A. The regression has an excellent coefficient of determination of $r^2 \approx 1$ and a small 2-sigma confidence interval of $\pm 4.78 \times 10^{-2} \text{ W.m}^{-2}.\text{K}^{-1}$, which is again a good fit. The average h values for RTD B do not show a good fit, with Equation A-2 having a coefficient of determination of $r^2 = 0.60$, and a 2-sigma confidence interval of $20.5 \text{ W.m}^{-2}.\text{K}^{-1}$, both of which show poor correlation, which is due to the large uncertainty in the 82°C measurements.

Following on from this work are examples of the raw data used to calculate the heat transfer coefficient of unforced air for the RTDs C and D in Chapter 4.5.1. The equations of the lines fitted are also included. The values are calculated from 410 s.

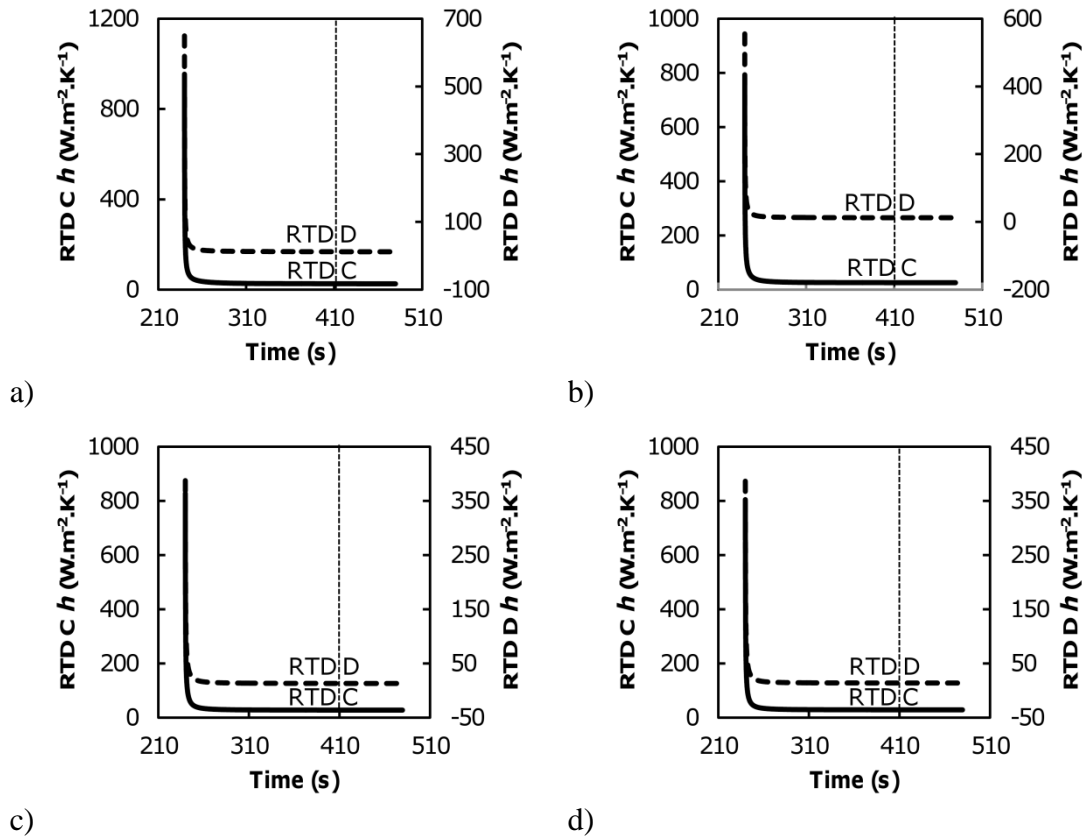


Figure A-2 An example of the calculation heat transfer coefficient, h , for RTDs C and D in still air. The dotted line represents the point at which the RTD temperature was stable and is the point that h is taken from. Each chart represents a different input power of a) 9 mW b) 75 mW c) 180 mW and d) 310 mW

$$h \text{ of RTD C} = 2.72 \times 10^{-2}x + 25.0 \quad \text{Equation A-3}$$

$$h \text{ of RTD D} = 2.21 \times 10^{-2}x + 11.0 \quad \text{Equation A-4}$$

Equation A-3 shows the linear relationship between the h values and temperature. This relationship has a high coefficient of determination of 0.993 and a 2-sigma confidence interval of $\pm 0.227 \text{ W.m}^{-2}.\text{K}^{-1}$, while Equation A-4 has a similarly high coefficient of determination of 0.997 and a narrow 2-sigma confidence interval of $\pm 0.124 \text{ W.m}^{-2}.\text{K}^{-1}$. Both RTDs showed a similar slope and was just offset by $12 \text{ W.m}^{-2}.\text{K}^{-1}$.

This next figure shows examples of the raw data used to calculate the heat transfer coefficient of forced air for the RTDs C and D in Chapter 4.5.1. The equations of the lines fitted are also included. The values are calculated from 410 s.

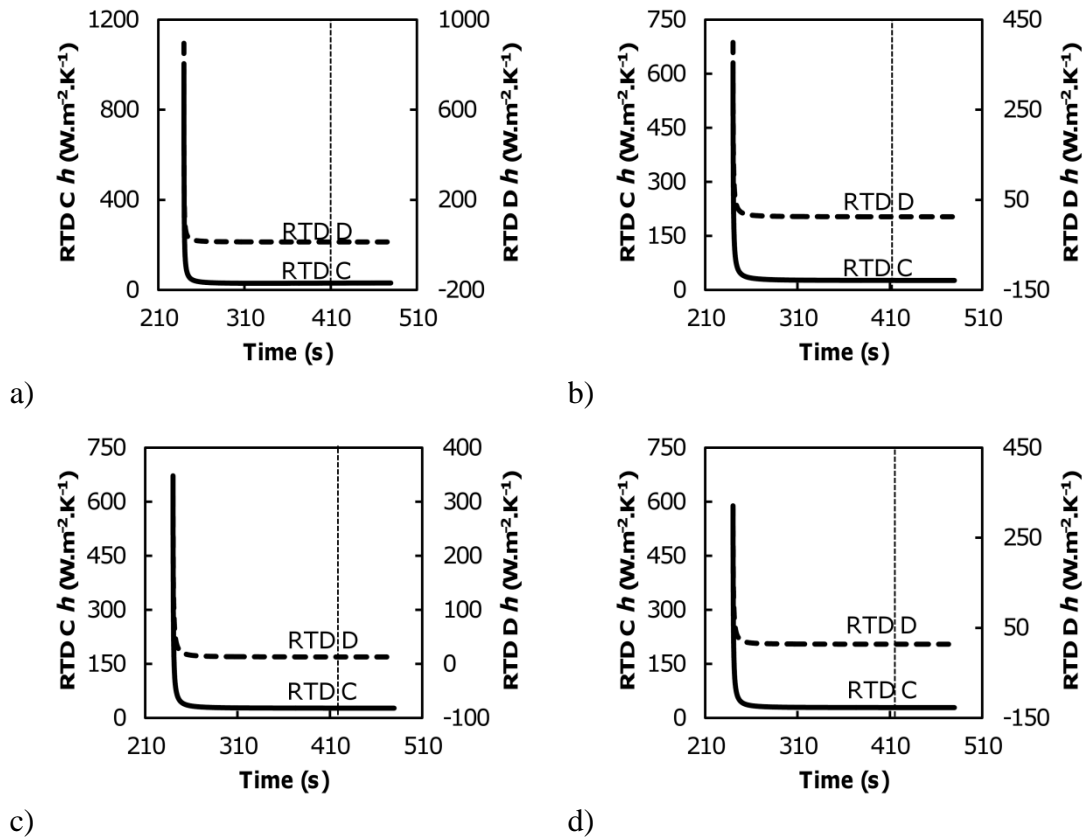


Figure A-3 An example of the calculation heat transfer coefficient, h , for RTDs C and D in 7.5 L/min flowing air. The dotted line represents the point at which the RTD temperature was stable and is the point that h is taken from. Each chart represents a different input power of a) 9 mW b) 75 mW c) 180 mW and d) 310 mW.

$$h \text{ of RTD C} = 1.44 \times 10^{-2}x + 26.4 \quad \text{Equation A-5}$$

$$h \text{ of RTD D} = 1.88 \times 10^{-2}x + 11.3 \quad \text{Equation A-6}$$

Equation A-5 shows a linear trend that has been fitted to the RTD C data. The correlation to this trend and the data is poor, with $r^2=0.62$ and a 2-sigma confidence interval of $\pm 1.08 \text{ W.m}^{-2}.\text{K}^{-1}$. Equation A-6 however has good linear correlation, with $r^2=0.99$ and a narrow 2-sigma confidence interval of $\pm 0.189 \text{ W.m}^{-2}.\text{K}^{-1}$. Both equations are similar to the RTD C and RTD D in still air (the uncertainty has dropped the slope of Equation A-5 and increased the intercept) which suggests that there is not much difference in h value for between still air and 7.5 L/min flowing air.

Finally, the following are examples of the raw data used to calculate the heat transfer coefficient of the water mist in Chapter 4.5.2. The values are calculated from 175 s.

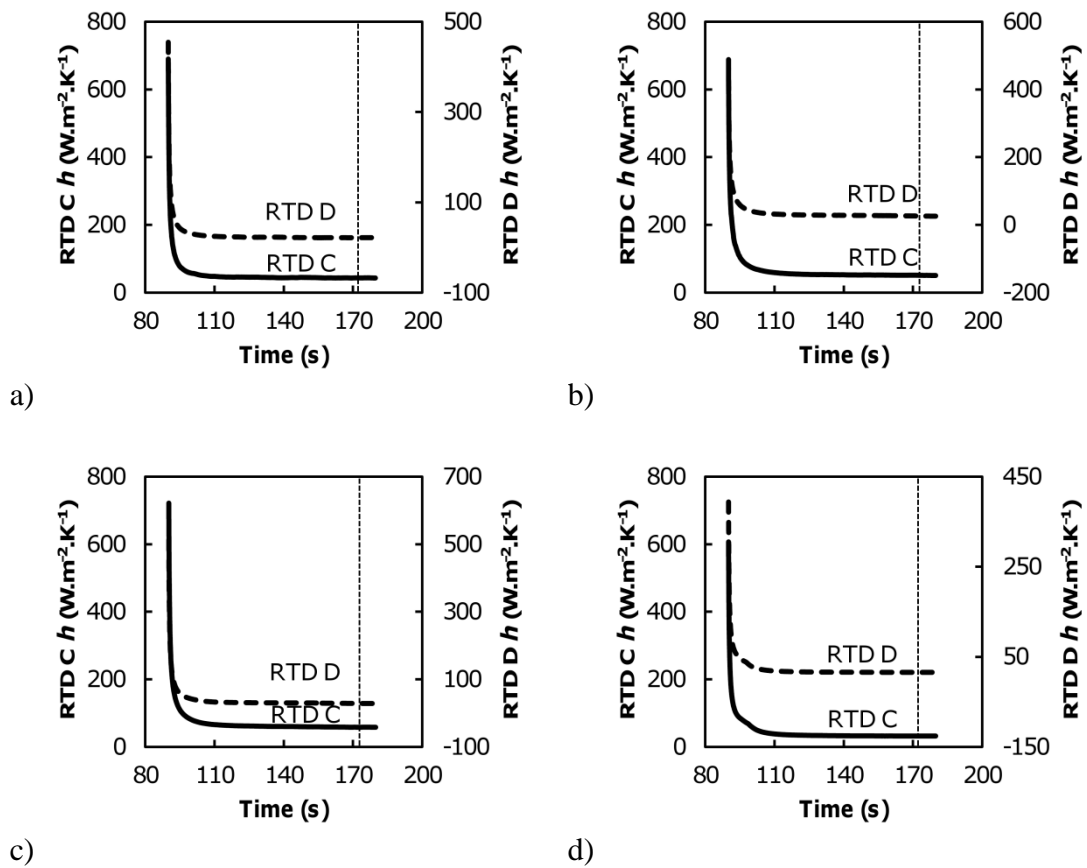


Figure A-4 An example of the calculation heat transfer coefficient, h , for RTDs C and D in water mist with and airflow of 7.5 L/min. The dotted line represents the point at which the RTD temperature was stable and is the point that h is taken from. Each chart represents a different input power of a) 9 mW b) 75 mW c) 180 mW and d) 310 mW.

The next series of tables is also work from Chapter 4.5 further detailing the calculated h values of the RTDs in the various fluids.

Table A-1 The h values for RTDs A and B in air at a stable value (approx. 400s) for each run at each heated power

Run	Time (s)	RTD B h ($W.m^{-2}.K^{-1}$)	RTD A h ($W.m^{-2}.K^{-1}$)
9 mW Run1	400	14.2	12.8
9 mW Run2	400	13.8	12.5
9 mW Run3	400	14.0	12.7
9 mW Run4	400	14.4	12.7
9 mW Run5	404	13.8	12.7
75 mW Run1	400	14.4	13.6
75 mW Run2	407	15.0	13.5
75 mW Run3	404	14.3	13.6
75 mW Run4	400	14.3	13.6
75 mW Run5	400	15.1	13.6
180 mW Run1	401	16.3	14.5
180 mW Run2	400	15.3	14.5
180 mW Run3	404	15.2	14.4
180 mW Run4	407	16.2	14.4
180 mW Run5	400	16.1	14.4
310 mW Run1	401	16.0	15.3
310 mW Run2	400	17.3	15.3
310 mW Run3	402	15.6	15.2
310 mW Run4	400	15.4	15.2
310 mW Run5	401	15.3	15.2

Table A-2 The h values for RTDs A and B in water at a stable value (approx. 110s) for each run at each heated power

Run	Time (s)	RTD B h ($W.m^{-2}.K^{-1}$)	RTD A h ($W.m^{-2}.K^{-1}$)
9 mW Run1	110	72.9	59.0
9 mW Run2	110	99.9	81.7
9 mW Run3	110	72.1	58.5
9 mW Run4	110	71.3	59.3
9 mW Run5	110	75.0	58.2
75 mW Run1	110	85.6	71.0
75 mW Run2	110	84.9	70.4
75 mW Run3	110	70.2	69.6
75 mW Run4	110	85.3	70.0
75 mW Run5	110	85.3	69.7
180 mW Run1	110	132.1	74.8
180 mW Run2	110	132.4	75.0
180 mW Run3	110	91.5	74.7
180 mW Run4	110	91.3	74.7
180 mW Run5	110	91.1	74.6
310 mW Run1	111	95.1	77.3
310 mW Run2	110	95.3	77.3
310 mW Run3	110	95.2	77.5
310 mW Run4	110	95.2	77.4
310 mW Run5	110	95.4	77.3

Table A-3 The h values for RTDs C and D in still air at a stable value (approx. 400s) for each run at each heated power

Run	Time (s)	RTD D h ($W.m^{-2}.K^{-1}$)	RTD C h ($W.m^{-2}.K^{-1}$)
9 mW Run1	400	11.6	25.6
9 mW Run2	403	11.7	25.7
9 mW Run3	403	11.7	26.3
9 mW Run4	400	11.5	25.3
9 mW Run5	429	11.5	25.9
75 mW Run1	402	12.1	26.1
75 mW Run2	403	12.1	26.2
75 mW Run3	403	12.2	26.2
75 mW Run4	400	12.1	26.3
75 mW Run5	400	12.1	26.2
180 mW Run1	401	12.9	27.1
180 mW Run2	400	12.9	27.2
180 mW Run3	400	12.8	27.2
180 mW Run4	400	12.9	27.2
180 mW Run5	405	12.8	27.2
310 mW Run1	402	13.6	28.1
310 mW Run2	404	13.6	28.2
310 mW Run3	404	13.6	28.2
310 mW Run4	400	13.6	28.2
310 mW Run5	401	13.6	28.1

Table A-4 The h values for RTDs C and D in air flowing at 7.5L/min at a stable value (approx. 400s) for each run at each heated power

Run	Time (s)	RTD D h ($W.m^{-2}.K^{-1}$)	RTD C h ($W.m^{-2}.K^{-1}$)
9 mW Run1	400	12.3	29.4
9 mW Run2	402	11.8	26.9
9 mW Run3	402	11.8	26.7
9 mW Run4	399	11.7	27.0
9 mW Run5	401	11.8	26.5
75 mW Run1	405	12.1	26.6
75 mW Run2	416	12.1	26.6
75 mW Run3	402	12.2	26.7
75 mW Run4	429	12.1	26.6
75 mW Run5	400	12.2	26.7
180 mW Run1	399	12.8	27.4
180 mW Run2	408	12.8	27.5
180 mW Run3	402	12.8	27.3
180 mW Run4	400	12.9	27.5
180 mW Run5	399	12.9	27.5
310 mW Run1	400	13.5	28.3
310 mW Run2	399	13.6	28.4
310 mW Run3	443	13.5	28.3
310 mW Run4	399	13.6	28.4
310 mW Run5	399	13.5	28.4

Table A-5 The h values for RTDs C and D in mist produced with 20% duty cycle at 7.5L/min at a stable value (approx. 140s) for each run at each heated power

Run	Time (s)	RTD D h ($W.m^{-2}.K^{-1}$)	RTD C h ($W.m^{-2}.K^{-1}$)
9 mW Run1	140	22.7	43.9
9 mW Run2	140	22.8	45.1
9 mW Run3	141	23.2	46.3
9 mW Run4	140	23.6	48.9
9 mW Run5	140	24.5	47.5
75 mW Run1	142	28.4	52.5
75 mW Run2	140	26.2	52.2
75 mW Run3	140	25.6	51.8
75 mW Run4	146	24.9	51.5
75 mW Run5	140	25.2	51.7
180 mW Run1	140	30.0	60.0
180 mW Run2	142	27.0	39.2
180 mW Run3	140	16.1	56.5
180 mW Run4	141	15.9	46.2
180 mW Run5	141	15.5	34.1
180 mW Run6	140	33.5	35.9
180 mW Run7	140	18.5	33.3
180 mW Run8	140	15.8	33.5
180 mW Run9	141	15.5	33.4
310 mW Run1	140	15.7	33.2
310 mW Run2	140	15.7	32.9
310 mW Run3	140	15.6	33.0
310 mW Run4	140	15.6	32.8
310 mW Run5	141	15.6	33.0

Table A-6 The h values for RTDs C and D in mist produced with 20% duty cycle at 7.5L/min at a stable value (approx. 150s) for each run at each heated power

Run	Time (s)	RTD D h ($W.m^{-2}.K^{-1}$)	RTD C h ($W.m^{-2}.K^{-1}$)
9 mW Run1	150	22.0	45.1
9 mW Run2	150	22.5	44.8
9 mW Run3	151	23.2	45.8
9 mW Run4	150	23.4	49.4
9 mW Run5	150	24.1	46.7
75 mW Run1	152	28.0	52.2
75 mW Run2	150	25.8	51.5
75 mW Run3	150	25.3	51.3
75 mW Run4	158	24.6	51.1
75 mW Run5	150	24.7	51.2
180 mW Run1	150	29.6	59.2
180 mW Run2	152	20.1	38.9
180 mW Run3	150	15.9	56.0
180 mW Run4	151	15.7	46.1
180 mW Run5	152	15.3	33.7
180 mW Run6	150	33.2	33.8
180 mW Run7	150	18.1	32.7
180 mW Run8	150	15.5	32.9
180 mW Run9	151	15.3	33.1
310 mW Run1	150	15.6	32.8
310 mW Run2	150	15.5	32.8
310 mW Run3	150	15.4	32.7
310 mW Run4	150	15.4	32.5
310 mW Run5	151	15.5	32.6

Table A-7 The h values for RTDs C and D in mist produced with 20% duty cycle at 7.5L/min at a stable value (approx. 175s) for each run at each heated power

Run	Time (s)	RTD D h ($W.m^{-2}.K^{-1}$)	RTD C h ($W.m^{-2}.K^{-1}$)
9 mW Run1	175	21.9	43.9
9 mW Run2	175	22.1	44.8
9 mW Run3	177	22.7	44.8
9 mW Run4	175	23.1	48.8
9 mW Run5	175	23.6	46.6
75 mW Run1	177	26.1	51.0
75 mW Run2	175	25.3	50.9
75 mW Run3	175	24.8	50.6
75 mW Run4	175	24.4	50.2
75 mW Run5	175	24.3	50.4
180 mW Run1	175	28.1	58.1
180 mW Run2	177	16.0	38.7
180 mW Run3	175	15.6	41.4
180 mW Run4	176	15.4	36.5
180 mW Run5	177	15.1	32.9
180 mW Run6	175	27.1	32.5
180 mW Run7	175	17.2	32.5
180 mW Run8	176	15.2	32.6
180 mW Run9	176	15.1	32.7
310 mW Run1	175	15.4	32.4
310 mW Run2	175	15.3	32.2
310 mW Run3	175	15.3	32.2
310 mW Run4	175	15.2	31.9
310 mW Run5	176	15.2	32.1

The following is the raw energy drawn from the droplet on heated sensors in Chapter 5.2.5 for RTDs set to a temperature of 105 °C and 130 °C.

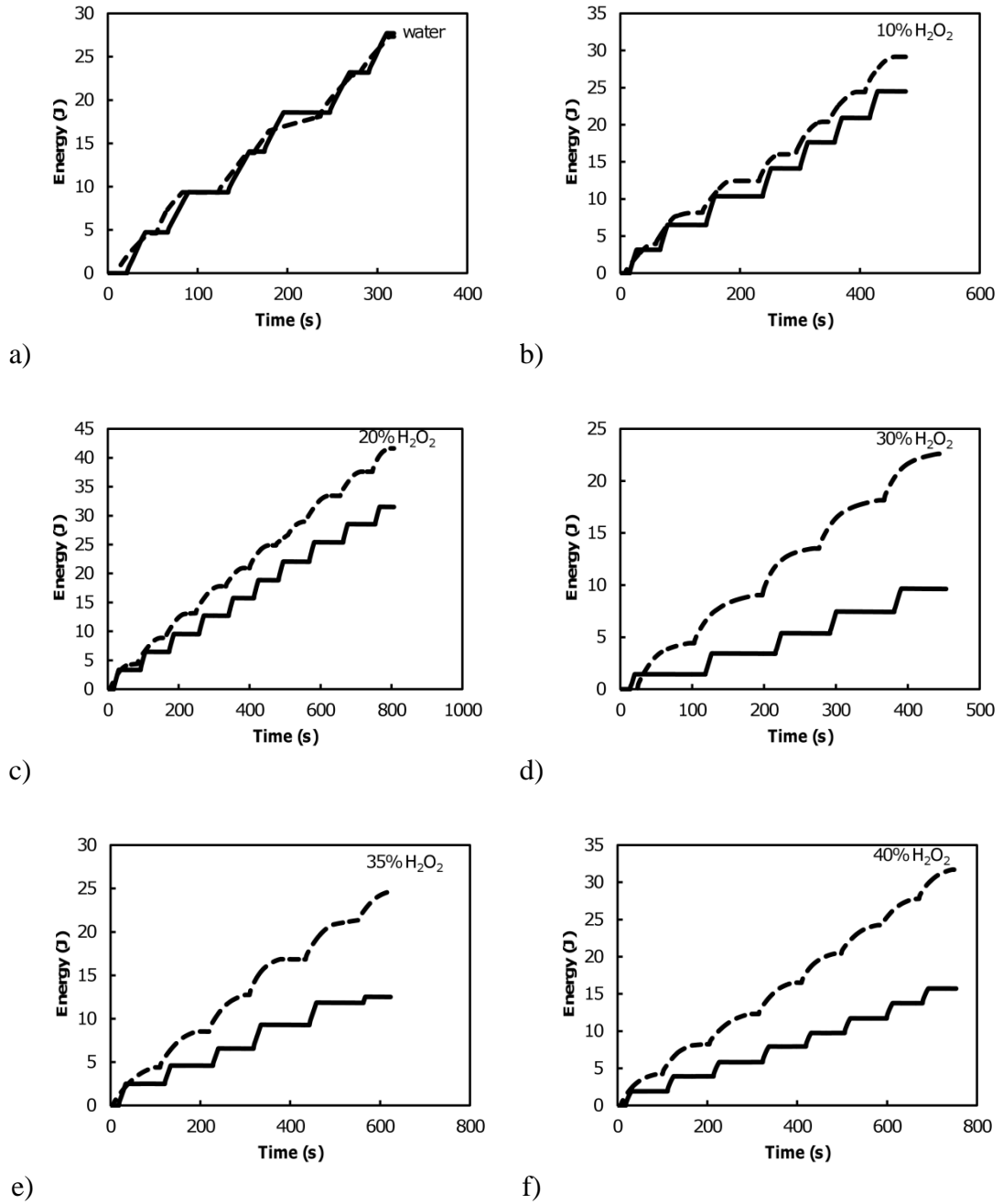
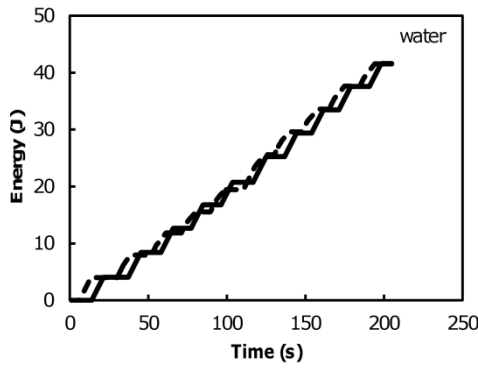
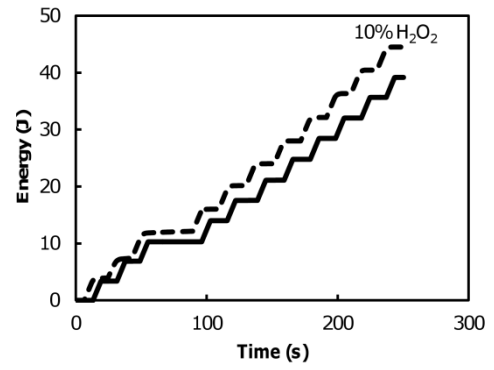


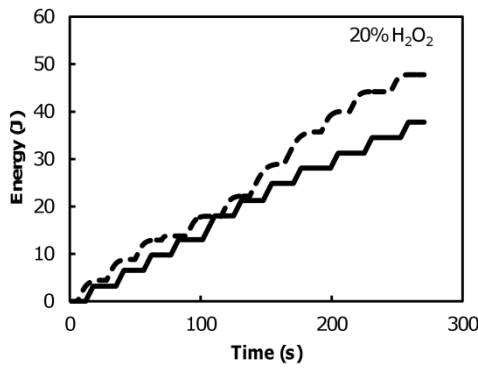
Figure A-5 The energy drawn over time of experiment when the each RTD was set to 105°C. Graphs show a) water, b) 10% hydrogen peroxide, c) 20% hydrogen peroxide, d) 30% hydrogen peroxide, e) 35% hydrogen peroxide and f) 40% hydrogen peroxide. Solid lines are coated RTD, dotted lines are uncoated.



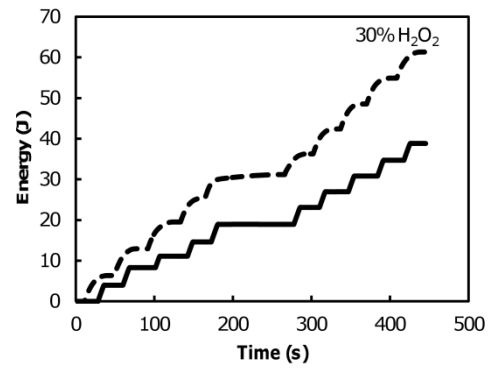
a)



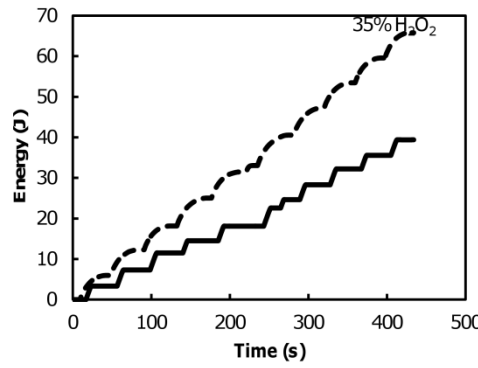
b)



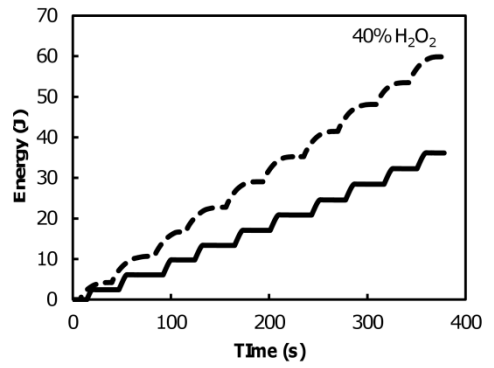
c)



d)



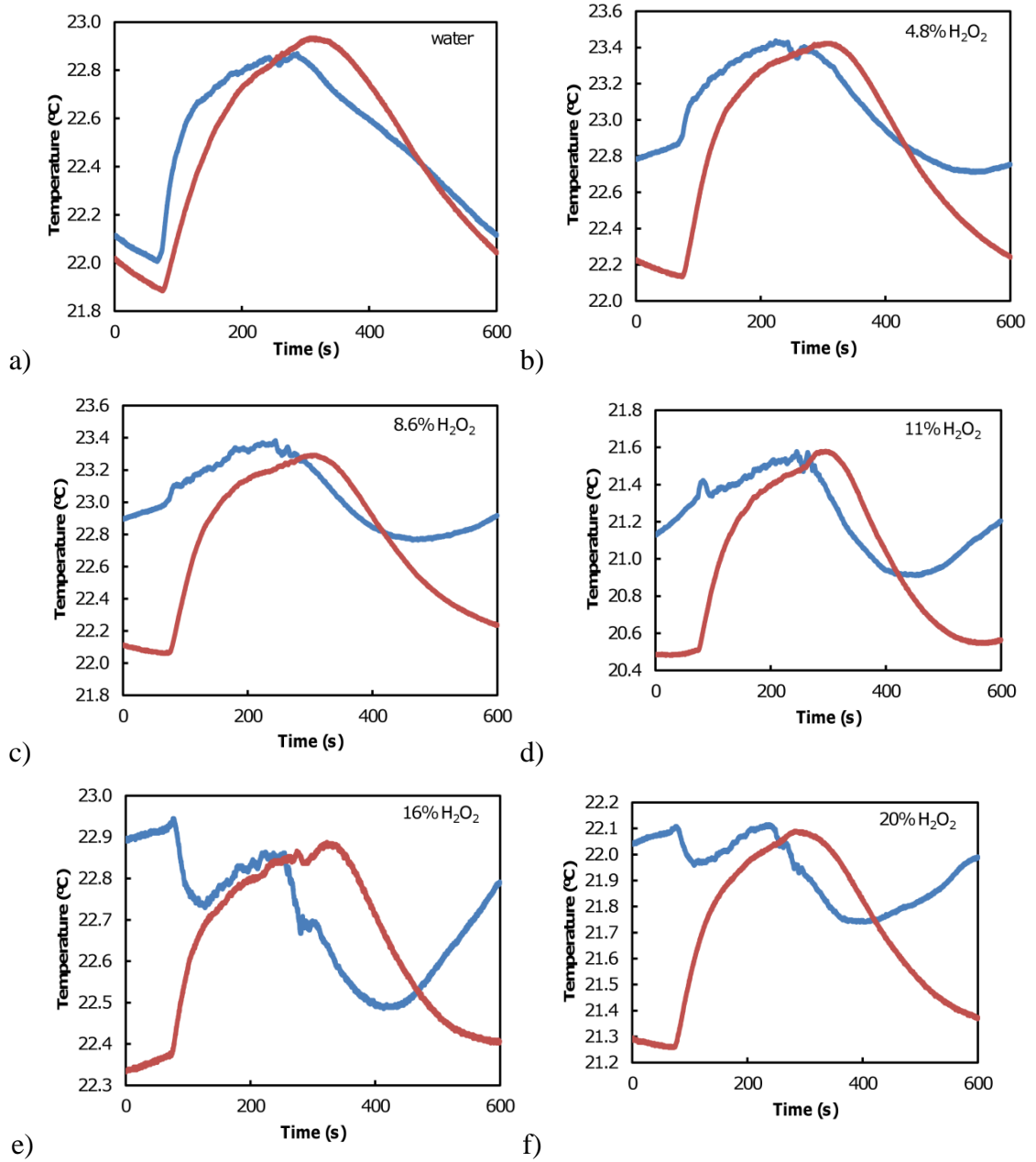
e)

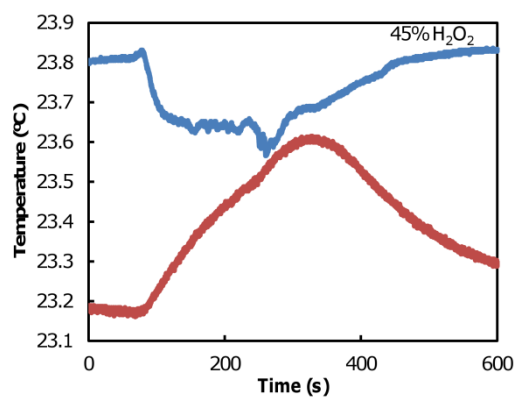
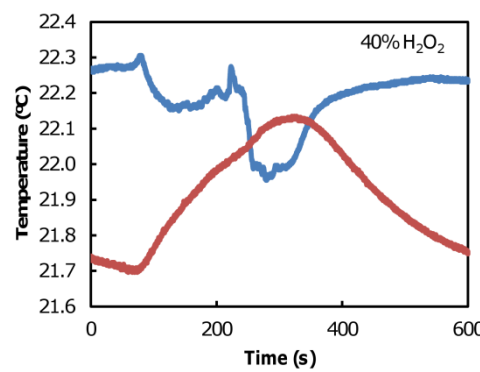
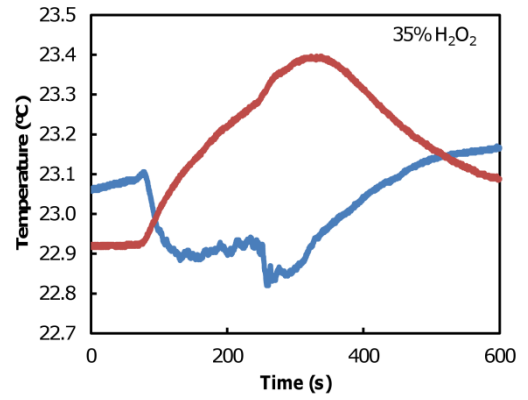
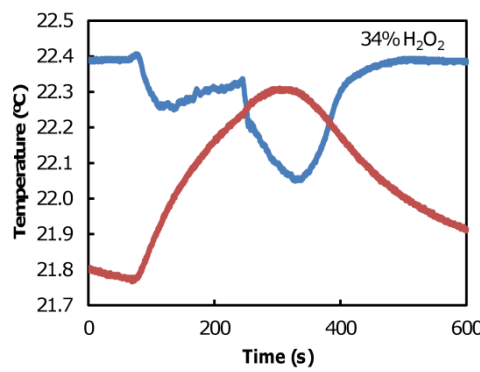
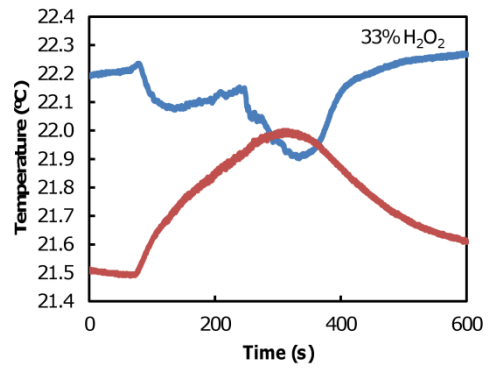
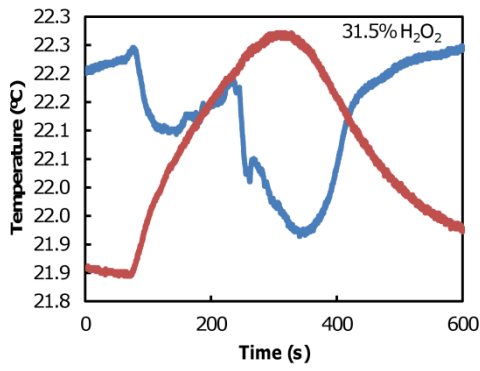
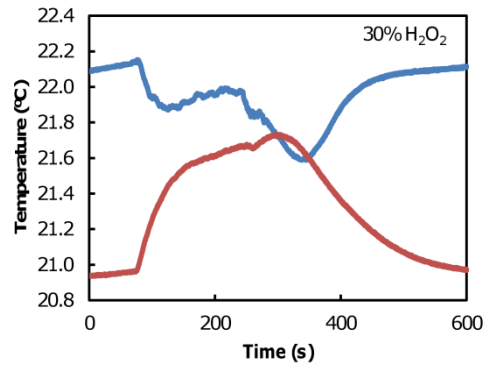
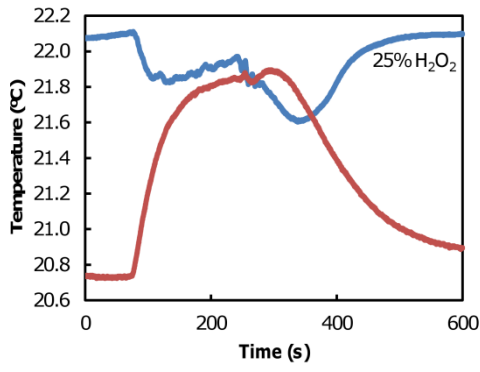


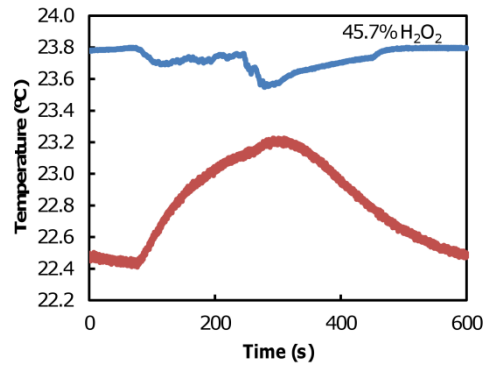
f)

Figure A-6 The energy drawn over time of experiment when the each RTD was set to 130°C. Graphs show a) water, b) 10% hydrogen peroxide, c) 20% hydrogen peroxide, d) 30% hydrogen peroxide, e) 35% hydrogen peroxide and f) 40% hydrogen peroxide. Solid lines are coated RTD, dotted lines are uncoated.

The data below is an example of the unheated MnO_2 sensors response to a mist of different concentration of hydrogen peroxide over 3 minute mist cycles. The processed data is seen in Chapter 6.2.5.







o)

Figure A-7 The typical response of the coated (blue line) and uncoated RTDs (red line) in 3 minute mist streams of hydrogen peroxide with concentrations of a) water, b) 4.8%, c) 8.6%, d) 11%, e) 16%, f) 20%, g) 25%, h) 30%, i) 31.5%, j) 33%, k) 34%, l) 35%, m) 40%, n) 45% and o) 45.7% hydrogen peroxide.

The tables below show the calculated K matrices for 10 micron and 100 micron thicknesses, as well as the K matrix for the combined data set. Each K value is given next to the wavelength it corresponds to. This was data was used to calculate the various refractive indices, k, in Chapter 7.2.2.

Table A-8 Matrix K for 10 micron thickness shown with the wavelengths to which it corresponds

Wavelength (μm)	K	
3.00	2.31E+05	3.60E+05
3.02	2.33E+05	3.44E+05
3.04	2.32E+05	3.44E+05
3.06	2.29E+05	3.44E+05
3.08	2.28E+05	3.46E+05
3.10	2.27E+05	3.42E+05
3.12	2.25E+05	3.43E+05
3.14	2.22E+05	3.46E+05
3.16	2.19E+05	3.51E+05
3.18	2.13E+05	3.59E+05
3.20	2.06E+05	3.61E+05
3.22	1.95E+05	3.70E+05
3.24	1.83E+05	3.76E+05
3.26	1.69E+05	3.79E+05
3.28	1.55E+05	3.81E+05
3.30	1.41E+05	3.77E+05
3.32	1.26E+05	3.76E+05
3.34	1.14E+05	3.76E+05
3.36	1.03E+05	3.76E+05
3.38	9.15E+04	3.84E+05
3.40	8.24E+04	3.91E+05
3.42	7.46E+04	4.11E+05
3.44	6.83E+04	4.33E+05
3.46	6.34E+04	4.60E+05
3.48	5.93E+04	4.91E+05
3.50	5.65E+04	5.14E+05

Wavelength (μm)	K	
3.52	5.29E+04	5.27E+05
3.54	4.95E+04	5.20E+05
3.56	4.52E+04	4.92E+05
3.58	4.09E+04	4.51E+05
3.60	3.77E+04	4.03E+05
3.62	3.47E+04	3.53E+05
3.64	3.28E+04	3.07E+05
3.66	3.12E+04	2.67E+05
3.68	3.06E+04	2.34E+05
3.70	2.96E+04	2.05E+05
3.72	2.94E+04	1.81E+05
3.74	2.89E+04	1.62E+05
3.76	2.86E+04	1.46E+05
3.78	2.83E+04	1.33E+05
3.80	2.83E+04	1.19E+05
3.82	2.79E+04	1.10E+05
3.84	2.73E+04	1.02E+05
3.86	2.76E+04	9.33E+04
3.88	2.73E+04	8.73E+04
3.90	2.68E+04	8.21E+04
3.92	2.69E+04	7.64E+04
3.94	2.70E+04	7.20E+04
3.96	2.70E+04	6.80E+04
3.98	2.72E+04	6.40E+04
4.00	2.73E+04	6.09E+04
4.02	2.72E+04	5.90E+04
4.04	2.80E+04	5.71E+04
4.06	2.92E+04	5.51E+04
4.08	2.95E+04	5.45E+04
4.10	2.93E+04	5.50E+04
4.12	3.01E+04	5.40E+04
4.14	3.19E+04	5.25E+04

Wavelength (μm)	K	
4.16	3.35E+04	5.26E+04
4.18	3.45E+04	5.47E+04
4.20	3.50E+04	5.68E+04
4.22	3.54E+04	5.99E+04
4.24	3.68E+04	6.26E+04
4.26	3.96E+04	6.41E+04
4.28	4.26E+04	6.72E+04
4.30	4.59E+04	7.04E+04
4.32	4.86E+04	7.45E+04
4.34	5.14E+04	8.21E+04
4.36	5.41E+04	8.95E+04
4.38	5.64E+04	9.51E+04
4.40	5.77E+04	9.74E+04

Table A-9 Matrix K for 100 micron thickness shown with the wavelengths to which it corresponds

Wavelength (μm)	K	
3.00	3.88E+04	7.56E+04
3.02	3.81E+04	7.87E+04
3.04	3.85E+04	7.47E+04
3.06	3.82E+04	7.41E+04
3.08	3.79E+04	7.55E+04
3.10	3.78E+04	7.60E+04
3.12	3.76E+04	7.61E+04
3.14	3.76E+04	7.45E+04
3.16	3.75E+04	7.48E+04
3.18	3.73E+04	7.43E+04
3.20	3.75E+04	7.39E+04
3.22	3.72E+04	7.38E+04
3.24	3.70E+04	7.43E+04
3.26	3.69E+04	7.29E+04
3.28	3.69E+04	7.39E+04
3.30	3.66E+04	7.38E+04
3.32	3.66E+04	7.22E+04
3.34	3.63E+04	7.23E+04
3.36	3.60E+04	7.45E+04
3.38	3.59E+04	7.20E+04
3.40	3.54E+04	7.36E+04
3.42	3.50E+04	7.56E+04
3.44	3.44E+04	7.64E+04
3.46	3.40E+04	7.63E+04
3.48	3.30E+04	8.10E+04
3.50	3.22E+04	8.02E+04
3.52	3.12E+04	8.60E+04
3.54	3.01E+04	8.87E+04
3.56	2.89E+04	9.09E+04
3.58	2.75E+04	9.55E+04
3.60	2.63E+04	9.70E+04

Wavelength (μm)	K	
3.62	2.45E+04	1.02E+05
3.64	2.29E+04	1.03E+05
3.66	2.15E+04	1.05E+05
3.68	2.00E+04	1.02E+05
3.70	1.86E+04	1.01E+05
3.72	1.76E+04	9.60E+04
3.74	1.67E+04	9.10E+04
3.76	1.61E+04	8.48E+04
3.78	1.56E+04	7.88E+04
3.80	1.52E+04	7.29E+04
3.82	1.51E+04	6.66E+04
3.84	1.50E+04	6.12E+04
3.86	1.50E+04	5.67E+04
3.88	1.51E+04	5.15E+04
3.90	1.53E+04	4.74E+04
3.92	1.55E+04	4.38E+04
3.94	1.58E+04	3.99E+04
3.96	1.61E+04	3.69E+04
3.98	1.64E+04	3.42E+04
4.00	1.69E+04	3.16E+04
4.02	1.73E+04	2.91E+04
4.04	1.77E+04	2.72E+04
4.06	1.82E+04	2.59E+04
4.08	1.86E+04	2.41E+04
4.10	1.92E+04	2.22E+04
4.12	1.97E+04	2.14E+04
4.14	2.02E+04	2.09E+04
4.16	2.07E+04	2.06E+04
4.18	2.12E+04	2.01E+04
4.20	2.17E+04	2.03E+04
4.22	2.23E+04	2.08E+04
4.24	2.29E+04	2.14E+04

Wavelength (μm)	K	
4.26	2.35E+04	2.20E+04
4.28	2.40E+04	2.30E+04
4.30	2.45E+04	2.46E+04
4.32	2.51E+04	2.58E+04
4.34	2.58E+04	2.70E+04
4.36	2.65E+04	2.89E+04
4.38	2.70E+04	3.05E+04
4.40	2.74E+04	3.12E+04

Table A-10 Matrix K for both 10 micron and 100 micron thickness shown with the wavelengths to which it corresponds

Wavelength (μm)	K	
3.00	4.09E+04	7.87E+04
3.02	4.02E+04	8.16E+04
3.04	4.05E+04	7.76E+04
3.06	4.03E+04	7.71E+04
3.08	3.99E+04	7.85E+04
3.10	3.99E+04	7.89E+04
3.12	3.96E+04	7.90E+04
3.14	3.96E+04	7.75E+04
3.16	3.95E+04	7.78E+04
3.18	3.91E+04	7.74E+04
3.20	3.93E+04	7.70E+04
3.22	3.89E+04	7.70E+04
3.24	3.86E+04	7.76E+04
3.26	3.83E+04	7.62E+04
3.28	3.81E+04	7.73E+04
3.30	3.77E+04	7.71E+04
3.32	3.75E+04	7.55E+04
3.34	3.71E+04	7.55E+04
3.36	3.68E+04	7.78E+04
3.38	3.65E+04	7.54E+04
3.40	3.59E+04	7.70E+04
3.42	3.54E+04	7.92E+04
3.44	3.47E+04	8.02E+04
3.46	3.43E+04	8.04E+04
3.48	3.33E+04	8.54E+04
3.50	3.25E+04	8.49E+04
3.52	3.14E+04	9.08E+04
3.54	3.03E+04	9.33E+04
3.56	2.91E+04	9.52E+04
3.58	2.77E+04	9.93E+04

Wavelength (μm)	K	
3.60	2.64E+04	1.00E+05
3.62	2.46E+04	1.05E+05
3.64	2.30E+04	1.06E+05
3.66	2.16E+04	1.06E+05
3.68	2.01E+04	1.04E+05
3.70	1.87E+04	1.02E+05
3.72	1.77E+04	9.69E+04
3.74	1.68E+04	9.17E+04
3.76	1.62E+04	8.55E+04
3.78	1.58E+04	7.94E+04
3.80	1.54E+04	7.34E+04
3.82	1.52E+04	6.70E+04
3.84	1.51E+04	6.17E+04
3.86	1.51E+04	5.71E+04
3.88	1.52E+04	5.19E+04
3.90	1.54E+04	4.78E+04
3.92	1.56E+04	4.41E+04
3.94	1.59E+04	4.03E+04
3.96	1.62E+04	3.72E+04
3.98	1.66E+04	3.45E+04
4.00	1.70E+04	3.19E+04
4.02	1.74E+04	2.94E+04
4.04	1.78E+04	2.75E+04
4.06	1.83E+04	2.62E+04
4.08	1.87E+04	2.44E+04
4.10	1.93E+04	2.26E+04
4.12	1.98E+04	2.18E+04
4.14	2.03E+04	2.13E+04
4.16	2.08E+04	2.09E+04
4.18	2.13E+04	2.05E+04
4.20	2.18E+04	2.07E+04
4.22	2.25E+04	2.13E+04

Wavelength (μm)	K	
4.24	2.31E+04	2.18E+04
4.26	2.37E+04	2.25E+04
4.28	2.42E+04	2.35E+04
4.30	2.48E+04	2.51E+04
4.32	2.54E+04	2.63E+04
4.34	2.61E+04	2.76E+04
4.36	2.68E+04	2.95E+04
4.38	2.73E+04	3.12E+04
4.40	2.77E+04	3.19E+04

The values of the pseudoinverse matrix, C_{cal}^{-1} for the individual 10 and 100 micron data sets is shown in Figure A-8

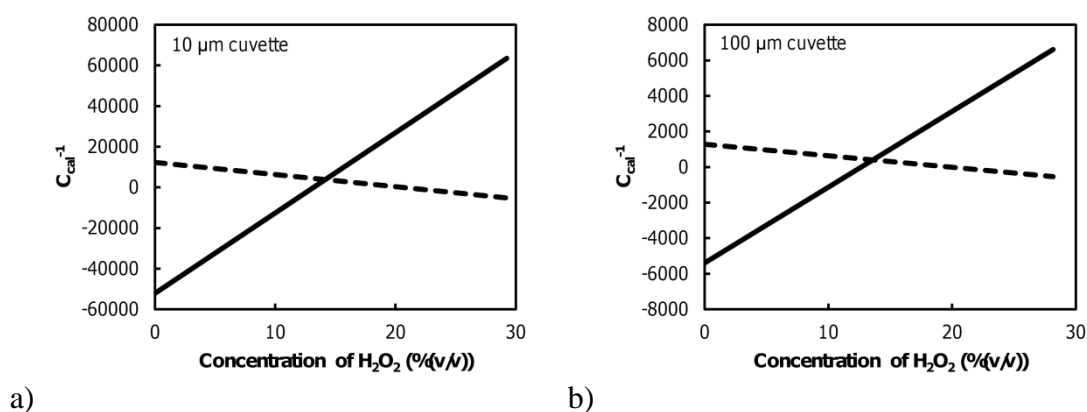
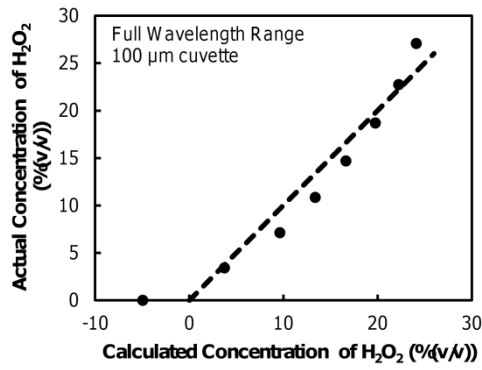


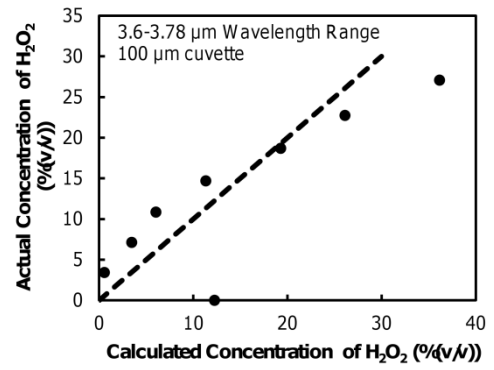
Figure A-8 The C_{cal}^{-1} for each concentration of hydrogen peroxide for thicknesses of a) 10 μm and b) 100 μm . The solid line represents the hydrogen peroxide values while the dotted line represents the water values.

The values of the pseudoinverse matrix, C_{cal}^{-1} for the combined data sets is shown in Figure A-10.

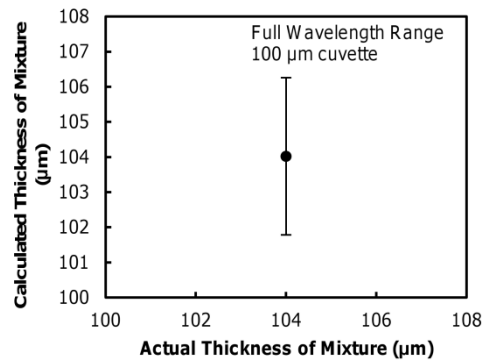
The calculated concentrations and thicknesses of hydrogen peroxide using the whole range and the range around the 3.7 micron peak for the 100 micron data can be seen in Figure A-9.



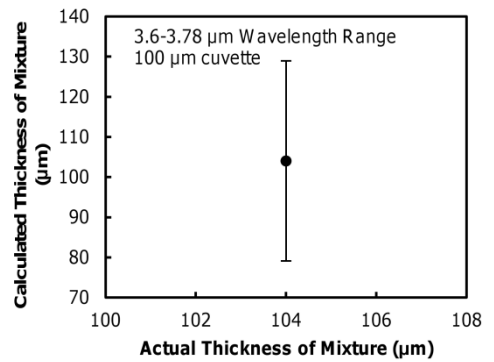
a)



b)



c)



d)

Figure A-9 The concentration of hydrogen peroxide and the total cuvette thickness calculated from the 100 thickness data using a) & c) the full range and b) & d) the 3.6-3.78 micron range. Dotted line represents a 1:1 linear line.

The values of the pseudoinverse matrix, C_{cal}^{-1} for the combined data sets is shown in Figure A-10.

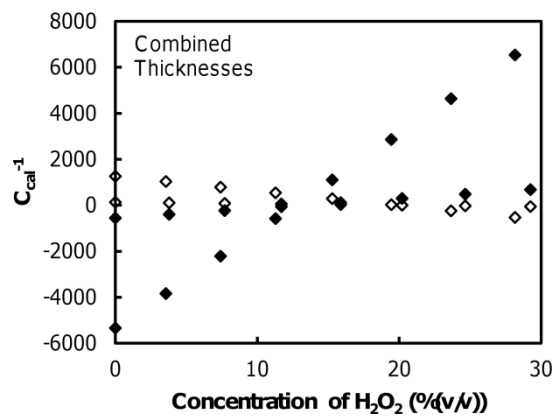


Figure A-10 The C_{cal}^{-1} values using the combined 10 μm and 100 μm thickness data sets for different concentrations of hydrogen peroxide. Hydrogen peroxide data is represented by (♦) and water data is represented by (◇).

The calculated concentrations and thicknesses of hydrogen peroxide using the combined data sets whole range, the range around the 3.5 micron peak visible in the 10 micron data and the range around the 3.7 micron peak for the 100 micron data can be seen in Figure A-11.

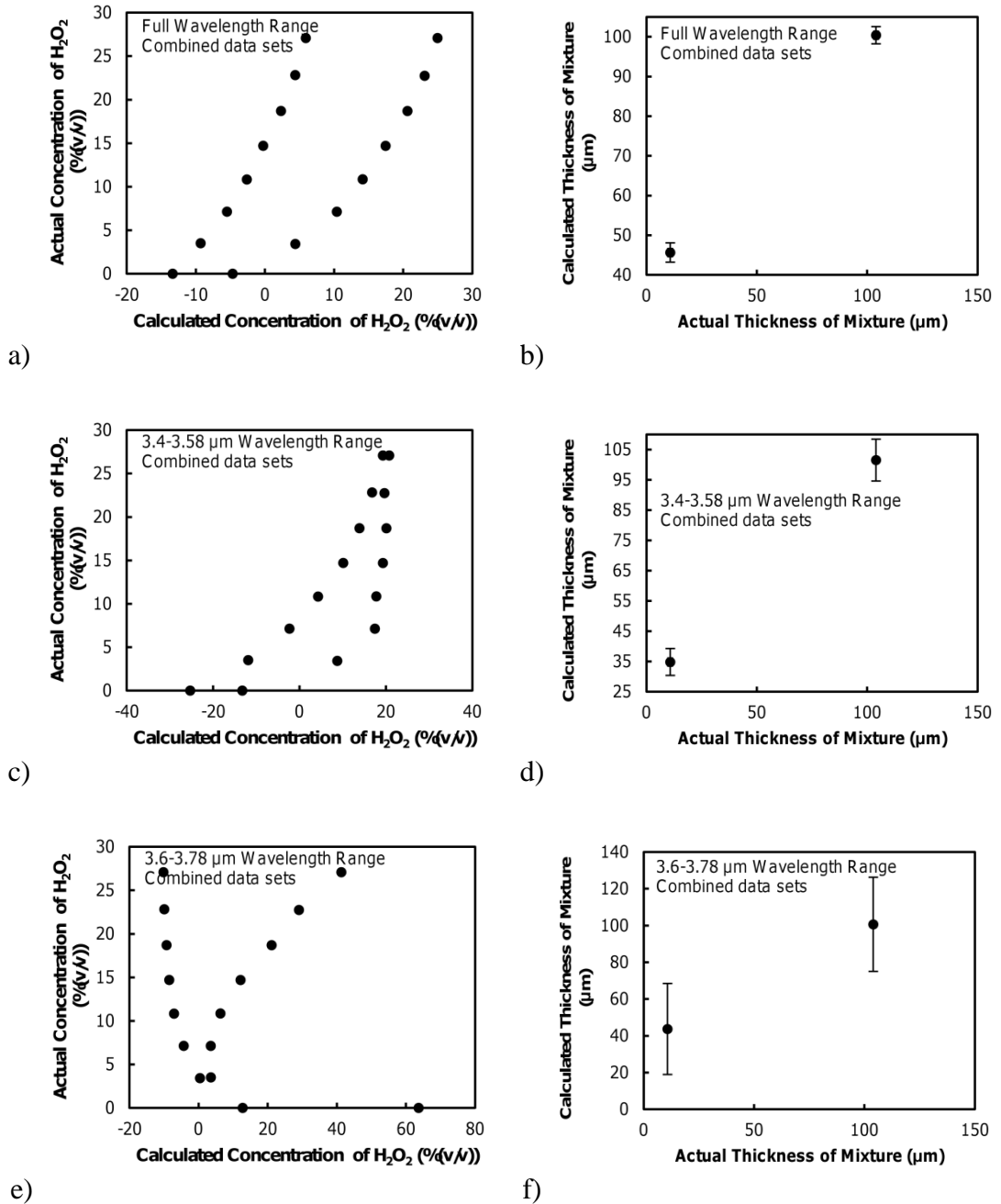


Figure A-11 The concentration of hydrogen peroxide and total mixture thickness estimated using the combined data set using a) & b) the whole range, c) & d) 3.4-3.58 microns and e) & f) 3.6-3.78 microns.